Micromechanical studies of ultrasonic fatigue in Ti-6Al-4V



Lazuardi Suryolaksono Pujilaksono

Corpus Christi College

University of Oxford

Supervisors: Prof Angus Wilkinson and Dr Jicheng Gong

A thesis submitted for the degree of

Doctor of Philosophy

Michaelmas 2025

Acknowledgements

First and foremost, I would like to express my sincere gratitude to my supervisors, Prof. Angus Wilkinson and Dr. Jicheng Gong, for their outstanding guidance and support throughout the entirety of this DPhil programme. Their patience, availability, and encouragement provided me with the confidence and resilience needed to navigate what has been a highly challenging and rewarding period of research. I am particularly grateful for the academic freedom they afforded me, including opportunities to attend conferences and undertake demonstration duties, which have been invaluable in developing my transferable research and communication skills. I would also like to thank Robin Scales and Hanqing Liu, members of the small Fatigue group, for their time, inspiration, and many stimulating intellectual discussions, which have greatly enriched my research experience.

My thanks also extend to the Oxford Micromechanics Group and Prof. Dave Armstrong for the welcoming and intellectually stimulating group environment. The group meetings provided an excellent platform to practice presentations and receive constructive feedback. I am grateful to Xinrui Huang for the many informal and insightful discussions, particularly on HR-EBSD. Thanks to Kieran Rivers, not only as a colleague within the group, but more importantly as a close friend whose constant invitations to socialise made the DPhil journey far more enjoyable.

I would like to acknowledge the support of the DCCEM staff, especially Dr. Phani Karamched, for their continued assistance, availability for discussing, and generosity in providing access to facilities essential to this work.

Finally, I wish to thank my family. I am deeply grateful to my parents, who, despite limited resources, prioritised education and instilled in me the belief that education can transform one's future. I thank my sister for her unwavering moral support throughout my life. I would like to thank my wife, the newest member of my family, for her love, patience, and understanding, particularly during the prolonged periods of long distance separation while I pursued higher education for our shared future.

Abstract

This thesis investigates the micromechanics of fatigue in Ti-6Al-4V through the development and application of an ultrasonic bending fatigue rig, combined with advanced electron backscatter diffraction (EBSD) characterisation techniques and supporting computational approaches. The fatigue life was examined across a wide life regime to very high cycle fatigue (VHCF), with particular emphasis on early crack formation and microstructure-sensitive short crack growth.

The sample preparation method was first evaluated in terms of the effects on fatigue performance. The removal of redeposit layers and improving surface quality by electropolishing were found to moderately improve fatigue strength of approximately 50 MPa at 10^7 cycles and up to 200 MPa at 10^9cycles. Comparisons with lower frequency fatigue data revealed a frequency dependence of fatigue strength. The results indicate that strain rate sensitivity in Ti-6Al-4V is most pronounced at low frequencies and diminishes as testing frequency increases. Environmental effects were also substantial: fatigue testing in high vacuum (10^{-6} mbar) produced higher fatigue strengths and markedly lower crack propagation rates than tests conducted in air.

Fractography and trace analysis demonstrated that fatigue crack initiation is inherently crystallographic, with all observed initiation events occurring on near-basal planes. While no direct correlation was found between global texture and fatigue strength, a strong relationship emerged when considering local microtexture at fatigue crack initiation (FCI) and 'hotspot' regions. Clustering of favourably oriented grains promoted both reduced fatigue strength and

accelerated short crack growth, whereas grain size alone showed no systematic influence. Local crack growth retardation and crack path deflections were linked to slip system transitions and grain boundary interactions, highlighting the microstructure-sensitive nature of short crack propagation.

Lastly, a different reference pattern selection technique for high-angular resolution EBSD (HR-EBSD) was proposed. A multi-reference pattern approach was introduced to mitigate reference-pattern bias in lattice rotation gradient and geometrically necessary dislocation (GND) density calculations, producing more physically consistent strain and GND maps. This framework was applied to interrupted fatigue experiments, enabling direct observation of elastic strain and dislocation evolution ahead of a fatigue crack tip over a quarter fatigue cycle.

Table of contents

List of figures **xi**

List of tables **xxi**

1 Literature Review **1**

1.1 Titanium alloys 1

1.1.1 Deformation of titanium 2

1.1.2 Alloying contents and microstructure variations in titanium alloys . 4

1.2 Fatigue design in alloys 8

1.2.1 Fatigue life 8

1.2.2 Fatigue crack initiation in very high cycle fatigue 10

1.2.3 Short crack growth 15

1.3 Ultrasonic fatigue testing 18

1.3.1 In comparison to fatigue testing at lower frequencies 18

1.3.2 Methodology of a general ultrasonic fatigue setup 20

1.3.3 Bending fatigue of meso cantilevers: a sample and setup variation in ultrasonic fatigue 21

1.4 Electron Backscatter Diffraction (EBSD) 23

1.4.1 The resolution of conventional EBSD (Hough-based indexing) . . . 25

1.4.2 High-Angular Resolution EBSD (HR-EBSD) 27

1.4.3 GND analysis using HR-EBSD 33
1.5 Aims of this work 36

2 Sample preparation and method development 39
2.1 Material and sample preparation 39
2.1.1 Sample preparation 40
2.1.2 Meso cantilever designs 42
2.1.3 Electropolishing 46
2.2 Experimental methods and method development 48
2.2.1 Ultrasonic fatigue testing protocol 55
2.2.2 Automation using live-image analysis 61
2.2.3 Fatigue crack growth measurements 65

3 Bending fatigue life of Titanium 6Al-4V 71
3.1 Introduction 71
3.2 Experimental methods 72
3.3 Results and Discussions 73
3.3.1 The effect of the redeposit layer on fatigue life 73
3.3.2 Ultrasonic bending fatigue data in comparison to data in the literature 80
3.3.3 The environmental effects on fatigue properties 83
3.4 Summary 96

4 Fatigue crack initiation in very high cycle fatigue 99
4.1 Introduction 99
4.2 Experimental methods 100
4.3 Results 100
4.3.1 IFS10 100
4.3.2 IFS19 107

4.3.3 IFS21 . . . 113
4.3.4 IFS24 . . . 119
4.3.5 IFS25 . . . 124
4.4 Discussions . . . 129
4.4.1 The grain orientation of fatigue crack initiation features . . . 129
4.4.2 The effect of texture on fatigue strength . . . 132
4.4.3 The influence of grain orientations and local texture on fatigue short crack growth . . . 135
4.4.4 The grain size distribution of fatigue crack initiation features . . . 137
4.5 Summary . . . 139

5 Crack tip strain evolution in fatigue short crack growth 143
5.1 Introduction . . . 143
5.2 Experimental methods . . . 144
5.3 High-angular Resolution EBSD . . . 146
5.4 Results and discussions . . . 149
5.4.1 The usage of multiple reference patterns . . . 149
5.4.2 Strain evolution and GND density analysis of a fatigue crack tip . . . 160
5.5 Summary . . . 176

6 The conclusions of this work 179

References 183

Appendix A Appendix 195
A.1 MATLAB script for image processing of captured laser streaks . . . 195
A.2 MATLAB script for detecting fatigue crack initiation . . . 196

List of figures

1.1 Slip system of the HCP crystal structure [5] 4

1.2 Processing method for obtaining a lamellar microstructure in $\alpha + \beta$ Ti alloys [11] 5

1.3 The effect of annealing cooling rate on Ti-6242 lamellar microstructures (a) 1 (b) 100 (c) 8000° C/min respectively [11] 6

1.4 Processing method for obtaining a bimodal microstructure in $\alpha + \beta$ Ti alloys [11] 7

1.5 Difference in grain size due to (a) slow cooling rate and (b) fast cooling rate in IMI 834 alloy [5] 7

1.6 Processing method for obtaining an equiaxed microstructure in $\alpha + \beta$ Ti alloys [11] 7

1.7 Curve fitting models in an S-N curve 9

1.8 SEM image of a fish eye fractured surface found in steel after being subjected to VHCF 11

1.9 A schematic illustration of fatigue crack growth in the VHCF regime [27, 28] 12

1.10 A duplex S-N curve from a mill-annealed Ti-6Al-4V [20] 13

1.11 The increase in ODA size with higher fatigue cycles to failure [37] 14

1.12 (a) Model profile of a deflected crack segment with the associated nomenclature, (b)-(d) Predicted crack propagation rates for deflected cracks as a function of the angle of deflection θ and the length of deflection $D/(D+S)$[42] 17
1.13 Cantilever specimen (a) describing the actuation and oscillation for bending and (b) finite element analysis describing the stress conditions in the gauge [57] 22
1.14 CAD design of the microfatigue setup used in Straub et al [57] 22
1.15 The formation of kikuchi lines in from EBSD [59] 24
1.16 (a) EBSP recorded from GaN (b) ROI extracted from analysis (c) Intensity and contrast of the edges are brought to zero using a weighted function (d) Fourier transform of the weighted ROI (e) Band pass filter to Fourier transform (f) Back transform (g) Cross-correlation with reference pattern (after similar image processing) [66] 31
1.17 Schematic diagram illustrating how strain and rotation alters zone axis direction **r** across the EBSD screen by **q** [66] 32

2.1 As-received titanium disc 40
2.2 Equiaxed microstructure of Ti-6Al-4V used in this study 41
2.3 Grinding and polishing tripod used in this research to prepare Ti-6Al-4V foils 42
2.4 Boundary condition for eigenfrequency and dynamic perturbation simulations in Abaqus 43
2.5 (a) Laser milling of meso cantilevers (b) Ti-6Al-4V foil with laser-machined meso cantilevers 45
2.6 Various sample designs. (a) First sample design with a 3 mm outer radius (b) Second design with ligaments to be broken for fractography (c) Third design for interrupted fatigue testing. The pictures are not in scale. 46
2.7 Diagram of electropolishing setup 48
2.8 Diagram of ultrasonic fatigue setup 50

2.9 Schematic of the mounting mechanisms (a) a modified M5 grub screw (b) 0.2 mm spacer and two M1.6 screws 51
2.10 Schematic of the geometry used for converting laser streak measurements to the bending angles in Equation 2.1. The red and blue colours on the gauge is used to visualise the states of tension and compression, respectively 52
2.11 An example of (a) stress distribution in the S11 (cantilever direction) and (b) displacement in U3, used for the calculations of stress per angles for each sample. The units are in Pa and m for the stress and displacement, respectively 53
2.12 An example of fatigue test using the step-stress method, revealing linear elastic response until the initiation of a fatigue crack which is reflected by the gain in compliance 54
2.13 Stress per angle measurements from FEA as a function of sample thickness 54
2.14 S-N plot of final runouts and failed data points 58
2.15 An example of a logistic regression with overlapping data points for a fatigue life of 10^7 cycles 59
2.16 An example of a logistic regression with no overlapping data points for a fatigue life of 10^4 cycles 60
2.17 S-N Curve processed using logistic regression 60
2.18 Image processing protocol employed in this study to automate the measurement of bending angles and stress amplitudes 62
2.19 Interrupted fatigue flowchart of the MATLAB script employed in this study to detect short crack growth 63
2.20 An example of a fatigue test categorised as runout/survived 64
2.21 An example of a fatigue test with detected fatigue crack initiation. The onset of fatigue crack initiation is determined in a semi-manual manner, by choosing a value that is above the average noise of the deflection angle during testing. 64

2.22 The change in bending angle as a function of crack length 66
2.23 Overestimation of fatigue crack lengths 67
2.24 Underestimation of fatigue crack lengths 67
2.25 (a) Global view of the meso cantilever with the crack seam (b) Magnified view of the crack seam showing the employed 3:1 length to width ratio (c) Magnified view of the contour lines 69

3.1 Recast layer on the side surfaces of samples (a) global view (b) magnified view 76
3.2 The removal of recast layers after (a) 40 and (b) 60 seconds of electropolishing 77
3.3 Surface quality of (a) as-received (b) electropolished meso cantilevers . . . 78
3.4 S-N plot of as-received Ti-6Al-4V meso cantilevers with recast layers indicated by Figures 3.1 and 3.3a 79
3.5 S-N plot of electropolished Ti-6Al-4V meso cantilevers with surface quality indicated by Figures 3.2b and 3.3b 79
3.6 Comparison of fatigue life performance between electropolished samples and as-received samples with recast layers. Data processed by logistic regression as discussed in Chapter 2 80
3.7 Comparison of fatigue life between bending ultrasonic fatigue at 20 kHz and uniaxial fatigue at lower frequencies. Selected literature were all performed at R = –1 [92–95] 82
3.8 Comparison of fatigue life between ultrasonic bending fatigue and ultrasonic uniaxial fatigue at 20 kHz. Selected literature were all performed at R = –1 [36, 92] 83
3.9 Comparison of fatigue life between electropolished samples performed in air and in vacuum 84
3.10 Fatigue crack propagation plot of samples tested in air and vacuum ($\sim 10^{-6}$ mbar 85

3.11 (a) Fracture surface of Ti-6Al-4V tested in air at 10^8 cycles (b) FCI facet (c) striations in the intermediate regions. An average striation spacing of 0.49 microns has been measured in this field of view 88
3.12 Surfaces of a fatigued sample performed in ambient air at 10^8 cycles (a) Crack initiation side (b) Opposing side 89
3.13 Fracture surface of Ti-6Al-4V tested in vacuum at 10^8 cycles 92
3.14 Surfaces of a fatigued sample performed in high vacuum at 10^8 cycles (a) Crack initiation side (b) Opposing side 93
3.15 STEM-EDS micrograph showing the oxygen and vanadium contents in an FCI grain from a sample tested in ambient air at 10^8 cycles. The area with a high vanadium content represents the β phase 94
3.16 STEM-EDS micrograph showing the oxygen content in an FCI grain from a sample tested in high vacuum at 10^8 cycles 94

4.1 (a) IPFX Map and (b) Pole Figure of IFS10 sample 101
4.2 Interrupted fatigue sequence for IFS10 sample 102
4.3 Schmid Factor (SF) analysis of the fatigue crack in IFS10 (a) Optical microscope image (b) IPFX Map with the outlined fatigue crack path and grain numbers (c) Basal SF (d) Prismatic SF 104
4.4 Trace analysis of the fatigue crack for IFS10. The ends of the batons are coloured red or blue to signify the corresponding slip trace, while the grayscale colour on the body signifies the intensity of the Schmid factor. 104
4.5 Orientations and grain sizes of FCI grains (coloured circles) in respect to the basal and prismatic isocurves and the orientation of 'hotspot' grains (white circles) in IFS10. 'Hotspot' grains are located in high stress areas of the gauge during cyclic bending, which are alongside the sides of the meso cantilever surfaces 105

4.6 Orientations of FCI and neighbouring grains in respect to the texture of 'hotspot' grains in IFS10 105
4.7 Luster-Morris parameter (m′) calculations based on (top) maximum m′ and (bottom) maximum Schmid factor for Grain 1 and 2. The red arrows point to the physical matching of the trace analysis 106
4.8 Texture analysis of IFS19 sample 107
4.9 Interrupted fatigue sequence for IFS19 sample 108
4.10 Schmid Factor (SF) analysis of the fatigue crack in IFS19 (a) Optical microscope image (b) IPFX Map with the outlined fatigue crack path and grain numbers (c) Basal SF (d) Prismatic SF 109
4.11 Trace analysis of fatigue crack in IFS19. The ends of the batons are coloured red or blue to signify the corresponding slip trace, while the grayscale colour on the body signifies the intensity of the Schmid factor. 110
4.12 Orientations and grain sizes of FCI grains in respect to the basal and prismatic isocurves and the orientation of 'hotspot' grains in IFS19 110
4.13 Orientations of FCI and neighbouring grains in respect to the texture of 'hotspot' grains in IFS19 111
4.14 Luster-Morris parameter (m′) calculations based on (top) maximum m′ and (bottom) maximum Schmid factor for Grain 1 and 2. The red arrows point to the physical matching of the trace analysis 112
4.15 Texture analysis of IFS21 sample 113
4.16 Interrupted fatigue sequence for IFS21 sample 114
4.17 Schmid Factor (SF) analysis of the fatigue crack in IFS21 (a) Optical microscope image (b) IPFX Map with the outlined fatigue crack path and grain numbers (c) Basal SF (d) Prismatic SF 115

4.18 Trace analysis of fatigue crack in IFS21. The ends of the batons are coloured red or blue to signify the corresponding slip trace, while the grayscale colour on the body signifies the intensity of the Schmid factor. 115
4.19 Orientations and grain sizes of FCI grains in respect to the basal and prismatic isocurves and the orientation of 'hotspot' grains in IFS21 116
4.20 Orientations of FCI and neighbouring grains in respect to the texture of 'hotspot' grains in IFS21 117
4.21 Luster-Morris parameter (m′) calculations based on (top) maximum m′ and (bottom) maximum Schmid factor for Grain 1 and 2. The red arrows point to the physical matching of the trace analysis 118
4.22 Texture analysis of IFS24 sample 119
4.23 Interrupted fatigue sequence for IFS24 sample. The ends of the batons are coloured red or blue to signify the corresponding slip trace, while the grayscale colour on the body signifies the intensity of the Schmid factor. . . 120
4.24 Schmid Factor (SF) analysis of the fatigue crack in IFS24 (a) Optical microscope image (b) IPFX Map with the outlined fatigue crack path and grain numbers (c) Basal SF (d) Prismatic SF 121
4.25 Trace analysis of fatigue crack in IFS24 121
4.26 Orientations and grain sizes of FCI grains in respect to the basal and prismatic isocurves and the orientation of 'hotspot' grains in IFS24 122
4.27 Orientations of FCI and neighbouring grains in respect to the texture of 'hotspot' grains in IFS24 122
4.28 Luster-Morris parameter (m′) calculations based on (top) maximum m′ and (bottom) maximum Schmid factor for Grain 1 and 2. The red arrows point to the physical matching of the trace analysis 123
4.29 Texture analysis of IFS25 sample 124

4.30 Interrupted fatigue sequence for IFS25 sample 124
4.31 Schmid Factor (SF) analysis of the fatigue crack in IFS25 (a) Optical microscope image (b) IPFX Map with the outlined fatigue crack path and grain numbers (c) Basal SF (d) Prismatic SF 125
4.32 Trace analysis of fatigue crack in IFS25. The ends of the batons are coloured red or blue to signify the corresponding slip trace, while the grayscale colour on the body signifies the intensity of the Schmid factor. 126
4.33 Orientations and grain sizes of FCI grains in respect to the basal and prismatic isocurves and the orientation of 'hotspot' grains in IFS25 127
4.34 Orientations of FCI and neighbouring grains in respect to the texture of 'hotspot' grains in IFS25 127
4.35 Luster-Morris parameter (m′) calculations based on (top) maximum m′ and (bottom) maximum Schmid factor for Grain 1 and 2. The red arrows point to the physical matching of the trace analysis 128
4.36 Normalised Schmid Factor (m') as a function of θ for all experimental FCI grains 130
4.37 Summary of basal texture of IFS-labeled meso cantilevers. X, Y and Z are parallel, transverse and normal to the cantilever axis, respectively 133
4.38 Summary of IPFX plots of FCI and neighbouring grains in relation to the 'hotspot' grains 134
4.39 Fatigue crack propagation rates of IFS-labeled samples as a function of the stress intensity factor 137
4.40 The grain size distribution of 'hotspot' grains and FCI features 138

5.1 Bespoke in-situ SEM bending setup used to probe meso cantilever specimens (a) Schematic of the setup (b) View of inside the SEM 145

5.2 An example of a reference EBSP with 40 ROIs (256×256 pixels) to be cross-correlated with test patterns 148
5.3 Two EBSP located from different subcell regions within a grain, displayed by the slightly different shade of colour in the IPFX map 150
5.4 Individual components of the lattice rotation using a different set of reference patterns. The locations of the reference patterns for (a) and (b) are displayed in the respective top subplots. Units are in radian 151
5.5 Offset between Figures 5.4a and 5.4b. Units are in radian 152
5.6 GND comparison using two different sets of reference patterns. The scale is logged and the units are in m^{-2} 153
5.7 An example of post-processing elastic strain and lattice rotation data simplified using an arbitrary data: (a) Synthetic map, (b-c) Relative maps, termed R1 and R2. The black circles are the respective reference points, (d) Constant offset at all coordinates between R1 and R2, (e-f) Gradient maps of R1 and R2, respectively 155
5.8 The usage of multiple reference pattern overlaid on a grain boundary map . 156
5.9 Weight-averaged elastic strain map 158
5.10 Weight-averaged lattice rotation map. Units are in radian. 159
5.11 Weight-averaged GND density map. Units are in m^{-2}. 160
5.12 SEM image of intragranular fatigue crack tip 161
5.13 Crystal orientation map 161
5.14 Bending angle vs number of life cycles for IFS10 162
5.15 Crystal plasticity finite element (CP-FE) with symmetry boundary conditions (U1 = UR2 = UR3 = 0 for X plane normal, etc) and strain applied to the X direction There are 240 × 319 × 7 elements used in this model 165

5.16 An example of the obtained stress distribution for S11 (stress in the X direction). Units are in MPa 165
5.17 The individual components of the elastic strain tensor at different bending angles (a) undeflected (b) 2.9 degrees (c) 5.1 degrees 170
5.18 The GND density maps subjected to different bending angles (a) undeflected (b) 2.9 degrees (c) 5.1 degrees 172
5.19 The GND density maps calculated using a single reference pattern (chosen by a combination of high IQ, furthest distance to grain boundaries and nearest orientation to the mean orientation of the grain) and subjected to different bending angles (a) undeflected (b) 2.9 degrees (c) 5.1 degrees 174
5.20 AFM topography ahead of the fatigue crack tip 175

List of tables

2.1 Certified composition of the as-received Ti-6Al-4V 40

2.2 User parameters employed in Abaqus 43

3.1 STEM-EDS peak heights of a sample fatigued in ambient air at 10^8 cycles . 95

3.2 STEM-EDS peak heights of a sample fatigued in high vacuum at 10^8 cycles 95

4.1 Fatigue strength (crack initiation) at 10^8 cycles for IFS-labeled samples . . 132

4.2 FCI grain sizes and the fatigue strength at 10^8 cycles for IFS-labeleds samples 137

5.1 User Material values used for CP-FE 163

Chapter 1

Literature Review

1.1 Titanium alloys

Titanium alloys are valued for their low density, high specific strength, and excellent corrosion resistance, making them particularly attractive for weight-critical engineering applications, such as found in the aerospace sector. With a density approximately half than that of steel, titanium alloys can deliver comparable strength at significantly reduced mass. This combination enables substantial weight savings while maintaining structural integrity, which improves fuel efficiency and payload capacity. For these reasons, titanium alloys have progressively replaced precedent structural materials in the aerospace sector, such as steels, since the 1950s [1].

Early notable introduction of titanium alloys was made to the famous Pratt and Witney J57 engine in 1952 where titanium replaced steel in compressor blades and discs, resulting in an immediate weight reduction of approximately 200 kg [2]. The adoption of titanium in gas turbine engines became increasingly important during the development of high-bypass-ratio turbofan engines in the 1960s, which required larger fan blades and incorporated multi-stage compressor designs. In gas turbine engines, weight reduction is essential not only for efficiency gains but also for managing centrifugal stresses in rotating components. Jahnke

noted that every unit of mass removed from an engine equates to four to eight units potentially removed from the airframe [3]. Outside of the engine, titanium alloys have also replaced steel in modern landing gear structures, resulting to a saving of 270 kg for the Boeing 777 [1]. Other than steel, titanium alloys have also been increasingly used in place of aluminium alloys for space-constrained applications, where their higher strength enables reductions in component size [1].

The importance of titanium alloys in the aerospace sector is reflected by the increasing proportion of structural weight comprised from 0.5% for the Boeing 707 in 1958 to 9% for the Boeing 777 in 1994. Much greater percentage of system weight for titanium alloys is seen in military aircraft, which generally varies from 35 to 50% of the weight of modern fighter aircraft [1]. A notable extreme is the Lockheed SR-71 Blackbird, in which approximately 93% of the structural weight was composed of titanium alloys [4]. Three different types of titanium alloys were extensively used in the panels and the fuselage of the SR-71, because it was considered the only material strong and light enough to withstand the extreme heat generated at Mach 3 sustained flights.

1.1.1 Deformation of titanium

At room temperature, pure titanium exhibits a hexagonal close-packed (HCP) crystal structure, referred to as α-titanium, with lattice parameters a = 0.295 nm, c = 0.468 nm, and a c/a ratio of approximately 1.59. Figure 1.1 illustrates the principal slip planes and slip directions in an HCP crystal structure. In α-titanium, plastic deformation occurs predominantly by slip in the close-packed $\langle a \rangle$ directions on the $\{0001\}$ basal , $\{10\bar{1}0\}$ prismatic and $\{1\bar{1}01\}$ pyramidal planes. Slip in the $\langle c+a \rangle$ directions on pyramidal planes is also crystallographically possible; however, activation of $\langle c+a \rangle$ slip requires significantly higher stresses at room temperature. Lütjering and Williams report that the critical resolved shear stress (CRSS) required to activate $\langle c+a \rangle$ slip in Ti-6.6Al alloys is approximately four times higher than that required for basal

and prismatic $\langle a \rangle$ slip systems at room temperature [5]. As a result, plastic deformation in α-titanium is dominated by $\langle a \rangle$ slip, with the possibility of $\langle c+a \rangle$ slip becoming active in specific cases such as when the applied load is parallel to the c axis, resulting to a zero resolved shear stress on the $\langle a \rangle$ slip systems.

Above 882°C, α-pure titanium undergoes transformation to a body-centred cubic (BCC) phase, known as β-titanium. This transformation follows a well-defined crystallographic orientation relationship, such that the (110) planes of the β phase are parallel to the (0001) basal planes of the α phase. In the β phase, slip typically occurs on $\{110\}$ slip planes and $\langle 111 \rangle$ slip directions where it most closely packed.

While dislocation slip constitutes the primary mode of plastic deformation in titanium alloys, particularly at room temperature, deformation twinning provides an additional mechanism for accommodating plastic strain when slip alone is insufficient. This is especially relevant in α-titanium, which possesses an HCP crystal structure with a limited number of independent slip systems. Deformation twinning occurs through shear of the parent lattice, producing a mirror-like reorientation across a specific twinning plane. In HCP crystal, Yoo discussed four twin systems which are the $\langle 10\bar{1}1 \rangle\{10\bar{1}2\}$ and $\langle \bar{1}\bar{1}26 \rangle\{11\bar{2}1\}$ tensile twins, and the $\langle 11\bar{2}\bar{3} \rangle\{11\bar{2}2\}$ and $\langle 10\bar{1}\bar{2} \rangle\{10\bar{1}1\}$ compressive twins [6]. The difference between tension and compression twins are reflected by the direction of the twinning shear. Tension and compression twins cause an extension and a compression along the $\langle c \rangle$ axis, respectively. The propensity for twinning in titanium is strongly influenced by alloying content. Increasing concentrations of aluminium in titanium raise the critical resolved shear stress (CRSS) for $\langle c+a \rangle$ and inhibit twinning [7, 8]. As a result, twinning is prevalent in commercially pure or near-α titanium alloys but is largely suppressed in $\langle c+a \rangle$ alloys such as Ti-6Al-4V.

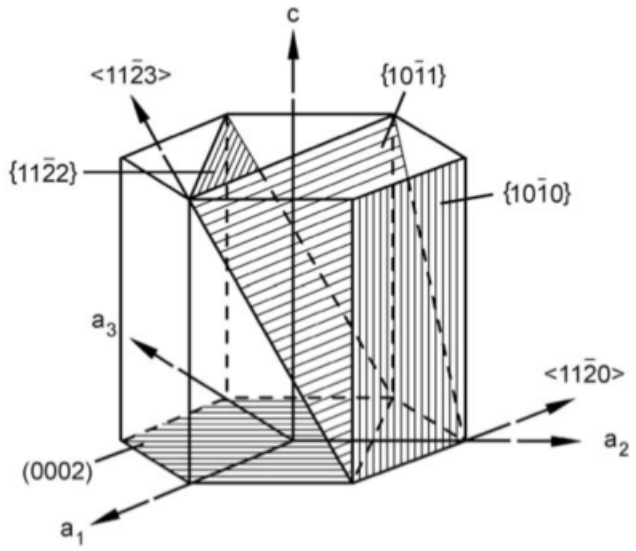


Fig. 1.1 Slip system of the HCP crystal structure [5]

1.1.2 Alloying contents and microstructure variations in titanium alloys

The properties of titanium alloys are influenced by alloying elements that are generally classified into α-stabilisers and β-stabilisers. α-stabilising elements promote the stability of the HCP α phase and increase the β-transus temperature. The most widely used α-stabiliser in titanium alloys is aluminium. In contrast, β-stabilising elements reduce the β-transus temperature, where vanadium is the most commonly employed. By varying the type and concentration of these alloying elements, titanium alloys can be categorised into three classes: α, $\alpha+\beta$, and β alloys.

α titanium alloys contain a high proportion of α-stabilisers and little or no β-stabilising elements. These alloys are characterised by their high temperature performance, oxidation resistance, and weldability compared to the other two categories of titanium alloys [9]. In addition, α alloys generally exhibit lower density than β-containing alloys due to the heavier β-stabilising elements. However, their room-temperature yield strength and formability are typically limited by the restricted number of active slip systems in the HCP structure. Conversely, β titanium alloys contain high concentrations of β-stabilising elements and

small amounts of α-stabilisers. The BCC structure provides a greater number of slip systems, leading higher strength in ambient temperatures and improved formability through thermomechanical processes compared with α alloys. However, these alloys generally have higher density and reduced elevated-temperature capability relative to α alloys. A balance of properties is achieved in $\alpha+\beta$ titanium alloys, which contain controlled proportions of both α- and β-stabilising elements. Ti–6Al–4V, the alloy of interest in this study, is the most widely used $\alpha+\beta$ titanium alloy and contains aluminium and vanadium in proportions that stabilise both phases. This dual-phase microstructure provides a favourable compromise between strength, ductility, fatigue resistance, fracture toughness, and processability, making Ti–6Al–4V particularly well suited for demanding aerospace applications [9].

The microstructure of $\alpha+\beta$ titanium alloys can be tailored through careful thermomechanical processing and heat treatments to produce three principal microstructural forms: lamellar, bimodal, and equiaxed. The process for obtaining a fully lamellar microstructures is summarised in Figure 1.2. The cooling rate after the recrystallisation (Step III) is the most important process in producing a desirable lamellar microstructure. Faster cooling rate decreases the size of α lamellae plates within the β grains and α thickness on the β grain boundaries, as displayed in Figure 1.3. The effect of smaller lamellar spacing due to faster cooling rates lead to higher yield strength and loss in ductility [5, 10].

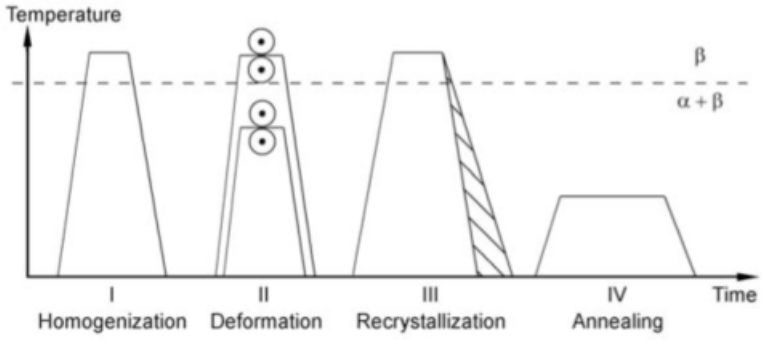


Fig. 1.2 Processing method for obtaining a lamellar microstructure in $\alpha+\beta$ Ti alloys [11]

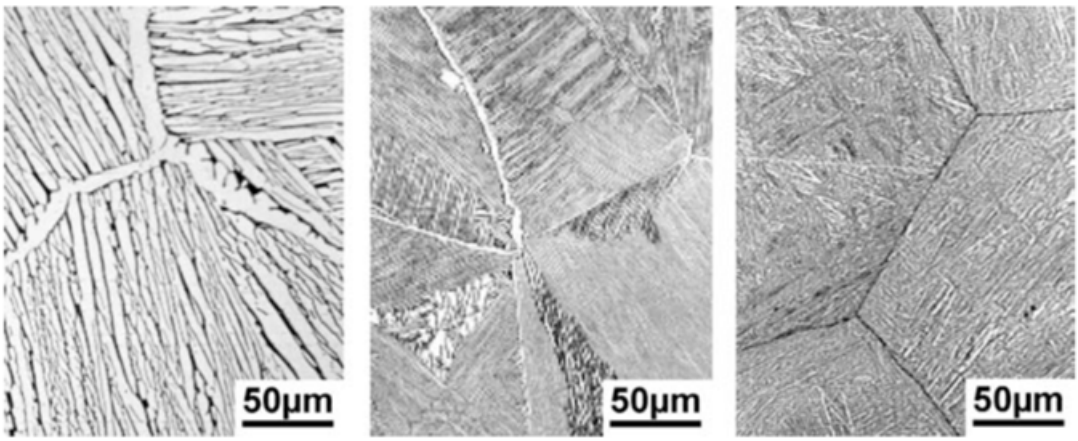


Fig. 1.3 The effect of annealing cooling rate on Ti-6242 lamellar microstructures (a) 1 (b) 100 (c) 8000° C/min respectively [11]

Several modifications to the thermomechanical process are made to obtain a bimodal microstructure, as shown in Figure 1.4. The first difference lies in the homogenisation cooling rate which serves to control the α lamellae width. The resulting difference in grain size due to different homogenisation cooling rates can be seen in Figure 1.5. The degree of deformation in Step II determines the texture of the bimodal microstructure. Deformation at low temperatures where the volume fraction is α phase is greater introduces greater texture to the α phase, whereas a higher deformation temperature develops higher texture for the β phase. Subsequently, the method of deformation determines the symmetry of the texture. In Step III, the recrystallisation temperature and cooling rate determine the volume fraction and grain size of equiaxed α_p which recrystallises in the triple-point of β grains [5]. Element partitioning of α and β stabilisers also occurs during this phase.

The processing route to obtain a fully equiaxed $\alpha + \beta$ Ti microstructure is identical to the bimodal processing route until the cooling stage of the recrystallisation step, as displayed in Figure 1.6. A low cooling rate in Step III allows the equiaxed α_p to continue growing and the lamellae α within β grains to disappear.

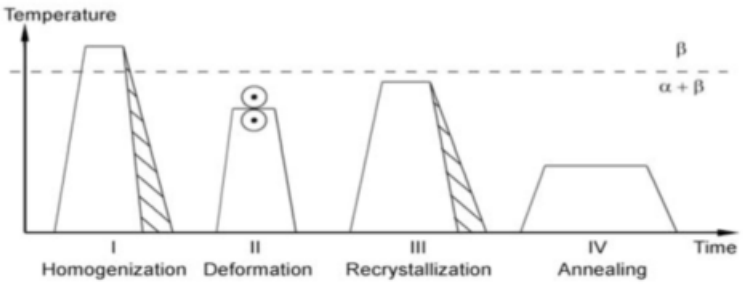


Fig. 1.4 Processing method for obtaining a bimodal microstructure in $\alpha + \beta$ Ti alloys [11]

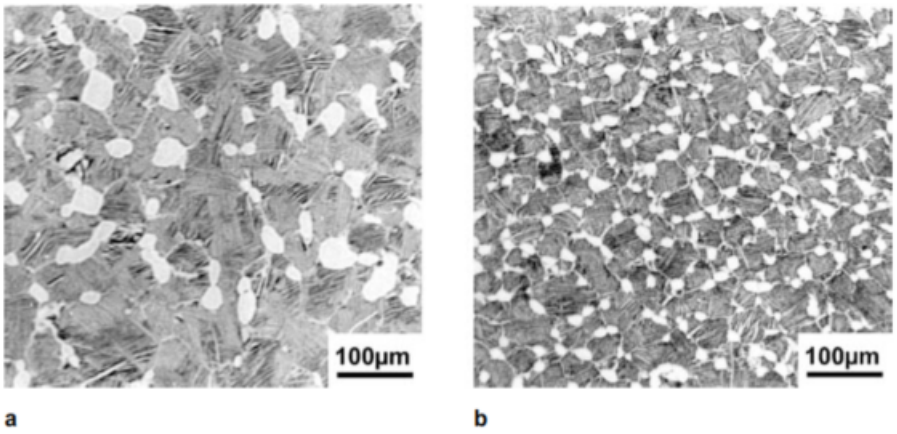


Fig. 1.5 Difference in grain size due to (a) slow cooling rate and (b) fast cooling rate in IMI 834 alloy [5]

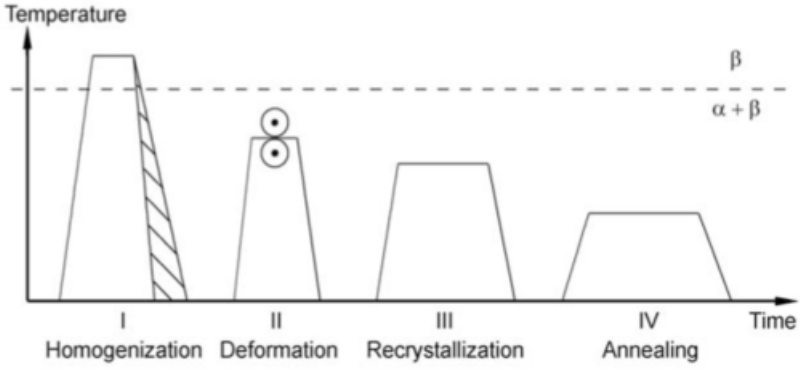


Fig. 1.6 Processing method for obtaining an equiaxed microstructure in $\alpha + \beta$ Ti alloys [11]

1.2 Fatigue design in alloys

The literature in fatigue is generally categorised into two distinct approaches: fatigue life and defect tolerance [12]. Fatigue life studies the number of fatigue cycles needed for the formation of a critical crack to cause failure. The defect tolerant approach revolves around the assumption that engineering components contain flaws. Fracture mechanics is then used in this approach to monitor the crack propagation behaviour of a miniscule flaw to reach a catastrophic dimension. Both distinct approaches to fatigue design are considered in this thesis.

1.2.1 Fatigue life

The history of metal fatigue dates to the 19th century during the European Industrial Revolution. Several early investigations were made on railway component failures which included August Wöhler, who investigated the massive train accident in Versailles, 1842 due to axle failure. Wöhler's profound work on fatigue from 1852 to 1869 provided extensive fatigue life data of ferrous metals that were commonly used in the growing industrial age during the time, particularly in the railway industry. He introduced the concepts of important fatigue variables such as the loading amplitude, stress ratio, and endurance limit. Wöhler's investigations concluded that the number of cycles to failure is more correlated to the cyclic stress range rather than the maximum stress value [13]. In the attempt to simplify the concept of fatigue, he also concluded that there is an approximate linear correlation between fatigue strength and ultimate strength for ferrous alloys, expressed as:

$$\sigma_R = C\sigma_U \tag{1.1}$$

where σ_R is the fatigue limit σ_U is the ultimate strength and C is a constant between 0.4 to 0.5.

In 1910, O H Basquin introduced the Basquin model which describes the Wöhler curve in the form of an exponential equation:

$$\sigma = C_1 N^{C_2} \tag{1.2}$$

where σ is the stress N is the number of cycles to failure and C_1 and C_2 are material constants [14].

Basquin showed that the stress versus fatigue cycle displayed a linear relationship when plotted in a double logarithmic plot. Several other expressions and curve fitting to the S-N curves were postulated throughout the years such from Stromeyer and Palmgren who defined the definite fatigue limit and knee point in exponential forms, respectively [12]. These findings modernised the S-N curve to the form as shown in Figure 1.7.

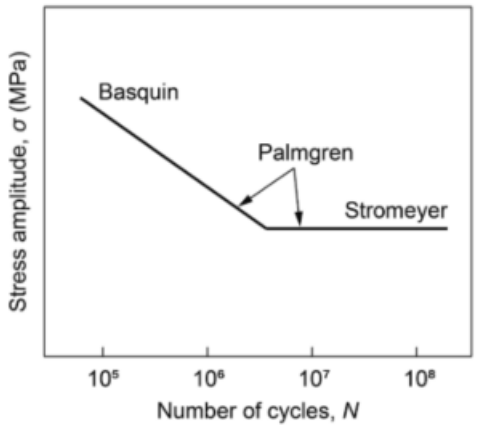


Fig. 1.7 Curve fitting models in an S-N curve [14]

In all cases, S-N curves show that life of materials increases with decreasing stress amplitude. In the LCF region, significant changes of stress amplitude are seen, whereas a much more gradual decrease occurs in the HCF and VHCF. In some materials, plateauing of the S-N curve is apparent and became known as the fatigue/endurance limit. A material is assumed to have infinite fatigue life when cycled at stress amplitudes below the fatigue limit.

Other materials such as aluminium alloys do not exhibit a plateau in the S-N curve and is such cases the fatigue limit is set as the obtained stress amplitude at 10^7 cycles.

1.2.2 Fatigue crack initiation in very high cycle fatigue

For a long time, fatigue data up to 10^7 cycles were sufficient to safely cover the operating life of engineering components. However, modern safety-critical engineering components are subjected to increasingly demanding operating conditions at longer life times. It has become imperative to further explore the very high cycle fatigue regime and understand its underlying fatigue mechanisms for safer materials design against fatigue failure.

Growing academic interests in VHCF were pioneered by Claude Bathias who organised the first conference dedicated to VHCF called 'Euromech 382: Fatigue Life in Gigacycle Regime' in 1998 [15]. This conference was later renamed as VHCF-1 and became a series of conferences dedicated to the topics of VHCF. In the early series, academics disputed the fatigue limit. Fractography from VHCF tests showed a gradual shift from surface crack initiation sites to crack initiation in internal structures with higher fatigue cycles [16–20]. These distinct behaviours in the VHCF regime led to the proposal to categorise VHCF properties into two classes [21]. Type 1 materials include ductile and homogeneous pure metals such as copper and nickel which exhibit a decrease of less than 50 MPa in fatigue strength between 10^6 and 10^9 cycles. Conversely, type 2 materials display a decrease of fatigue strength from 50 to 300 MPa, which include most of high strength steels and other alloys such as Al, Ti, and Mg [22]. Materials within the type 2 category possesses a heterogeneous microstructure containing pores, inclusions or secondary phases which act as internal crack initiation sites. For type 1 materials, crack initiation still occurs from the surface due to persistent slip band formations from surface roughening [23]. Although strains in the VHCF regime are below the persistent band threshold, Mughrabi argued that irreversible slip can still accumulate, which leads to failure. These characteristics emphasize the importance

to identify where crack initiations happen and understand the mechanisms under VHCF conditions.

Similarly, efforts to understand the FCI mechanisms in the very high cycle regime have grown. It has become clear that the controlling factors are highly dependent on the studied material. For example, many steels exhibit a distinct 'fish eye' fractured surface where an inclusion is often found in the middle of the 'fish eye' indicating the internal crack initiation site, as shown in Figures 1.8 and 1.9 [24, 25]. A dark optical area (ODA) can be found surrounding the non-metallic inclusion. SEM observations by Murakami et al show that ODA has a much greater surface roughness than other areas within the 'fish eye' and is believed to be assisted by hydrogen trapped near the inclusion. Spriesterbach et al studied how different chemical compositions of inclusions affect the FCI mechanisms in high strength steels. Their work showed that CaO inclusions detach from the matrix acting as pores, whereas TiN inclusions crack inside the feature [26]. This difference leads to different stress intensity factor thresholds, and therefore shorter fatigue lives from TiN inclusions due to the higher strength concentrations from cracked inclusions.

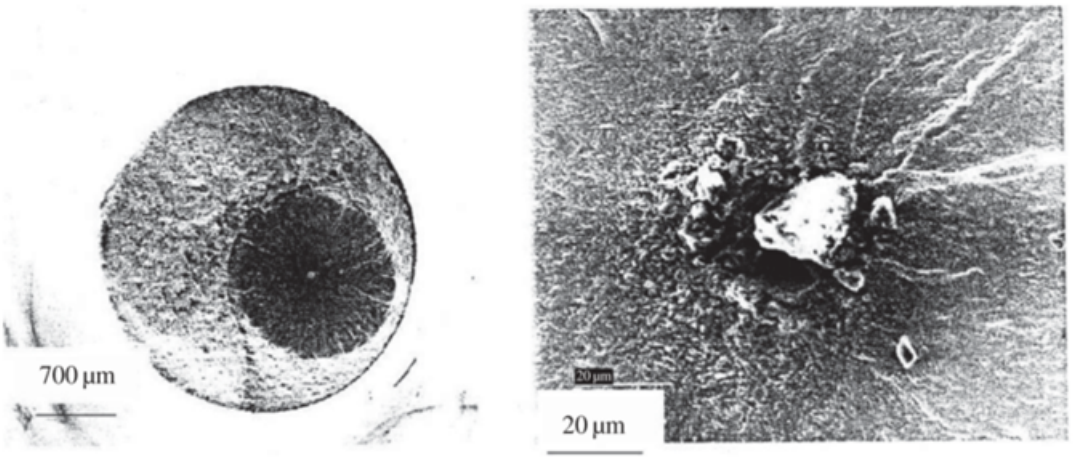


Fig. 1.8 SEM image of a fish eye fractured surface found in steel after being subjected to VHCF [24]

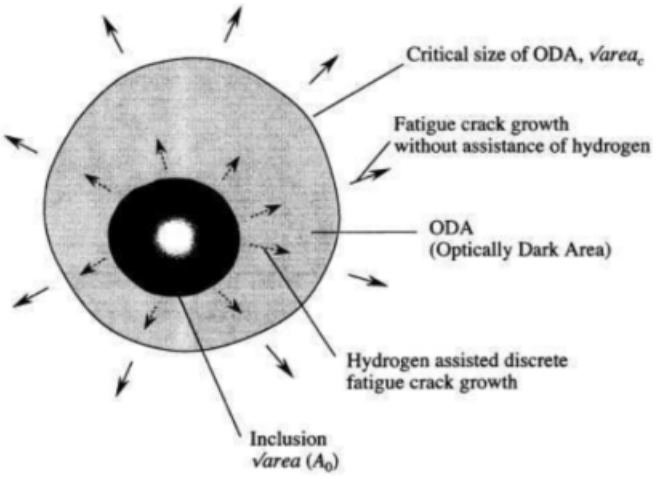


Fig. 1.9 A schematic illustration of fatigue crack growth in the VHCF regime [27, 28]

Overall, the VHCF behaviour of titanium alloys is less explored than of steels [27]. In contrast to steels, where non-metallic inclusions often dominate crack initiation, high-quality wrought titanium alloys generally exhibit a lower population of such inclusions and processing-induced defects. As a result, VHCF crack initiation mechanisms in titanium alloys are less consistently associated with inclusions and remain less conclusive [29]. The dominant HCF crack initiation sites for Ti alloys are more expected to be metallurgical discontinuities such as a grain or phase boundaries [18]. Early attempts to understand internal crack initiations of a Ti-6Al-4V in the HCF regime was made by Atrens et al in 1983, and the change from surface crack initiations below 10^7 cycles to internal crack initiations when above was observed [20]. Another interesting results from Atrens et al was that the mill-annealed Ti-6Al-4V also displayed a duplex S-N curve which illustrates the change in FCI mechanism, as shown in Figure 1.10. However, no inclusions or pores were seen within the detection limit of 100 nm, and therefore was inconclusive which features acted as initiation sites.

By the Third International Conference on Very High Cycle Fatigue (VHCF-3), understanding the mechanisms of FCI was emphasized and became a priority over fatigue crack propagation because of its dominant consumption of the VHCF life. Due to Ti alloys' general lack of inclusions, yet exhibiting internal crack initiations, it was suggested that Ti alloys

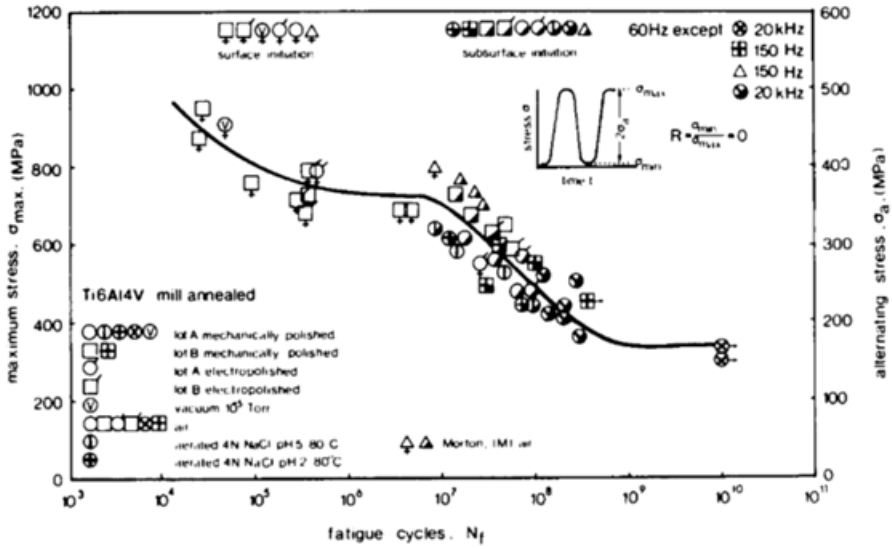


Fig. 1.10 A duplex S-N curve from a mill-annealed Ti-6Al-4V [20]

along with other multiphase alloys with the similar VHCF cases should be categorized as a type 3 material in the VHCF regime [23]. In 1997, Hall published a review on identifying crack initiation sites of $\alpha + \beta$ Ti alloys from the LCF to the HCF regime. The review explained that strain accumulations were observed in α grains and the value of accumulation depended on the coarseness and the degree of micro texture [30]. The desired microstructure for greater resistance against FCI is believed to be finer primary α grains and minimum micro texture or macro zones where similarly oriented α grains are clustered to effectively behave as a very coarse α grain. These lists exhibit similar desired microstructures for greater yield strength and fracture toughness. Margolin also believed that increasing the primary α grain spacing may also increase the resistance to crack nucleation by limiting slip transmissions and plastic deformation between them [31]. Further attempts to clarify the internal fatigue crack mechanisms of Ti alloys were made by Szczepanski et al on a $\alpha + \beta$ Ti-6Al-2Sn-4Zr-6Mo alloy. Fractography in this work showed that facets on fractured surface were found to be oriented approximately 45 degrees to the loading direction and that the majority of the surrounding grains were also oriented parallel to the basal or prism planes which indicate micro texture within the vicinity of crack initiation areas [32]. Experimental works on a bimodal Ti-6Al-4V

alloy by Liu et al observed a transition from non-faceted surface crack initiation sites to faceted surface and internal initiation sites with increasing load ratios [33–35]. Heinz et al observed a distinct 'fish eye' and ODA feature in the fractured surface of a VHCF tested Ti-6Al-4V alloy which grew in size with increasing number of fatigue cycles to failure, as shown in Figure 1.11 [36, 37].

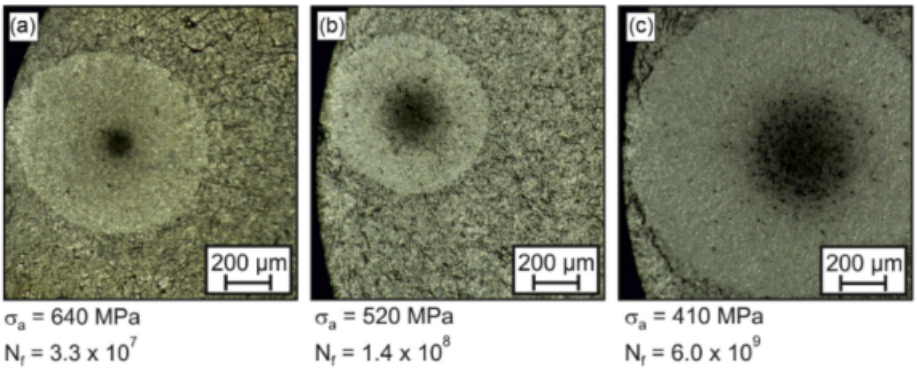


Fig. 1.11 The increase in ODA size with higher fatigue cycles to failure [37]

Everaerts et al conducted varying heat treatments to systematically modify primary α grain sizes of Ti-6Al-4V wires in order to quantify the role of facet and α grain sizes on internal crack initiations [38]. Four different heat treatments were performed to obtain α grain sizes of approximately 1, 2, 5, and 10 microns. The results show that increasing the α grain size led to a decrease in fatigue life. Within the same stress amplitude, samples with an average α grain size of 5 micron failed after 9.6×10^7 cycles, whereas samples with 10 microns average grain sizes failed after 7.6×10^6 cycles. An order of magnitude difference was therefore observed. These results contradict the works from Furuya and Takeuchi, who saw no difference between α grain sizes. Furuya and Takeuchi explained that internal crack initiation occurs in multiple facets; therefore, the dependence is upon the cluster number of facets, rather than the size of individual facets [39]. The facet formation mechanisms in a bimodal Ti-6Al-4V were explored by Bantounas et al using TEM and EBSD. The fractured surface of a HCF tested sample showed a cluster of facets oriented in the basal plane near the

initiation sites which raised the "question as to whether or not microtexture plays a significant role in the extent of faceting" [40]. The authors believe that microtextures with their c-axis oriented to the loading direction are responsible for the faceting of clustered α grains.

1.2.3 Short crack growth

Fatigue crack propagation is extensively covered in the literature within the framework of fracture mechanics. It generally involves the introduction of a pre-crack onto specimens and the monitoring of crack propagation rates using various measurement techniques. When linear elasticity is predominant and the crack tip is confined to small-scale yielding, the material behaviour conforms to linear elastic fracture mechanics (LEFM). Under LEFM, fatigue crack propagation rates (da/dN) are commonly expressed as a function of the cyclic stress intensity factor range (ΔK), resulting in the characteristic Paris-Law behaviour:

$$\frac{da}{dN} = C(\Delta K)^m \tag{1.3}$$

where C and m are material constants.

However, when the material is non-linear elastic and significant yielding occurs at the crack tip, LEFM assumptions no longer hold. In such cases, the crack tip fields are better described by elastic-plastic fracture mechanics (EPFM), using the cyclic J-integral (ΔJ) parameter to capture inelastic energy dissipation. This transition is particularly relevant in the early stages of crack growth where plasticity dominates, or in geometries and loading conditions that generate large plastic zones.

The concept of similitude governs the theoretical basis of fracture mechanics. It implies that crack tips of different configurations behaves similarly when subjected to the same defining load parameter such as ΔK or ΔJ. During monotonic loading, two crack configurations will grow at the same critical driving force. However, this concept breaks down when the crack length, plastic zone and microstructural features are within the same length scale. The

breakdown of the similitude concept questions the applicability of conventional fracture mechanics parameters such as ΔK and ΔJ in the short crack growth regime. Under the conventional framework of LEFM, short cracks propagate at faster rates within the same nominal ΔK driving force. Additionally, it also propagates at driving forces below the conventional threshold. Ritchie and Suresh refer the dissimilarity as the 'small-crack problem' [41]. The practical impact of short crack dissimilarity is significant as the subthreshold crack growth may lead to over-predictions to operating life of engineering components.

Fracture mechanics assumes the material to behave as a homogenous isotropic continuum. It is based on the premise that crack path is linear and grows perpendicular to the loading direction during opening mode. However, microstructural features play a strong role in the growth behaviour in the length scale of short crack growth. In the microscopic level, crack paths are seldom linear. Crack path deflections are caused by numerous factors such as local stress states, environment and local microstructural discontinuities. Studies on short crack growth show sporadic behaviour at certain microstrctural features such as the arresting or slowing down of short crack growth at grain boundaries and in hard secondary phases. Suresh developed 2D crack path deflection models to estimate the changes in propagation rates of dual phase steel and demonstrated the erroneous predictions that may occur when crack path deflection is not taken into account as shown in Figure 1.12 [42]. Additionally, Tokaji et al showed that small cracks in coarse-grained commercially pure titanium grows faster than those in fine-grains, which demonstrates the arresting effects of short crack growth at grain boundaries [43].

Many researchers also argue the lack of crack closure to play an important role in short crack growth [41, 44, 45]. Premature crack face contact during cyclic loading is well understood to reduce the effective stress intensity range (ΔK_{eff}) at the crack tip. The phenonemon is categorised into four mechanisms which are plasticity-induced closure, roughness-induced closure, oxide-induced closure, and transformation-induced closure. Plasticity-induced clo-

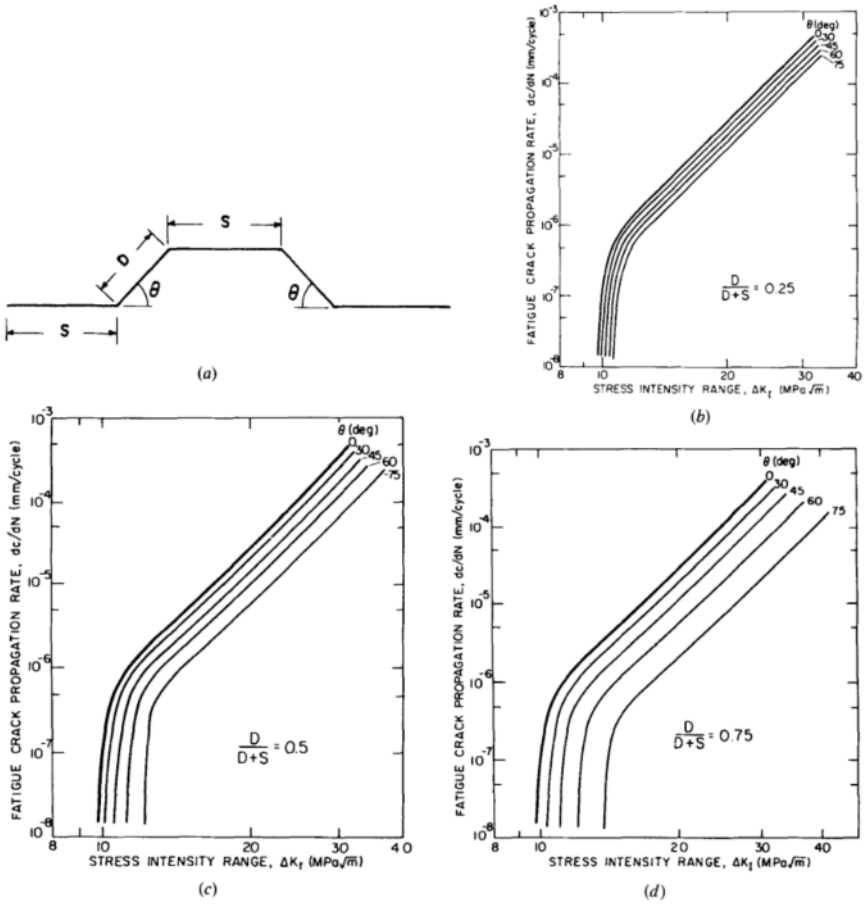


Fig. 1.12 (a) Model profile of a deflected crack segment with the associated nomenclature, (b)-(d) Predicted crack propagation rates for deflected cracks as a function of the angle of deflection θ and the length of deflection $D/(D+S)$[42]

sure occurs during cyclic fatigue loading when plastic deformation near the crack tip leaves behind a plastic wake in the crack's path. This wake causes the crack faces to contact earlier during unloading, effectively shielding the crack tip from the full applied stress range. Roughness-induced crack closure arises from roughening of crack faces caused by shearing during plastic deformation. Oxide-induced crack closure is based on the phenomenon that oxide layers forms on newly created crack faces which are caused by fretting oxidation. This mechanism is promoted by highly oxidising environment, low load ratio and rough crack faces. The formed oxide layers are expected to occupy larger volume and therefore cause premature crack face contact during the unloading phase. Lastly, phase transformation-induced closure

occurs due to phase transformation that causes local volume expansion such as martensitic transformation. These four crack closure mechanisms may act independently or in conjunction. Direct experimental crack closure measurements have demonstrated the role of crack closure at low ratios in long crack growth. The lack of crack closure effects in short crack growth occurs due to the insufficient length of significant plastic wake and minimal crack surface roughness. Researches have shown the coinciding crack propagation rate graph of short cracks and long cracks when using the effective stress intensity factor range (ΔK_{eff}) [46].

1.3 Ultrasonic fatigue testing

The fatigue tests in this research project have been performed on an ultrasonic testing rig. For this reason, a review of this testing method is needed. This section discusses the comparisons of ultrasonic fatigue rigs to conventional servo-hydraulic fatigue testing rigs, the general ultrasonic fatigue methodology and the variation of ultrasonic fatigue that will be used in this research project.

1.3.1 In comparison to fatigue testing at lower frequencies

One of the main enablers of fatigue studies beyond a million cycles have been the development of ultrasonic fatigue and the attempt to standardise the method. An ultrasonic fatigue testing rig uses piezoelectric actuators to transform generally above 20 kHz electric signals into mechanical vibrations of the same frequency. This ultrasonic frequency triumphs over the frequency of common servo-hydraulic fatigue equipment which range between tens to a few hundred hertz. HCF studies (10^7 cycles) with a 100 Hz servo-hydraulic testing rig would take 27 hours to complete, whereas it would only take 8 minutes and 20 seconds for ultrasonic rigs. The difference of experimental time needed is further amplified when exploring VHCF (10^9

cycles), where it would take 14 hours for ultrasonic fatigue rigs, compared to 115 continuous days through conventional methods.

In addition to time-saving benefits, there is also a massive difference in energy consumption. Servo-hydraulic fatigue rigs operate by generating different hydraulic pressures for each section of a cycle. This procedure requires a massive energy consumption. Due to the nature of the hydraulics system, a significant part of the energy input is transformed to heat and requires an appropriate cooling system [47]. An extensive review of the progress in ultrasonic fatigue testing rigs by Mayer claims that an ultrasonic fatigue testing rig is "by a factor of about ten thousand more energy efficient than a servo-hydraulic testing system" [48].

Although the advantages are clear, several limitations and potential drawbacks must also be considered. One of the primary concerns is the strain-rate sensitivity of materials, as ultrasonic testing operates at frequencies several orders of magnitude higher than conventional fatigue tests at much lower frequencies. For strain-rate sensitive materials, this can lead to differences in fatigue response [49–52]. Consequently, care must be taken when comparing ultrasonic fatigue data directly with results obtained at lower frequencies.

A further limitation arises from the design requirement of specimens to resonate at the operating frequency of the ultrasonic system. This constraint necessitates careful tuning of specimen geometry to couple its natural frequency to the excitation frequency, which may significantly constrain sample design. As samples begin to fail due to plastic deformation and the development of cracks, the sample's natural frequency will decrease and may deviate outside of the system's operating frequency. This will cause the loss of excitation and renders the sample incompatible to the system.

Thermal effects also present a challenge in ultrasonic fatigue testing. At high frequencies, cyclic plastic deformation can lead to self-heating within the specimen, particularly at elevated stress amplitudes. If not adequately controlled through intermittent loading, cooling strategies,

or thermal monitoring, this heat generation can alter material properties locally, influence deformation mechanisms, and compromise the validity of fatigue life measurements [53, 54].

Collectively, these factors underscore the importance of careful experimental design, validation against conventional fatigue data, and cautious interpretation of ultrasonic fatigue results, particularly when extending findings to engineering components operating under lower-frequency loading conditions.

1.3.2 Methodology of a general ultrasonic fatigue setup

Bathias, Stanz-Tschegg and Mayer's extensive review discussed the general components and understanding of a common ultrasonic fatigue rig [24, 47, 48, 55]. As mentioned above, an ultrasonic fatigue rig operates by transforming a 20 kHz electric signal from a power source to mechanical vibrations of the same frequency in a sinusoidal waveform. The mechanical vibrations are then amplified by an acoustic horn. The degree of amplification is determined by the dimensions of the horn component. The sample is then attached to the free end of the acoustic horn.

The natural frequency of the sample needs to resonate near the driving frequency of the ultrasonic rig to experience adequate cyclic stress. Mayer's review states that the rig's driving frequency must match the rig set up and the sample's natural frequency [48]; however, the author of this thesis believes that it should be avoided. The ultrasonic rig should not operate at the natural frequency of the sample, as the sample will experience its resonant frequency and experience maximum stress. It is believed that this will cause the sample and components of the ultrasonic fatigue to fail prematurely due to the sensitive changes in stress amplitude that changes at resonance. Other than careful consideration of the sample's natural frequency, the designated strained and stressed area should be reflected onto the sample's design. The most common ultrasonic fatigue specimen design is the dog bone specimen. Other specimen design such as cantilevers exists with slight variations to the ultrasonic fatigue setup.

Modifying the load ratio can be done in several methods. Allowing a free movement of one end of the sample is done to perform a fully reversed fatigue load (R = -1). For R $\neq$ 1 load ratios, the sample needs to be attached on both ends [56]. Detecting crack growth can be done in various methods. For example, detecting a change in the specimen's frequency signify that a crack has formed. As cracks grow, the sample loses stiffness and a loss in the natural frequency is observed. Other methods include the direct current (DC) potential drop method which measures the change in electrical resistance of the specimen as crack grows within a sample [47].

1.3.3 Bending fatigue of meso cantilevers: a sample and setup variation in ultrasonic fatigue

This research used a different version of the general ultrasonic fatigue setup that was described above. The general sample design of meso cantilevers for ultrasonic bending fatigue has been developed by Dr. Jicheng Gong. The samples are fatigued through the sample's inertia rather than direct physical contact.

Techniques similar to this method were used in Straub et al for microfatigue [57]. The fatigue frequency was below 1000 Hz; therefore, not ultrasonic. The sample is mounted in the actuation section of the cantilever in Figure 1.13. As the sample is vibrated, oscillation occurs in the free-moving section due to the unrestricted mass of the hammer. The fatigue set up is displayed in Figure 1.14. A laser beam is used to measure the sample deflection, which is proportional to the stress experienced in the gauge section of the specimen, with the assumption of elastic deformation. Finite element analysis determines the stress-strain correlation in the gauge.

The general meso cantilever specimen design possesses significantly smaller dimensions and a higher surface-to-volume ratio compared with conventional ultrasonic dog-bone specimens. The meso cantilevers have a thickness of 150 microns and an outer specimen radius of

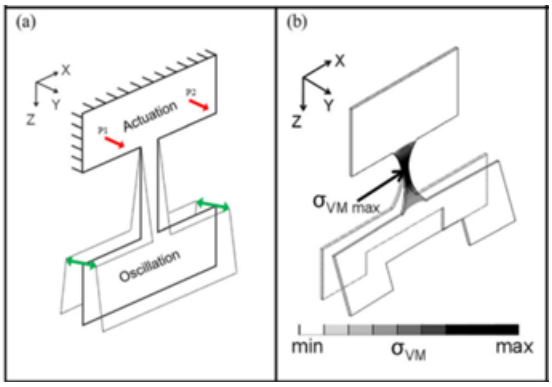


Fig. 1.13 Cantilever specimen (a) describing the actuation and oscillation for bending and (b) finite element analysis describing the stress conditions in the gauge [57]

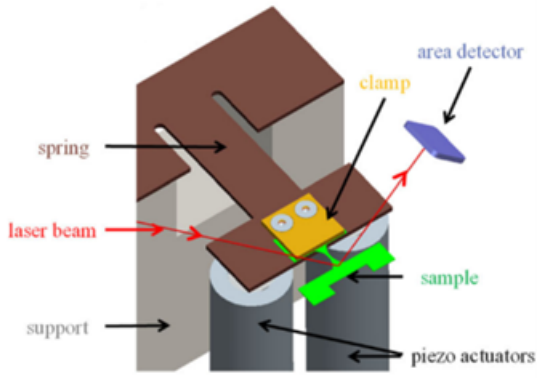


Fig. 1.14 CAD design of the microfatigue setup used in Straub et al [57]

3 mm, whereas typical ultrasonic dog-bone specimens are on the order of 50 mm in length with cross-sectional dimensions of several millimetres. This substantial reduction in specimen size introduces distinct beneficial characteristics.

Firstly, the reduced specimen size enhances heat dissipation arising from cyclic plastic deformation. As a result, temperature rises during testing are significantly constrained, mitigating thermal effects that can otherwise influence fatigue behaviour at ultrasonic frequencies. In addition, the small mass of the meso cantilever constitutes a much smaller fraction of the overall system, resulting in a wider operational frequency window than that achievable with ultrasonic dog-bone specimens. As discussed previously, the development of plastic deformation or crack initiation leads to a reduction in the specimen's natural resonance

frequency. If this frequency shift exceeds the operating range of the ultrasonic system, the sample vibration loses coupling. Due to their larger mass, ultrasonic dog-bone specimens exhibit a much narrower operating frequency range.

Another important consideration is that the reduced specimen dimensions significantly minimise the volume of material required for sample preparation. This is particularly advantageous for studies involving high-value or limited materials, such as irradiated specimens, which are time-consuming to prepare or prohibitively expensive to reproduce. From a characterisation perspective, the smaller fracture surface area greatly facilitates fractography and the identification of fatigue crack initiation mechanisms. The meso cantilevers can also be readily mounted in an SEM for various forms of in-situ characterisation techniques.

Furthermore, the small specimen volume results in a high sensitivity to compliance changes, allowing fatigue crack initiation to be detected through subtle variations in stiffness. This capability is especially beneficial for studying fatigue crack initiation and short crack growth, as it permits early interruption of fatigue tests. Finally, the high surface-to-volume ratio of the meso cantilever specimens enhances their interaction with the testing environment, making them particularly well suited for investigating the influence of different environments.

1.4 Electron Backscatter Diffraction (EBSD)

EBSD is the main characterisation technique in this study to characterise Ti-6Al-4V. For this reason, the technique and its capabilities will also be discussed. The technique stemmed from observations of unique diffraction bands that scattered from the reflection of an electron beam onto a crystal. It was first observed by Seishi Kikuchi in 1928, who passed a cathode ray beam through a thin sheet of mica [58]. Kikuchi diffraction patterns, which they are now more known as, are formed due to a complex interaction of electrons with a family of lattice planes that occur once the electron beam strikes a sample surface. The pattern formation is shown in Figure 1.15.

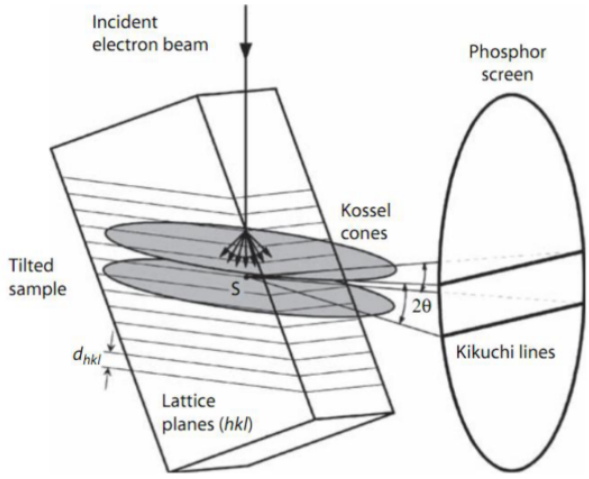


Fig. 1.15 The formation of kikuchi lines in from EBSD [59]

Modern EBSD is typically performed with the specimen tilted to approximately 70° relative to the incident electron beam with a phospor screen set up relatively perpendicular to collect diffracted electrons from the sample surface. This geometry is adopted to maximise the yield of backscattered electrons (BSEs) escaping the specimen surface in the direction of the EBSD detector. Kikuchi patterns are formed by BSEs that undergo inelastic scattering followed by diffraction within a shallow interaction volume near the surface. At high tilt angles, the effective escape depth is reduced and a greater proportion of BSEs are directed towards the detector, resulting in enhanced pattern intensity and contrast. Although this configuration introduces some trade-offs, including a reduction in spatial resolution due to an elongated interaction volume and increased sensitivity to surface topography, the improvement in Kikuchi pattern quality makes a high tilt angle of approximately 70° the standard operating condition for EBSD analysis. Once the pattern is generated and captured by the EBSD detector, the patterns can be used to identify the crystallographic orientation of the data point by using material-unique parameters such as the crystal structure and lattice spacing.

Before the indexing process occurs, several image-processing techniques are needed to increase the band contrast. These techniques include background corrections, noise reductions, and contrast and edge enhancements. The detection of Kikuchi bands is performed using a

commercial EBSD software such as from Oxford Instruments and Bruker. The technique generally involves processing electron backscattered patterns (EBSPs) by Hough Transform, which converts points in the EBSP into sinusoidal curves. The intensity of each point in the EBSP is also used as a weight to ease the detection of peak intensity points in the Hough Space. The position in the Hough space where many curves intersect corresponds to a Kikuchi band in the pattern. The coordinates of these peak intensities in the Hough Space are then transformed back to the original EBSP coordinates to highlight detected Kikuchi Bands. The angles of Kikuchi bands and their width are then used to detect the phase and orientation of each pixel. This complex transform is used because EBSP contains overlapping Kikuchi bands that may have low signal to noise ratio. Moreover, Kikuchi bands are not perfectly parallel, and may have a non-uniform intensity and width throughout their length. These uncertain qualities are prone to mis-detecting bands when using direct edge detection techniques.

1.4.1 The resolution of conventional EBSD (Hough-based indexing)

In its basic form, EBSD allows for the characterisation of grain orientations, local texture, and local misorientations; however, researchers continuously push the application of EBSD as a deformation measurement technique. Samples that undergo plastic deformation will see a degradation of pattern quality due to the local distortions of lattice planes within a diffraction volume. A visual assessment from an experienced operator allowed for simple qualitative studies. Early efforts to quantify plastic deformation from pattern quality involved material-dependent calibration of pattern 'blurriness' and known plastic deformation. To reduce the subjectivity of the method, researchers looked for ways in image processing such as fast Fourier Transform [60]. A more modern approach in analysing plastic deformation involves analysing lattice rotations such as using the Kernel Average Misorientation (KAM), which quantifies the local misorientation of a coordinate in comparison towards its neighbouring

points. In addition, lattice curvatures that are visible in EBSD can also be used to assess dislocation densities. In 1953, Nye observed that the presence of dislocations in a crystal causes the lattice to become curved [61]. The calculation was first made from a glide on a single slip system and then implemented to a three-dimensional tensor of multiple slip systems. Dislocations that contribute to lattice curvatures are termed as geometrically necessary dislocations (GND).

The resolution of a measurement technique determines its capability. In EBSD, there are two types of resolutions that are considered: spatial and angular. The spatial resolution of EBSD is generally determined by parameters that influence volume interaction. For example, samples with higher atomic number have smaller interaction volume; therefore, higher spatial resolution. Likewise, lower probe currents and accelerating voltage results to smaller volume interactions; however, this leads to lower contrast and brightness in diffraction patterns for proper indexing. For this reason, there is a compromise for optimal probe current and accelerating voltage. Lastly, the physical EBSD setup (i.e working distance, specimen tilt and specimen-to-detector distance) also affects the quality of patterns. Generally, EBSD is performed at high sample tilt angle of 70° due to a calculated compromise between high signal but also high degree of distortion and impracticability. With all parameters considered, the spatial resolution of EBSD is typically between 25-100 nm.

On the other hand, the angular resolution of EBSD relates to the indexing precision of Kikuchi diffraction patterns and is primarily determined by parameters that influence pattern quality. The typical angular precision of commercial EBSD softwares is of 0.5 to 1°. This value is too large to analyse elastic strains in most materials systems. A more detailed review of spatial and angular resolutions of SEM and EBSD have been discussed by Humphreys [62–64].

1.4.2 High-Angular Resolution EBSD (HR-EBSD)

Several works have been made to push the angular resolution of EBSD to evaluate elastic strains. These include using a large (∼140 mm) specimen-to-detector distance to gain better resolution in measuring the shift of zone axes [65]. However, this method comes at the expense of small capture angles or also known as the 'zoom effect' which requires zone axes shift to measured one at a time and impractical for orientation indexing. Convergent beam electron diffraction in the TEM offers a combination of high spatial resolution and strain sensitivity; however, electron transparent foils do not share the same strain conditions to the bulk sample.

In 2006, Wilkinson et al developed a novel pattern processing technique based on cross-correlation methods to quantify shifts between two intragranular EBSD patterns [67]. This technique comes with a practical benefit in which the system setup of this technique is standard; therefore, making it an excellent complement to conventional EBSD. The image processing steps are outlined in Figure 1.16. Firstly, regions of interest (ROIs) of high contrast and intensity are extracted from the patterns. The intensity and contrast of the edges in the ROI are then brought down to zero by subtracting every pixel in the ROI with the mean intensity and multiplying the new intensities with the following weighting function:

$$f(x,y) = \cos\left(\frac{\pi x}{N}\right)\cos\left(\frac{\pi y}{N}\right) \tag{1.4}$$

where x and y are pixel coordinates, and N is the pixel size of the ROI.

The weight-processed ROI is then processed by Fourier transform, applied with band pass filter and then cross-correlated to the same ROI from a test pattern after the same image pre-processing technique, as shown in Figure 1.16g. From this technique, the cross-correlation peak height (PH) and mean angular error (MAE) arise as two metrics used to assess the quality and reliability of cross-correlation between two patterns. The PH quantifies the degree of similarity between corresponding features in the reference and test EBSP within each

subregions. It reflects the strength of the cross-correlation signal and is normalised against the ideal self-correlation value, obtained when the reference pattern is correlated with itself. The MAE represents the level of inconsistency among the measured displacement shifts across the ROIs. It provides an indication of the internal precision of the cross-correlation procedure, where lower MAE values correspond to higher internal consistency and, consequently, more reliable strain and rotation measurements. Together, these two metrics provide an objective assessment of HR-EBSD data quality, which are affected by multiple factors such as plastic deformation and sample surface quality.

The measured displacement from the pattern shifts are then used to evaluate the relative deformation. Pattern shifts that occur when applying arbitrary strain to a crystal is illustrated in Figure 1.17, where Q is the displacement induced by strain and rotation from **r** to **r'** and **q** is the measured shift in the zone axis. The tensor **A** describing the displacement gradient from **r** to **r'** is formed as follows:

$$\mathbf{A}-\mathbf{I}=\begin{pmatrix} \frac{\partial u_1}{\partial x_1} & \frac{\partial u_1}{\partial x_2} & \frac{\partial u_1}{\partial x_3} \\ \frac{\partial u_2}{\partial x_1} & \frac{\partial u_2}{\partial x_2} & \frac{\partial u_2}{\partial x_3} \\ \frac{\partial u_3}{\partial x_1} & \frac{\partial u_3}{\partial x_2} & \frac{\partial u_3}{\partial x_3} \end{pmatrix} \tag{1.5}$$

and

$$r' = \mathbf{A}r \tag{1.6}$$

where u_i is the displacement at position x_i in the crystal and I is the identity matrix. The displacement (**Q**) caused by strain and rotations are related to the tensor **A** by:

$$\mathbf{Q} = r' - r = (\mathbf{A}-\mathbf{I})r \tag{1.7}$$

However, as EBSD can only measure shifts that is projected to the phosphor screen (i.e. the projection of **Q** perpendicular to r), the equation is reduced to using **q**:

$$\mathbf{q} = \mathbf{Q} - \lambda r = [\mathbf{A} - (\lambda + 1)I]\, r \tag{1.8}$$

where λ is an unknown scalar, and $\mathbf{q}$ is the component of $\mathbf{Q}$ perpendicular to $\mathbf{r}$. This is rearranged into two equations containing eight variables as follows [67]:

$$r_2 r_3 \left[\frac{\partial u_2}{\partial x_2} - \frac{\partial u_3}{\partial x_3}\right] + r_1 r_3 \frac{\partial u_2}{\partial x_1} + r_3^2 \frac{\partial u_2}{\partial x_3} - r_1 r_2 \frac{\partial u_3}{\partial x_1} - r_2^2 \frac{\partial u_3}{\partial x_2} = r_3 q_2 - r_2 q_3 \tag{1.9}$$

$$r_1 r_3 \left[\frac{\partial u_1}{\partial x_1} - \frac{\partial u_3}{\partial x_3}\right] + r_2 r_3 \frac{\partial u_1}{\partial x_2} + r_3^2 \frac{\partial u_1}{\partial x_3} - r_2 r_1 \frac{\partial u_3}{\partial x_2} - r_1^2 \frac{\partial u_3}{\partial x_2} = r_3 q_1 - r_1 q_3 \tag{1.10}$$

A minimum of four widely-spaced directions r across the EBSP is required to produce unique solutions for eight of the nine strain and rotation components which are $\frac{\partial u_1}{\partial x_2}$, $\frac{\partial u_2}{\partial x_1}$, $\frac{\partial u_1}{\partial x_3}$, $\frac{\partial u_3}{\partial x_1}$, $\frac{\partial u_3}{\partial x_2}$, $\frac{\partial u_2}{\partial x_3}$, $\left[\frac{\partial u_1}{\partial x_1} - \frac{\partial u_3}{\partial x_3}\right]$, and $\left[\frac{\partial u_2}{\partial x_2} - \frac{\partial u_3}{\partial x_3}\right]$.

Once the individual components of the displacement gradient tensor are calculated, $\mathbf{A}$ can be rotated into the sample frame where the elastic strains and lattice rotations can be calculated using the infinitesimal strain theory. The elastic shear strain (e_{ij}) is the symmetric part of the displacement tensor:

$$e_{ij} = \frac{1}{2}\left(\frac{\partial u_i}{\partial x_j} + \frac{\partial u_j}{\partial x_i}\right) \tag{1.11}$$

and the lattice rotations (w_{ij}) are the anti-symmetric part of the displacement tensor associated to plastic strains:

$$w_{ij} = \frac{1}{2}\left(\frac{\partial u_i}{\partial x_j} - \frac{\partial u_j}{\partial x_i}\right) \tag{1.12}$$

Currently, the cross-correlation method is not able to separate the diagonal terms of the displacement gradient tensor which are $\frac{\partial u_1}{\partial x_1}$, $\frac{\partial u_2}{\partial x_2}$, $\frac{\partial u_3}{\partial x_3}$. These terms are reflected in the contraction of the lattice parameter, but does not generate changes in the angles between zone axes. However, as the volume interaction of EBSD is miniscule (10-20 nm), the stress normal to the surface (σ_{33}) is brought to zero which allows the separation of all three normal strains. Hooke's law is then used to obtain the elastic stress components. Although only four ROIs are needed to obtain unique solutions, around 15-20 ROIs of 256×256 pixels are commonly used as a compromise between computational time and 'best fit' accuracy as reported by Wilkinson [67]. The cross-correlation method achieves an elastic strain resolution of around 10^{-4} and a misorientation sensitivity of between 0.005 to 0.002° [68].

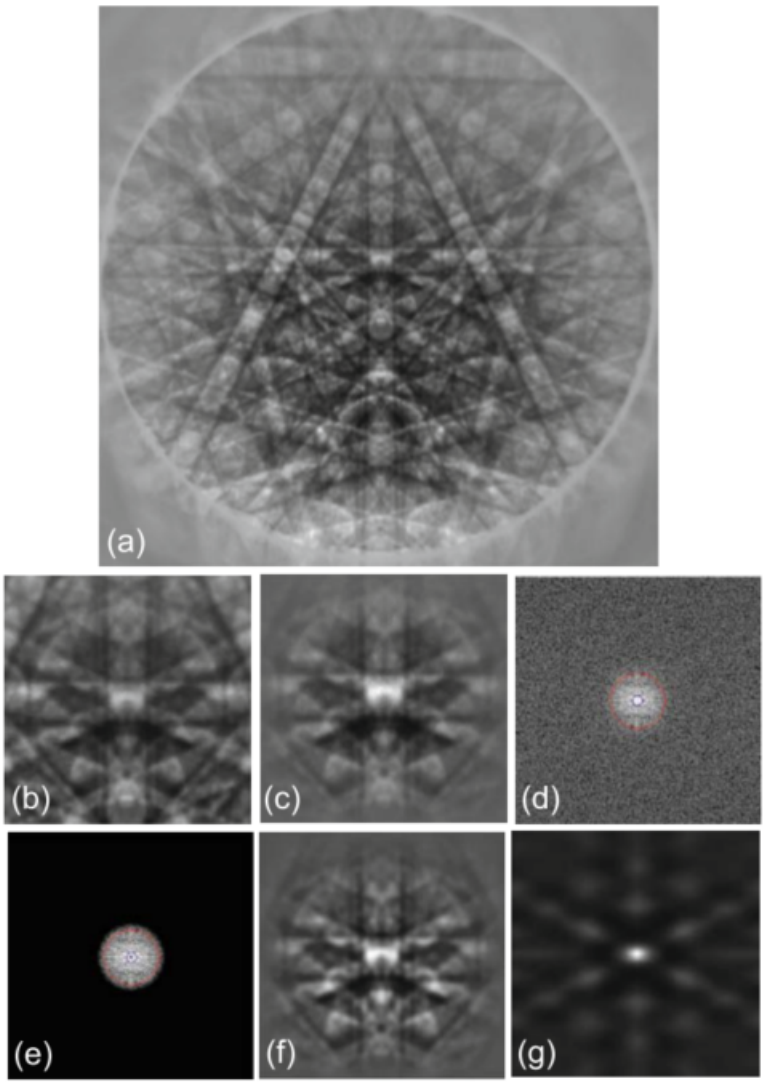


Fig. 1.16 (a) EBSP recorded from GaN (b) ROI extracted from analysis (c) Intensity and contrast of the edges are brought to zero using a weighted function (d) Fourier transform of the weighted ROI (e) Band pass filter to Fourier transform (f) Back transform (g) Cross-correlation with reference pattern (after similar image processing) [66]

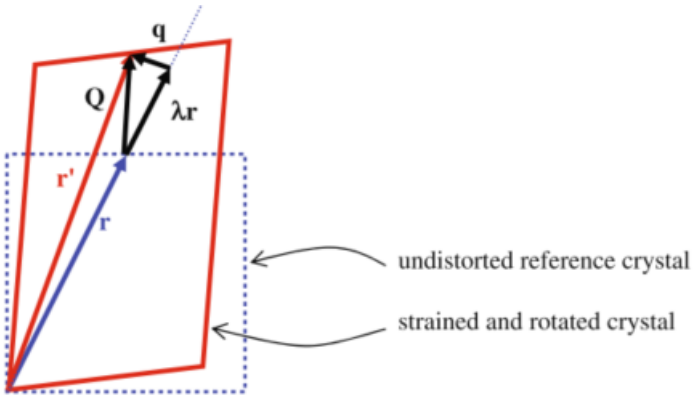


Fig. 1.17 Schematic diagram illustrating how strain and rotation alters zone axis direction **r** across the EBSD screen by **q** [66]

1.4.3 GND analysis using HR-EBSD

Nye observed that dislocations present within a crystal resulted to a curvature of the crystal[61]; therefore, they can also be calculated using HR-EBSD. The calculation of GNDs begins with the requirement for continuity in the displacement field and thus the contour integral are as follows:

$$\oint_C du = Adx = 0 \tag{1.13}$$

where A is the displacement gradient tensor and $A = \frac{du}{dx}$.

The displacement gradient tensor comprises of an elastic (A^{el}) and plastic (A^{pl}). According to Stoke's theorem, the integration around C can be replaced by integration over any surface S bounded by C, so the previous equation can be rewritten as:

$$\iint_S curl(A^{el} + A^{pl})ds = 0 \tag{1.14}$$

The Burger's circuit (B) and the Nye tensor (α) are defined as:

$$B = -\oint_C A^{pl}dx = -\iint_S curl(A^{pl})ds \tag{1.15}$$

$$B = \iint_S curl(\alpha)ds \tag{1.16}$$

Thus:

$$\alpha = curl(A^{el}) = -curl(A^{pl}) \tag{1.17}$$

The term written in derivatives of lattice rotation and elastic gradients gives [69]:

$$\alpha = \begin{pmatrix} \frac{\partial w_{12}}{\partial x_3} - \frac{\partial w_{13}}{\partial x_2} & \frac{\partial w_{13}}{\partial x_1} & \frac{\partial w_{21}}{\partial x_1} \\ \frac{\partial w_{32}}{\partial x_2} & \frac{\partial w_{23}}{\partial x_2} - \frac{\partial w_{21}}{\partial x_2} & \frac{\partial w_{21}}{\partial x_2} \\ \frac{\partial w_{32}}{\partial x_3} & \frac{\partial w_{13}}{\partial x_3} & \frac{\partial w_{31}}{\partial x_2} - \frac{\partial w_{32}}{\partial x_1} \end{pmatrix} + \begin{pmatrix} \frac{\partial \varepsilon_{12}}{\partial x_3} - \frac{\partial \varepsilon_{13}}{\partial x_2} & \frac{\partial \varepsilon_{13}}{\partial x_1} - \frac{\partial \varepsilon_{11}}{\partial x_3} & \frac{\partial \varepsilon_{11}}{\partial x_2} - \frac{\partial \varepsilon_{12}}{\partial x_1} \\ \frac{\partial \varepsilon_{22}}{\partial x_3} - \frac{\partial \varepsilon_{23}}{\partial x_2} & \frac{\partial \varepsilon_{23}}{\partial x_1} - \frac{\partial \varepsilon_{21}}{\partial x_3} & \frac{\partial \varepsilon_{21}}{\partial x_2} - \frac{\partial \varepsilon_{22}}{\partial x_1} \\ \frac{\partial \varepsilon_{32}}{\partial x_3} - \frac{\partial \varepsilon_{33}}{\partial x_2} & \frac{\partial \varepsilon_{33}}{\partial x_1} - \frac{\partial \varepsilon_{31}}{\partial x_3} & \frac{\partial \varepsilon_{31}}{\partial x_2} - \frac{\partial \varepsilon_{32}}{\partial x_1} \end{pmatrix} \tag{1.18}$$

The HR-EBSD technique is only able to measure the elastic and rotation gradients in the surface plane; therefore any gradient with respect to the third direction (x_3) is not accessible. The inaccessible third direction limits the number of determined Nye tensor components to three of nine. However, the literature have shown that the rotation gradients are considerably larger than the elastic gradients [69–72]. Entirely neglecting the elastic components allows five of the nine tensor components to be directly accessible. In addition, Pantleon showed that the sixth component (the difference between α_{11} and α_{22}) can also be measured.

$$\alpha = \begin{pmatrix} \frac{\partial w_{12}}{\partial x_3} - \frac{\partial w_{13}}{\partial x_2} & \frac{\partial w_{13}}{\partial x_1} & \frac{\partial w_{21}}{\partial x_1} \\ \frac{\partial w_{32}}{\partial x_2} & \frac{\partial w_{23}}{\partial x_2} - \frac{\partial w_{21}}{\partial x_3} & \frac{\partial w_{21}}{\partial x_2} \\ \frac{\partial w_{32}}{\partial x_3} & \frac{\partial w_{13}}{\partial x_3} & \frac{\partial w_{31}}{\partial x_2} - \frac{\partial w_{32}}{\partial x_1} \end{pmatrix} \tag{1.19}$$

Nye formulated the dislocation density (ρ_s) for s slip systems to the local dislocation density tensor (α_{ij}) as:

$$\alpha_{ij} = \sum_{s=1}^{s_{max}} b_i^s l_j^s \rho_s \tag{1.20}$$

where b_i^s and l_j^s are the Burgers vector and the unit line direction, respectively, for different s dislocation types. The individual components of the dislocation density tensor, rotation gradient, Burgers vector, line direction and dislocation density can be broken down as follows:

$$\begin{pmatrix} \alpha_{12} \\ \alpha_{13} \\ \alpha_{21} \\ \alpha_{23} \\ \alpha_{33} \\ \alpha_{11}-\alpha_{22} \end{pmatrix} = \begin{pmatrix} \frac{\partial w_{13}}{\partial x_1} \\ \frac{\partial w_{21}}{\partial x_1} \\ \frac{\partial w_{32}}{\partial x_2} \\ \frac{\partial w_{21}}{\partial x_2} \\ \frac{\partial w_{31}}{\partial x_2}-\frac{\partial w_{32}}{\partial x_1} \\ -\frac{\partial w_{13}}{\partial x_2}-\frac{\partial w_{23}}{\partial x_1} \end{pmatrix} = \begin{pmatrix} \sum_s b_1^s l_2^s \rho_s \\ \sum_s b_1^s l_3^s \rho_s \\ \sum_s b_2^s l_1^s \rho_s \\ \sum_s b_2^s l_3^s \rho_s \\ \sum_s b_3^s l_3^s \rho_s \\ \sum_s b_1^s l_1^s \rho_s - \sum_s b_2^s l_2^s \rho_s \end{pmatrix} \tag{1.21}$$

Converting the six components of rotation gradients and the Burgers vector and line direction as vector Λ and matrix $\boldsymbol{B}$, respectively, Equation 1.21 can be simplified to:

$$\Lambda = B\rho \tag{1.22}$$

In HCP-Ti, there are 33 potential slip systems which are considered: three $\langle a \rangle$ screw, three $\langle a \rangle$ edge basal slip planes, three $\langle a \rangle$ edge prismatic slip planes, six $\langle a \rangle$ edge on pyramidal slip planes, six $\langle a+c \rangle$ screw, and twelve $\langle a+c \rangle$ edge pyramidal slip planes. These slip systems are used to populate a 6×33 $\boldsymbol{B}$ matrix in Equation 1.22. To solve for the GND densities on 33 individual slip systems with the constraint of six curvatures, a linear programming algorithm in MATLAB is used. Currently, the L^1 optimisation routine is used to minimise the total dislocation line energy for each data point. The energy associated with edge and screw dislocations are as follows:

$$\frac{E_{edge}}{E_{screw}} = \frac{1}{1-\upsilon} \tag{1.23}$$

where υ is the Poisson's ratio.

Other optimisation methods exist in the literature such as using the L^2 minimisation which minimises the sum of squares of the dislocation density [73]; however, it lacks physical relevance [69]. The comparison between GND densities processed using the L^2 and L^1 minimisation technique is thoroughly discussed in the works of Wilkinson and Randman [69].

1.5 Aims of this work

This chapter has outlined the established literature in the fields of fatigue design, ultrasonic fatigue testing, and electron backscattered diffraction techniques. The work presented in this thesis is structured around three main topics.

The first aim of this thesis is to contribute to the standardisation and wider adoption of ultrasonic fatigue testing. While ultrasonic fatigue offers a powerful means of accessing the VHCF regime within practical testing times, its application remains less established than conventional fatigue methods. This work therefore aims not only to demonstrate the reliability and limitations of ultrasonic fatigue testing, but also to unlock its potential through the integration of advanced characterisation techniques, enabling detailed post-mortem and in-situ analyses of fatigue damage.

The second aim is to expand the existing VHCF dataset and short crack growth for Ti-6Al-4V. Although Ti-6Al-4V is one of the extensively studied titanium alloys, data in the VHCF regime are commonly of dog bone specimens, which limit SEM-based characterisation that requires flat surfaces. Additionally, the bulk of short crack growth data in the literature is done in high stress amplitudes and LCF fatigue due to time constraints with servo-hydraulic fatigue rigs. The ultrasonic frequency in this study will allow us to delve into short crack growth studies in VHCF regimes. The author seeks to provide new experimental data to compare with other testing techniques and better understand variability in this regime.

The third aim is to develop a more comprehensive understanding of the microstructural factors governing fatigue crack initiation and short crack growth in Ti-6Al-4V. The meso scale cantilever addresses the issue of traditional bulk specimens, which often suffer from classical 'needle-in-a-haystack' challenge when identifying and analysing early fatigue damage. Emphasis is placed on the roles of crystallographic orientation, texture, slip activity, and local microstructural interactions. By combining ultrasonic fatigue testing with advanced characterisation techniques, this work aims to clarify how microstructure influences the earliest stages of fatigue damage and the transition from crack initiation to microstructure-sensitive early crack propagation.

Chapter 2

Sample preparation and method development

This chapter presents the details of essential experimental procedures that have been performed throughout the entirety of this work. The material that has been studied and its metallographic preparation techniques will first be outlined. The experimental techniques and method development will then be discussed in detail.

2.1 Material and sample preparation

Ti-6Al-4V is the material of interest in this DPhil thesis. The alloy has been received as a 20 cm diameter disc from the Science and Technology Facilities Council, as shown in Figure 2.1. The certified composition of the alloy is shown in Table 2.1. The final heat treatment was processed by annealing for one and a half hours at 750°C and then air cooled. The process produced a predominantly equiaxed microstructure of the α phase with traces of secondary α in the intergranular β phase, as shown in Figure 2.2.

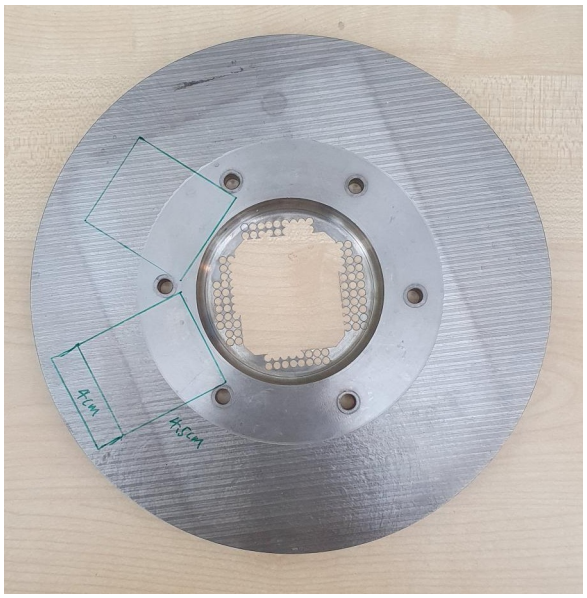


Fig. 2.1 As-received titanium disc

Ti	Al	V	Fe	C	N	O	Y	H
Bal.	6.31	4.19	0.19	0.002	< 0.001	0.19	< 0.005	0.002

Table 2.1 Certified composition of the as-received Ti-6Al-4V

2.1.1 Sample preparation

Blocks of 4 cm long by 4.5 cm wide and 1 cm thick are taken out of the Ti-6Al-4V forged disc by using the water jet facility in the Begbroke Site. The blocks are then sliced to 550-micron thick foils using electric discharge machining (EDM). A bespoke tripod has been developed in the group to achieve relatively uniform thickness in the sample preparation of foils. It consists of three micrometres to adjust the foil tilt during the grinding and polishing process as below:

- The first step is to remove EDM damage and residual stress from both sides of the foil using 600-grit paper. The removal of EDM damage from only one side causes the foil to bend and detach from the tripod due to the remaining residual stress on the other side. The worst outcome of only removing one side of EDM damage can lead to a large variation in thickness in the final thickness, which renders the foil useless. The

thickness of the EDM damage is usually around 30 microns for each side, depending on the specific EDM processing parameters.

- Thinning of the foil can be done quicker using the 800-grit paper. Constantly checking the variation in foil thickness must be done periodically using a micrometer.
- Once the foil reaches approximately 350 microns in thickness, use 1200, 2500 and 4000-grit papers subsequently to reach 300 microns.
- Flip the foil to the other side and start the fast-thinning process using 800-grit paper as mentioned above to approximately 200 microns. As the foil becomes thinner, it becomes more imperative to carefully check the variation in foil thickness as it will become increasingly difficult to correct the thickness variation.
- Once the foil reaches 200 microns, start using 1200, 2500 and 4000 papers to polish and reach 150 microns in thickness.

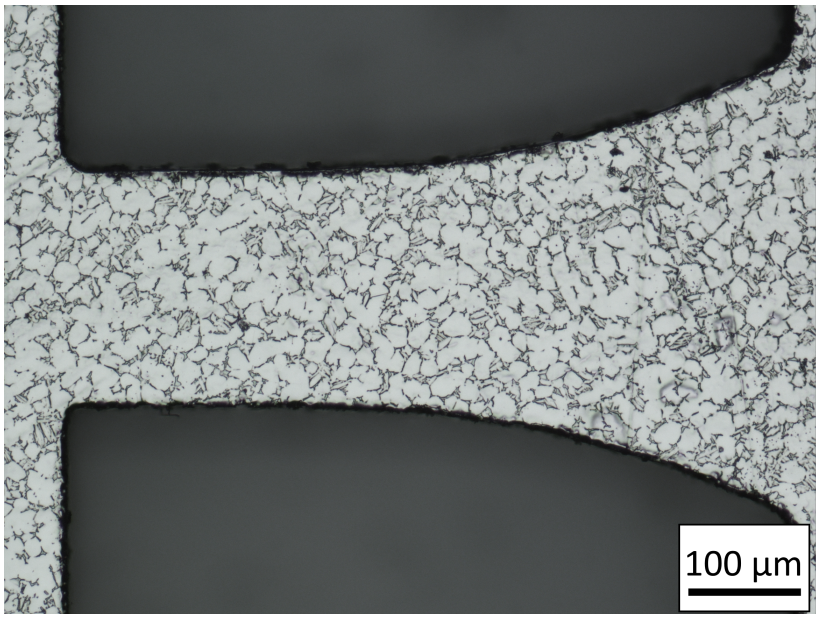


Fig. 2.2 Equiaxed microstructure of Ti-6Al-4V used in this study

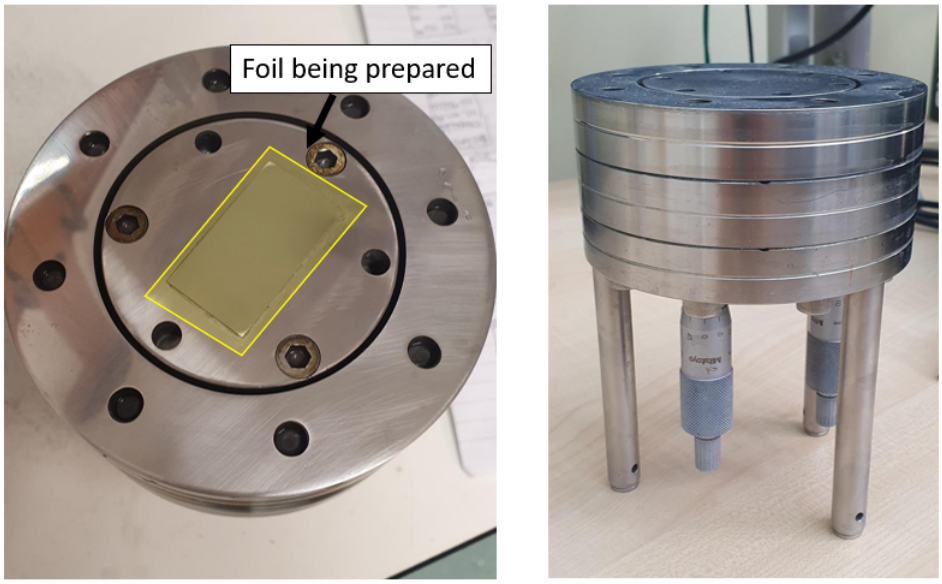


Fig. 2.3 Grinding and polishing tripod used in this research to prepare Ti-6Al-4V foils

2.1.2 Meso cantilever designs

Once the foils are prepared, meso cantilevers can be milled by laser micro-machining as shown in Figure 2.5. The various meso cantilever designs that have been made throughout this DPhil programme will be discussed. For the sample to function properly with an ultrasonic fatigue setup, the sample must have a resonance frequency that is similar to the operating frequency of the apparatus (19500 Hz) and to avoid unwanted stress concentrations to avoid premature failure. Careful sample design were firstly performed computationally using finite element modelling in Abaqus using primarily eigenfrequency and dynamic perturbation solvers to calculate the natural frequency and evaluate the stress distribution around the specimen gauge during ultrasonic oscillation. The main parameters used in Abaqus are outlined in Table 2.2, while the vertical displacement as the boundary condition is visualised in Figure 2.4. The boundary condition aims to resemble restricting nature of the sample's mounting mechanisms. In the case of Figure 2.4, the perimeter is the inner diameter of a grub screw that is used to mount this particular sample design. The various mounting mechanisms for different sample designs are discussed later in this chapter. Once the computational phase

is deemed promising, the performance and characteristics of the samples then verified by during experimental fatigue testing.

Table 2.2 User parameters employed in Abaqus

Elastic modulus (GPa)	114
Poisson's ratio	0.33
Linear brick element	C3D8
Element size (m)	10^{-5}
Vertical displacement (m)	10^{-5}

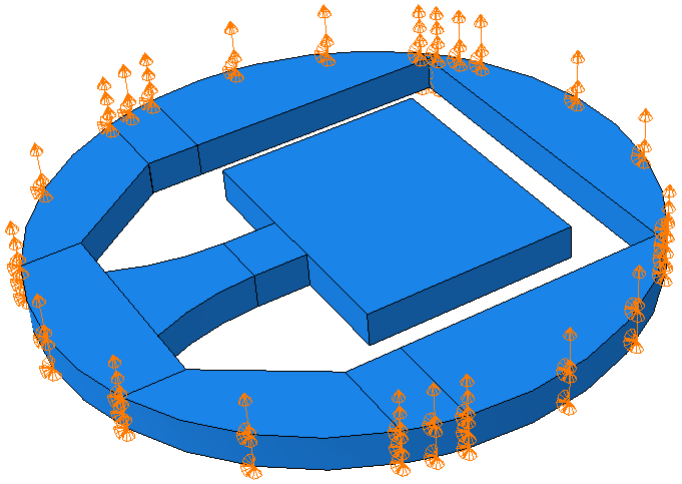


Fig. 2.4 Boundary condition for eigenfrequency and dynamic perturbation simulations in Abaqus

The first approach of the design is to ensure coupling between the natural frequency of the sample and the operating frequency of the equipment. The sample design is mainly comprised of three sections: pad geometry, gauge geometry, and sample thickness, which collectively determine the natural frequency of the sample. The influence of each parameter is summarised as follows:

1. The pad geometry relates to the free-moving mass. An increase in mass results in a reduction of the natural frequency.

2. The gauge geometry design primarily determines the stress distribution during testing; however, longer gauge length also reduces the natural frequency of the sample.

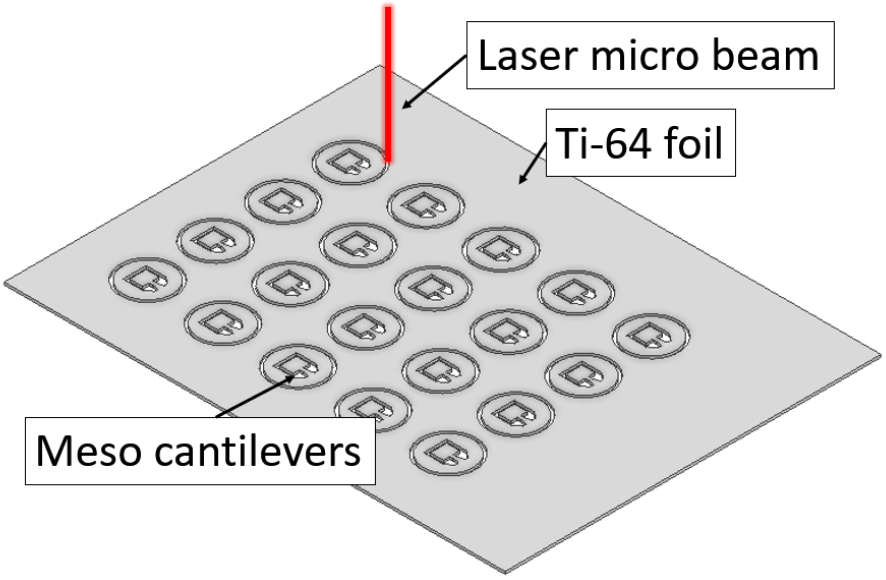
3. The sample thickness is primarily determined by metallographic preparation. Thicker samples increases the natural frequency of the sample.

The specimens in this study were designed to operate in a sub-resonant regime, with a natural frequency of approximately 25 kHz. This design ensures that testing is conducted above the operating frequency, as the amplitude response at exact resonance is highly sensitive to small geometric deviations, making it difficult to control. In addition, the stiffness of the specimen decreases during fatigue crack initiation and early propagation, resulting in a reduction in the sample frequency and a corresponding acceleration in fracture as it approaches resonance. While this behaviour reduces the duration of the crack growth phase, it mitigates a key limitation associated with resonant testing systems. Specifically, if a specimen initially possesses a resonant frequency below 20 kHz, the stiffness reduction associated with crack initiation would further deviate away from the operating frequency of the system, thereby reducing the achievable driving amplitude. Under such conditions, crack propagation may be suppressed or arrested, potentially leading to non-failure of the specimen.

Another design criteria is to avoid stress raisers and to achieve a relatively homogenised stress distribution around the gauge. This is primarily done by ensuring there is no sharp corners at high-stress regions. Using the initial specimen design, fatigue cracks were consistently observed to initiate within the gauge length during fatigue experiments, indicating that the specimen did not introduce unintended stress concentrators. However, the outer ring made it difficult to analyse the fracture surface. For this reason, a new design was made as shown in Figure 2.6b. This new design incorporates ligaments for easy breakage of the outer ring, allowing for characterisation to be performed directly perpendicular to the fracture surface.

Lastly, another sample design with a completely new mounting system was developed as shown in Figure 2.6c. The design philosophy stemmed from the need to obtain similar

mounting conditions when dismounting and mounting samples during the interrupted fatigue campaigns. This design also makes it feasible to be probed when mounted on the bespoke EBSD bending setup. The interrupted fatigue campaigns and HR-EBSD characterisation will be discussed in more details in later chapters.



(a)



(b)

Fig. 2.5 (a) Laser milling of meso cantilevers (b) Ti-6Al-4V foil with laser-machined meso cantilevers



(a) (b) (c)

Fig. 2.6 Various sample designs. (a) First sample design with a 3 mm outer radius (b) Second design with ligaments to be broken for fractography (c) Third design for interrupted fatigue testing. The pictures are not in scale.

2.1.3 Electropolishing

A pristine specimen surface is essential for both reliable fatigue testing and accurate microstructural characterisation. In the context of mechanical testing, particularly fatigue, surface condition plays a critical role in crack initiation. Scratches, machining marks, and other manufacturing-induced defects act as local stress concentrators. These features can reduce fatigue life by promoting premature crack initiation at the surface, thereby obscuring the intrinsic fatigue behaviour of the material. Furthermore, residual stresses introduced during machining or inadequate surface preparation can alter the local stress state, further influencing fatigue performance and reducing the reproducibility of results.

In addition to mechanical effects, surface quality is equally critical for advanced microstructural characterisation techniques such as EBSD. EBSD relies on the formation of Kikuchi patterns from backscattered electrons originating within a shallow near-surface interaction volume. Surface scratches, deformation layers, or contamination can disrupt the crystallographic coherence required for diffraction, leading to degraded or blurred Kikuchi patterns. This reduces indexing accuracy, lowers spatial resolution, and can introduce noise or artefacts in the measured orientation and strain fields.

Once the meso cantilevers are laser-machined, there will be some degree of redeposition and laser damage on the sample edges. Electropolishing is used to remove the damages that may cause stress concentrations during testing. More importantly, electropolishing will polish the sample surface to the quality that is necessary for high resolution characterisation techniques. Figure 2.7 displays the schematic of the electropolishing setup. The method of electropolishing is described below:

- The electrolyte solution used in this thesis is made up of 6% Perchloric Acid, 35% Ethylene Glycol, and 59% Methanol in volume.
- Pour liquid nitrogen into a bath of methanol to –50°C
- Place the bath on top of a magnetic stirrer that is set to 300 rotations per minute
- Pour 118 mL of methanol into a 250 mL beaker. Place the magnet inside
- Place the 250 mL beaker into the cooled methanol bath
- Pour 70 mL ethylene glycol and then 12 mL perchloric acid into the 250 mL beaker
- Attach the negative wiring to the beaker using a metal cylinder dipped into the beaker and attach the positive wiring to the sample
- Set the power supply to 25V and ensure a low current below 0.05 A
- Grip the sample using a tweezer and attach the tweezer to the positive connection
- Turn on the power supply and dip the sample onto the electrolyte solution
- Use a precise timer relay to accurately control the electropolishing time
- The sample is then cleaned using clean methanol and then isopropyl alcohol to remove the remnants of the electrolyte solution from the sample surface

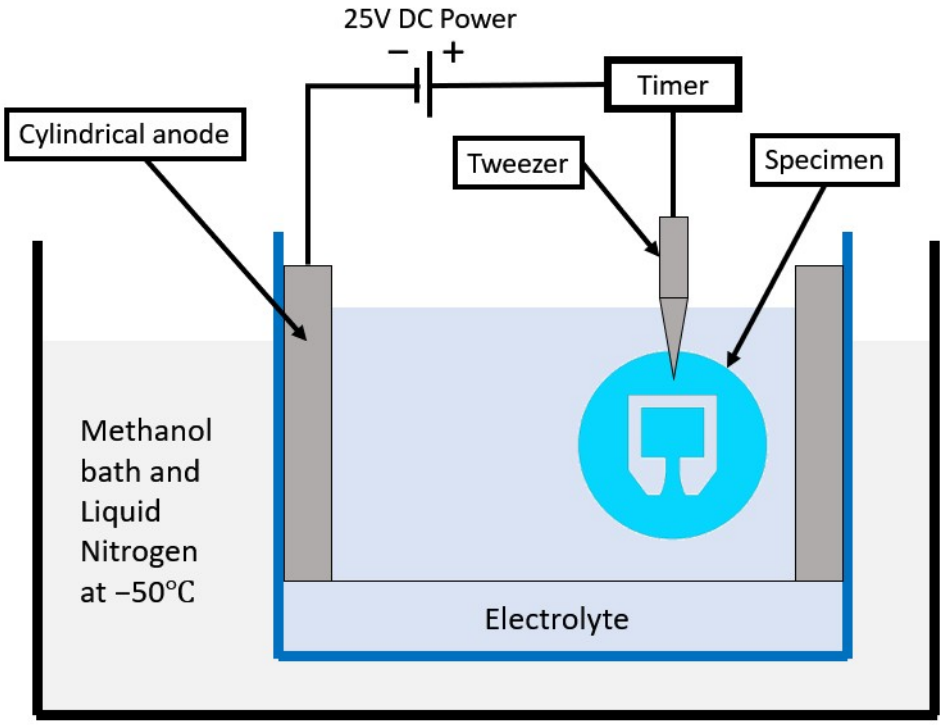


Fig. 2.7 Diagram of electropolishing setup

2.2 Experimental methods and method development

Fatigue tests in this study were performed using an ultrasonic fatigue setup that functions by using piezoelectric actuators to convert approximately 20 kHz power supply to mechanical vibrations. Ultrasonic fatigue setups are mainly used to delve into VHCF regimes, when it is not financially or timely feasible to perform at much lower frequencies using conventional equipment. Despite its success in this niche fatigue regime, ultrasonic fatigue testing has some limitations, particularly in sample design. Large samples used in ultrasonic fatigue testing generate large amount heat during testing and are difficult for investigating crack initiation and short crack growths. For this reason, ultrasonic fatigue testing is constrained to minuscule samples.

The base setup in this study is shown in Figure 2.8. The system incorporates a PC running a MATLAB-based control script, which provides user-defined input parameters such as

vibration amplitude and test duration. The PC sends a digital signal that is converted to an analogue waveform via a digital-to-analogue converter (DAC) and subsequently generated by the ultrasonic power source. The electrical signal is then passed through the piezoelectric actuator which converts it to mechanical vibrations of the same frequency. These vibrations are transmitted through a booster (amplitude converter), which adjusts the displacement amplitude, and then through an acoustic amplification horn, which further amplifies the vibration amplitude. The specimen is geometrically designed to resonate with the excitation system, thereby concentrating cyclic stress within the gauge section under near fully reversed loading conditions (R = –1). The rig is additionally equipped with a continuous dry and compressed air cooling system to maintain resonance stability and limit self-heating. The mounting mechanism depends on the sample design. In the case of the circular samples shown in Figures 2.6a and 2.6b, the mounting mechanism is a modified grub screw, shown in Figure 2.9a. In the case of the third sample deisgn shown in Figure 2.6c, the mounting mechanism is a 0.2 mm plate with two M1.6 screws as shown in Figure 2.9b. To monitor the sample, a laser source is aimed at the free-moving section of the cantilever. A 120 fps monochrome and low distortion camera is used to capture the laser streak reflected onto the workbench, while a digital endoscope camera with a 25-200x zoom capability is used to see the sample inside the acoustic horn in order to properly mount it and to position the laser onto the free-moving section of the cantilever. A live image analysis software has been developed by the author of this thesis to enable and automate deflection measurements and data analysis. It will be discussed in more detail in this chapter.

The sample schematic and the setup geometry during fatigue testing is shown in Figure 2.10. With the assumption of this schematic, the laser streak that is observed during testing can be converted to bending angle using Equation 2.1.

$$\alpha = \frac{1}{2}\tan^{-1}\left(\frac{L/2}{WD}\right) \tag{2.1}$$

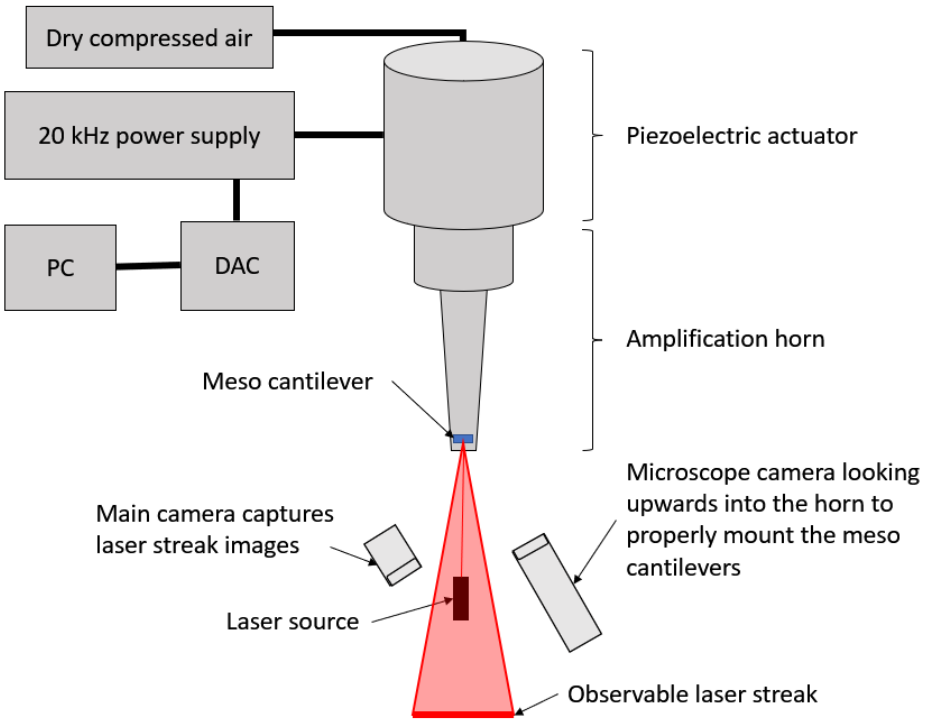
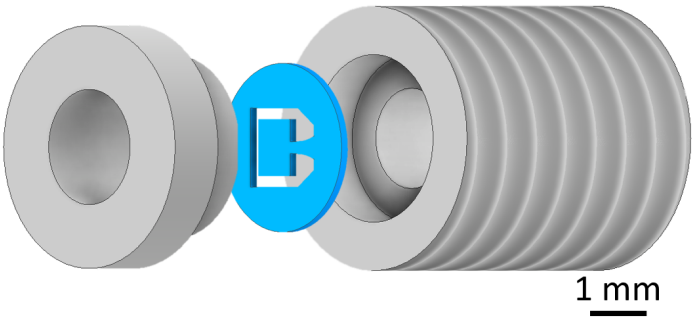


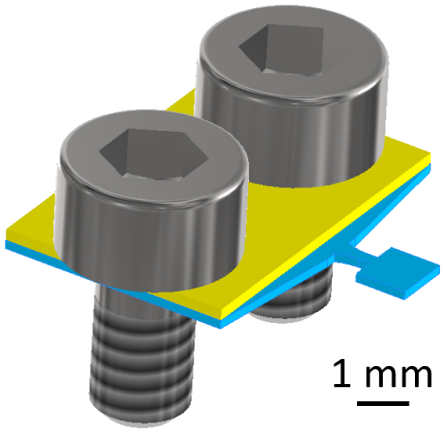
Fig. 2.8 Diagram of ultrasonic fatigue setup

where L is the laser length that is measured on the workbench, WD is the working distance from the sample to the workbench and α is the deflection amplitude of the cantilever vibration.

The bending angle can then be converted to the bending stress amplitude with outputs from finite element modelling in the Abaqus solver. The finite element modelling involves conducting dynamic perturbation simulations at an elastic bending angle for sample thicknesses from 130 to 160 microns. The extracted outputs of the simulation are the resulting bending angles and surface stress distribution when a given displacement boundary condition is given at the mounted end of the cantilever. The stress distribution at the surface of the gauge for a given bending angle is then used to convert the experimental bending angles to the stress amplitudes, resulting to the ratio between stress amplitude and deflection angle (ω), expressed in Equation 2.2.



(a)



(b)

Fig. 2.9 Schematic of the mounting mechanisms (a) a modified M5 grub screw (b) 0.2 mm spacer and two M1.6 screws

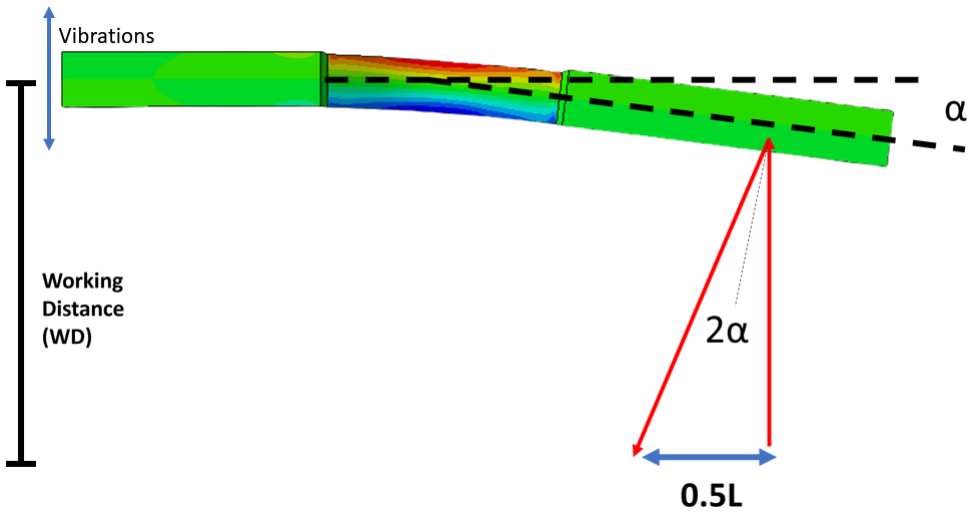
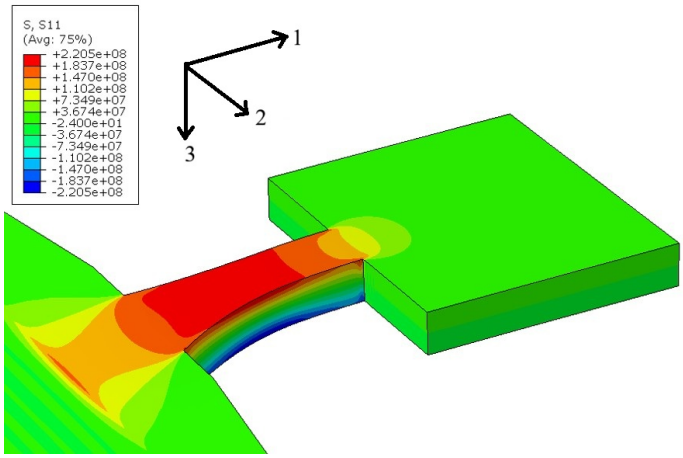


Fig. 2.10 Schematic of the geometry used for converting laser streak measurements to the bending angles in Equation 2.1. The red and blue colours on the gauge is used to visualise the states of tension and compression, respectively

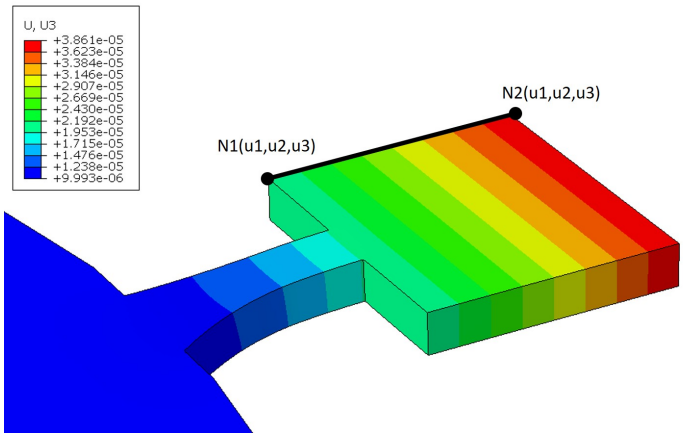
$$\sigma_{\text{amp}} = \omega \times \alpha_{\text{amp}} \tag{2.2}$$

where σ_{amp} is the stress amplitude in MPa, ω is the specimen-specific value for stress per angle in MPa/rad and α_{amp} is the bending angle in rad. This calculation is modelled based on the elastic relationship between the deflection angle and the yield stress of the material, therefore, in theory, is mainly applicable in elastic regimes. A typical elastic response with increasing displacement amplitude is shown in Figure 2.12, justifying the use of a stress-per-angle (ω) value extracted from FEA. Figure 2.11 illustrates the stress distribution around the gauge and displacements used to calculated the stress-per-angle (ω). The stress value used in this calculation corresponds to the maximum tensile principal stress aligned with the cantilever length (i.e. S11) within the gauge section, while the bending angle is determined from the relative displacement in the Z-direction (U3) between two selected nodes shown in Figure 2.11b. Lastly, Figure 2.13 displays the linear change in stress per angle as a function of sample

thickness at two vibration frequencies (i.e. 19.7 and 19.9 kHz), allowing quick prediction of the stress-per-angle for various sample thicknesses.



(a)



(b)

Fig. 2.11 An example of (a) stress distribution in the S11 (cantilever direction) and (b) displacement in U3, used for the calculations of stress per angles for each sample. The units are in Pa and m for the stress and displacement, respectively

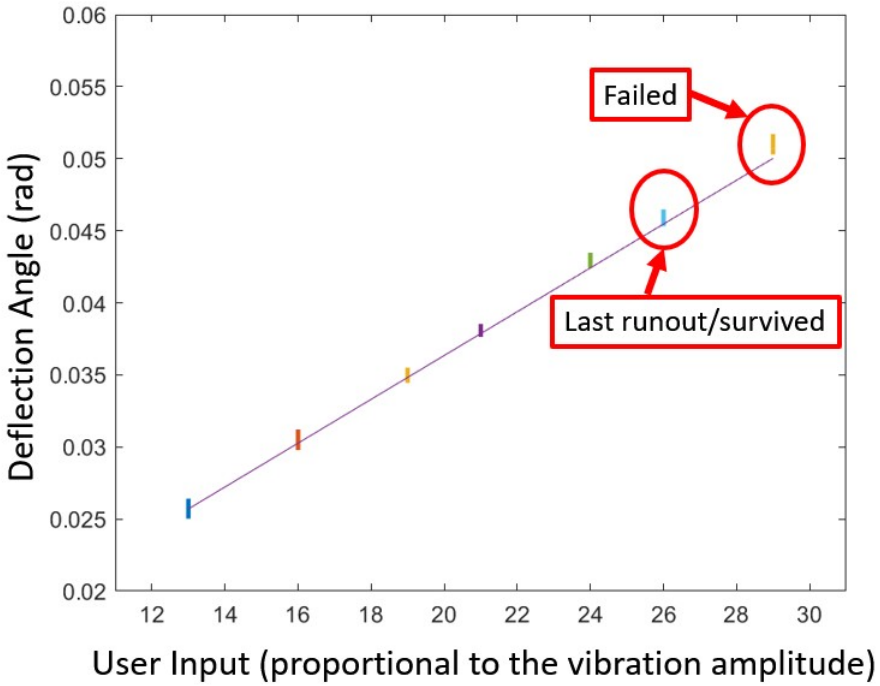


Fig. 2.12 An example of fatigue test using the step-stress method, revealing linear elastic response until the initiation of a fatigue crack which is reflected by the gain in compliance

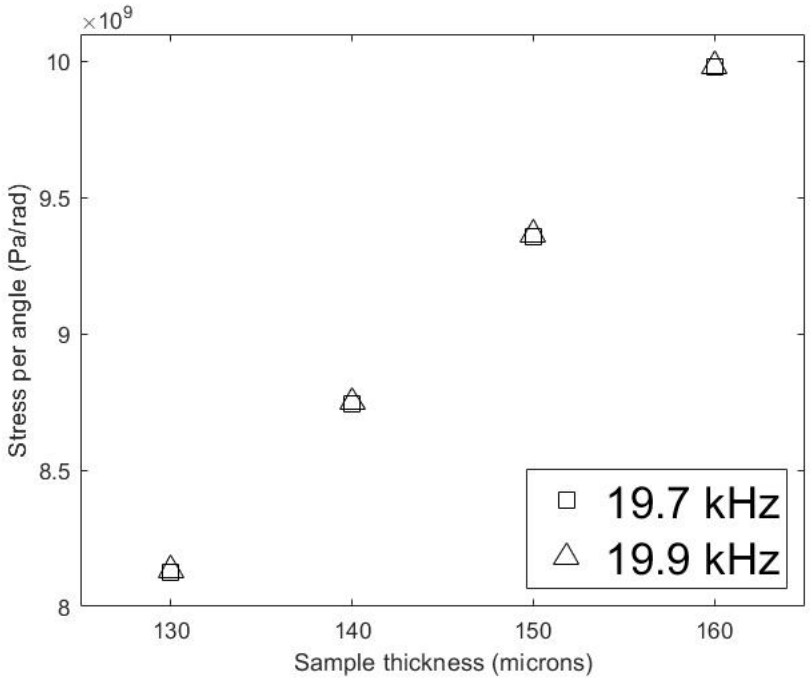


Fig. 2.13 Stress per angle measurements from FEA as a function of sample thickness

2.2.1 Ultrasonic fatigue testing protocol

The most common approach for populating an S-N diagram is through load-controlled fatigue testing. These tests typically aim to evaluate either the fatigue life for a given stress amplitude or the fatigue strength for a given life cycle. However, these approaches struggle at the shallow sections of the S-N curve in the HCF regime where data scatter is high and overlapping across multiple decades of life cycles.

In order to improve the time, cost and sample efficiency, other fatigue sampling techniques have been developed. The staircase method is the most widely employed protocol for estimating the fatigue strength corresponding to a specific life. It is a procedure adapted from the Dixon-Mood method [74]. In this method, specimens are tested under a constant stress amplitude at a target life. The stress level chosen for the first specimen is usually an educated guess. Each specimen either survives and reaches the runout criterion or fails. Subsequently, the next specimen is tested at a new stress level adjusted by a fixed stress step, which is either added or subtracted from the previous stress level depending on the preceding result (failure or survival). The recommended stress step is generally chosen as a fraction of the estimated standard deviation of the fatigue strength distribution. However, in practice, the actual standard deviation is unknown beforehand, making the selection of an appropriate step size challenging. Additionally, the staircase method requires a large number of specimens (typically 15-20 specimens) to conduct a single decade of life cycles. For this reason, it is usually only used to determine the fatigue limit at 10^7 cycles [75].

The step-stress method offers an alternative approach that seeks to further improve testing efficiency by extracting more information from each specimen. Similar to the staircase method, the step-stress method begins with a low initial stress amplitude and applies a runout criterion (i.e. a predefined number of cycles). However, unlike staircase testing, specimens that survive the runout criterion are not discarded. Instead, they are restarted at a higher stress level, incremented by a determined stress step, and the process is repeated until the specimen

ultimately fails. Only specimens that fail at the first load level are discarded, as they do not provide information about multiple stress levels. This approach allows a single specimen to generate multiple data points, thereby increasing experimental efficiency and enabling more rapid coverage of the S-N curve. However, it introduces uncertainty due to prior loading history effects, which influence the fatigue behaviour of the specimen at subsequent load steps.

When a specimen undergoes successive fatigue loading at different stress levels, prior fatigue cycles can alter the material's resistance to subsequent loading. Two opposing phenomena have been observed in metals: cumulative damage and coaxing. In many materials, including titanium alloys, prior cyclic loading at lower stress amplitudes introduces microstructural damage in the form of persistent slip bands, dislocation cell structures, or microcrack nucleation sites. This accumulated damage reduces the remaining fatigue life when the stress amplitude is later increased, leading to a weakened fatigue resistance compared to an untested specimen at the same stress. This phenomenon is often described by linear damage accumulation models such as Miner's rule, which assume that fatigue damage accumulates proportionally with the fraction of life consumed at each load level [76].

Conversely, certain materials exhibit a coaxing effect which is the artificial increase in fatigue limit due to prior stress loadings. Indication of coaxing has been reported in steel, but its effects on titanium alloys have not been detected [77]. When using the step-stress method to populate the S-N curve, the true fatigue strength at a given life may be either underestimated (due to cumulative damage) or overestimated (due to coaxing) depending on the characteristic of the alloy system and loading history. Bellows et al. used the step-stress technique to generate a Haigh diagram for Ti-6Al-4V [77]. The study used a 3-5% step size and the results are satisfactory from a statistical point of view. Bellows et al also advised using less than five number of loading steps to avoid potential coaxing effects.

Throughout this thesis, the author employed the step-stress method to extract as much fatigue data as possible from a single specimen. It is generally recognised that coaxing effects are negligible in the HCF and VHCF regimes. In these regimes, the applied cyclic stresses are sufficiently low and predominantly elastic. Additionally, the literature has also reported negligible coaxing effects in Ti-6Al-4V when employing the step-stress method which justifies the usage in this study [77, 78].

A step-size of 8 to 12% has been used to minimise the accumulative damage effect that may potentially occur when using the step-stress method. The logic behind this is that a significantly larger deformation level may render the damage caused by previous step loadings negligible. However, the step-size may not be too large, as it will introduce a large nominal stress gap between the last runout and failure point. For this reason, the step-stress method for a specific decade of fatigue life will first begin with a large step-size. The step-size is gradually decreased as it reaches the expected failure load. Figure 2.12 displays the typical progression of a step-stress sequence for a common test. As the cyclic amplitude increases, the bending angle begins to deviate from the linear response displayed by the fitting line. This deviation indicates the presence of plastic deformation and/or the initiation of a fatigue crack. For each decades of life cycle, at least three specimens were assessed for statistical reasons.

The S-N plot is shown in Figure 2.14, where only the final runout and failure points of each specimens are retained for analysis. Earlier runout segments from the same specimen are intentionally removed for two primary reasons: significance and decluterring of data points. Earlier runout data points represent stress levels that the specimen survived without failure, but they do not provide significant value as the specimen is subsequently continued to higher stress amplitudes. Since each specimen may experience multiple runouts before failure, plotting all intermediate points would overcrowd the S-N plot. By retaining only the final runout (last survived stress level) and the failure point, the S-N plot remains focused on

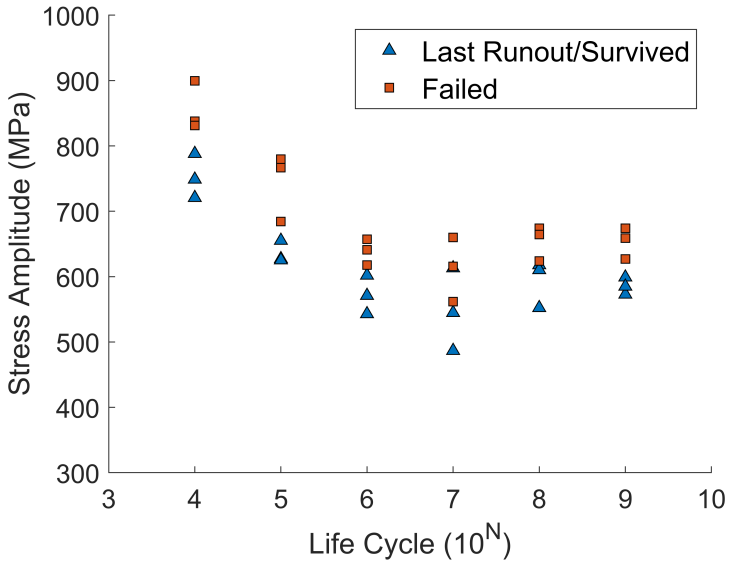


Fig. 2.14 S-N plot of final runouts and failed data points

the most informative data, namely the upper bound of survival and the lower bound of failure for each specimen.

It is also important to note that the failure data point in a step-stress test does not correspond to an exact life at that stress level, as failure may occur at any time before reaching the runout criterion. Therefore, it would be incorrect to interpret the final failure point alone as the sole representative of the true S-N curve. Instead, the true fatigue strength lies between the last runout and the subsequent failure, defining an interval of uncertainty rather than a single deterministic point. Because the step-stress method inherently yields binary outcomes of either a failure or a survived/runout, the fatigue data can be appropriately treated as probabilistic. To account for this binary nature, logistic regression is employed to statistically model the relationship between stress amplitude and the probability of failure at a given fatigue life. Processing the data using logistic regression produces the probability ($p(x)$) that an explanatory variable (i.e. the stress amplitude) either runs out or fails (categorical variable). The probability of fatigue failure for a given stress amplitude is formulated as follows:

$$p(\sigma_i) = \frac{1}{1 + e^{-(\beta_0 + \beta_1 \sigma_i)}} \tag{2.3}$$

where σ_i is the stress amplitude, $p(\sigma_i)$ is the probability of failure at the given stress amplitude and β_0 and β_1 are curve coefficients obtained through the maximum likelihood estimation using numerical methods.

From the fitted logistic regression model, the 50% failure probability curve is taken as the nominal S-N curve, representing the median fatigue strength for the population. To capture the variability of the fatigue response, the 25% and 75% failure probability levels are also extracted from the model and used as confidence bounds (error bars) around the median curve. Figure 2.15 and 2.16 display the logistic regression plot of a dataset with overlapping and non-overlapping data, respectively. When the data do not overlap, the 50% failure is the average of the lowest failure and the highest runout point. The 25% and 75% probabilities are therefore non-existent. Non-overlapping data points are commonly encountered in LCF. Figure 2.17 shows the complete S-N curve processed using logistic regression from 10^4 to 10^9 cycles.

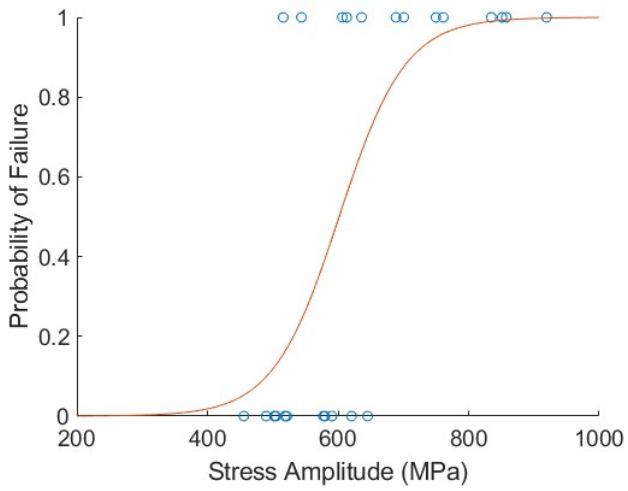


Fig. 2.15 An example of a logistic regression with overlapping data points for a fatigue life of 10^7 cycles

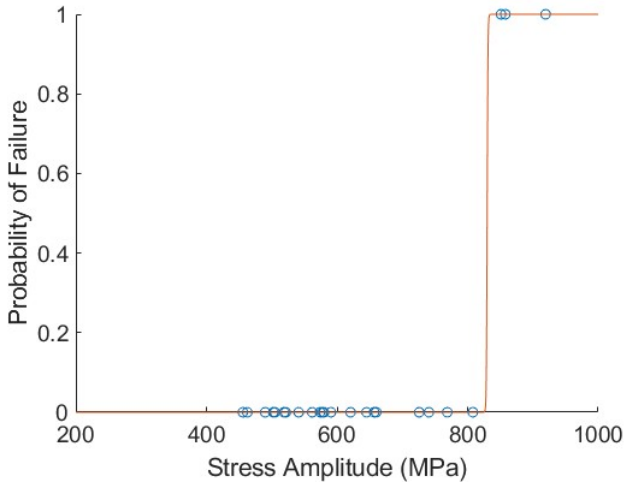


Fig. 2.16 An example of a logistic regression with no overlapping data points for a fatigue life of 10^4 cycles

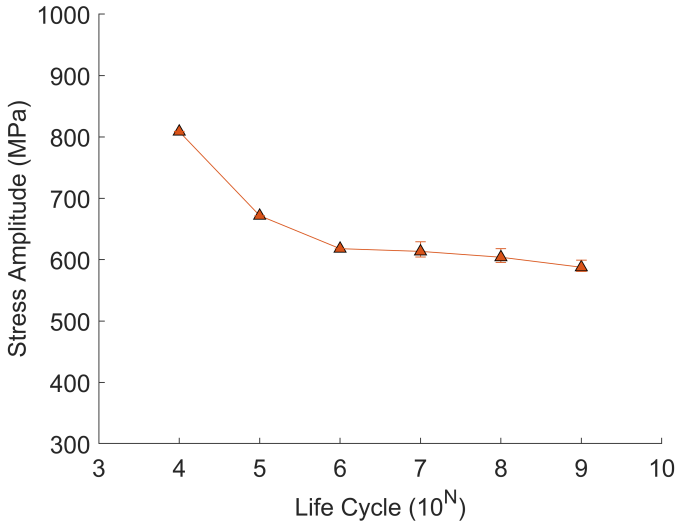


Fig. 2.17 S-N Curve processed using logistic regression

2.2.2 Automation using live-image analysis

To support the experimental campaign of ultrasonic fatigue testing, a robust live image analysis script was developed in MATLAB to automate the measurement of cantilever bending angles and convert them into corresponding stress amplitudes. This automated approach significantly reduces human intervention, enhances measurement precision, and enables advanced fatigue testing protocols that would otherwise be improbable under high-frequency testing conditions.

The system employs a low distortion modular camera (maximum frame rate of 120 fps) to continuously capture the laser streaks generated by a laser reflection on the vibrating specimen. Images are acquired at predetermined time intervals to monitor the cyclic response of the specimen.

To enable reliable computational analysis, the acquired grayscale images are processed as follows:

1. Each RGB image (Figure 2.18a) is converted into a binary image to enhance contrast between the laser streak and the background (Figure 2.18b).

2. The binary streaks are skeletonised to reduce the laser trace to a one-pixel-wide representation, simplifying the geometric analysis (Figure 2.18c).

3. Using the Pythagorean theorem, the script calculates the distance between the extremities of the skeletonised laser streak (Figure 2.18d).

The bending angle of the specimen is then inferred from the streak length and the known geometry of the physical setup. To translate these bending angles into stress amplitudes, a finite element model of the specimen is simulated in Abaqus to generate the stress per angle value. The geometric calibration between measured bending angle and computed stress distribution enables the live conversion of laser streak lengths into stress values with high accuracy. In addition to significant time savings, this automated image analysis technique eliminates the subjective interpretation errors inherent in manual measurements of laser streaks. It ensures

reproducible, high-resolution tracking of bending behaviour across throughout the step-stress testing, which is critical when working with ultrasonic fatigue frequencies.

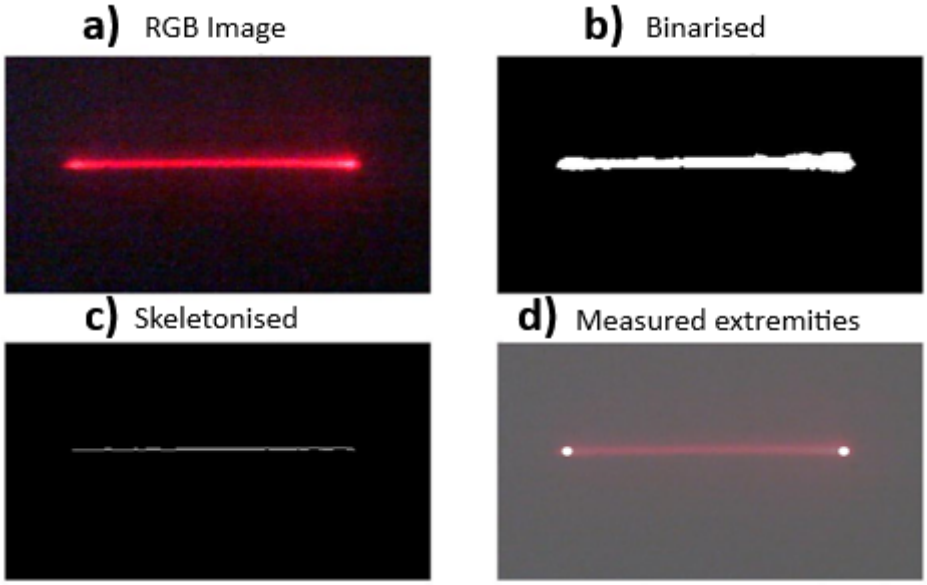


Fig. 2.18 Image processing protocol employed in this study to automate the measurement of bending angles and stress amplitudes

A major advancement introduced by this image analysis technique is the development of an interrupted fatigue testing procedure, which is central to this thesis. The general flowchart of the algorithm is shown in Figure 2.19. Under ultrasonic loading conditions, fatigue crack growth progresses extremely rapidly, making manual interruption impractical. Typically, specimens would fail completely before any human intervention could occur. However, by continuously monitoring the laser streak geometry in real time, the system can detect deviations from the linear bending response, which signify the onset of fatigue crack initiation. This detection is sensitive to short crack growth on the order of 50-100 microns (shown and discussed in Chapter 4), enabling automated test interruption before catastrophic failure. Figures 2.20 and 2.21 show the difference between a runout fatigue test and a fatigue test where it has been interrupted due to a detected fatigue crack growth. This capability allows for controlled investigation of short-crack behaviour, which will be discussed in detail in later chapters. Moreover, to ensure further robustness of the system, the script

also captures reference images of the laser reflection point before each step-stress sequence. Any displacement of the laser reflection point between tests is analysed to determine whether plastic deformation or early crack initiation has occurred. This additional check ensures that subtle changes in specimen geometry are detected even before significant compliance degradation becomes apparent.

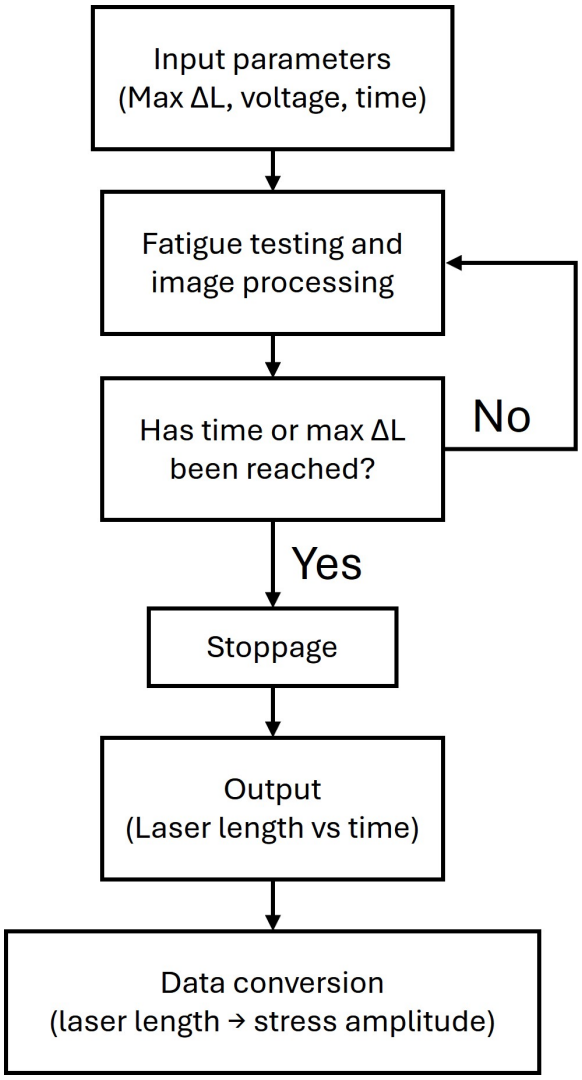


Fig. 2.19 Interrupted fatigue flowchart of the MATLAB script employed in this study to detect short crack growth

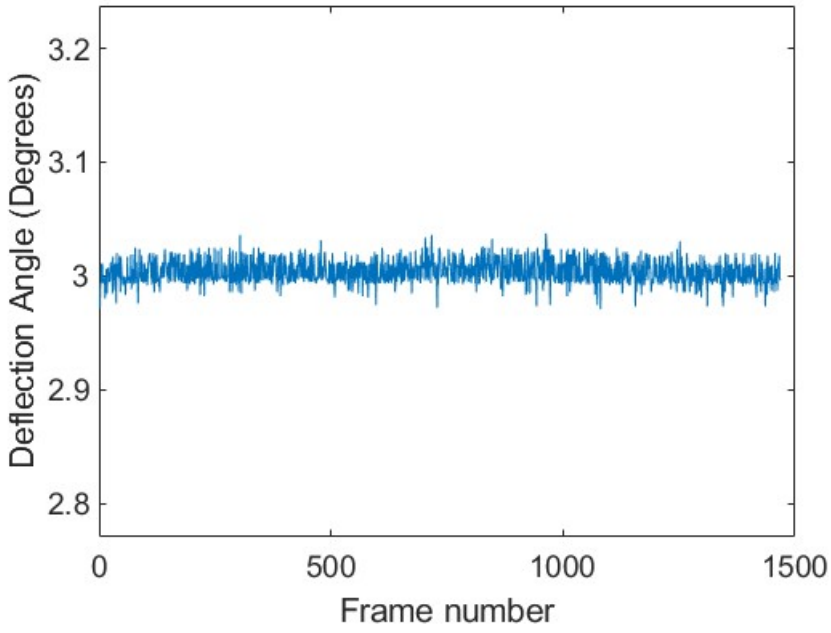


Fig. 2.20 An example of a fatigue test categorised as runout/survived

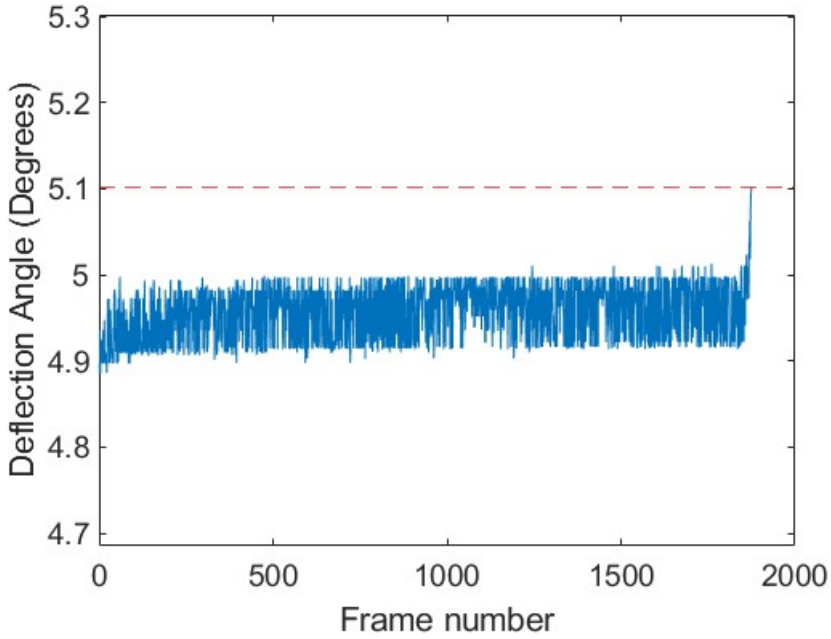


Fig. 2.21 An example of a fatigue test with detected fatigue crack initiation. The onset of fatigue crack initiation is determined in a semi-manual manner, by choosing a value that is above the average noise of the deflection angle during testing.

2.2.3 Fatigue crack growth measurements

The interrupted fatigue protocol has unlocked the ability to detect crack initiation and early growth through the apparent change of sample compliance. An example of this is shown by the sudden surge of deflection angle at the end of Figure 2.21. From this technique, one obtains the bending angles at initiation (a_0,θ_0) and at stoppage (a_{final},θ_{final}). To fully unlock the fracture mechanics investigation of this research, a method must be developed to estimate the crack lengths (a) at the intermediary bending angles (θ).

It is important to note that the quantifiable loss of compliance in ultrasonic fatigue is a combined effect of harmonics, plasticity and crack growth. In conventional crack propagation tests, the compliance loss is fully caused by plasticity and crack growth, which allows it to be generally be categorised as either displacement- or load-controlled. However, due to the coupling effects in ultrasonic fatigue, it is neither displacement- nor load-controlled. To the writer's knowledge, it is difficult to decouple the effects of specimen resonance and crack growth on the loss of sample compliance in the ultrasonic system. However, the combined effects can be quantified using finite element simulations in Abaqus. This was done by calculating the change in bending angles across multiple crack lengths at a representative harmonics condition (i.e. at 19900 Hz). By fitting the bending angle trend as a function of crack lengths, the experimental bending angles can be used to obtain the estimated crack lengths. When the crack initiation has occurred at a predominantly elastic regime (usually in HCF and VHCF tests), the Abaqus simulation results match well with experimental results as shown in Figure 2.22. In this plot, Abaqus results signifies the simulated bending angles as a function of crack lengths. The experimental results show the only two data points with known crack lengths and bending angles which are the initiation and the final interruption points. Lastly, the blue triangular data points are estimated crack lengths from the experimental bending angles during the interrupted fatigue segment that are polynomially fitted to the

Abaqus dynamic perturbation simulations. The estimated crack lengths from the experimental bending angles has unlocked the measurements of crack propagation rates.

However, when the Abaqus simulations do not fit well with the experiment, two outcomes can occur: overestimation and underestimation. An example of an overestimation of the interrupted crack length is shown in Figure 2.23. In this instance, the compliance loss of the experimental results are greater than the predicted results from the Abaqus simulation. Fitting the experimental bending angles to the Abaqus simulation resulted to an overestimation of approximately 30 microns at the interrupted state. Conversely, an example of underestimation is shown in Figure 2.24. The experimental results displayed a stiffer compliance compared to the Abaqus simulations which results to underestimation of approximately 30 microns at the given experimental bending angle. These two examples show that Abaqus simulations failed to capture the complex hardening or softening effects of fatigue. For this reason, when the offset is large, a linear estimation is used as displayed by the green triangular markers in Figure 2.23 and 2.24.

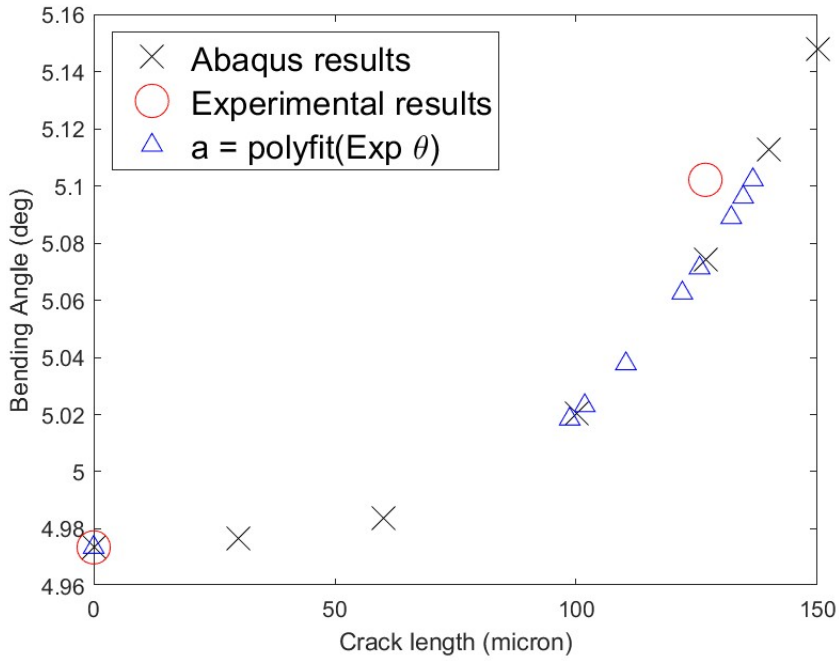


Fig. 2.22 The change in bending angle as a function of crack length

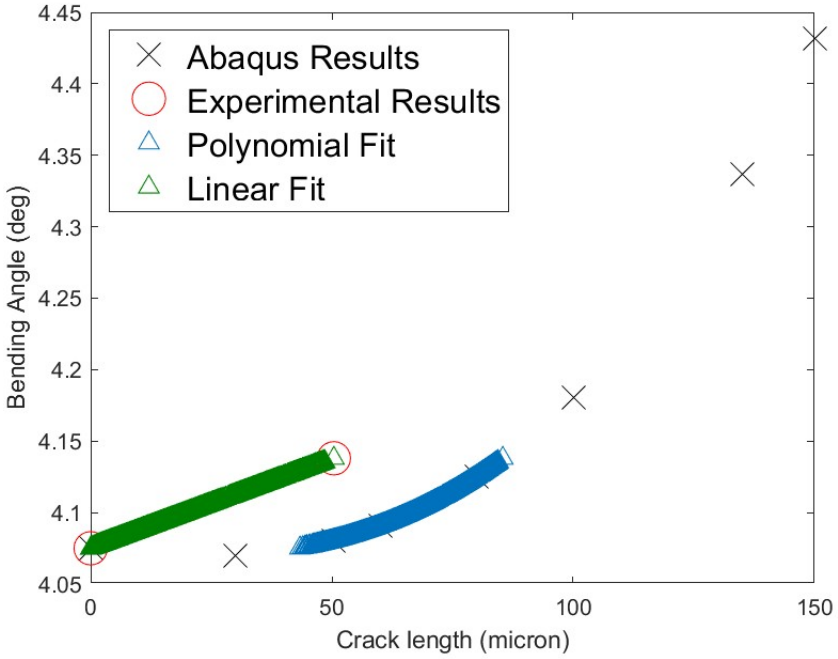


Fig. 2.23 Overestimation of fatigue crack lengths

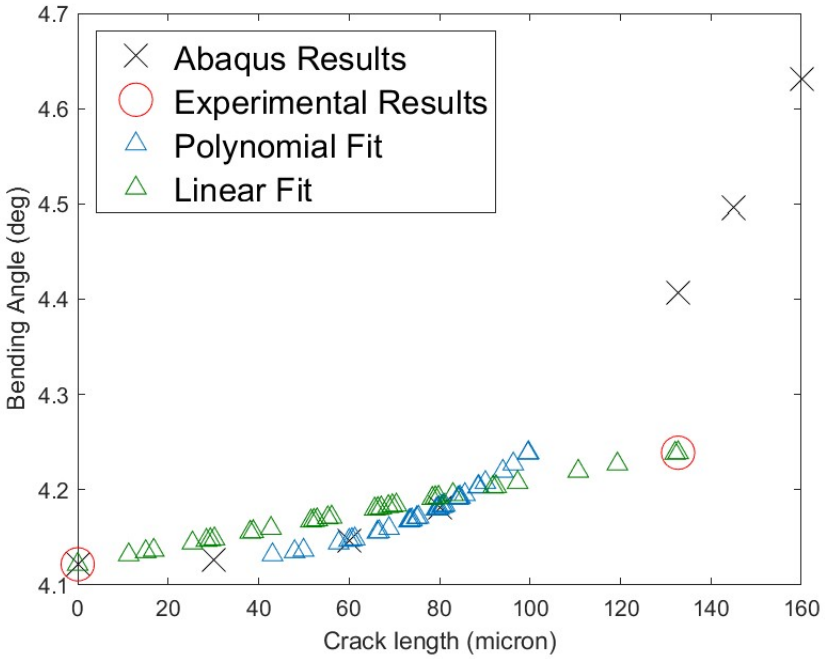
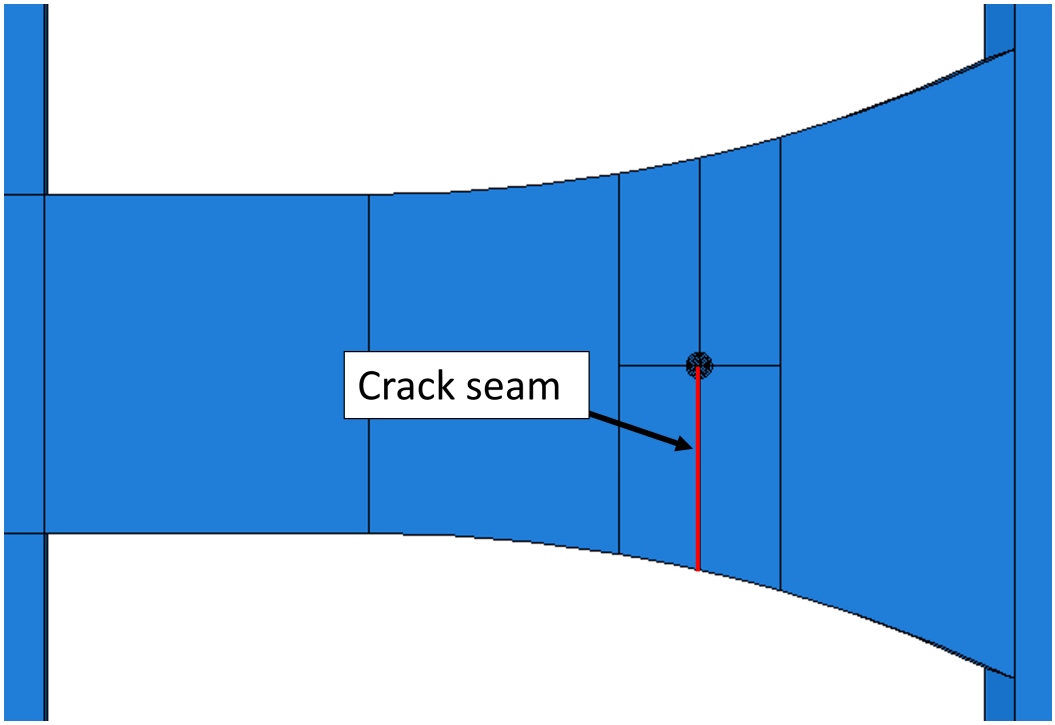


Fig. 2.24 Underestimation of fatigue crack lengths

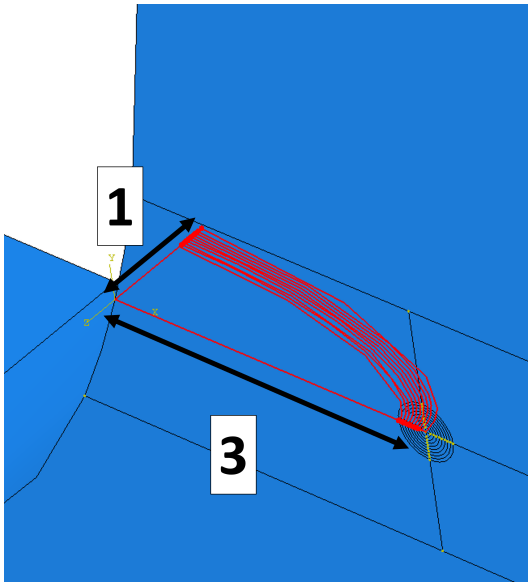
The calculation of independent fracture mechanics parameters is essential for enabling meaningful comparisons of fatigue crack propagation rates across different testing conditions and specimens. In fracture mechanics, the stress intensity factor (K) is a primary parameter governing crack-tip driving force, and its magnitude is determined by three key factors: the applied nominal stress (σ_0), the crack size (a), and a dimensionless geometric correction factor (Y) that accounts for the influence of specimen geometry and crack shape. For conventional standardised specimen geometries, such as compact-tension (CT) specimens specified in ASTM E647, values of Y are readily available as equations and can be applied directly.

In contrast, the ultrasonic bending fatigue configuration employed in this study involves a non-standard specimen geometry with complex stress states and crack growth. Under these conditions, the solution for Y is not readily available. To overcome this limitation, the stress intensity factor range (ΔK) was determined numerically using the finite element method (FEM) implemented in Abaqus CAE. This approach allowed the incorporation of the actual specimen geometry and loading conditions, ensuring an accurate evaluation of the local crack driving force.

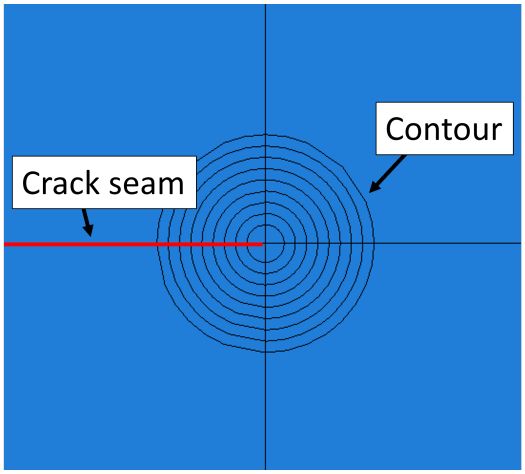
Based on fractography observations, the crack front geometry was approximated as a quarter-elliptical surface crack with a constant length-to-depth ratio of 3:1. To ensure the robustness of the computed fracture mechanics parameters, eight contour integrals were employed in the finite element analyses. The convergence of these integrals to a plateau value is essential to confirm the path independence of K and the J-integral calculations, thereby validating the reliability of the numerical results used in subsequent fatigue crack growth evaluations. Once the K and J-integral calculations and crack length estimations are achieved, the data can be converted to fatigue crack propagation rates (da/dN) as a function of the cyclic driving force (ΔK), which will be discussed in subsequent chapters. Figure 2.25 displays the Abaqus meso cantilever with magnified views of the crack seam and contour lines.



(a)



(b)



(c)

Fig. 2.25 (a) Global view of the meso cantilever with the crack seam (b) Magnified view of the crack seam showing the employed 3:1 length to width ratio (c) Magnified view of the contour lines

Chapter 3

Bending fatigue life of Titanium 6Al-4V

3.1 Introduction

This chapter investigates the bending fatigue life of Ti-6Al-4V, focusing on three main aspects: the influence of laser machining-induced surface features, the comparability of ultrasonic fatigue testing to conventional methods, and the environmental effects of vacuum versus air on fatigue performance.

The first focus of this chapter evaluates the effect of laser-machining on the fatigue performance of Ti-6Al-4V. In this study, meso-scale cantilevers used for ultrasonic fatigue testing are fabricated via laser-cutting, a process common for thin sheet metals. Laser-cutting provides higher machining accuracy and versatility compared to other thin sheet processes such as stamping and punching [79, 80]. However, the process results in the formation of redeposit layers along the cut edges, which have different microstructures and mechanical properties than the base material. These features typically exhibit increased surface roughness and irregularities, which can act as stress concentrators under cyclic loading. Such rough surface conditions have been associated with a reduction in fatigue strength [81–83]. This study aims to evaluate whether these laser-induced redeposits affect the fatigue life of Ti-6Al-4V.

The second aspect addresses the validity of ultrasonic fatigue testing compared to conventional fatigue testing methods. Ultrasonic fatigue testing, operating at frequencies around 20 kHz, allows for accelerated testing into the VHCF regime. However, concerns exist regarding the comparability of results due to potential frequency effects. As such, fatigue results from ultrasonic fatigue testing are highly reliant open the material's susceptibility to strain rate effects. This research includes fatigue testing of Ti-6Al-4V specimens from 10^4 to 10^9 cycles, comparing the results to existing literature to assess the reliability of ultrasonic fatigue testing.

Lastly, this chapter examines the environmental effects on fatigue performance by comparing tests conducted in vacuum and air. Environmental conditions can significantly influence fatigue crack propagation rates. This study utilises a bespoke ultrasonic fatigue and vacuum chamber to perform fatigue tests of Ti-6Al-4V in vacuum from 10^4 to 10^9 cycles, comparing the performance to that in air to understand the environmental impact on fatigue behaviour.

3.2 Experimental methods

Foils of Ti-6Al-4V were prepared by grinding to 4000 SiC grit paper using a bespoke tripod (Figure 2.3) and then polished using a 5:1 mixture of colloidal silica and hydrogen peroxide for one and a half hours. The metallographic preparation resulted in clear grains contrast visible under polarised light microscope. The foils were then laser machined into meso cantilevers, and individually electropolished in a solution made of 6% Perchloric acid, 35% Ethylene Glycol and 59% Methanol at –50°C for 60 seconds. Due to the slightly unpredictable nature of electropolishing, the electropolishing time may be increased to achieve satisfactory surface finishing. The thickness and main geometry of each meso cantilever are measured using a micrometer and an optical microscope, respectively.

Fatigue tests were performed from 10^4 to 10^9 cycles under two sample surface conditions and two environmental conditions at a load ratio (R) of –1. The two surface conditions included as-received and electropolished samples. To evaluate the influence of surface finish

on fatigue performance, both surface types were tested in ambient air. Subsequently, to isolate the effect of environment, only electropolished samples were tested under two conditions: in air and in vacuum. The vacuum tests were conducted in a bespoke environmental chamber integrated with the ultrasonic fatigue setup. The vacuum environment was maintained at a pressure of approximately 10^{-6} mbar, which qualifies as high vacuum and ensures minimal oxygen or moisture interference during testing. This testing matrix was designed to independently investigate the effects of surface condition and environmental exposure on the fatigue behaviour of Ti-6Al-4V in the VHCF regime. As fatigue data is known to produce large data spread, each decade of fatigue life was repeated a minimum of three times. The error bars indicate the 25 and 75 percentage probability of failure for each decade of fatigue life. The lack of error bars seen in some decades of life cycles demonstrates that no overlapping occurs in the binary dataset. Discussion on how the data was processed can be read in more detail in Chapter 2. Fractography was then performed using the Zeiss Merlin SEM in the David Cockayne Centre of Electron Microscopy.

3.3 Results and Discussions

3.3.1 The effect of the redeposit layer on fatigue life

Figure 3.1 shows the laser redeposit layer that is in question. These layers can be a concern in some applications, and its removal or mitigation can be achieved through various methods. In this circumstance, electropolishing was employed to remove a significant portion of redeposits in addition to generating SEM and EBSD quality sample surfaces. The progressive removal of redeposited material following electropolishing for 40 and 60 seconds is shown in Figure 3.2. After 40 seconds of electropolishing, a substantial reduction in redeposit layers is observed along the side profiles; however, redeposit features remain visible along the top and bottom edges of the specimens. With further electropolishing to 60 seconds, these

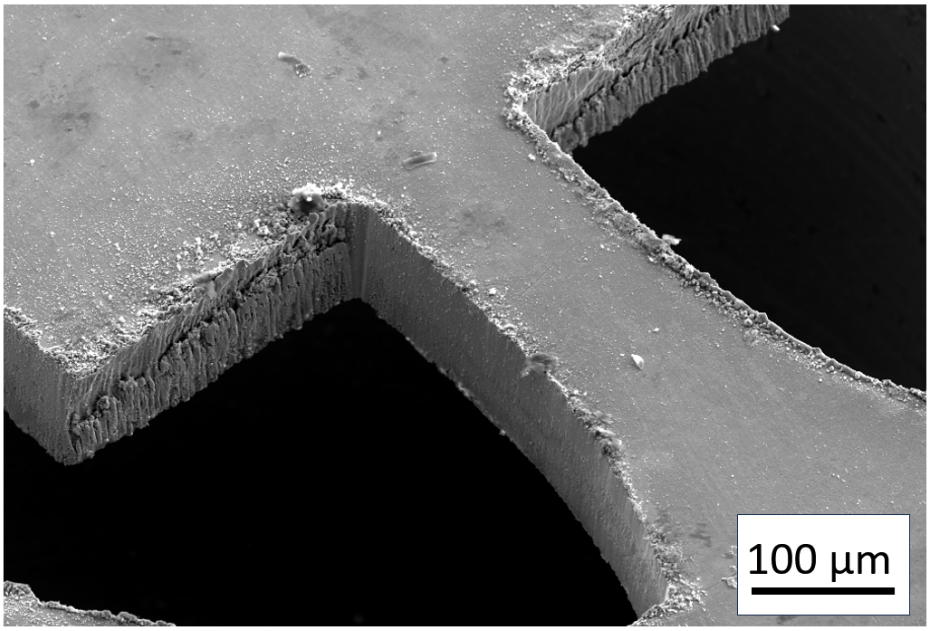
redeposits are largely eliminated, accompanied by the onset of edge chamfering, indicating increased material removal. Similarly, Figure 3.3 illustrates the effect of electropolishing on the top surface, showing the effective removal of surface scratches and the emergence of the underlying microstructure. This image also demonstrates that the specimen edges become markedly more uniform following electropolishing, in contrast to the as-received samples, which exhibit pronounced gradients and non-uniformity in edge depth.

Figure 3.4 and 3.5 display the individual S-N plots of as-received and electropolished samples, respectively. Comparing the fatigue testing between as-received specimens (with redeposit layer) and electropolished specimens (where the layer is reduced/removed) reveals a visible improvement in fatigue strength following electropolishing, as shown in Figure 3.6. This enhancement is pronounced at longer lifetimes, with the differences growing from approximately 50 MPa at 10^7 cycles to around 200 MPa at 10^9 cycles. While the improvement in fatigue performance is evident, it is important to recognise that it likely arises from a combination of the removal of the redeposit layer and the overall improvement in surface quality achieved through electropolishing. A notable increase in data scatter is also observed for the as-received samples, suggesting more variability in fatigue life among specimens with redeposit layers. Such observations underscore the increased sensitivity of fatigue performance to surface defects at lower stress amplitudes. In the VHCF regime, where cyclic stresses are low and crack initiation dominates the total fatigue life, even minor surface anomalies such as those introduced by the redeposit layer and scratches from an unpolished surface can serve as preferential crack initiation sites, thereby reducing the fatigue strength.

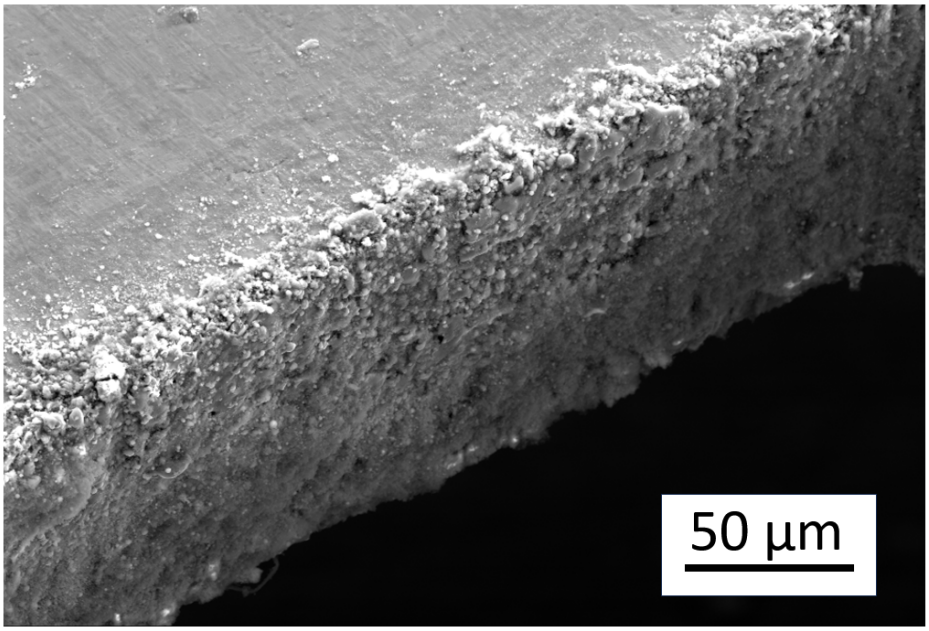
The influence of surface roughness on fatigue properties has been reported to vary across different materials and testing setups in the literature. For example, Weldon et al investigated the effect of several surface polishing treatments on 316L stainless steel tested at 120 Hz and $R = 0.1$, and reported no measurable influence on the endurance limit [84]. Similarly, some studies have reported a limited influence of surface roughness on the four point bending fatigue

life of Ti-6Al-4V in LCF [85, 86]. Surface roughness is an important topic in the fatigue performance of additively manufactured materials. A comparative literature review by Sanaei et al examined fatigue behaviour in powder bed fusion (PBF) Ti-6Al-4V [87]. HIPed and non-HIPed treatments were distinguished to account for the influence of internal defects. For HIPed PBF Ti-6Al-4V, non-polished surfaces were shown to reduce the fatigue limit at 10^7 cycles to approximately 300 MPa, demonstrating the strong sensitivity of fatigue performance to surface condition. Additionally, redeposit layers are a concern in machining EDM- or laser-machined cooling holes in turbine blades. Redeposit layers generated during EDM have been shown to promote early fatigue failure and reduce endurance limit by approximately 20-30%, with the severity of the degradation scaling with redeposit layer thickness [88–91]. It is important to note that none of the mentioned literature on the effects of surface roughness and redeposit layers were evaluated in the VHCF regime and were all performed at conventional cyclic frequencies.

Due to the stark differences in fatigue performance between as-received and electropolished samples, this study moves forward with electropolished samples for all further testing. Moreover, electropolishing not only removes the recast layer to improve fatigue performance, but also significantly enhances the surface finish that is necessary for the application of high-resolution characterisation techniques. These techniques are essential for accurate identification of crack initiation sites and microstructural features associated with fatigue crack propagation, thereby justifying the use of electropolished specimens in ongoing investigations.

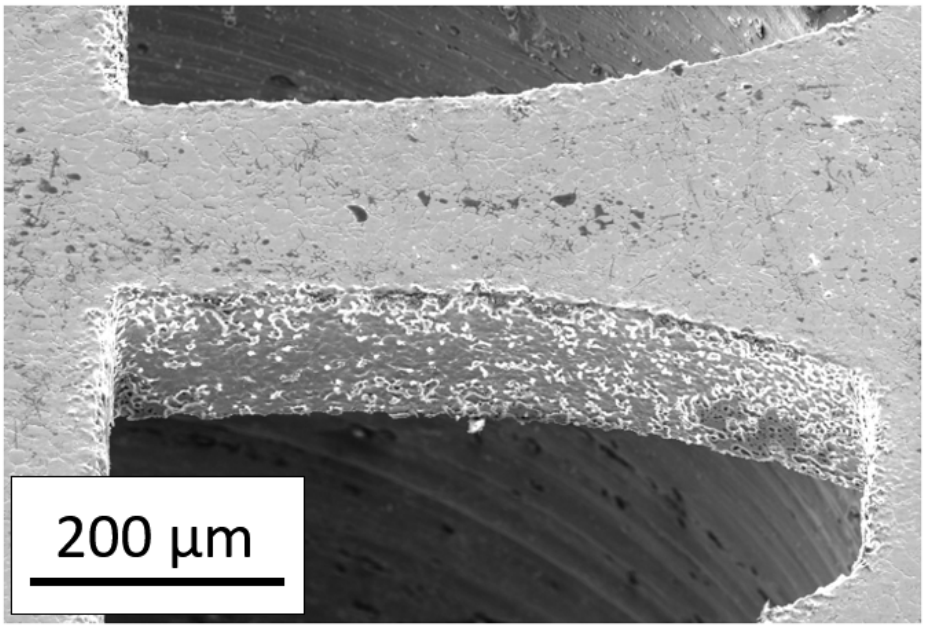


(a)

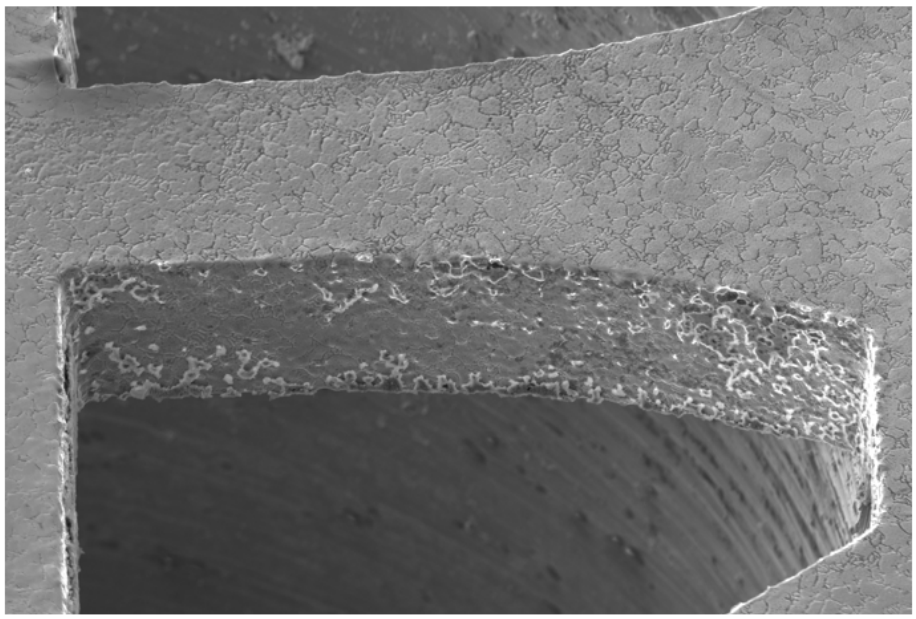


(b)

Fig. 3.1 Recast layer on the side surfaces of samples (a) global view (b) magnified view

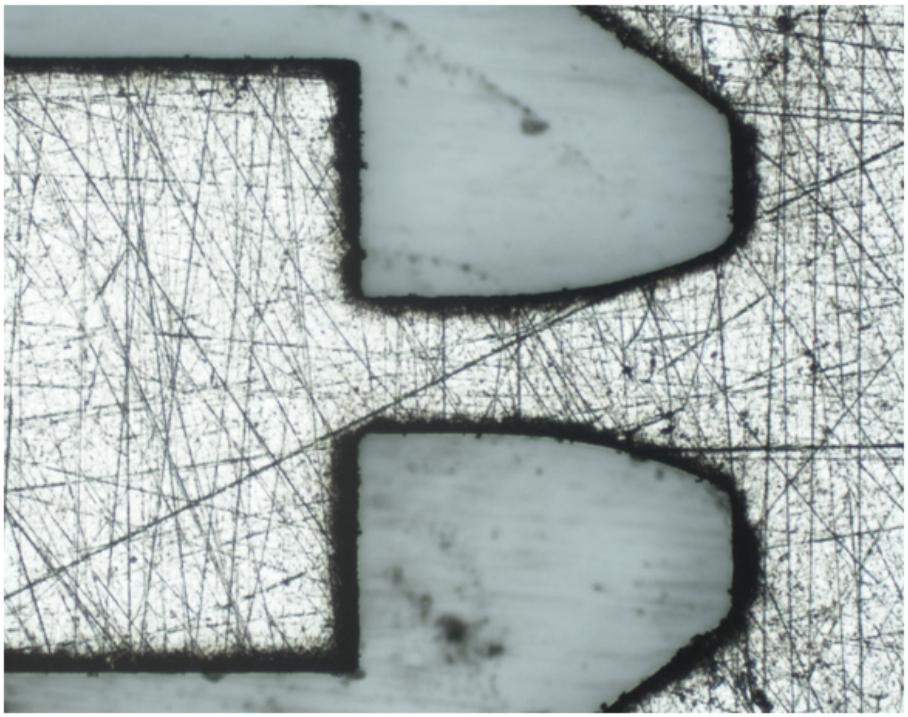


(a)

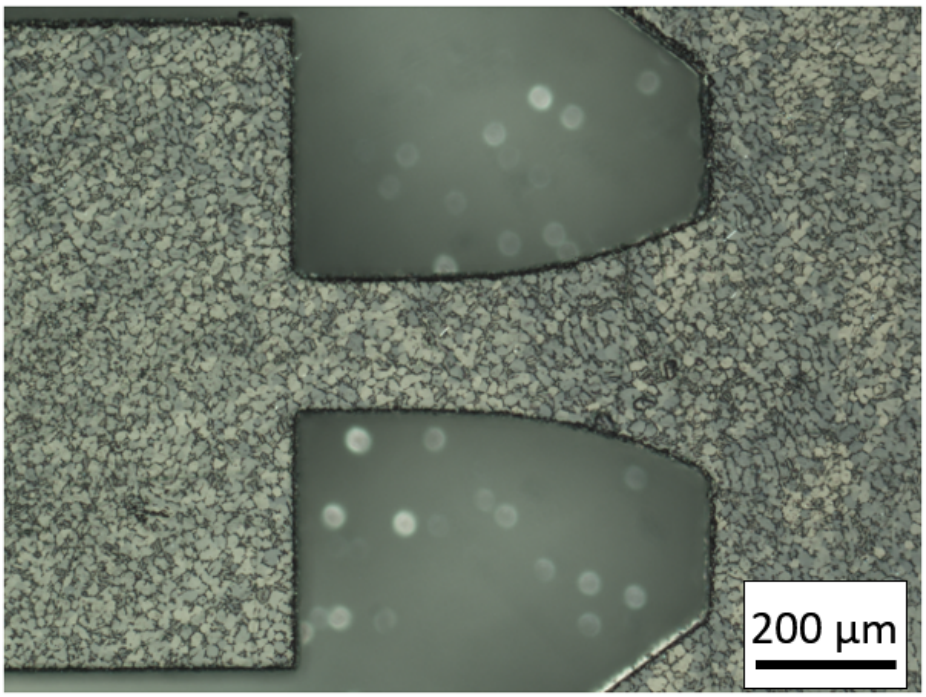


(b)

Fig. 3.2 The removal of recast layers after (a) 40 and (b) 60 seconds of electropolishing



(a)



(b)

Fig. 3.3 Surface quality of (a) as-received (b) electropolished meso cantilevers

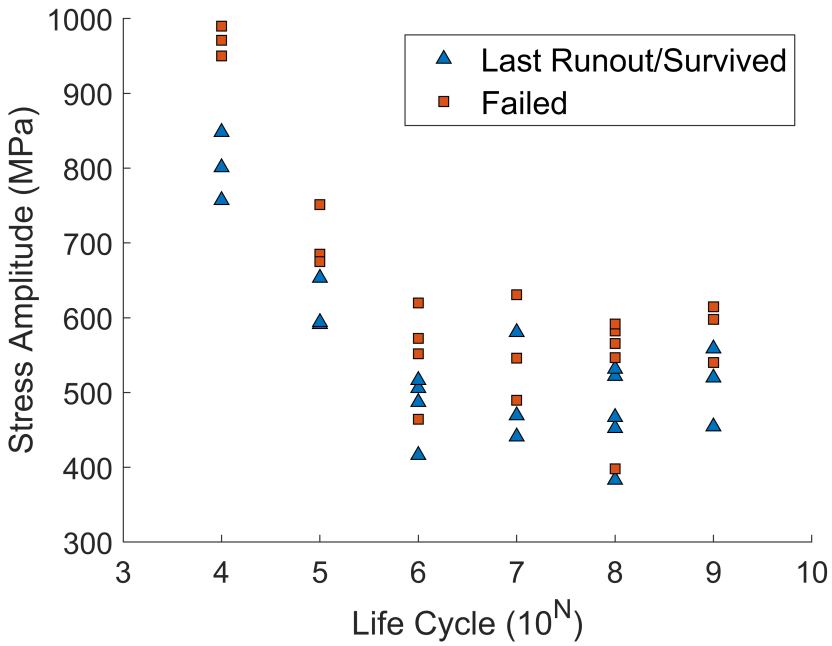


Fig. 3.4 S-N plot of as-received Ti-6Al-4V meso cantilevers with recast layers indicated by Figures 3.1 and 3.3a

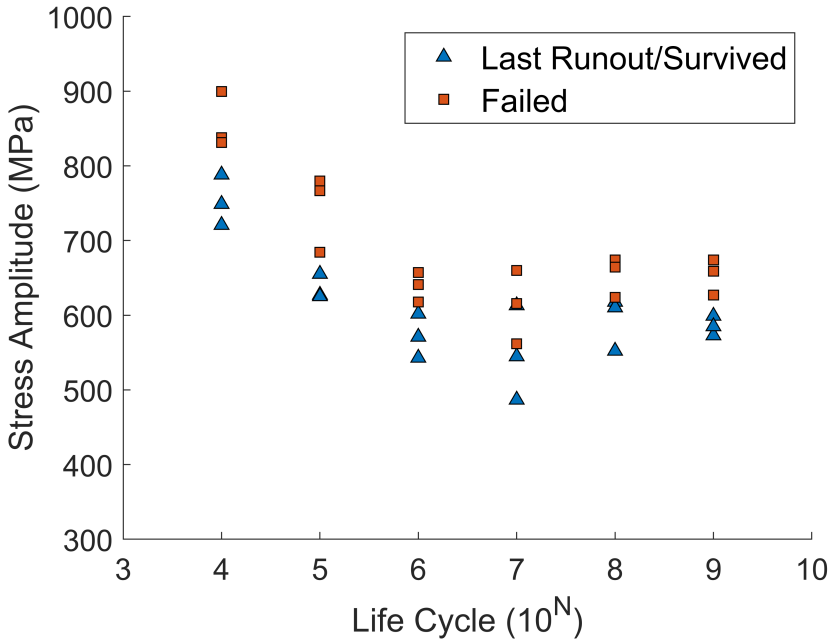


Fig. 3.5 S-N plot of electropolished Ti-6Al-4V meso cantilevers with surface quality indicated by Figures 3.2b and 3.3b

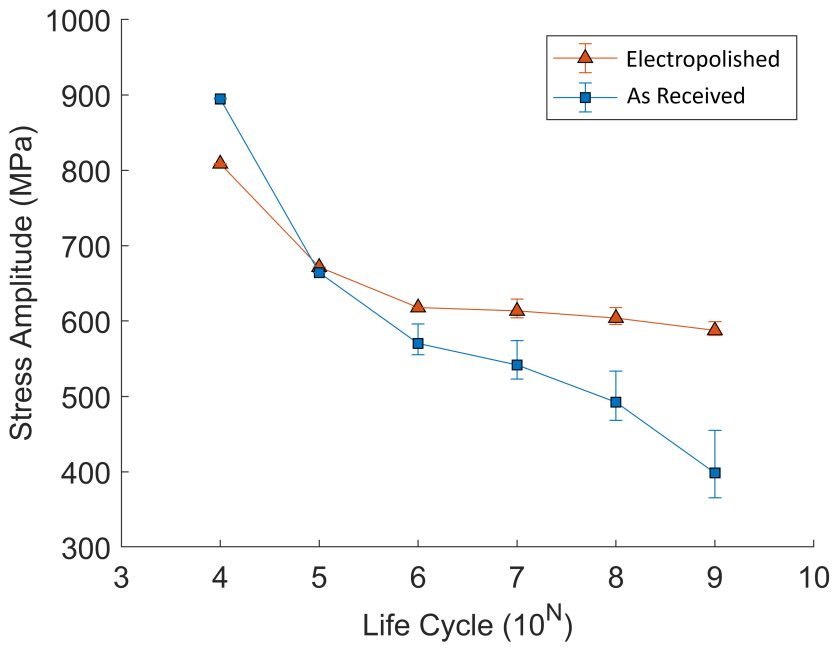


Fig. 3.6 Comparison of fatigue life performance between electropolished samples and as-received samples with recast layers. Data processed by logistic regression as discussed in Chapter 2

3.3.2 Ultrasonic bending fatigue data in comparison to data in the literature

Ultrasonic fatigue testing, operating at the frequency of approximately 20 kHz, enables the rapid assessment of fatigue life in the VHCF regime in a relatively short duration. This makes it a powerful tool for evaluating the long term durability of structural materials such as Ti-6Al-4V. However, concerns remain regarding the comparability of ultrasonic fatigue results to those obtained through conventional low-frequency fatigue testing using common servo-hydraulic apparatus. Potential frequency effects, such as differences in heat generation, deformation mechanisms, and crack initiation behaviour, raise questions about the validity of extrapolating ultrasonic fatigue data to real-world loading conditions. In this study, fatigue tests on Ti-6Al-4V were conducted from 10^4 to 10^9 cycles at 20 kHz and R = –1. The results

are compared against existing conventional fatigue data to evaluate the influence of frequency and the reliability of ultrasonic fatigue testing for life prediction.

The comparison of bending ultrasonic fatigue data with fatigue testing at lower frequencies is shown in Figure 3.7. In an attempt to best isolate the strain-rate effects, data from the literature were selected exclusively from studies on Ti-6Al-4V with bimodal/nearly equiaxed microstructures and fully reversed loads (R = –1). In addition, the lower frequency fatigue data were derived from specimens with larger gauge lengths, typically ranging from several tens to hundreds of millimetres, whereas the meso cantilever specimens employed in the present work have a gauge length of approximately 600 microns. Fatigue data from the literature has been replotted using digital measurements from their respective sources [92–95]. When subjected to ultrasonic fatigue testing at 20 kHz, the alloy exhibits a higher fatigue strength compared to data reported at conventional lower loading frequencies. Specifically, the fatigue strength at around 10^7 cycles is approximately 200 MPa higher under ultrasonic loading relative to tests performed at 5 Hz. However, this enhancement diminishes progressively as the loading frequency increases. At other traditional fatigue testing frequencies of 15 Hz, 100 Hz, and 120 Hz, the corresponding differences in fatigue strength relative to the ultrasonic regime are reduced to approximately 120 MPa, 80 MPa, and 50 MPa, respectively. This trend indicates a pronounced strain-rate effect at lower frequencies and becoming less significant at higher frequencies.

A comparison between the present bending ultrasonic fatigue results and existing literature on uniaxial ultrasonic fatigue testing of Ti-6Al-4V (R = –1) is displayed in Figure 3.8. This comparison was also constricted to bimodal and near-equiaxed microstrucutres. It reveals a generally similar performance within the LCF and HCF regime. However, notable deviations arise in the VHCF regime, depending on the literature source. For example, Heinz et al reported a significant reduction in fatigue strength in the VHCF regime that is attributed to a transition from surface- to internal crack initiation mechanisms [36]. This also manifests as

a characteristic double plateau S-N curve. In contrast, the bending ultrasonic fatigue tests conducted in this study did not exhibit such a secondary plateau. This can be attributed to the fact that cyclic bending fatigue does not promote internal crack initiation in any fatigue regimes due to the stress distributions along top and bottom sample surfaces. This results to a classic shape of the S-N curve. A similar distinction between surface and internal crack initiation mechanisms is highlighted by Takeuchi et al, who reported approximately a 50 MPa difference in fatigue strength associated with the transition to internal crack initiation [92].

The comparison of fatigue data across different testing frequencies and between bending and uniaxial loading modes is essential for establishing the validity and comparability of the novel bending ultrasonic fatigue test employed in this work. Existing literature addressing strain rate effects in fatigue presents mixed and sometimes contradictory conclusions, with some studies reporting negligible differences in fatigue response, while others observe substantial deviations. Notably, such discrepancies have even been reported within studies authored by the same research groups [52, 96].

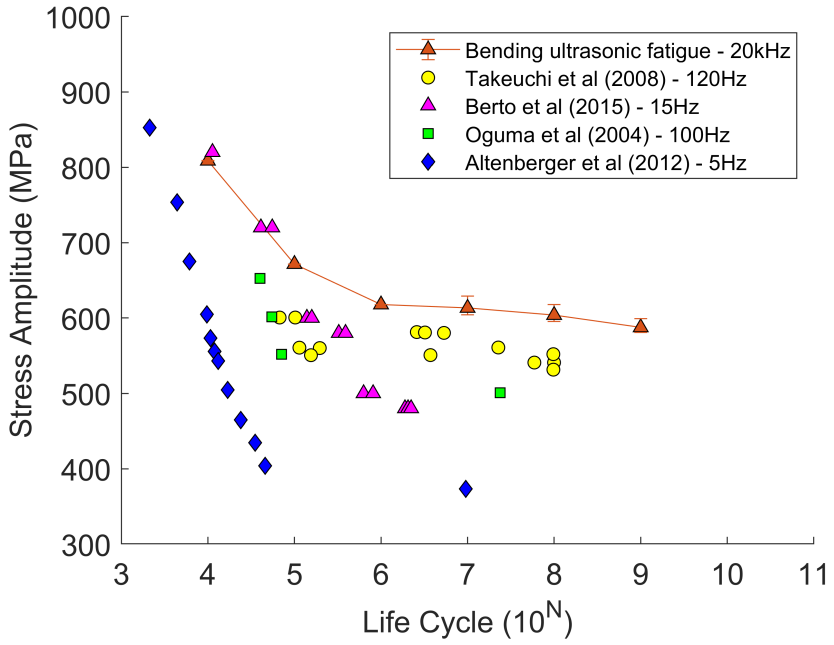


Fig. 3.7 Comparison of fatigue life between bending ultrasonic fatigue at 20 kHz and uniaxial fatigue at lower frequencies. Selected literature were all performed at R = –1 [92–95]

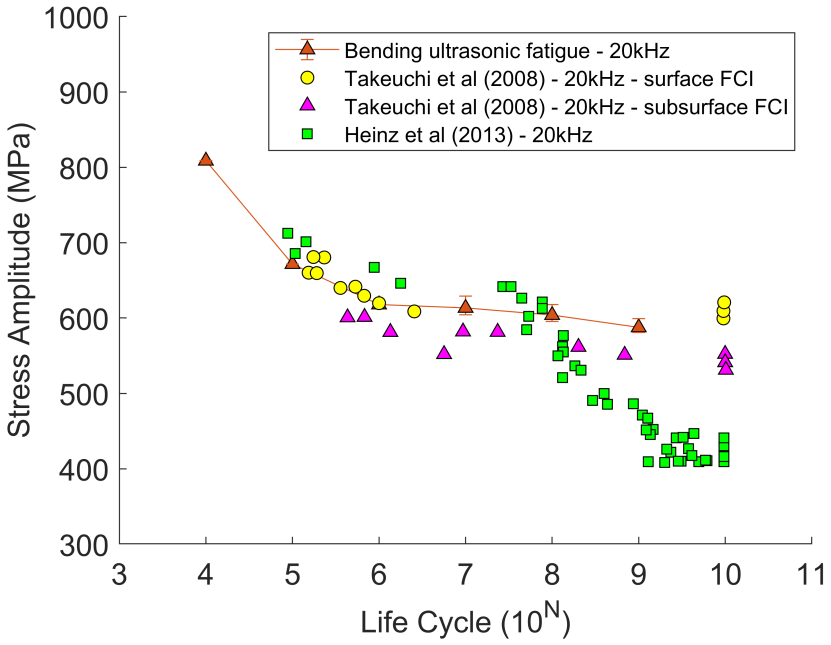


Fig. 3.8 Comparison of fatigue life between ultrasonic bending fatigue and ultrasonic uniaxial fatigue at 20 kHz. Selected literature were all performed at R = –1 [36, 92]

3.3.3 The environmental effects on fatigue properties

The difference in fatigue performance observed between tests conducted in air and ones in high vacuum (10^{-6} mbar) is shown in Figure 3.9. Firstly, it is important to note that fatigue data below 10^5 cycles were not obtained in the vacuum study. This is because the vacuum fatigue strength of Ti-6Al-4V in this decade of life cycle exceeded the maximum cyclic displacement amplitude that the current ultrasonic fatigue rig can safely generate. As a result, specimens in this regime could not be fractured within the safe limits of the apparatus. On the other end of the spectrum, fatigue testing beyond 10^8 cycles was also not conducted. In vacuum, heat generation within the fatigue rig becomes significant for testing in the VHCF regime. The resulting thermal buildup affects the temperature stability of the system and leads to a reduction in operating frequency, which compromise the validity and consistency of the

results. For these reasons, this vacuum study focuses on the fatigue behaviour of Ti-6Al-4V between 10^5 and 10^8 cycles, where reliable experimental control was maintained.

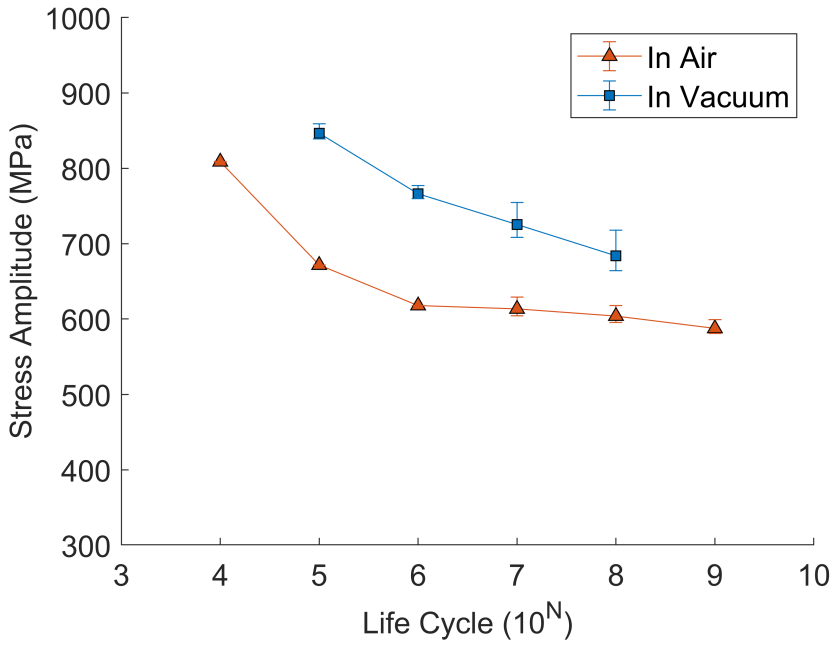


Fig. 3.9 Comparison of fatigue life between electropolished samples performed in air and in vacuum

Fatigue tests performed in vacuum show notably higher fatigue strength across all regimes. In the LCF regime, samples tested in vacuum exhibited significantly improved fatigue performance, with fatigue strength approximately 150 MPa higher than those tested in air at 10^5 cycles. However, as the number of cycles increased toward the VHCF regime, the difference in fatigue strength between the two environments decreased to about less than 100 MPa at 10^8 cycles. Larger data scatter is also visible in the higher fatigue cycles, which may indicate the increased reliance upon the microstructure in vacuum.

The influence of the testing environment on fatigue crack propagation rates has also been evaluated. To enable a meaningful comparison of crack propagation rates between environments, it is necessary to evaluate the data in terms of the stress intensity factor range (ΔK), which is considered a crack size-independent fracture mechanics parameter. The procedure

for calculating ΔK for the unconventional sample configuration of this study was discussed in Chapter 2. Figure 3.10 presents the comparison of fatigue crack propagation behaviour between specimens tested in air (IFS-labeled) and in vacuum (C-labeled). Further discussion of IFS-labeled samples is provided in the following Chapter 4. The results indicate that the specimen tested in vacuum exhibits a markedly lower short crack propagation rate than those tested in air when compared within equivalent ranges of ΔK. Short fatigue crack propagation rates of samples tested in ambient air varied from 10^{-6} to 10^{-4} mm/cycles whereas the sample tested in vacuum propagated in majority between 10^{-8} and 10^{-7} mm/cycles. It is also interesting to note that the vacuum fatigue crack propagation data sits below an $\langle a \rangle$ type Burgers amplitude per cycle. Crack propagation in the order of angstroms per loading cycle have been similarly reported in near-threshold fatigue crack propagation in vacuum, although at load ratios above zero [97–100]. It is therefore clear that vacuum influences the two aspects of fatigue properties (i.e. fatigue life and fatigue crack propagation rates).

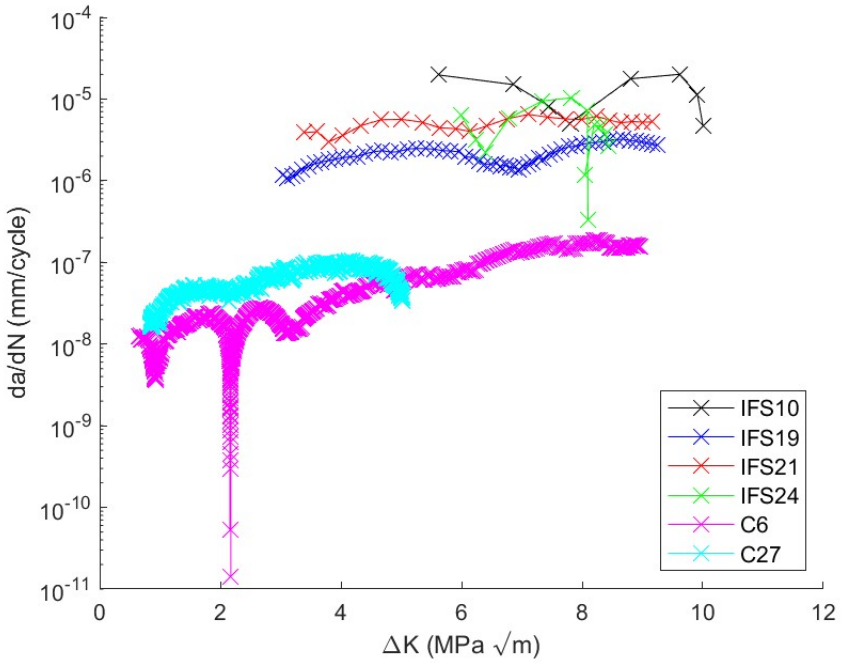


Fig. 3.10 Fatigue crack propagation plot of samples tested in air and vacuum (∼ 10^{-6} mbar

Microstructural examinations have been performed to elucidate the significant differences in fatigue performance caused by vacuum. Figure 3.11 displays the fractography of a sample tested at 10^{-8} cycles in ambient air. Distinct FCI features are found in one of the four edges of the cross section due to the surface stress distribution in cyclic bending. HCF exhibits features that are similar to brittle fracture initiation mechanisms as there is little to no apparent macroscopic plastic deformation. These initiation features are facets of near-basal planes which will be discussed with more details in Chapter 4. Facets are common features found in low cyclic stress intensity factor ranges and therefore near crack initiation sites [101, 102]. These facets are thought to form by cyclic slip along favourable slip planes which then progress into crack nucleation [103, 104]. As the crack grows, striations become visible in the intermediate region, indicating an interval of stable crack growth [102]. Although striations may occasionally be observed within individual grains during the early stages of crack propagation, they are typically less distinct and more discontinuous. The well-defined striations magnified in Figure 3.11c form a quarter ellipse shape from the top surface to the depth profile of the cantilever, providing clear visualisation of the evolving crack geometry. Striation spacing is often understood as the incremental step-by-step growth of a fatigue crack during each loading cycle at high ΔK in mode I. In the field of view of Figure 3.11c, the average striation spacing has been measured to be 0.49 microns, which is an order magnitude higher than the calculated short fatigue crack growth rate shown in Figure 3.10. Some studies have shown that this relationship is not universally valid, particularly in materials exhibiting intermittent or microstructure-sensitive crack propagation [105–107]. For Ti-6Al-4V, Wanhill et al, who evaluated the complex transition of structure-sensitive and continuum-mode crack growth, saw that the striation spacings were also an order of magnitude larger than macroscopically determined crack growth rate per cycle [105]. Lastly, a distinct triangular feature is usually found in the opposite diagonal direction of the crack

initiation feature, which signifies the transition to Stage III fatigue crack growth. Within this region, a mixture of fibrous ductile β features and brittle α cleavage planes are visible.

Surface examination (Figure 3.12) of the same specimen fatigued in the VHCF regime revealed a minimal degree of visible plastic deformation on both sides of the sample. At the crack initiation corner, no visible evidence of plasticity was observed. As the crack front propagated across the initiation surface, only subtle indications of PSBs were detected, suggesting that crack nucleation and early stage growth occurred predominantly under elastic conditions, consistent with the expected characteristics of VHCF behaviour. Occasional signs of plastic deformation, manifested as PSBs, were observed on the opposing surface of the specimens. Notably, the PSBs were generally confined to a single dominant slip system that are easily traced through EBSD. This restriction to one slip system indicates a high degree of deformation localisation and further underscores the limited plastic activity in the vicinity of the crack path.

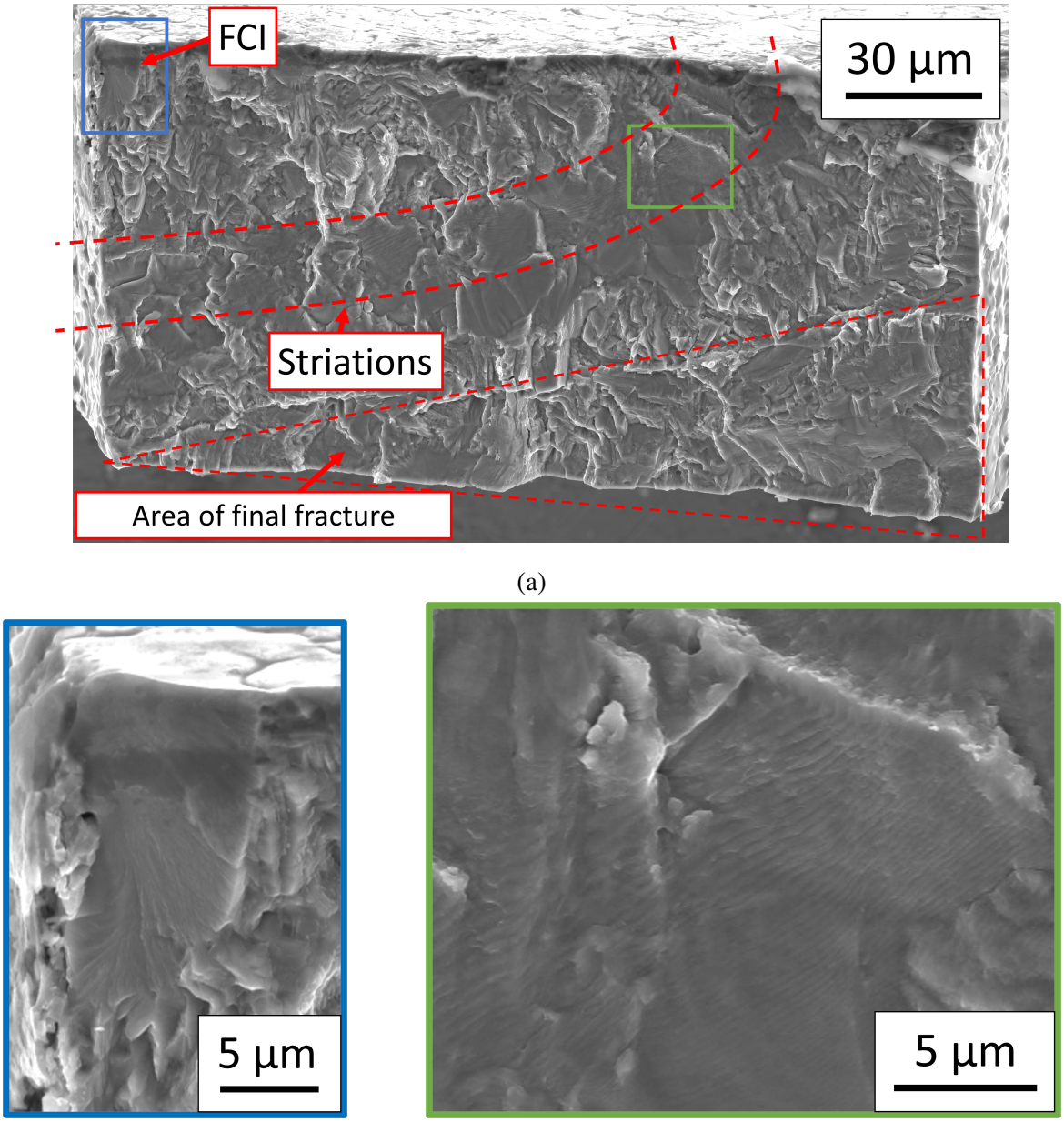
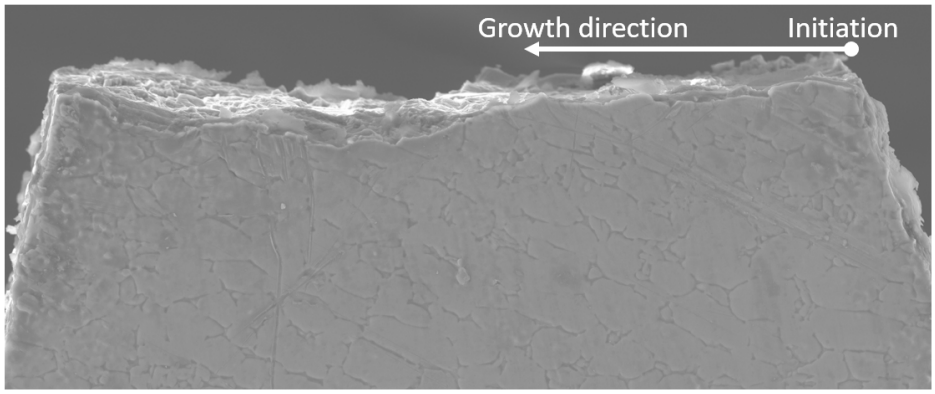
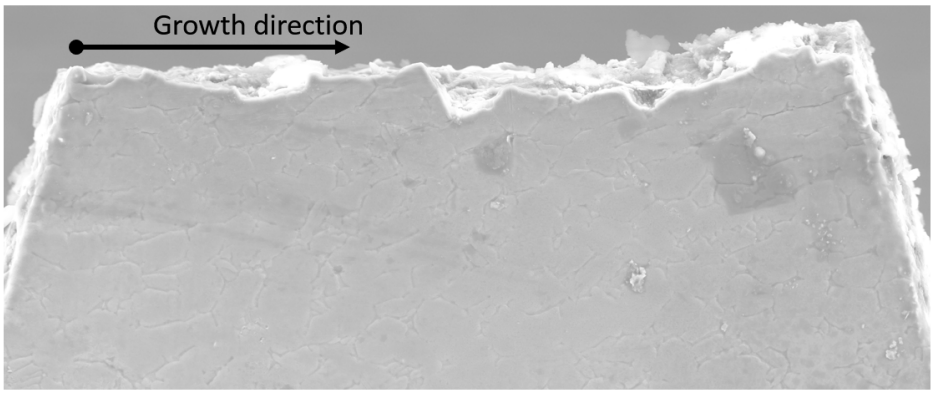


Fig. 3.11 (a) Fracture surface of Ti-6Al-4V tested in air at 10^8 cycles (b) FCI facet (c) striations in the intermediate regions. An average striation spacing of 0.49 microns has been measured in this field of view



(a)



(b)

Fig. 3.12 Surfaces of a fatigued sample performed in ambient air at 10^8 cycles (a) Crack initiation side (b) Opposing side

Figure 3.13 displays the fracture surface of a sample tested in vacuum at 10^8 cycles. The fracture surface of VHCF samples tested in vacuum exhibit substantially more ductile fracture features compared to the ones tested in ambient air. Crack initiation and the early crack growth stage shows large crack path deflections, shown by the pronounced triangular feature in the bottom left of Figure 3.13. The fracture surface exhibits more topographical features such as dimples which are depressions formed by the coalescence of microvoids during ductile fracture [108]. Overall, the fractography of samples tested in vacuum are much more complex. The sample top and bottom surfaces, shown in Figure 3.14, exhibit greater signs of plastic deformation compared to HCF testing in air, primarily due to the delayed onset of the crack initiation stage occurring at higher stress amplitudes. The crack initiation and early crack propagation surface features do not show plastic deformation, similar to the FCI features in samples tested in ambient air. However, as the fatigue crack advanced, pronounced plastic deformation became evident near the termination of crack growth on the initiation side of the specimen. Furthermore, with continued crack propagation through the specimen thickness, substantial plastic activity was observed on the opposing surface. A notable distinction from the air-tested condition is that, in vacuum, individual grains frequently exhibited slip activity across multiple slip systems, rather than being restricted to a single dominant system. This behavior indicates a greater accommodation of plastic deformation during fatigue crack growth under vacuum, suggesting that the absence of environmental interactions facilitates more extensive slip activation and plastic deformation in the later stages of fatigue crack propagation.

The overall enhancement in fatigue properties under vacuum conditions aligns with existing literature. Increased fatigue life throughout the entire regime is caused by the delayed crack initiation stage occurring at higher stress amplitudes [109–113]. The prevailing explanation for the better fatigue life in vacuum is the role of oxygen adsorption during the crack initiation phase [99, 109, 114, 115]. In vacuum, minimal oxygen adsorption allows

for a greater extent of reversible slip activity [108, 109]. Internal heating has also been discussed to cause higher slip activity at crack tips in vacuum [108, 109, 114]. In ambient air, the presence of oxygen interacts with cyclic slip features which promotes accelerated crack initiation [108–110, 114]. Consequently, the kinematics of molecular adsorption, particularly of oxygen and water vapour, also provide significant contributions to the accelerated fatigue crack propagation rates of samples tested in ambient air [111, 116–118].

To investigate the extent of oxygen adsorption along fatigue crack paths, scanning transmission electron microscopy (STEM) coupled with EDS was employed to evaluate elemental distributions in FCI grains. TEM lamellae were prepared from specimens subjected to 10^8 cycles using a focused ion beam (FIB). Figure 3.15 and 3.16 display the FCI micrographs of samples tested in ambient air and high vacuum, respectively. Table 3.1 and 3.2 present the peak heights of individual elements across different regions of interests and compares the normalised values across samples. Careful approach must be made when comparing results across samples in STEM-EDS due to sample thickness effects as thicker lamellae tend to attenuate more low-energy X-rays. To evaluate the potential thickness effects, the Ti-Lλ peaks were normalised to Ti-Kα peaks. The Ti-Lλ/Ti-$K\alpha$ results show that the values are in the similar order of magnitudes across samples. Normalising the V-Kα and Al-Kα peak heights similarly revealed the same orders of magnitudes, except for the fourth ROI in Table 3.1, where it exhibited a depreciated content in alumunium and elevated content in vanadium, signifying the β phase. Likewise, the STEM-EDS analysis revealed that oxygen concentrations in the bulk α phase are similar (≈ 0.015) across samples, which further strengthens the feasibility to conduct this comparative study across TEM samples.

The distinct difference in normalised oxygen content were apparent when comparing the normalised oxygen contents along crack surfaces. The normalised oxygen content in ambient air-tested specimens were significantly higher (0.488 and 0.874) than those observed in specimens fatigued in vacuum (0.078). These findings provide strong experimental support

stating that oxygen adsorption and environmental embrittlement significantly degrade fatigue performance in air. Interestingly, while much lower in intensity, traces of oxygen segregation were still detected in vacuum-tested samples, indicating that oxygen ingress and adsorption can still occur, albeit at a reduced concentration, even under nominally inert conditions. Further investigation is required to elucidate the mechanisms of oxygen transport, adsorption kinetics, and their interactions with microstructural features during crack propagation; however, these characterisation efforts reveal the significant differences of oxygen adsorption for fatigue samples tested in vacuum and air. Understanding these mechanisms is critical for predicting and mitigating environmentally assisted fatigue for titanium alloys.

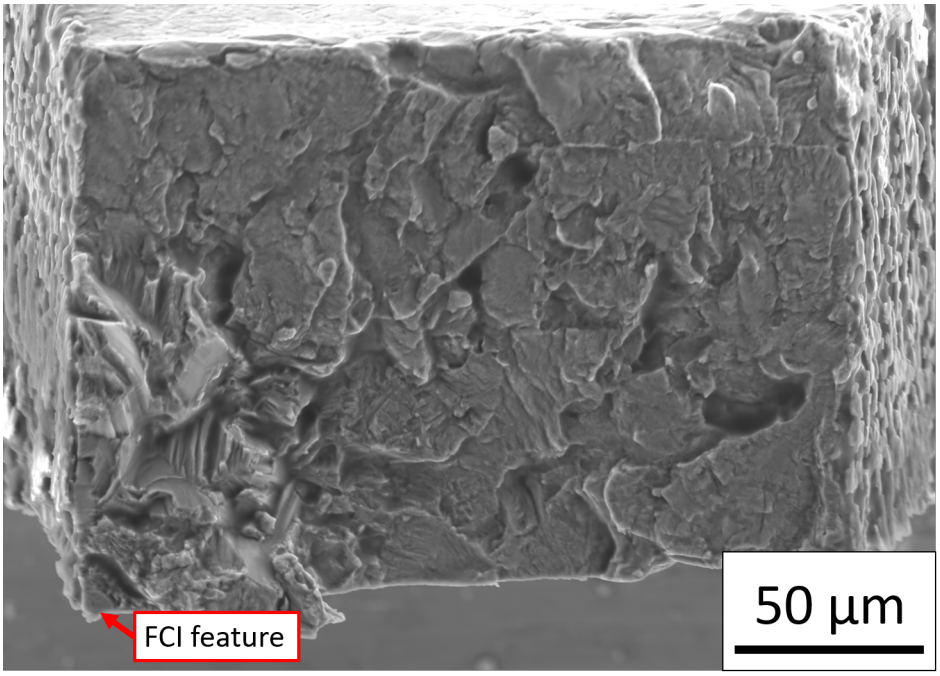
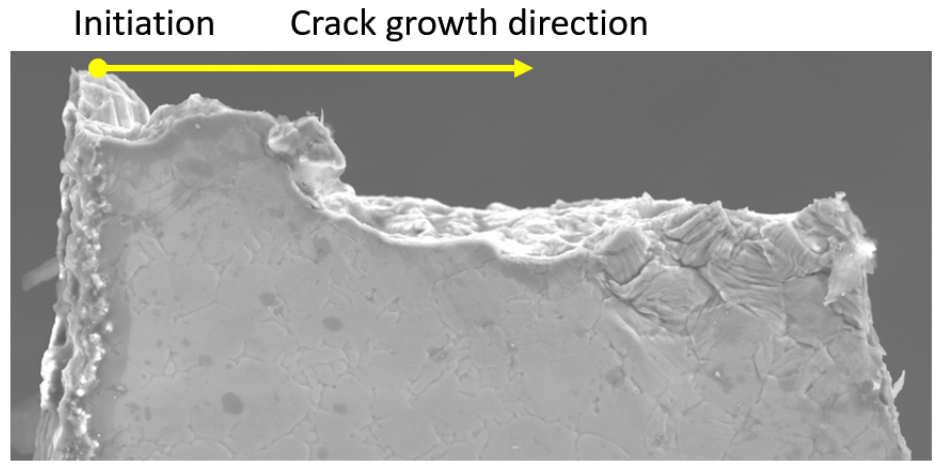
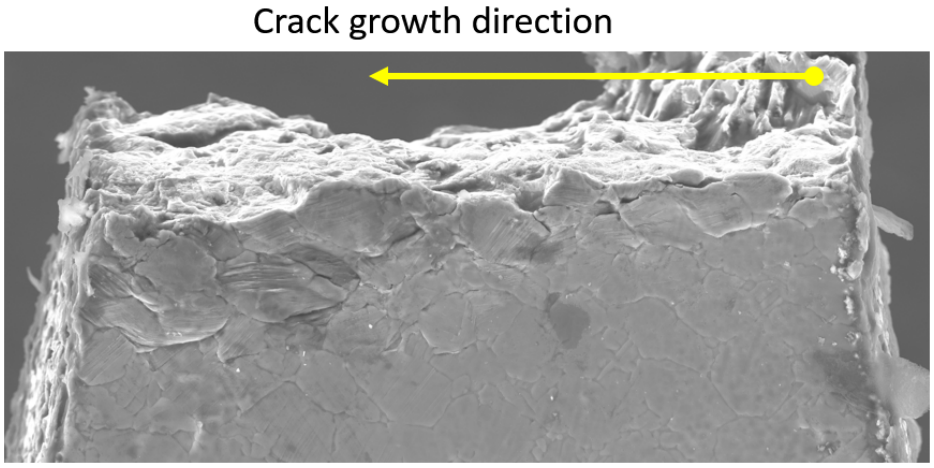


Fig. 3.13 Fracture surface of Ti-6Al-4V tested in vacuum at 10^8 cycles



(a)



(b)

Fig. 3.14 Surfaces of a fatigued sample performed in high vacuum at 10^8 cycles (a) Crack initiation side (b) Opposing side

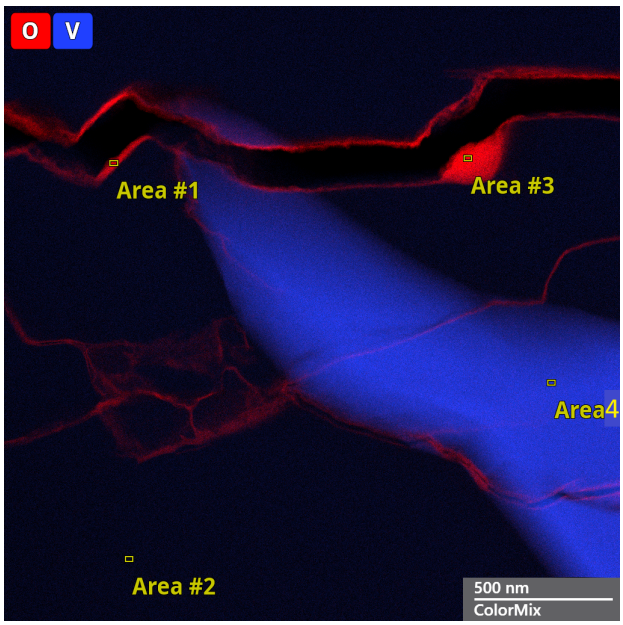


Fig. 3.15 STEM-EDS micrograph showing the oxygen and vanadium contents in an FCI grain from a sample tested in ambient air at 10^8 cycles. The area with a high vanadium content represents the β phase

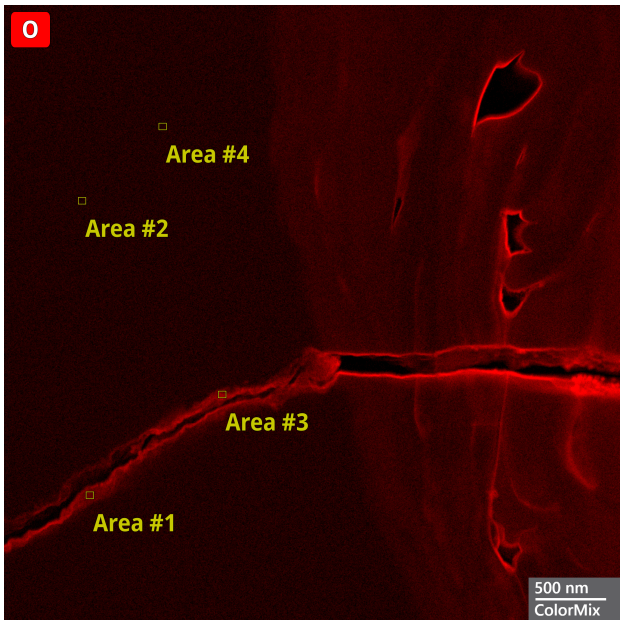


Fig. 3.16 STEM-EDS micrograph showing the oxygen content in an FCI grain from a sample tested in high vacuum at 10^8 cycles

Table 3.1 STEM-EDS peak heights of a sample fatigued in ambient air at 10^8 cycles

ROI	Area 1	Area 2	Area 3	Area 4
Feature	Crack	Alpha/Bulk	Crack	Beta
Ti-L	0.524	0.799	0.551	0.759
O-K	1.073	0.077	1.505	0.137
Al-K	0.262	0.583	0.291	0.202
Ti-K	2.197	5.023	1.723	4.118
V-K	0.353	0.822	0.308	1.856
Ti-L/Ti-K	0.239	0.159	0.320	0.184
Al-K/Ti-K	0.119	0.116	0.169	0.049
V-K/Ti-K	0.161	0.164	0.179	0.451
O-K/Ti-K	0.488	0.015	0.874	0.033

Table 3.2 STEM-EDS peak heights of a sample fatigued in high vacuum at 10^8 cycles

ROI	Area 1	Area 2	Area 3	Area 4
Feature	Crack	Alpha/Bulk	Crack	Alpha/Bulk
Ti-L	1.918	2.402	2.100	2.616
O-K	0.794	0.283	1.232	0.265
Al-K	1.316	1.908	2.142	2.028
Ti-K	10.173	17.921	15.886	17.986
V-K	1.606	2.835	2.437	2.771
Ti-L/Ti-K	0.189	0.134	0.132	0.145
Al-K/Ti-K	0.129	0.106	0.135	0.113
V-K/Ti-K	0.157	0.158	0.153	0.154
O-K/Ti-K	0.078	0.016	0.078	0.015

3.4 Summary

This chapter has investigated the influence of redeposit layers induced from laser machining, the comparability of ultrasonic fatigue testing to conventional methods, and the environmental effects of vacuum versus air on fatigue performance, by performing ultrasonic fatigue testing from 10^4 to 10^9 cycles, followed by complementary advanced characterisation techniques. The main findings are summarised as follows:

1. The influence of redeposit layers induced from laser machining shows a significant drop in fatigue strength in HCF and VHCF regimes The removal of redeposit layers through electropolishing resulted to pronounced increase in fatigue strength from approximately 50 MPa higher at 10^7 to 200 MPa higher at 10^9 cycles.

2. The comparison of this study's ultrasonic bending fatigue data to fatigue data at lower frequencies from the literature reveals a generally higher fatigue strength with increasing testing frequencies. At approximately 10^7 cycles, the fatigue strength performed at an ultrasonic frequency was about 200 MPa greater than that obtained from tests conducted at 5 Hz. However, this difference gradually decreased with increasing frequency. At other typical testing frequencies (i.e. 15 Hz, 100 Hz, and 120 Hz) the corresponding increases in fatigue strength relative to the ultrasonic regime were reduced to approximately 120 MPa, 80 MPa, and 50 MPa, respectively. This trend suggests that the strain-rate sensitivity of the alloy is more pronounced at lower frequencies and becomes progressively less significant as the testing frequency increases.

3. A comparison between the present bending ultrasonic fatigue results and previously published uniaxial ultrasonic fatigue data for Ti-6Al-4V at R = –1 was also performed. Overall, the fatigue performance observed in this study aligns closely with the literature within both the low-cycle fatigue (LCF) and high-cycle fatigue (HCF) regimes. However, noticeable deviations emerge in the very-high-cycle fatigue (VHCF) regime,

with the extent and nature of these differences was primarily caused by the mechanistic differences between cyclic uniaxial and cyclic bending.

4. The difference in fatigue performance between tests conducted in air and ones in high vacuum (10^{-6} mbar) was conducted through the generation of SN curves, fractography and STEM-EDS. Fatigue tests performed in vacuum show notably higher fatigue strength across all regimes from approximately 150 MPa in LCF to 100 MPa in VHCF. The results also indicate that the specimen tested in vacuum exhibits a markedly lower crack propagation rate than those tested in air when compared within equivalent ranges of ΔK. Fatigue crack propagation rates of samples tested in ambient air varied between 10^{-6} to 10^{-4} mm/cycles whereas the sample tested in vacuum propagated in majority between 10^{-8} and 10^{-7} mm/cycles. It is therefore clear that vacuum influences the two aspects of fatigue properties (i.e. fatigue life and fatigue crack propagation rates).

5. Fractography has been performed to elucidate the significant differences in fatigue properties. Overall, fractography of samples tested in ambient air were much clearer to investigate. The FCI features were characteristic of brittle fracture, with minimal macroscopic plastic deformation. These features were identified as facets oriented near basal planes, formed through localized cyclic slip along favorably oriented crystallographic planes. As the cracks propagated, striations developed in the intermediate growth region, displaying a quarter-elliptical pattern that clearly delineated the advancing crack front from the surface into the specimen depth. The later stages of crack growth were marked by a distinct triangular region on the opposing diagonal of the initiation site, where a mixture of fibrous ductile β features and brittle α cleavage features are visible. For vacuum-tested samples, the fracture surface exhibits significantly more topographical features such as dimples which are depressions formed by the coalescence of microvoids during ductile fracture. The sample surfaces also exhibit greater signs of

plastic deformation compared to HCF testing in air, primarily due to the delayed onset of the crack initiation stage occurring at higher stress amplitudes.

6. STEM-EDS was performed to evaluate the difference in oxygen adsorption across two mediums. To overcome potential sample thickness effects and perform a comparison across samples, the O-Kα peaks were normalised to Ti-Kα peaks. The normalised oxygen content in ambient air-tested specimens were significantly higher (0.488 and 0.874) than those observed in specimens fatigued in vacuum (0.078), while maintaining a consistent normalised value across other elements (i.e. normalised Ti, Al, and V content). These findings provide strong experimental support stating that oxygen adsorption and environmental embrittlement significantly degrade fatigue performance in air.

Chapter 4

Fatigue crack initiation in very high cycle fatigue

4.1 Introduction

This chapter presents the characterisation of fatigue crack initiation and short crack growth in the VHCF regime. Research shows that the majority of the fatigue life is consumed to initiate crack growth. Understanding the mechanisms of fatigue crack initiation and early crack propagation is critical for improving fatigue resistance. However, fatigue crack initiation in Ti-64Al-4V is less understood than in other alloys such as steel [27]. FCI features in other alloys are commonly found to be from inclusions and porosity; however these are are not commonly found in titanium alloys due to lesser inclusion density. Identifying the orientations and microstructural configurations most susceptible to fatigue crack initiation is essential for developing effective mitigation strategies. This chapter focuses on the initiation and early propagation behaviour of short cracks in Ti-6Al-4V, aiming to highlight important microstructural features and orientations that govern fatigue life in the VHCF regime.

4.2 Experimental methods

Four samples are evaluated in these tests, named IFS10, IFS19, IFS24, and IFS25. These samples were ground to 4000 SiC paper, polished in a 5:1 mixture of colloidal silica and hydrogen peroxide for one and a half hours, laser-cut into individual meso cantilevers and then individually electropolished in 6% Perchloric acid, 35% Ethylene Glycol and 59% Methanol at –50°C. Prior to fatigue testing, each side of the sample was observed using secondary electrons and EBSD with the a Bruker or Oxford Instruments Symmetry detector on a Zeiss Merlin at the David Cockayne Centre for Electron Microscopy. The samples then underwent interrupted fatigue tests at 10^8 cycles using the stress-step protocol. Once a fatigue crack is detected by the algorithm, each sample is observed in both optical and electron microscopes to evaluate the FCI and short crack growth features by matching the features with pre-fatigue EBSD maps.

4.3 Results

4.3.1 IFS10

Figure 4.1 shows the IPFX map and pole figure of IFS10. The pole figure shows a maximum of 6.4 multiples of random distribution (mrd) of basal texture in the longitude direction of the cantilever. The particular unit expresses how common a crystallographic orientation is to a completely random texture. Figure 4.2 displays the stress amplitude as a function of the number of life cycles. The sample underwent step-stress testing to 573 MPa at 10^8 cycles, followed by interruption after 1.97×10^6 cycles at a stress amplitude of 618 MPa. The observation reveals a predominantly transgranular mode of fatigue crack propagation, with crack paths exhibiting strong crystallographic features. Figure 4.3 displays the orientation and Schmid factor of grains along the transgranular crack path. This plot revealed crack propagation within high basal Schmid factor in the early stages of short crack propagation

(grain 1 to 7), followed by a transition to grains with high prismatic Schmid factor (grains 8 to 11).

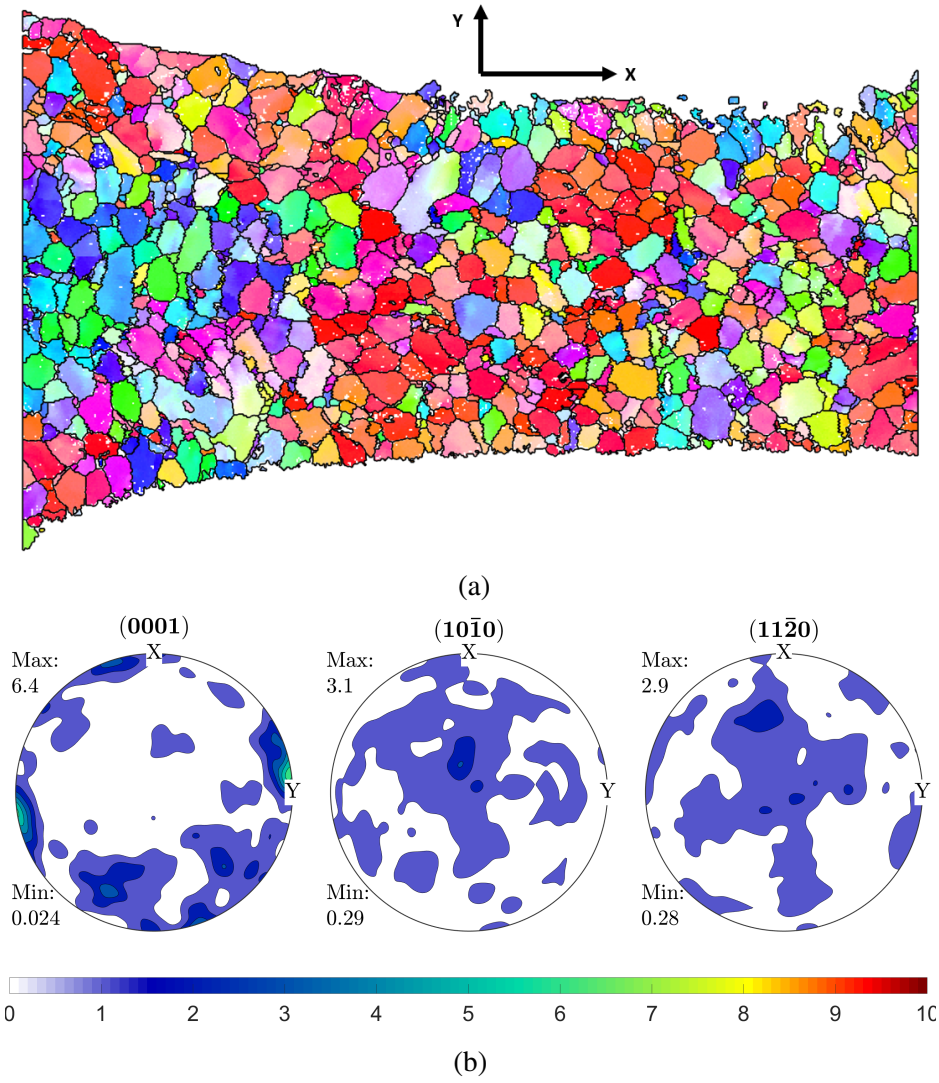


Fig. 4.1 (a) IPFX Map and (b) Pole Figure of IFS10 sample

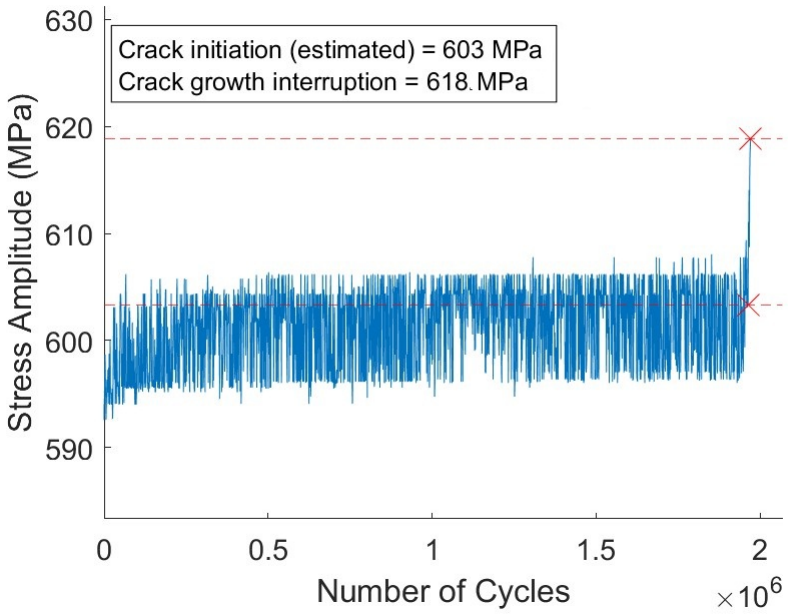


Fig. 4.2 Interrupted fatigue sequence for IFS10 sample

To further investigate the crystallographic nature of short crack propagation, slip trace analysis (Figure 4.4) was performed on the fracture surfaces. In the crack initiation regions (grain 1 and 2), the slip traces showed excellent alignment with basal planes, corroborating the previous prediction based on the Schmid factor maps that were displayed in Figure 4.3c and d. The alignment to near-basal slip traces remained strong until grain number 7. As the crack extended further, the propagation path continued to exhibit strong crystallographic alignment; however, it has become favoring towards prismatic planes as shown in grain 10 and 11. This is again consistent with the Schmid factor map that is more favourably oriented towards the prismatic planes for grain 8 to 11.

The grain orientations associated with FCI features (filled circles) were compared to the orientations of potential crack initiation grains (unfilled circles) located along the side profiles of the gauge section, as visualised in Figure 4.5. These 'hotspot' grains experience the highest bending stress distributions throughout the fatigue test due to the cyclic bending motion. The size of the circles are proportional to the sizes of the respective grains to evaluate

any size trends. Schmid factor isocurves for both basal (red text colour) and prismatic (blue text colour) slip systems were overlaid onto the orientation distribution plot to visualise the slip favourability across the grain population. This plot revealed that the grains where cracks initiated were located in regions of high basal Schmid factor (above 0.45). In the attempt to evaluate potential effects of microtexture, Figure 4.6 displays the mean orientation of FCI and FCI-neighbouring grains in respect to the texture of 'hotspot' grains. The plot shows that FCI and FCI-neighbouring grains in this sample initiated in areas of noticeable (2-3 mrd) texture.

Figure 4.7 displays the Luster-Morris (m') calculations of the two FCI grains (grain 1 and 2). The parameter quantifies the geometric alignment between potential slip systems in adjacent grains and serve to evaluate the difficulty of slip transfer. The value of m' ranges from 0 (impenetrable grain boundary) to 1 (perfect slip transfer). The figure reveals a high compatibility of slip transfer in the basal-to-basal planes using both calculations based on the maximum m' (top table) and on the maximum Schmid factor analysis (bottom table). This suggests minimal barriers to dislocation motion across the grain boundaries. This high slip transfer feasibility is once again corroborated by the matching slip trace analysis displayed in Figure 4.4.

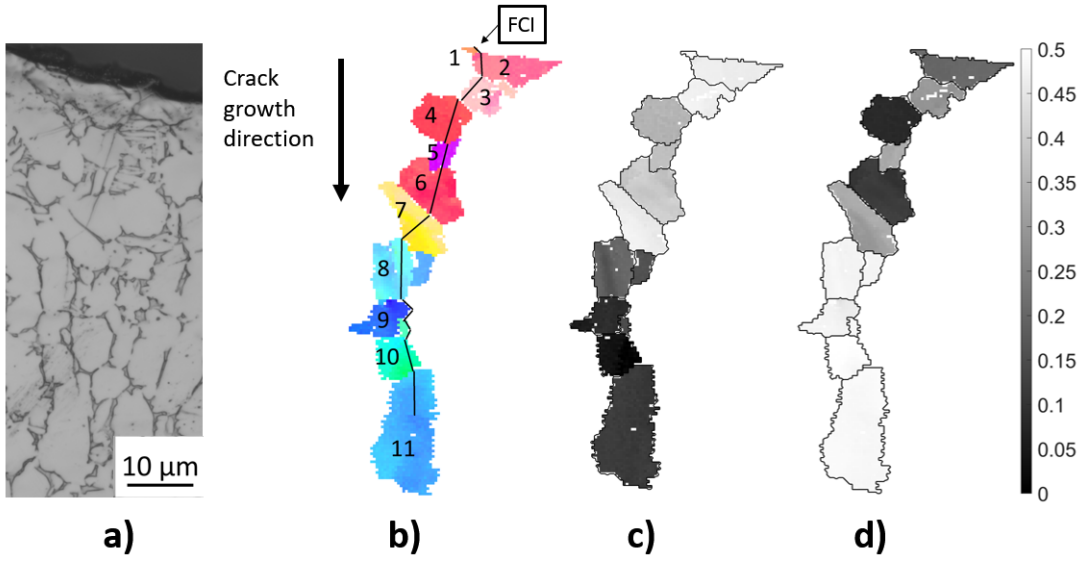


Fig. 4.3 Schmid Factor (SF) analysis of the fatigue crack in IFS10 (a) Optical microscope image (b) IPFX Map with the outlined fatigue crack path and grain numbers (c) Basal SF (d) Prismatic SF

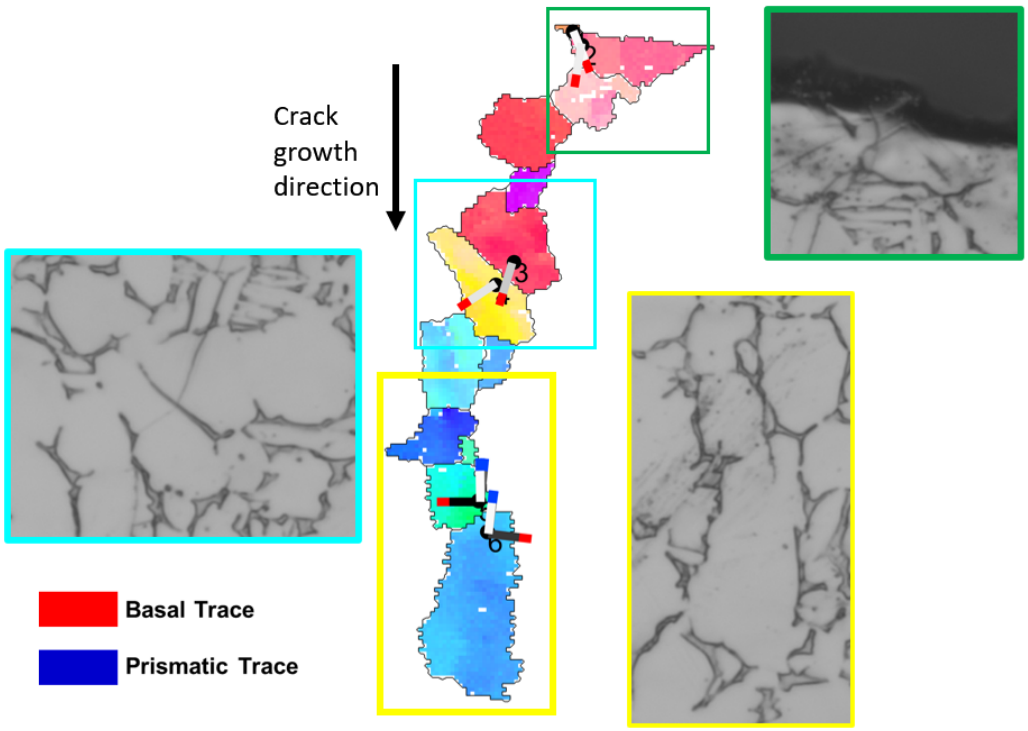


Fig. 4.4 Trace analysis of the fatigue crack for IFS10. The ends of the batons are coloured red or blue to signify the corresponding slip trace, while the grayscale colour on the body signifies the intensity of the Schmid factor.

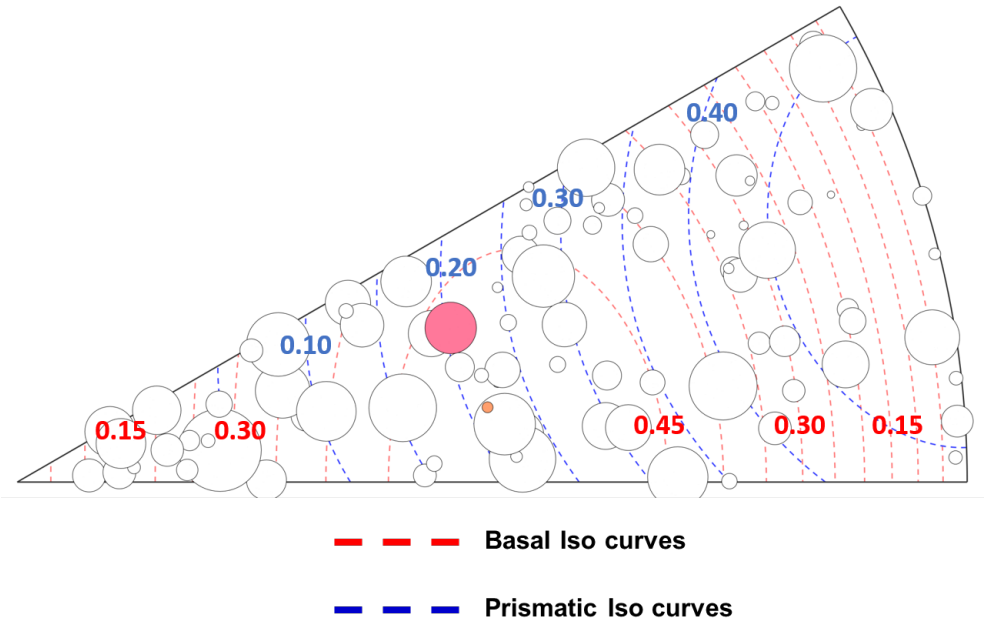


Fig. 4.5 Orientations and grain sizes of FCI grains (coloured circles) in respect to the basal and prismatic isocurves and the orientation of 'hotspot' grains (white circles) in IFS10. 'Hotspot' grains are located in high stress areas of the gauge during cyclic bending, which are alongside the sides of the meso cantilever surfaces

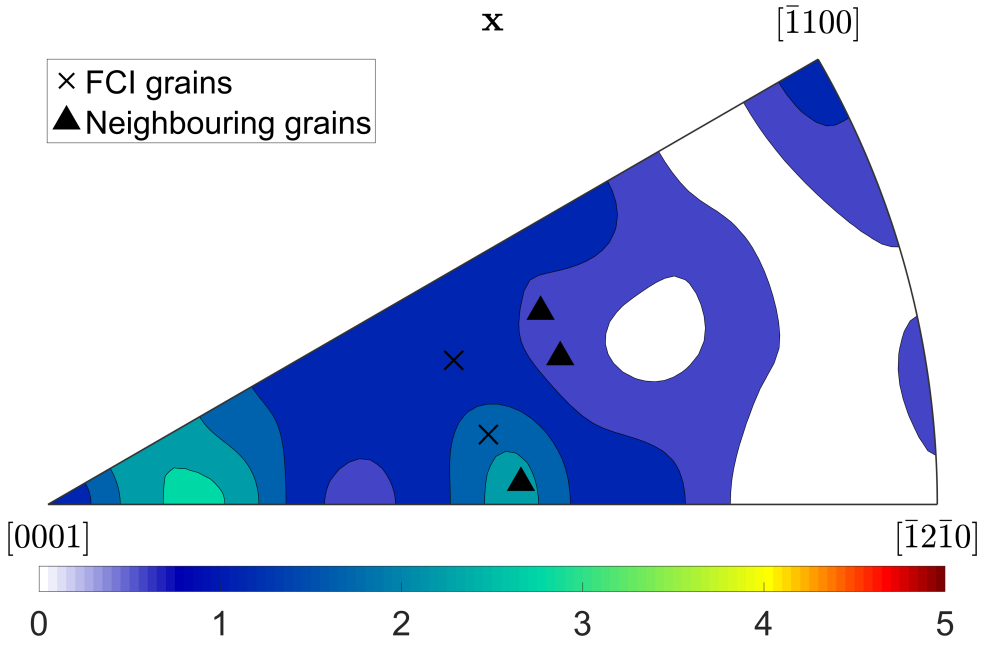


Fig. 4.6 Orientations of FCI and neighbouring grains in respect to the texture of 'hotspot' grains in IFS10

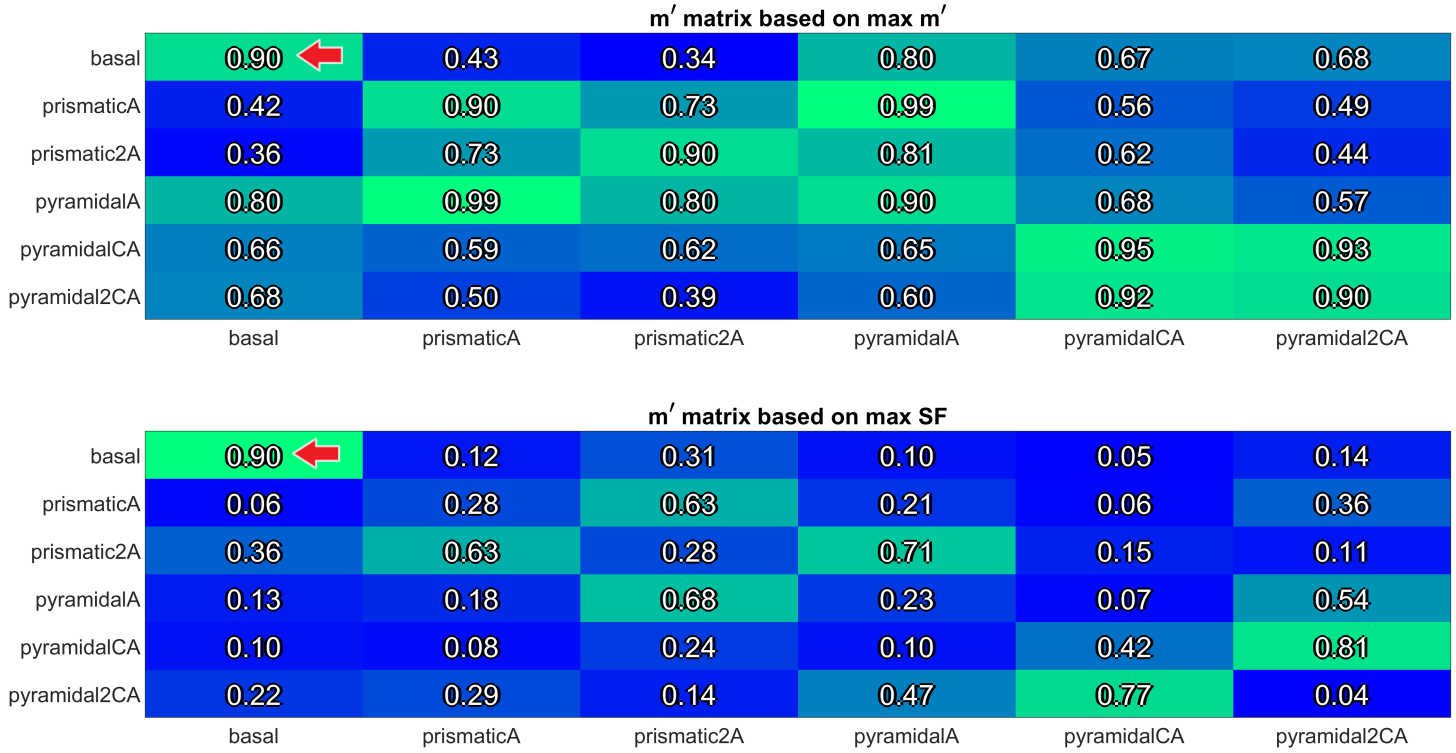


Fig. 4.7 Luster-Morris parameter (m′) calculations based on (top) maximum m′ and (bottom) maximum Schmid factor for Grain 1 and 2. The red arrows point to the physical matching of the trace analysis

4.3.2 IFS19

Figure 4.8 illustrates the relatively low level of crystallographic texture in sample IFS19, with a maximum intensity of 3.6 mrd in the basal direction. This indicates a more random grain orientation compared with sample IFS10, which exhibits a higher maximum intensity of 6.4 mrd. In sample IFS19, crack initiation has been detected by the algorithm at a stress amplitude of 633 MPa after 4.47×10^5 cycles, as shown in Figure 4.9. The previous step-stress testing was performed at a stress amplitude of 595 MPa for 10^8 cycles.

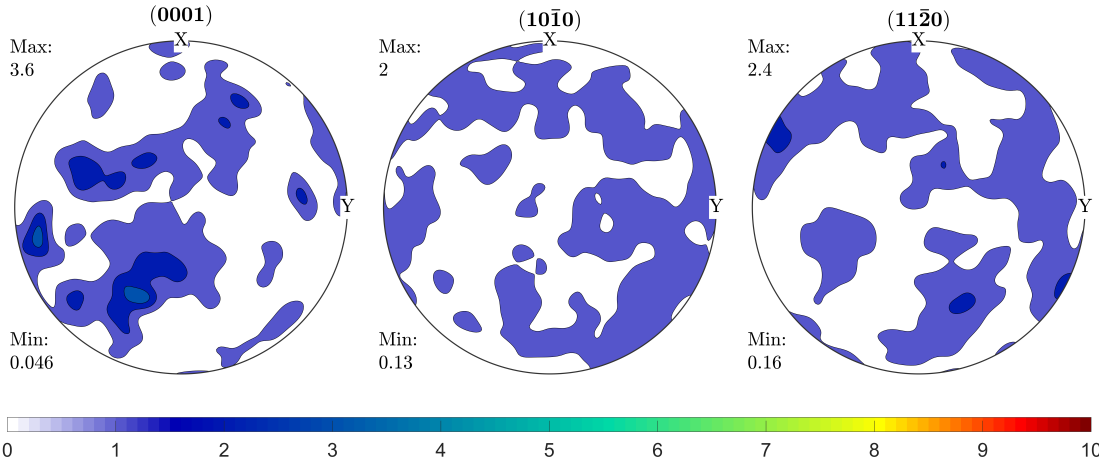


Fig. 4.8 Texture analysis of IFS19 sample

The Schmid factor analysis presented in Figure 4.10 shows less pronounced basal and prismatic intensity compared with the strong preferential trends observed in sample IFS10. From the observation of the trace analysis (Figure 4.11), it is revealed that the crack initiation occurred in near-basal planes, similar to FCI observations in sample IFS10. Following initiation, the fatigue crack propagated predominantly in a transgranular manner along basal planes, exhibiting multiple significant crack deflections exceeding 90°. These large deflection angles occurred at grain boundaries between grains 9 and 10, 11 and 12, and 12 and 13, highlighting the strongly crystallographic nature of short crack growth. In addition, an uncommon instance of intergranular crack propagation (marked number 5 and 6 in the slip

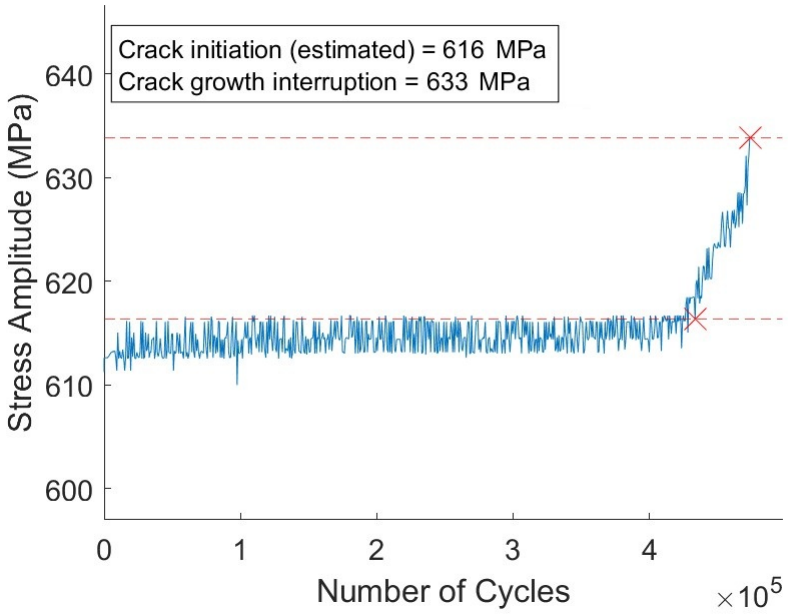


Fig. 4.9 Interrupted fatigue sequence for IFS19 sample

trace analysis) was observed along a tilted basal-basal grain boundary between grains 13 and 14.

Figure 4.12 illustrates the crystallographic orientations and grain sizes of the FCI grains in comparison with the 'hotspot' grains located in the high stress regions of the meso cantilever. The results indicate that the FCI grains (grains 1-4) in sample IFS19 fall towards the smaller end of the overall grain size distribution. The basal Schmid factors of the three FCI grains are relatively low, ranging from 0.40 to 0.45, compared with those observed for the FCI grains in sample IFS10. Nevertheless, the slip trace analysis shown in Figure 4.11 confirms that these grains are still favourably oriented for fatigue crack initiation along near-basal planes.

Furthermore, the Luster-Morris parameter (m') values for grains 1 and 2 , presented in Figure 4.14, indicate a relatively low basal-basal slip transfer compatibility, with values of 0.39 and 0.20 based on the maximum m' and maximum Schmid factor criteria, respectively. This reduced slip transfer capability is reflected in the pronounced crack deflection observed between grain 1 and grain 2 in Figure 4.11. Lastly, Figure 4.13 shows no discernible correla-

tion between the crystallographic texture of the ‘hotspot’ grains and that of the FCI grains or their neighbouring grains.

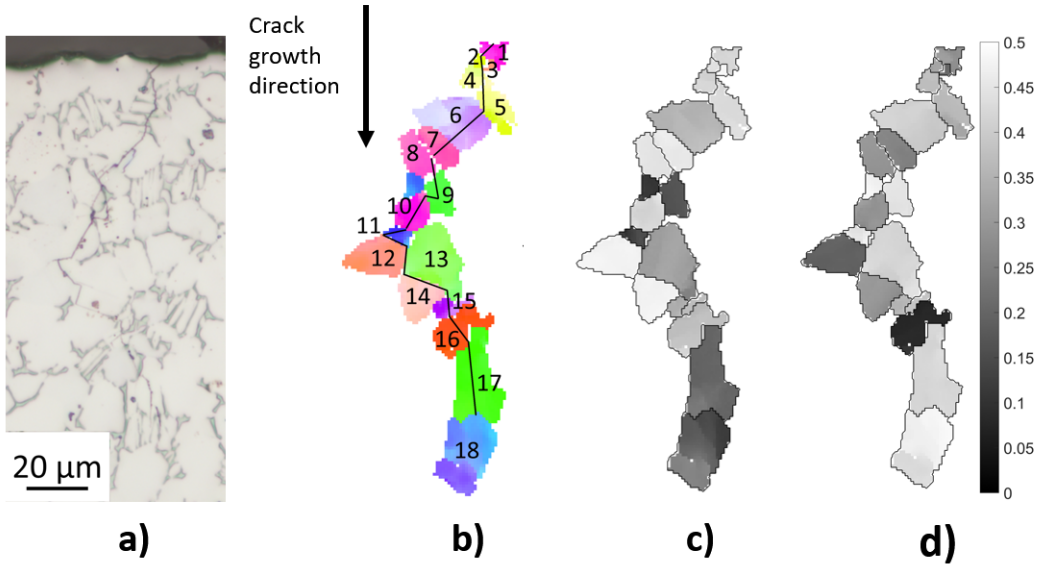


Fig. 4.10 Schmid Factor (SF) analysis of the fatigue crack in IFS19 (a) Optical microscope image (b) IPFX Map with the outlined fatigue crack path and grain numbers (c) Basal SF (d) Prismatic SF

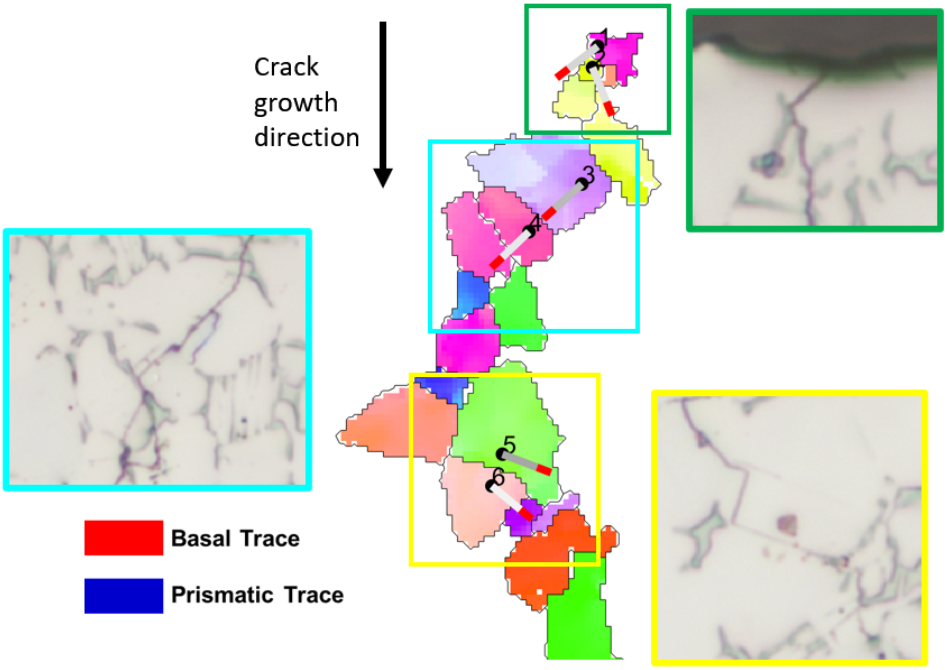


Fig. 4.11 Trace analysis of fatigue crack in IFS19. The ends of the batons are coloured red or blue to signify the corresponding slip trace, while the grayscale colour on the body signifies the intensity of the Schmid factor.

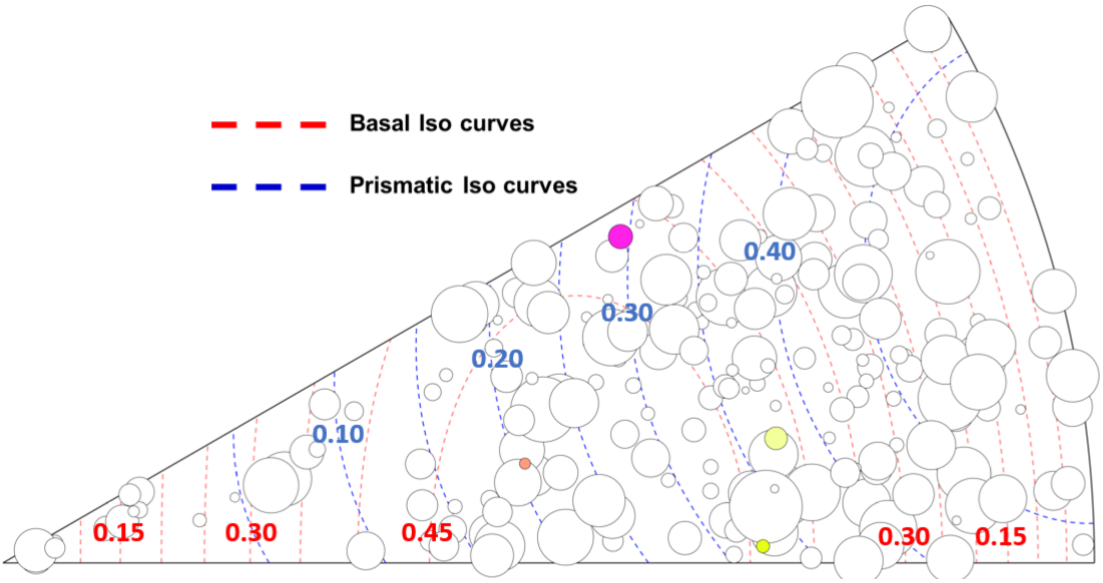


Fig. 4.12 Orientations and grain sizes of FCI grains in respect to the basal and prismatic isocurves and the orientation of 'hotspot' grains in IFS19

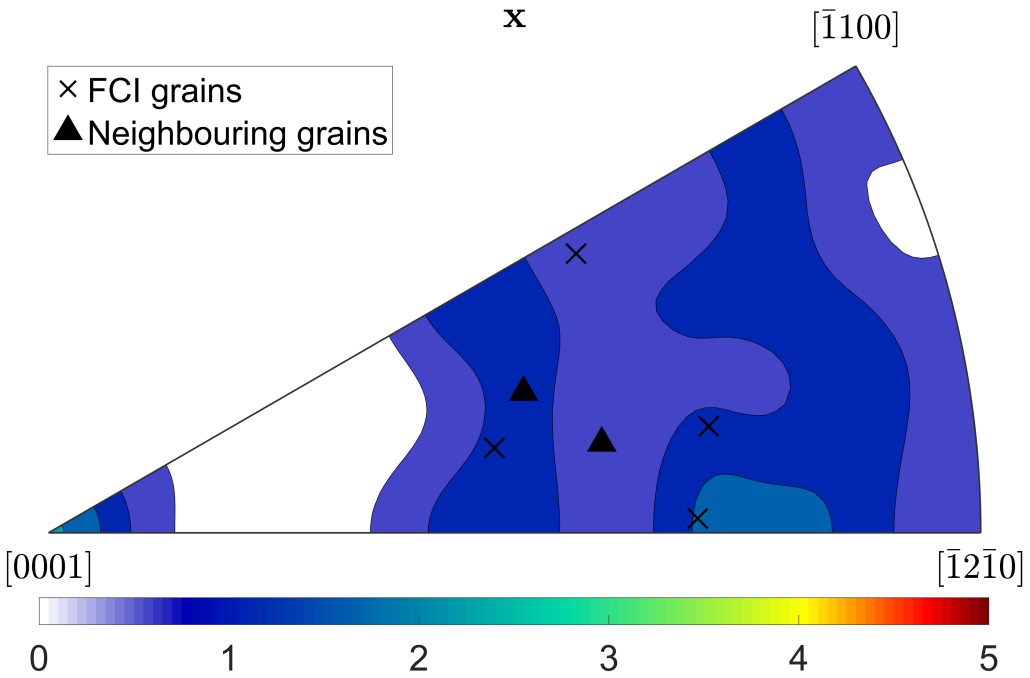


Fig. 4.13 Orientations of FCI and neighbouring grains in respect to the texture of 'hotspot' grains in IFS19

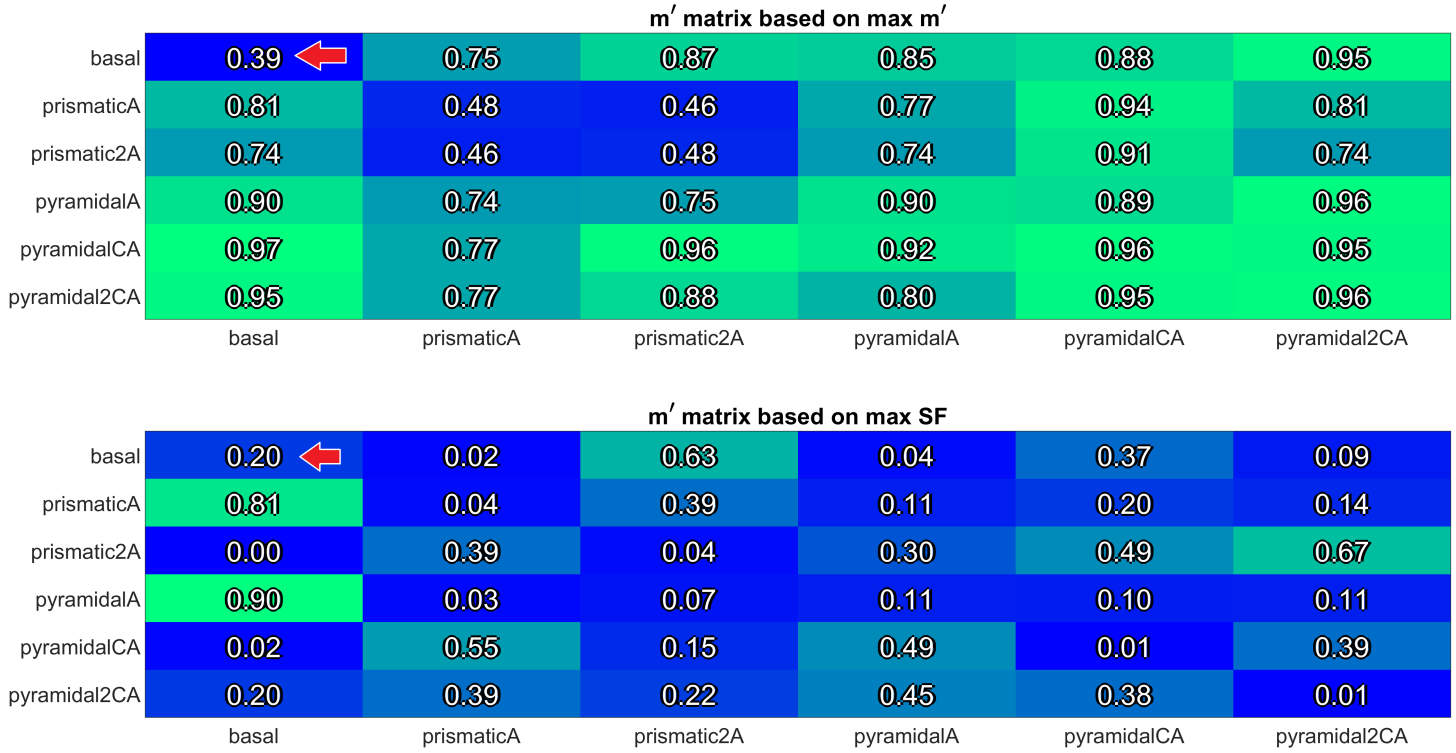


Fig. 4.14 Luster-Morris parameter (m′) calculations based on (top) maximum m′ and (bottom) maximum Schmid factor for Grain 1 and 2. The red arrows point to the physical matching of the trace analysis

4.3.3 IFS21

The pole figures shown in Figure 4.15 indicate a basal texture intensity of 4.3 mrd for sample IFS21. This represents a slightly higher level of basal texture compared with sample IFS19, while remaining significantly lower than that observed for sample IFS10. Consequently, the overall crystallographic texture of IFS21 may be characterised as relatively weak, indicating largely random grain orientations.

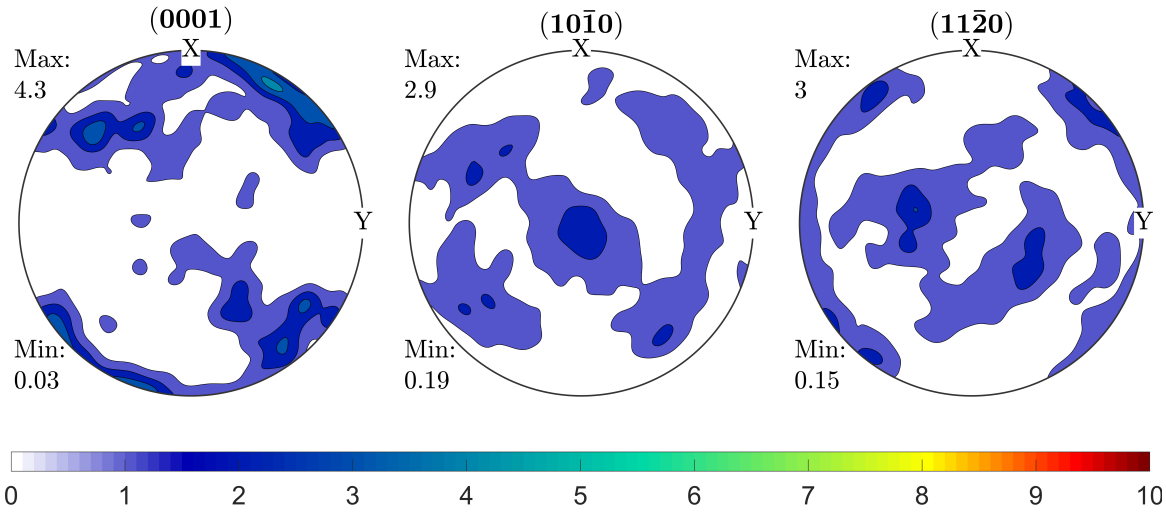


Fig. 4.15 Texture analysis of IFS21 sample

Figure 4.16 presents the stress amplitude of sample IFS21 as a function of number of cycles. The prior step-stress testing of IFS21 was performed to 633 MPa at 10^8 cycles. Fatigue crack initiation was detected during the subsequent step-stress testing at a stress amplitude of 795 MPa after 4.78×10^6 cycles. Although the pole figure from Figure 4.15 does not indicate any significant texture in the sample; the Schmid Factor analysis plot in Figure 4.17 and slip trace analysis in Figure 4.18 clearly highlight a predominantly near-basal slip during crack growth. This crystallographic behaviour is reflected by the low prismatic Schmid Factor plot in 4.18d. In addition, Figure 4.18b reveals an almost linear path throughout the crack growth, in stark contrast to the previous sample (IFS19) which exhibited large deflection angles along its fatigue crack trajectory.

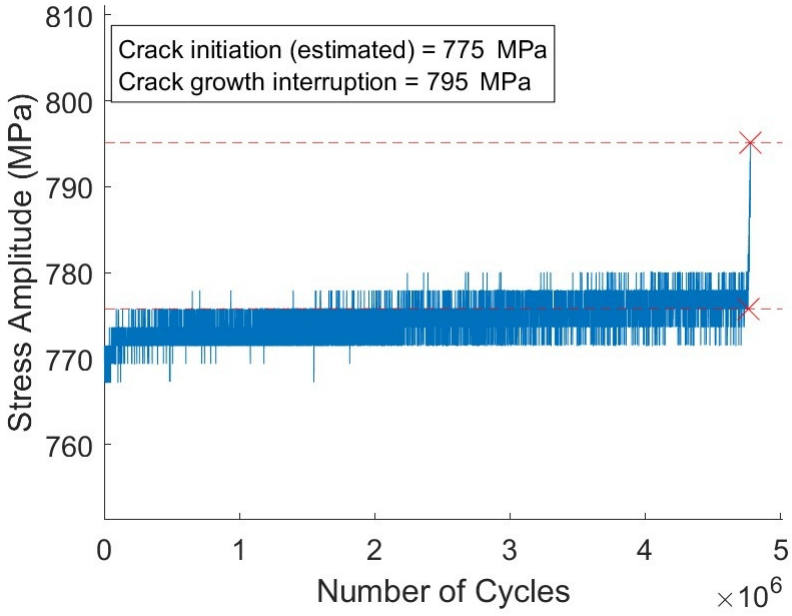


Fig. 4.16 Interrupted fatigue sequence for IFS21 sample

Conversely, the inverse pole figure of FCI grains in Figure 4.19 revealed that fatigue crack initiated in very low Schmid factors of 0.29 and 0.25 for grain number 1 and 2, respectively. These values are considerably lower than the basal Schmid factor values for the FCI grains in IFS10 and IFS19. Moreover, Figure 4.21 reveals low compatibility of slip transfer between grain 1 and 2, which is evidenced by the Luster-Morris parameter value of 0.28 and 0.13 in the basal-basal slip transfer, calculated based on the maximum m' and maximum Schmid factor, respectively. This combination of low Schmid factor and m' values are reflected by the abnormally high fatigue stress amplitude of 795.11 MPa. Lastly, the inverse pole figure plot shows texture for the 'hotspot' grains; however, it showed no strong relevance towards the FCI grains.

Conversely, the inverse pole figure of the fatigue crack initiation (FCI) grains shown in Figure 4.19 indicates that crack initiation occurred in grains exhibiting very low basal Schmid factors of 0.29 and 0.25 for grains 1 and 2, respectively. Grain 1 additionally exhibits a relatively high prismatic Schmid factor of 0.36. The basal values are substantially lower

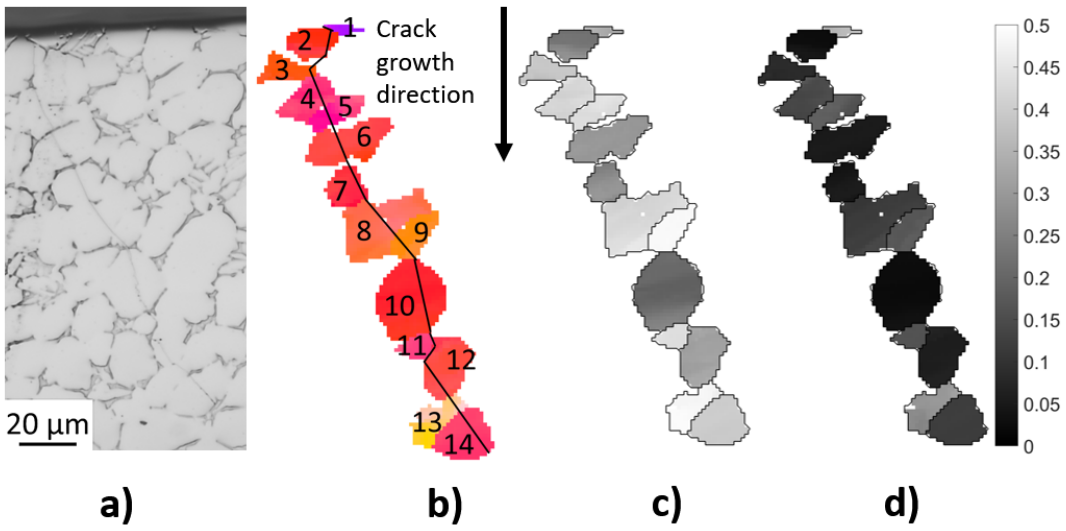


Fig. 4.17 Schmid Factor (SF) analysis of the fatigue crack in IFS21 (a) Optical microscope image (b) IPFX Map with the outlined fatigue crack path and grain numbers (c) Basal SF (d) Prismatic SF

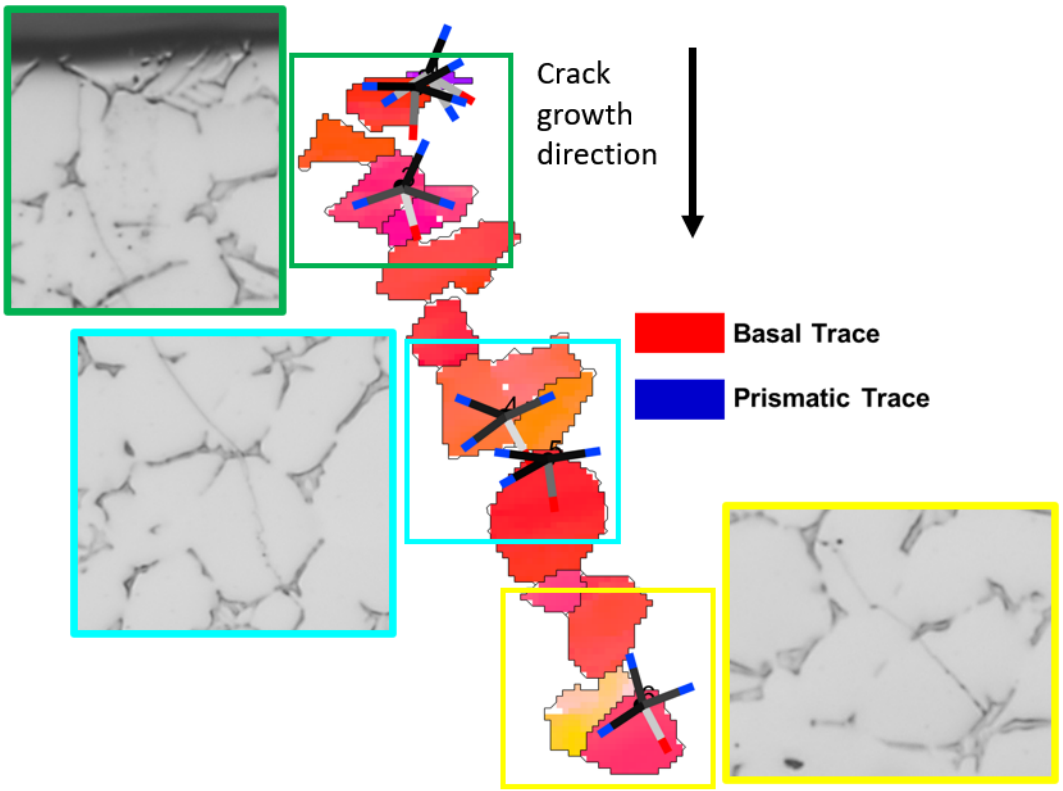


Fig. 4.18 Trace analysis of fatigue crack in IFS21. The ends of the batons are coloured red or blue to signify the corresponding slip trace, while the grayscale colour on the body signifies the intensity of the Schmid factor.

than those observed for the FCI grains in samples IFS10 and IFS19. Furthermore, Figure 4.21 demonstrates a low degree of slip transfer compatibility between grains 1 and 2, as evidenced by Luster-Morris parameter (m′) values of 0.28 and 0.13 for basal-basal slip transfer, calculated using the maximum m′ and maximum Schmid factor criteria, respectively. This combination of low basal Schmid factor and low m′ values is consistent with the unusually high fatigue stress amplitude required for crack initiation, measured at 795.11 MPa. Finally, although the inverse pole figure (Figure 4.27) reveals some degree of texture within the 'hotspot' grains, no strong correlation is observed between their crystallographic orientation and that of the FCI grains.

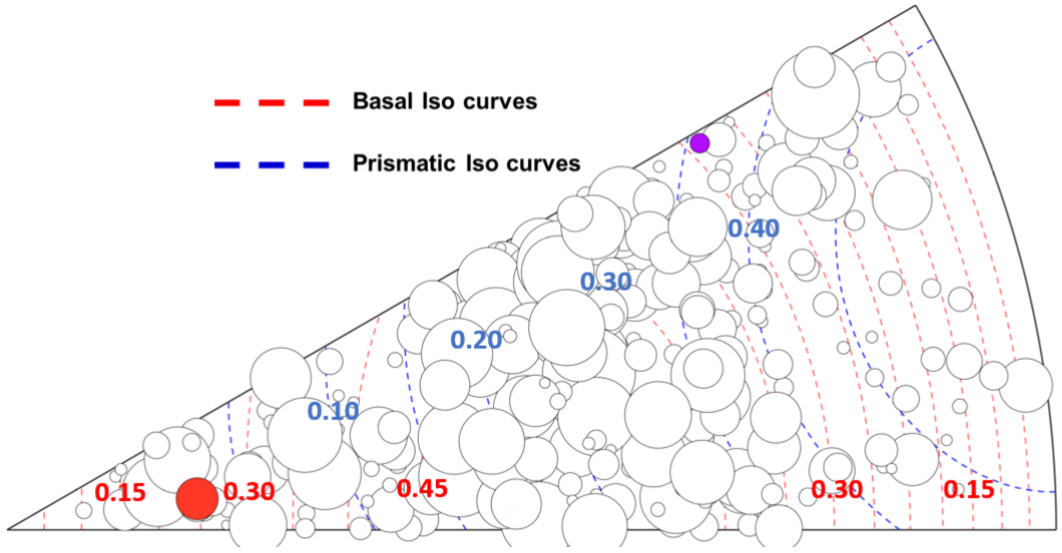


Fig. 4.19 Orientations and grain sizes of FCI grains in respect to the basal and prismatic isocurves and the orientation of 'hotspot' grains in IFS21

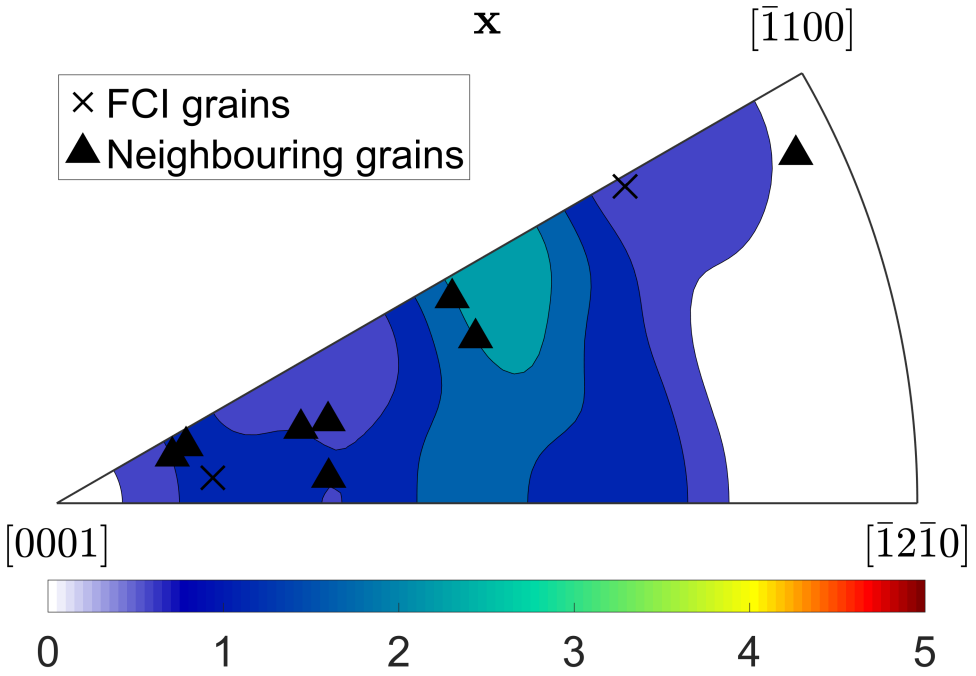


Fig. 4.20 Orientations of FCI and neighbouring grains in respect to the texture of 'hotspot' grains in IFS21

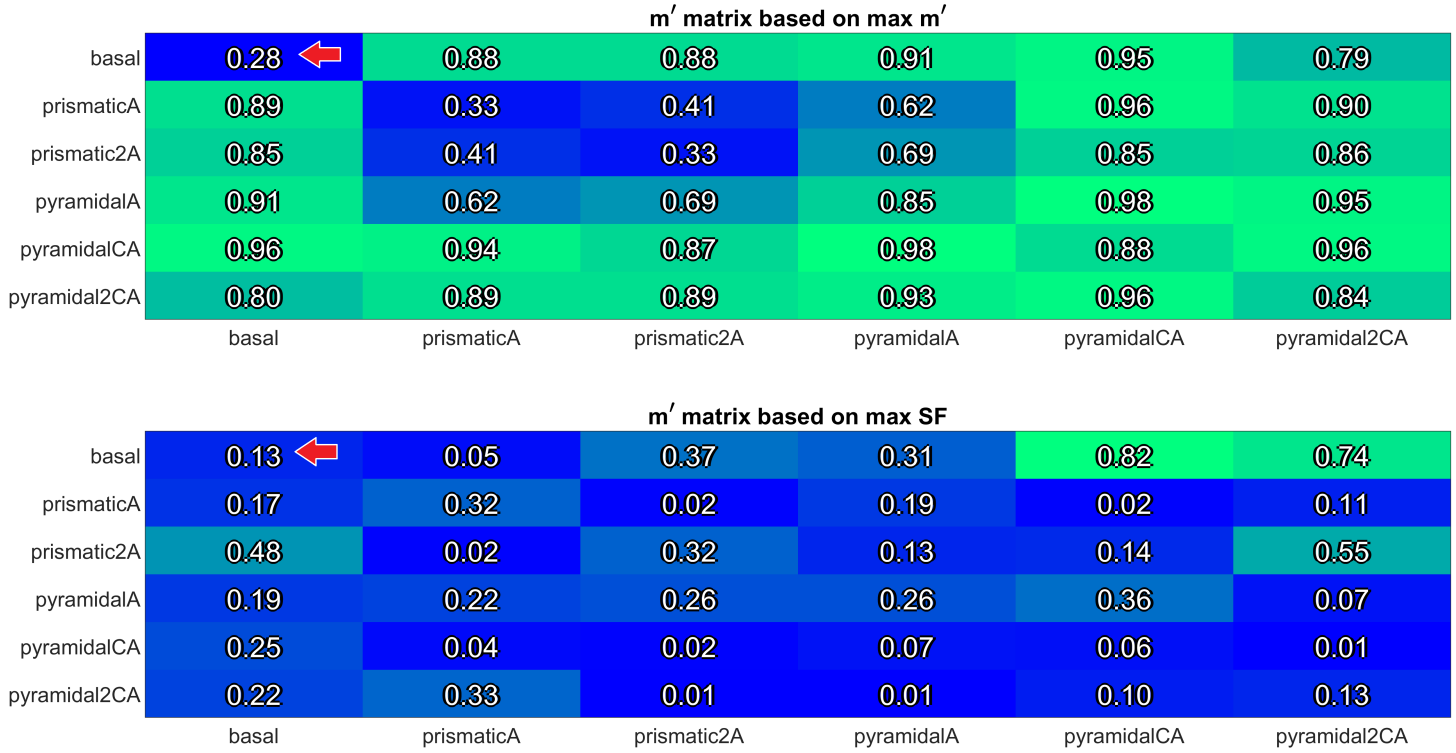


Fig. 4.21 Luster-Morris parameter (m′) calculations based on (top) maximum m′ and (bottom) maximum Schmid factor for Grain 1 and 2. The red arrows point to the physical matching of the trace analysis

4.3.4 IFS24

Figure 4.22 shows a pronounced basal texture in sample IFS24, with a maximum intensity of 8.2 mrd along the Z axis. It represents the highest degree of basal texture observed within the dataset. This sample was subjected to step-stress testing up to a stress amplitude of 613 MPa for 10^8 cycles, followed by a test interruption after 1.49×10^6 cycles at an increased stress amplitude of 662 MPa, as illustrated in Figure 4.23.

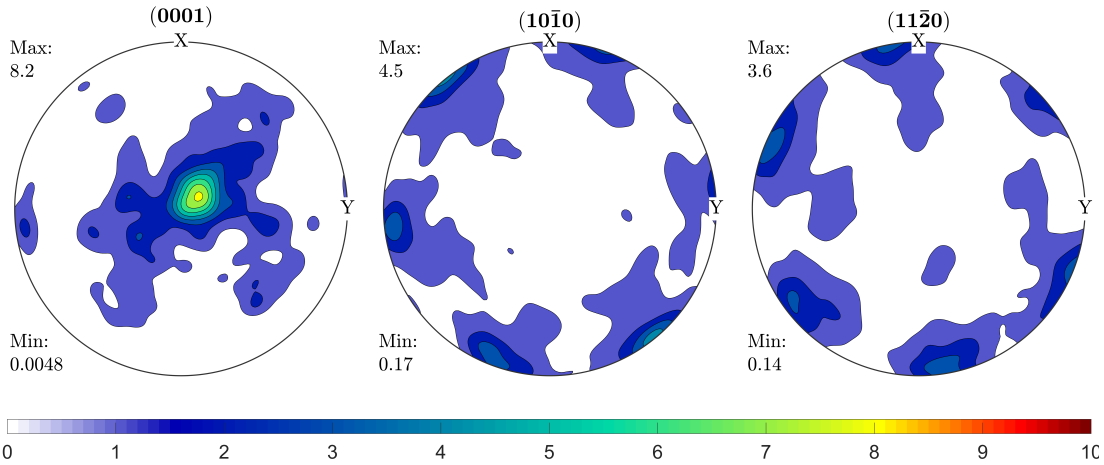


Fig. 4.22 Texture analysis of IFS24 sample

The Schmid factor map presented in Figure 4.24 indicates high basal Schmid factor values for the first three grains, with a subsequent preferential orientation towards prismatic slip systems from grains 4 to 8. The slip trace analysis shown in Figure 4.25 confirms basal crack propagation within grains 1 and 2; however, in grain 3, the crack propagated along the grain boundary before continuing predominantly along prismatic planes from grains 4 to 8.

The inverse pole figure in Figure 4.26 reveals relatively high basal Schmid factors for the three FCI grains, between 0.4 and 0.5. Although the pole figure indicated a strong texture aligned with the Z axis, which is also reflected by the [$\bar{1}2\bar{1}0$] texture projected along the X axis along the 'hotspot' grains, the orientation contour plot in Figure 4.27 shows a highly dispersed distribution of orientations for both the FCI and neighbouring grains, with no clear correlation to the 'hotspot' texture.

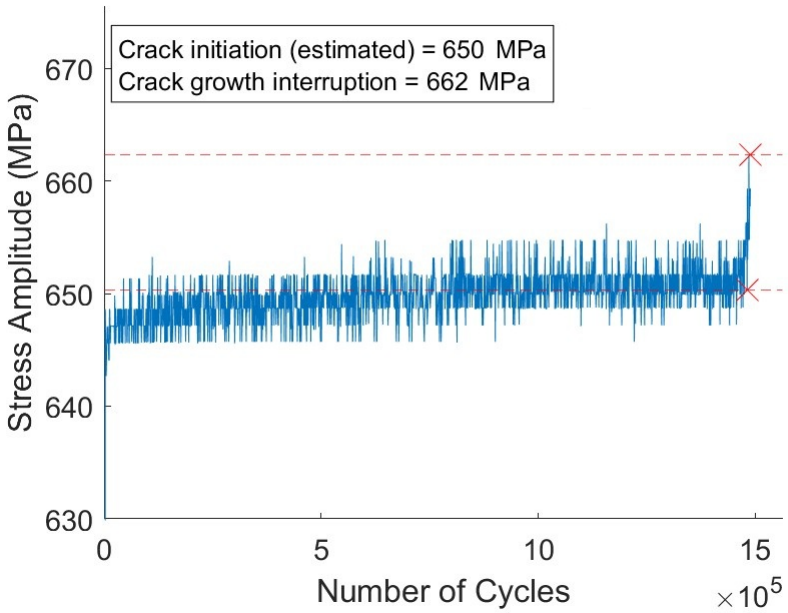


Fig. 4.23 Interrupted fatigue sequence for IFS24 sample. The ends of the batons are coloured red or blue to signify the corresponding slip trace, while the grayscale colour on the body signifies the intensity of the Schmid factor.

Fatigue crack initiation within grains 1 and 2 occurred along near-basal planes and was accompanied by a high basal-basal slip transfer compatibility, with a Luster-Morris parameter (m') value of 0.84 based on the maximum (m') criterion. In contrast, the basal-basal slip transfer based on the maximum Schmid factor criterion was relatively low (0.28), as shown in Figure 4.28.

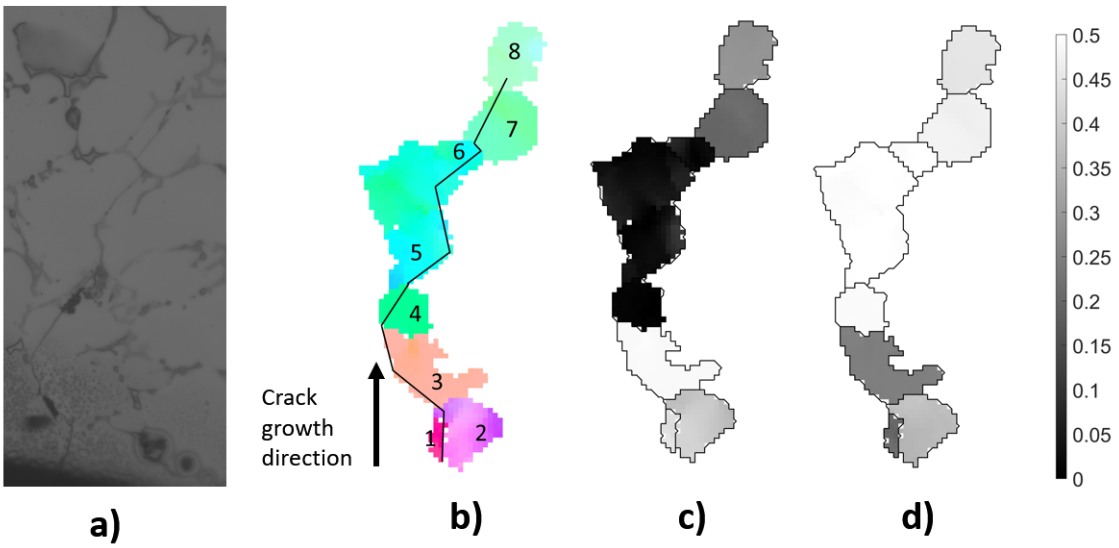


Fig. 4.24 Schmid Factor (SF) analysis of the fatigue crack in IFS24 (a) Optical microscope image (b) IPFX Map with the outlined fatigue crack path and grain numbers (c) Basal SF (d) Prismatic SF

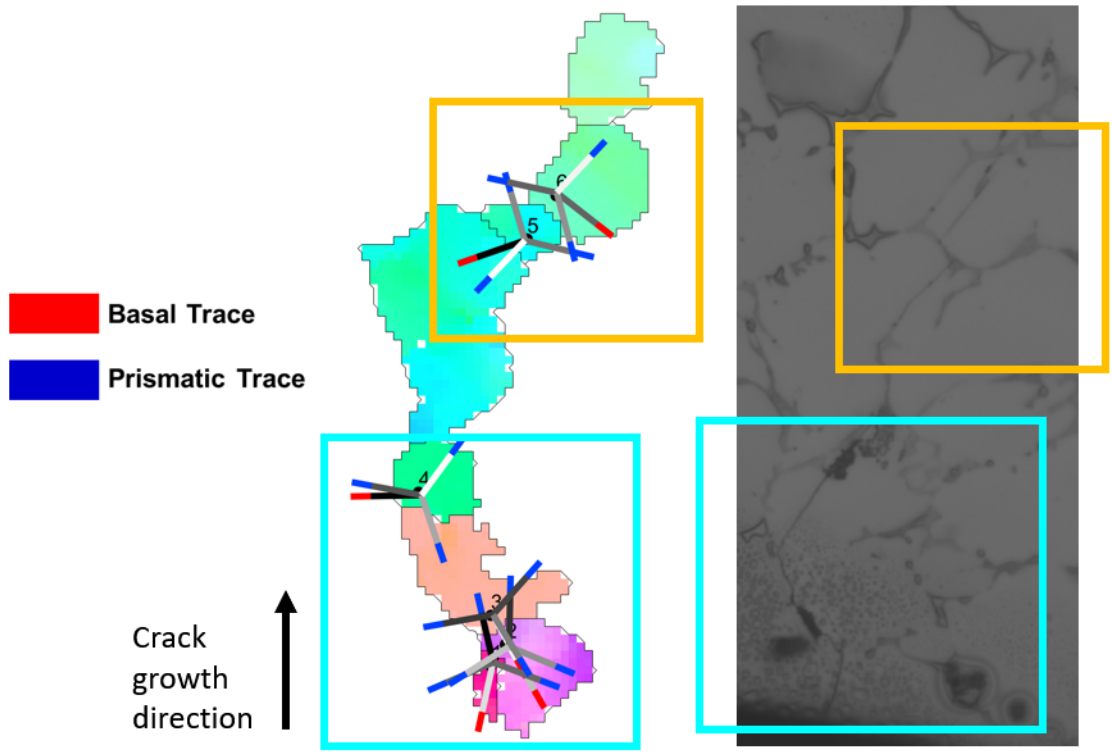


Fig. 4.25 Trace analysis of fatigue crack in IFS24

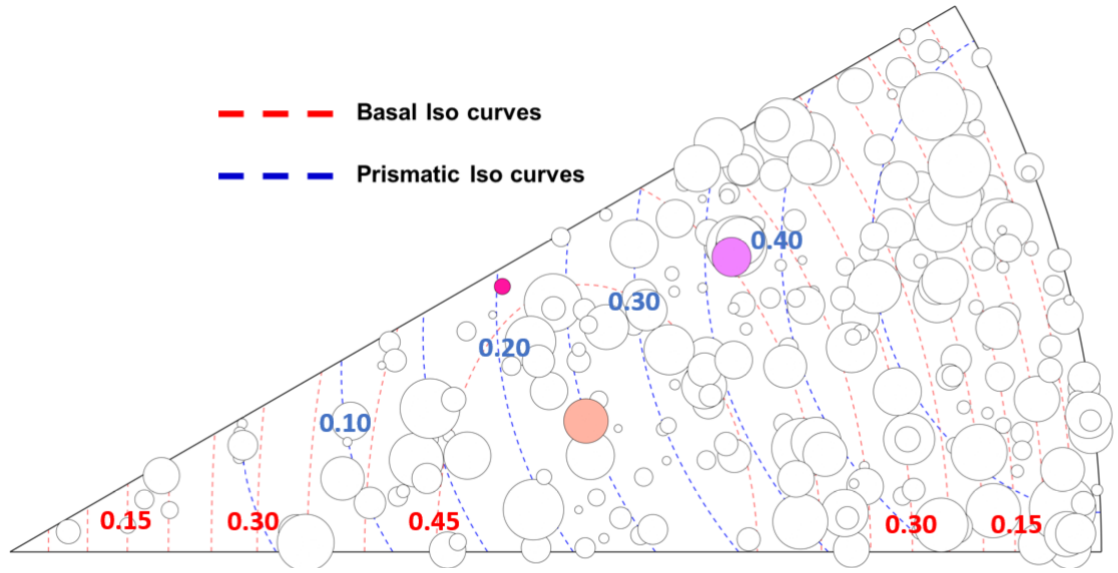


Fig. 4.26 Orientations and grain sizes of FCI grains in respect to the basal and prismatic isocurves and the orientation of 'hotspot' grains in IFS24

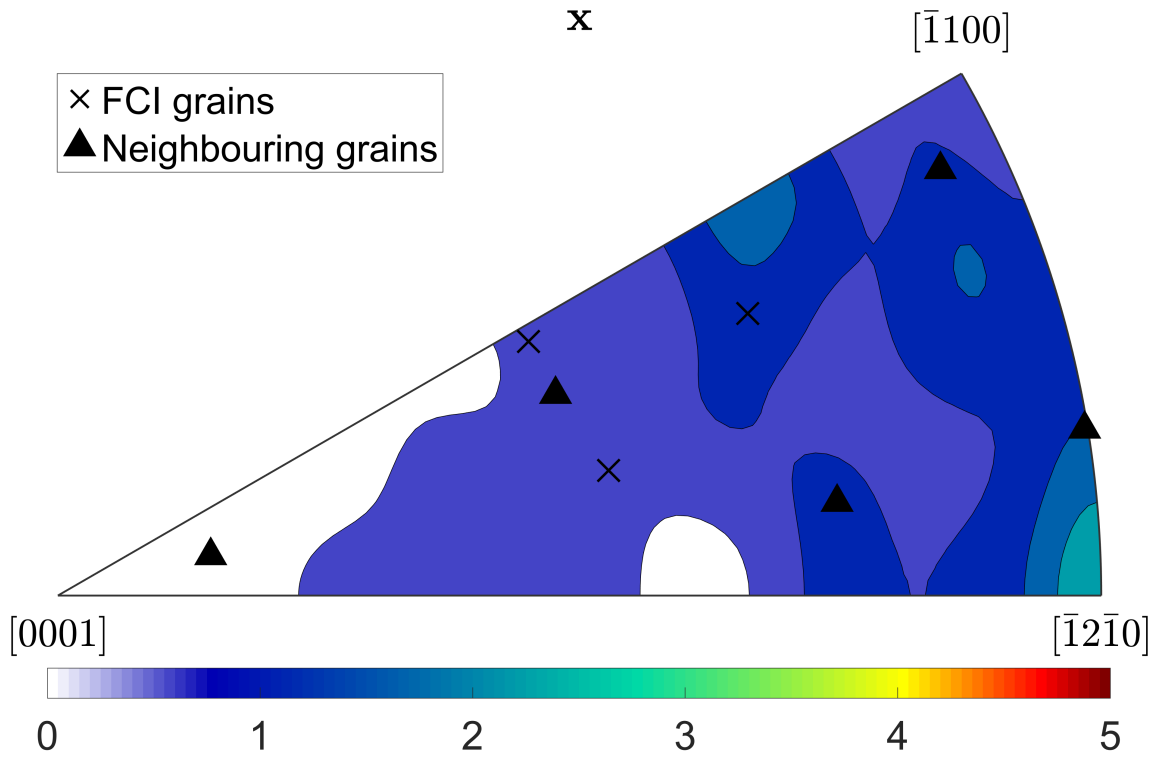


Fig. 4.27 Orientations of FCI and neighbouring grains in respect to the texture of 'hotspot' grains in IFS24

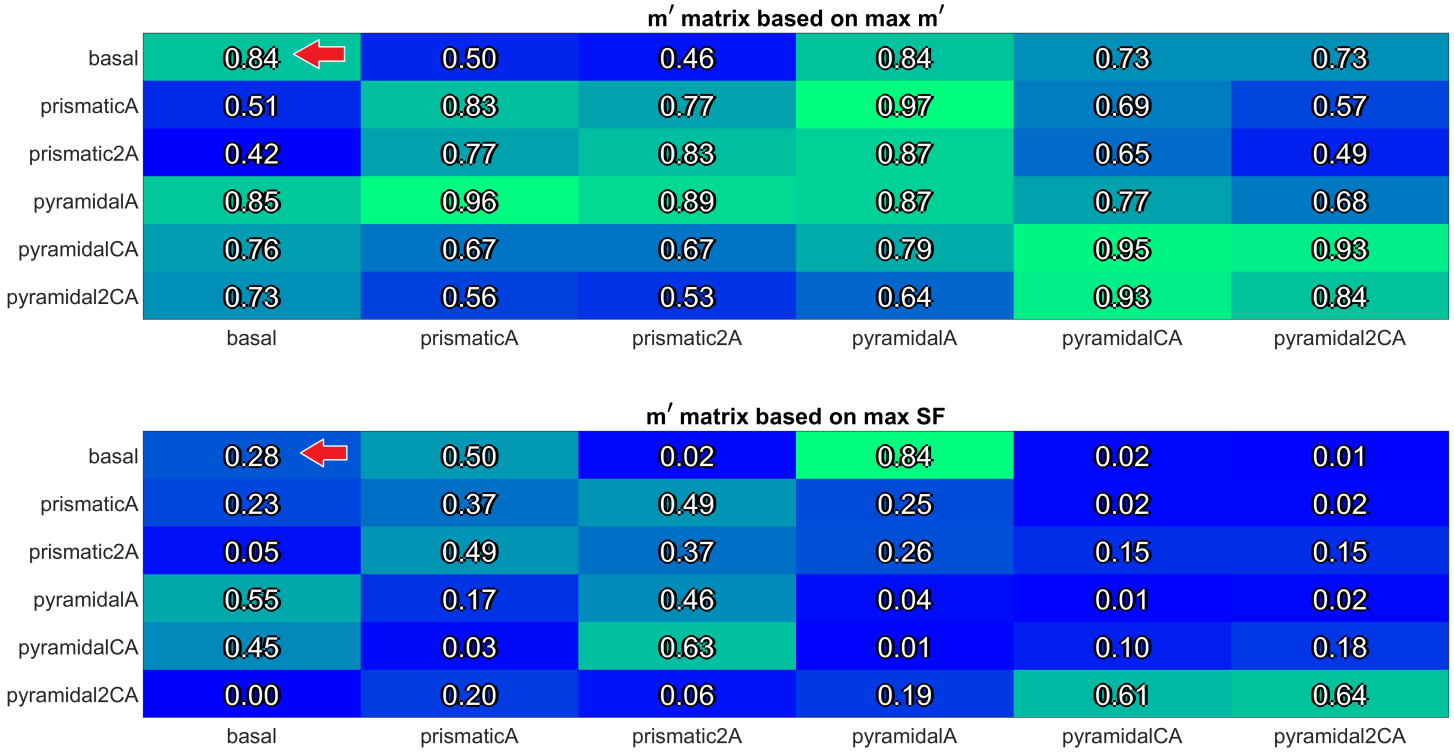


Fig. 4.28 Luster-Morris parameter (m′) calculations based on (top) maximum m′ and (bottom) maximum Schmid factor for Grain 1 and 2. The red arrows point to the physical matching of the trace analysis

4.3.5 IFS25

Figure 4.29 reveals a mild basal texture intensity of 4.9 mrd. Sample IFS25 was subjected to step-stress testing up to a stress amplitude of 694 MPa for 10^8 cycles, followed by an interruption after 7.24×10^4 cycles at an increased stress amplitude of 759 MPa, as shown in Figure 4.30.

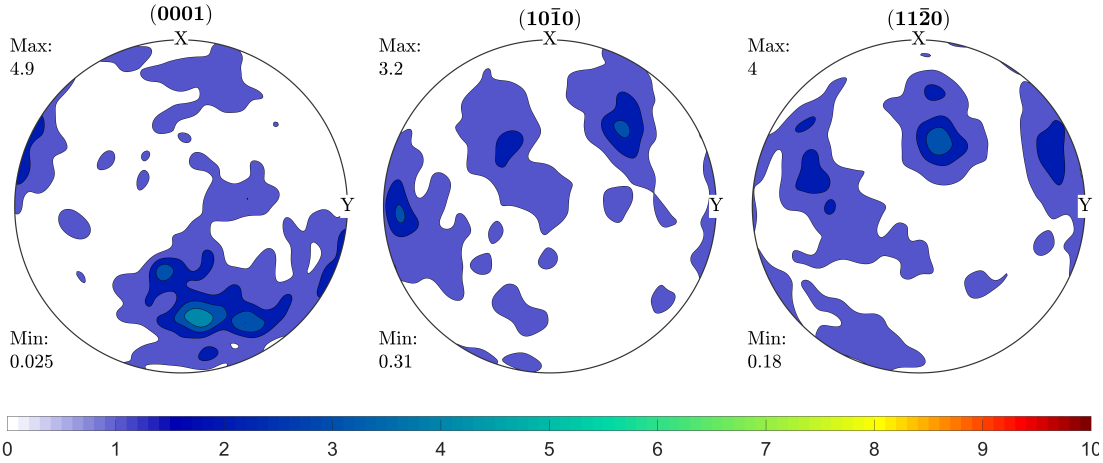


Fig. 4.29 Texture analysis of IFS25 sample

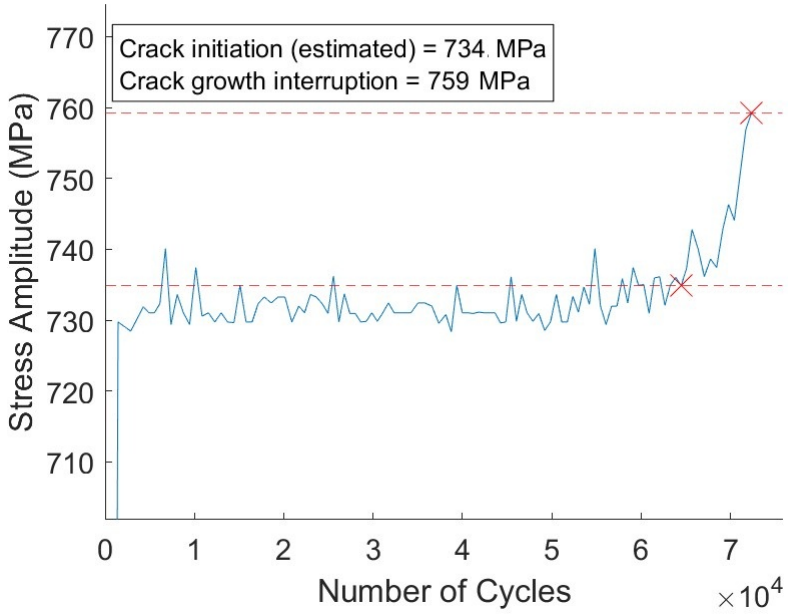


Fig. 4.30 Interrupted fatigue sequence for IFS25 sample

The Schmid factor map presented in Figure 4.31 indicates a mixed distribution of high and low basal and prismatic Schmid factors. Despite this heterogeneity, the slip trace analysis shown in Figure 4.32 demonstrates that the early fatigue crack path remained predominantly within basal planes up to grain 6. This occurred despite grains 1 and 3 exhibiting very low basal Schmid factors. The fatigue crack subsequently propagated along the grain boundary between grains 8 and 9 due to the extremely low basal Schmid factors in these regions. Beyond grain 10, the crack path transitioned to predominantly follow prismatic slip planes.

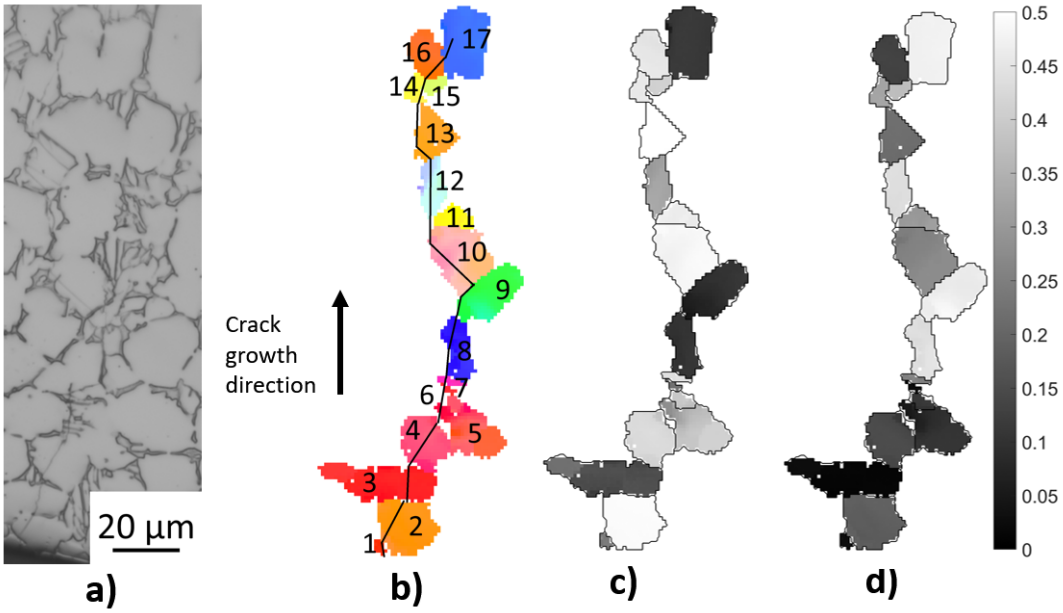


Fig. 4.31 Schmid Factor (SF) analysis of the fatigue crack in IFS25 (a) Optical microscope image (b) IPFX Map with the outlined fatigue crack path and grain numbers (c) Basal SF (d) Prismatic SF

The inverse pole figure shown in Figure 4.33 reveals that the two fatigue crack initiation (FCI) grains are located at both a high basal Schmid factor isocurve of 0.48 and a very low isocurve of 0.24. Grain 1 is characterised by a very small grain size, which may have been reduced by the laser machining process. In this case, Figure 4.34 reveals a strong correlation between the crystallographic orientations of the FCI and neighbouring grains and the texture of the 'hotspot' grains, similar to that observed in sample IFS10. As shown in Figure 4.35, the two FCI grains exhibit moderately low basal-basal slip transfer compatibility, with Luster-

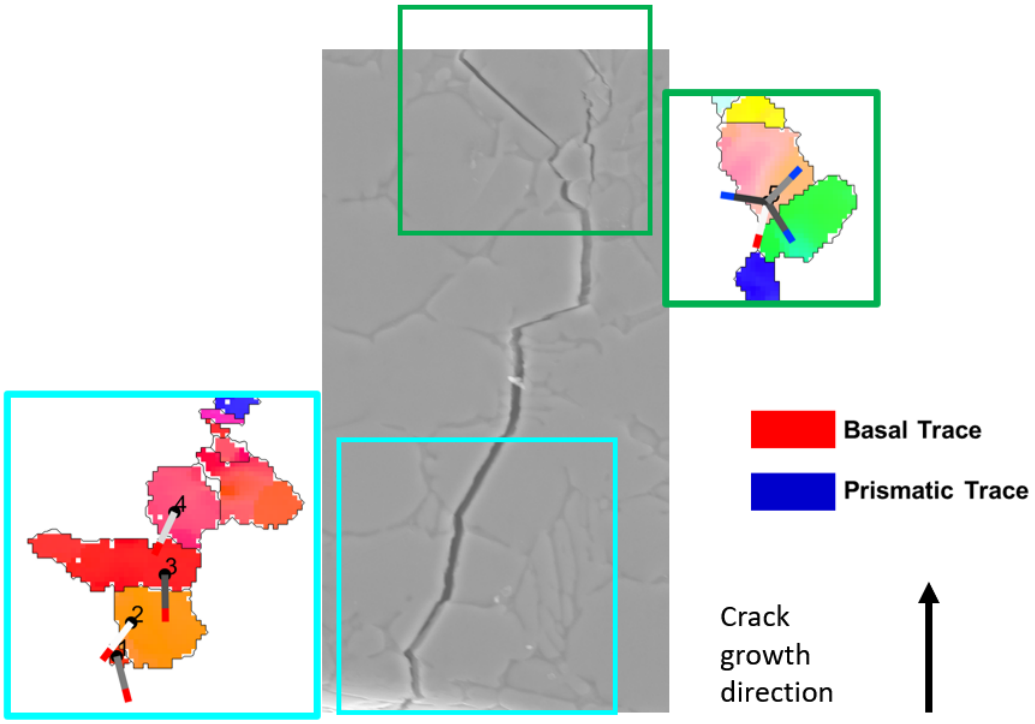


Fig. 4.32 Trace analysis of fatigue crack in IFS25. The ends of the batons are coloured red or blue to signify the corresponding slip trace, while the grayscale colour on the body signifies the intensity of the Schmid factor.

Morris parameter m′ values of 0.51 and 0.31, calculated based on the maximum m′ and maximum Schmid factor criteria, respectively.

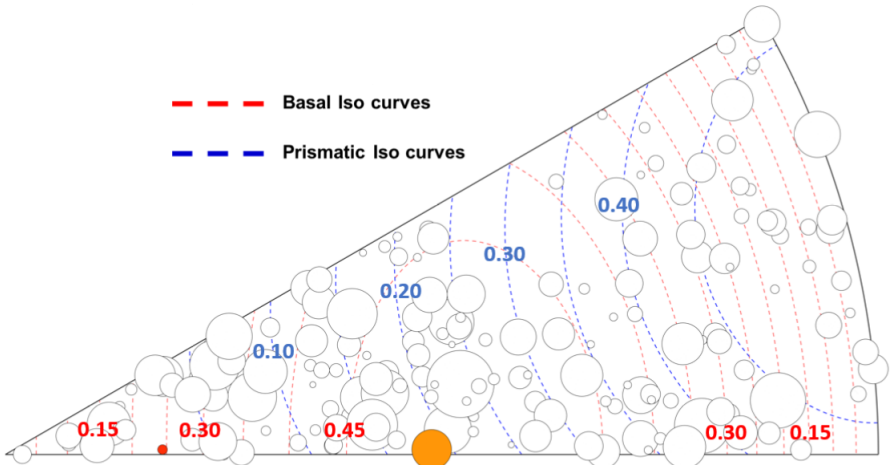


Fig. 4.33 Orientations and grain sizes of FCI grains in respect to the basal and prismatic isocurves and the orientation of 'hotspot' grains in IFS25

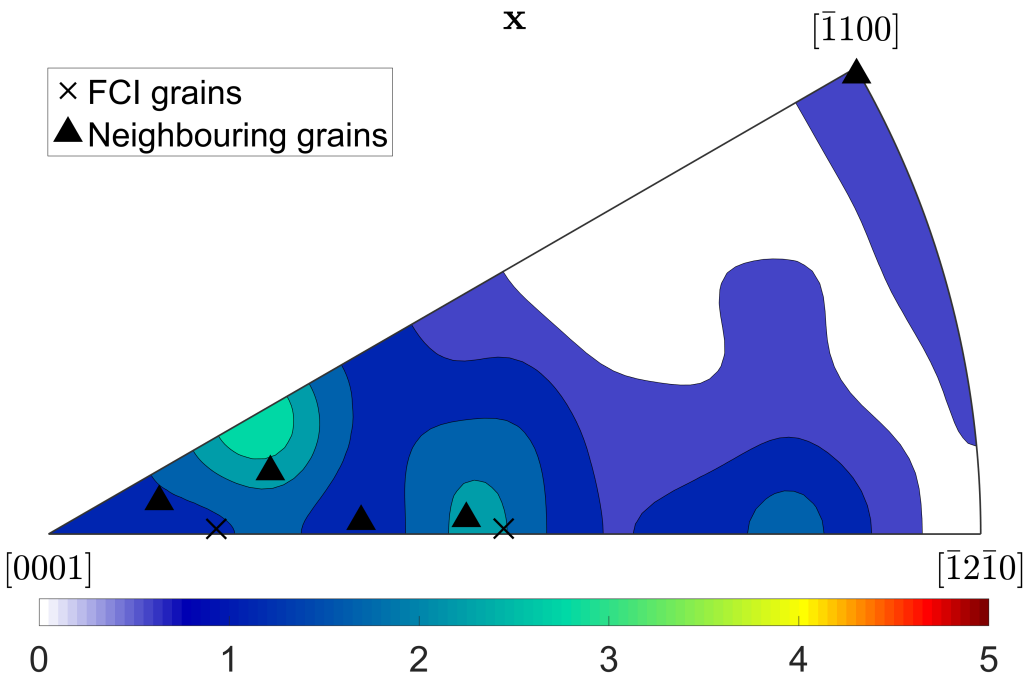


Fig. 4.34 Orientations of FCI and neighbouring grains in respect to the texture of 'hotspot' grains in IFS25

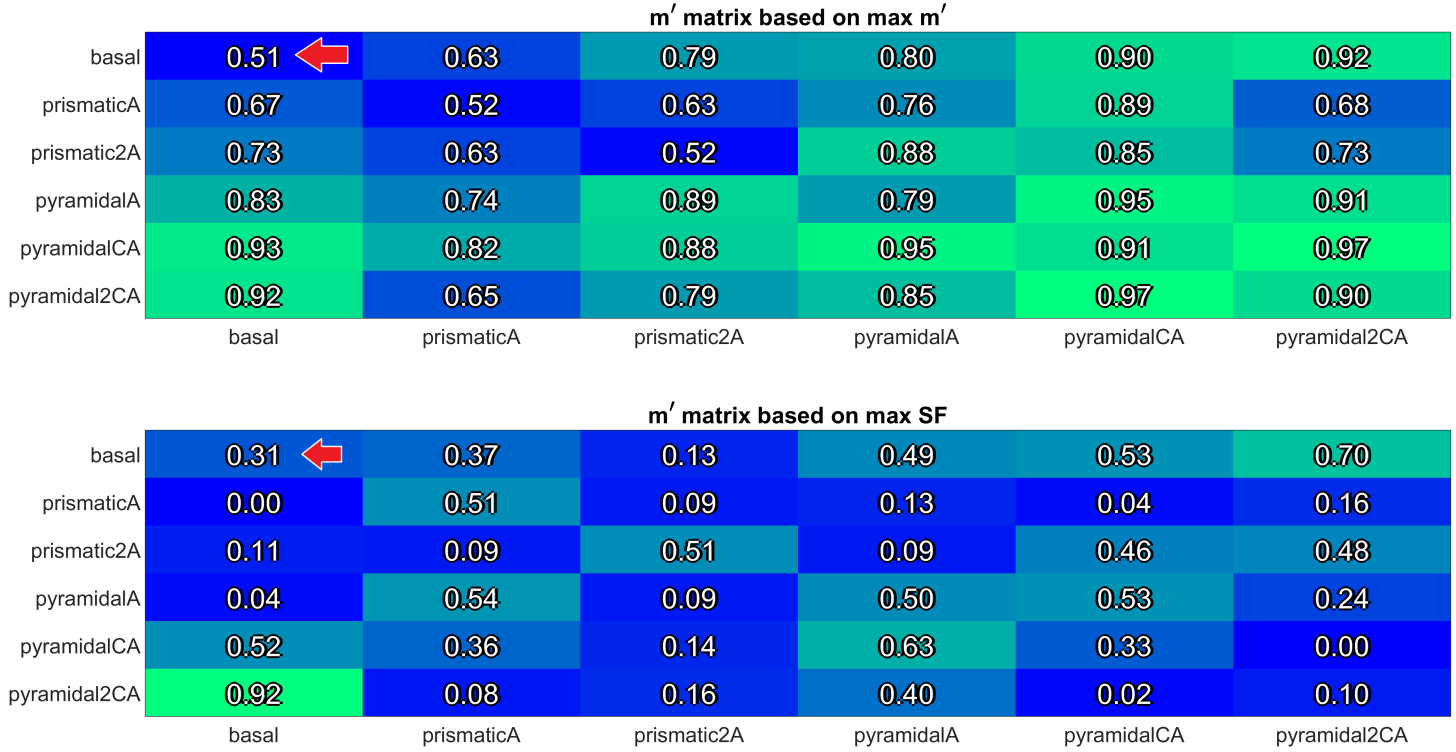


Fig. 4.35 Luster-Morris parameter (m′) calculations based on (top) maximum m′ and (bottom) maximum Schmid factor for Grain 1 and 2. The red arrows point to the physical matching of the trace analysis

4.4 Discussions

4.4.1 The grain orientation of fatigue crack initiation features

Fatigue crack initiation in titanium alloys has been observed to occur through the formation of facets in HCF and VHCF regimes. These facets are generally believed to originate from the development of slip bands [104]; however, they often exhibit little visible evidence of macroscopic plastic deformation. Consequently, facet-based fatigue crack initiation features are commonly described as exhibiting quasi-cleavage behaviour. Despite their brittle appearance, many research works believe that the underlying mechanism remains fundamentally slip-controlled [119–122]. Slip localisation occurs on favourably oriented crystallographic slip systems, with activation governed by two key parameters: the Schmid factor, which quantifies the alignment of the slip system relative to the applied loading direction, and the critical resolved shear stress (CRSS) required to initiate dislocation motion.

In this research, slip trace analyses (displayed in Figures 4.4, 4.11, 4.18, 4.25, and 4.32) of FCI grains from fatigue tests performed at 10^8 cycles revealed strong preferences towards crack initiation on near-basal planes. Further analysis must be made to rationalise these results. One EBSD-based method of evaluating active slip systems involves using the normalised Schmid factor (m′), which is a product of the Schmid factor (m) and the ratio of the CRSS of the given slip system to the CRSS of the easiest activated slip system [123, 124]. In this case, the easiest activated slip systems are equal between basal and prismatic $\langle a \rangle$ slips with a 1:1:2.64 ratio for $\langle a \rangle$ basal, $\langle a \rangle$ prismatic and $\langle c+a \rangle$ pyramid slip, respectively [124]. The normalised Schmid factor is plotted as a function of the angle between the c-axis and the loading direction, as shown in Figure 4.36. In general, the plot displays two angles (i.e. at 10° and 66.7°) in which the dominant slip transitions from pyramidal to basal and basal to prismatic. Figure 4.36 overlays the experimental data of FCI grains across the IFS-labeled samples on the normalised Schmid factor plot and reveals that all FCI grains are oriented in

the basal-dominant zones. No initiation features were associated with prismatic or pyramidal systems, despite the large variety of grain orientations available along the 'hotspot' regions.

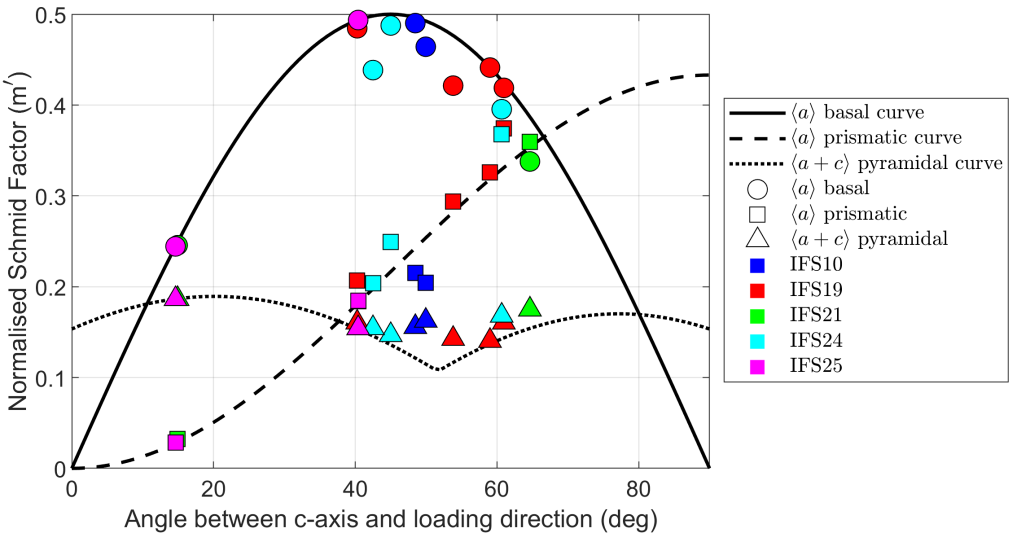


Fig. 4.36 Normalised Schmid Factor (m') as a function of θ for all experimental FCI grains

The predominance of near-basal crack initiation features observed in the present work is consistent with previous findings reported in the literature [124–127]. Bantounas et al. investigated the effect of grain orientation on fracture morphology in Ti-6Al-4V under high-cycle fatigue and an R ratio of 0.3 [124]. The authors reported that the majority of initiation facets were oriented between 15 and 40° to the loading direction which provided both a sufficiently high resolved shear stress for basal slip activation and a tensile normal stress component across the basal plane, which together promote the formation of fatigue facets. They further suggested that prismatic features observed near crack initiation sites likely form to accommodate crack growth between neighboring grains once basal cracking has initiated. The absence of prismatic or pyramidal initiation facets in the current observations supports this interpretation and suggests that these systems contribute mainly to slip transfer and local crack propagation rather than to the initiation process itself.

A similar crystallographic preference for basal cracking has also been reported in Bridier et al, who examined slip and fatigue crack formation in $\alpha + \beta$ titanium alloys under low-

cycle fatigue conditions [126]. Their work showed that cracks formed along basal planes represented the critical damage mode leading to final fracture, whereas cracks nucleated on prismatic planes were typically secondary and did not contribute to the fatal failure. This distinction between primary (basal) and secondary (prismatic) initiation sites highlights the dominant role of basal slip localisation and facet formation in the early stages of fatigue damage accumulation.

More recently, Liu et al. performed a multi-dimensional study on a near-α titanium alloy, integrating EBSD and DIC to examine early slip activity and its relationship to fatigue crack initiation [127]. Their results demonstrated that the first detectable slip activity, and subsequent crack initiation, were strongly correlated with grains favorably oriented for basal slip, even when other systems such as prismatic or pyramidal were geometrically permissible. The study further revealed that local stress heterogeneity and grain-to-grain interactions enhance slip localisation in basal-oriented grains, promoting the nucleation of fatigue short cracks along basal facets. This observation complements both the current results and earlier studies by Bantounas et al. and Bridier et al., confirming that basal-oriented grains are the preferred initiation sites across a wide range of microstructures, loading ratios, and fatigue regimes.

Overall, the current findings reveal that basal-oriented grains are the most susceptible FCI features in Ti-6Al-4V in the VHCF regime. The absence of non-basal initiation features in this study, despite the abundance of suitably oriented grains for other slip systems, underscores the strong crystallographic and mechanical preference for basal plane activation during cyclic loading. Furthermore, the consistency of this behaviour across different titanium alloy systems and testing conditions highlights that the mechanisms governing basal-dominated fatigue crack initiation are robust and intrinsic to the crystallography of the α phase.

4.4.2 The effect of texture on fatigue strength

The fatigue performance of Ti-6Al-4V is governed by a complex interplay of factors that act across multiple length scales. Among these, crystallographic texture, macrozones, grain size distribution, and the Schmid factor associated with FCI features exert significant influence on fatigue life at the microstructural level. However, due to the interpendency, isolating the influence of any single parameter on fatigue strength is inherently challenging, as each operates synergistically with others to define the overall fatigue response of the alloy.

This section addresses the influence of crystallographic texture on the fatigue strength at 10^8 cycles and the fatigue crack propagation rates in Ti-6Al-4V. Table 4.1 summarises the fatigue stress achieved at 10^8 cycles, while Figure 4.37 illustrates the basal texture of the IFS-labelled meso cantilever samples. It is evident that two samples (IFS10 and IFS24) display strong basal texture in the Y and Z directions respectively, whereas the remaining three appear relatively randomly oriented. Figure 4.38 further presents inverse pole figures for the FCI grains, neighbouring grains and the 'hotspot' grains, plotted along the X direction.

Table 4.1 Fatigue strength (crack initiation) at 10^8 cycles for IFS-labeled samples

Sample	Fatigue Stress (MPa)
IFS10	603
IFS19	616
IFS21	775
IFS24	650
IFS25	734

The effect of macro texture alone does not exhibit a clear trend towards the fatigue strength. By evaluating IFS10 and IFS24, one expects the strong basal texture in the Y and Z direction result to weak fatigue strengths, as reported by Bache et al. and Peters et al [123, 103]. Indeed, IFS10 displayed the lowest fatigue stress amongst the population; however, IFS24 failed at a moderate stress that lies within the range of the non-textured samples (IFS19, IFS21 and IFS25).

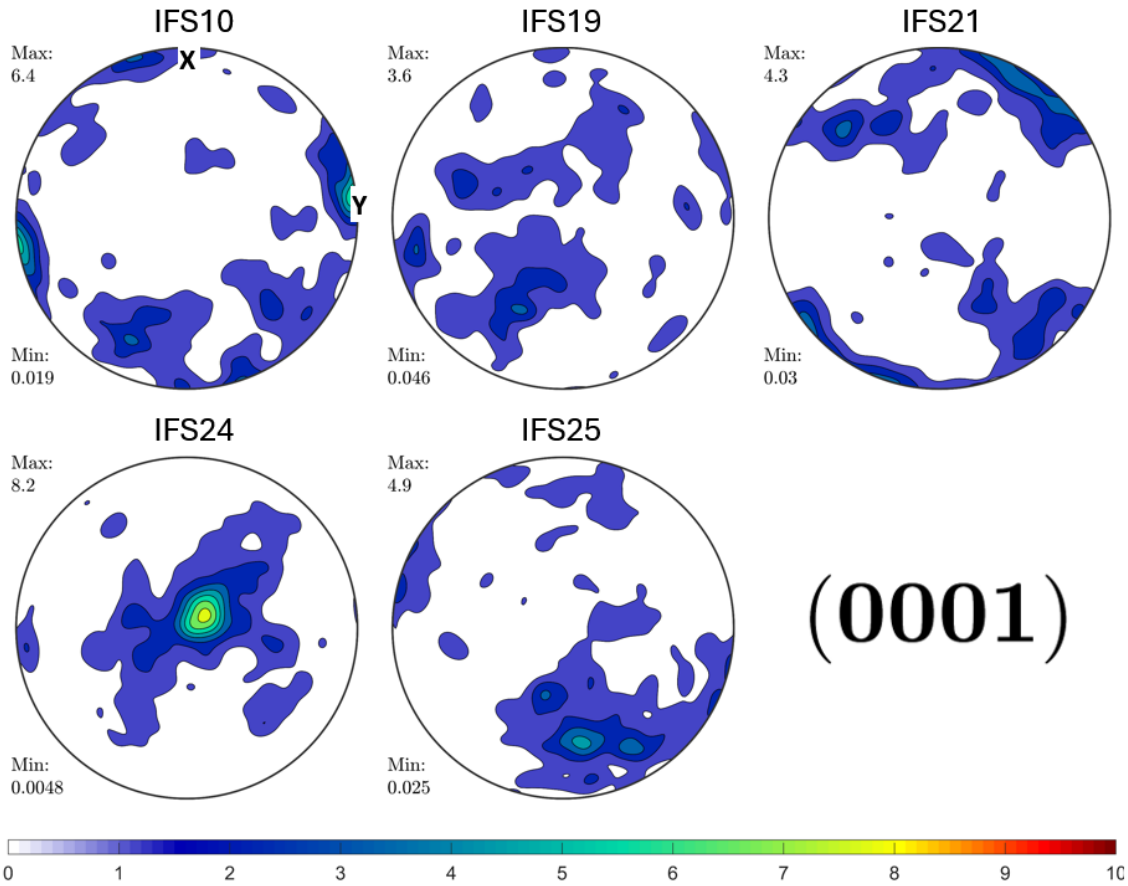


Fig. 4.37 Summary of basal texture of IFS-labeled meso cantilevers. X, Y and Z are parallel, transverse and normal to the cantilever axis, respectively

A more discernible trend emerges when focusing on the 'hotspot' grains. These are grains located in regions of high stress distribution within the meso cantilever, which serve as potential FCI sites. The sample with the lowest fatigue strength (IFS10) shows FCI grains clustered in a region of local texture associated with a high Schmid factor. The clustering of similarly oriented FCI grains revealed a very high basal-basal Luster-Morris parameter of 0.90. These factors collectively suggest their roles to the reduced fatigue strength. Conversely, the sample exhibiting the second highest fatigue strength (IFS25) initiated fatigue cracks in the vicinity of a local texture with a very low Schmid factor, which then propagated into another local texture with a high Schmid-factor, corresponding to a low Luster-Morris parameter (0.51) for basal-basal slip transfer. In the two non-textured samples (IFS19 and IFS24), FCI

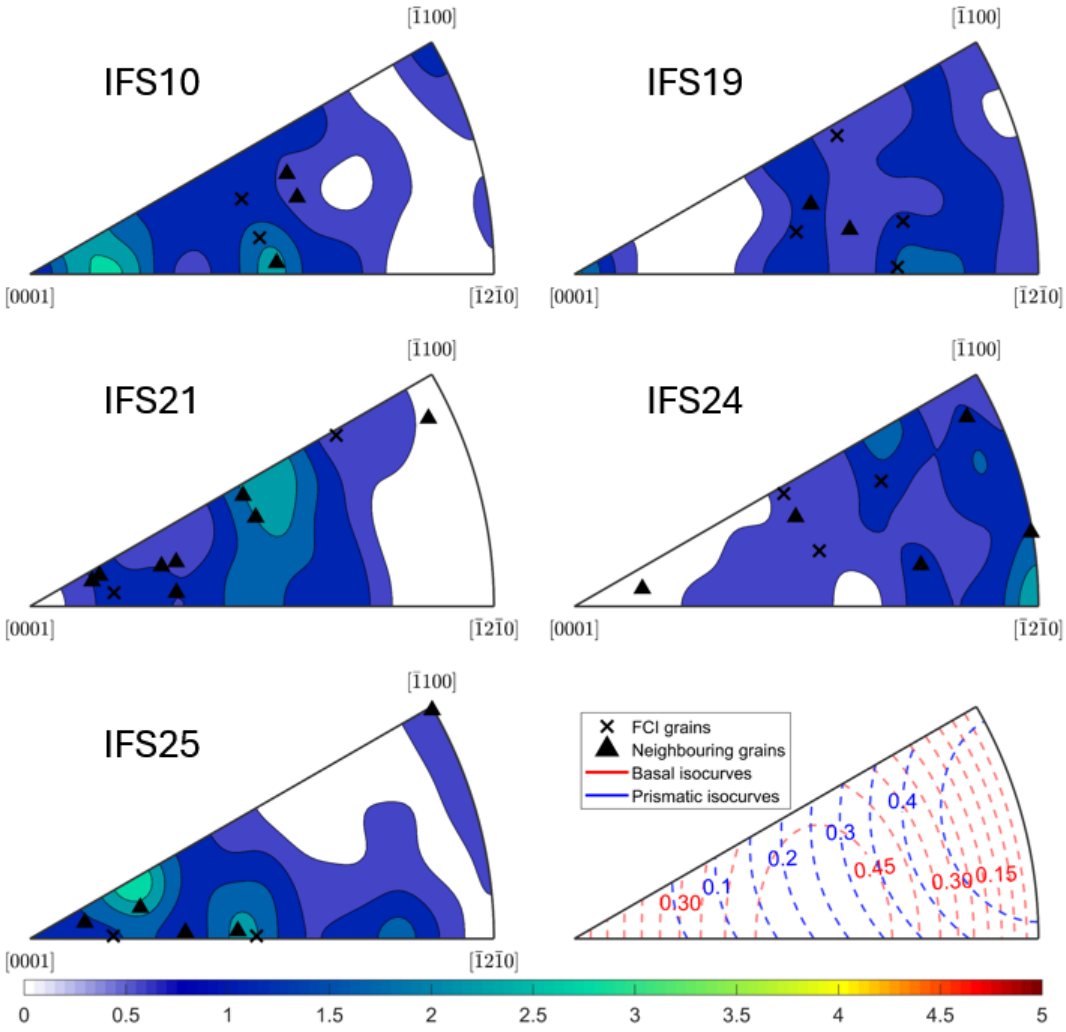


Fig. 4.38 Summary of IPFX plots of FCI and neighbouring grains in relation to the 'hotspot' grains

grains occurred in moderately high Schmid factors (above 0.4) and yielded moderate fatigue stresses. Lastly, the highest resulting fatigue stress (IFS21) revealed two FCI grains at both very low Schmid factors and large angular misorientation. This is reflected in the lowest basal-basal slip transfer (0.28) amongst other samples.

It is evident that texture exerts some influence on fatigue-crack-initiation behaviour, as often reported in the literature [32, 103, 123]. Two out of five samples revealed the tendency of an FCI occurring at a local texture along the 'hotspot' location. However, the larger

influence appears to lie with slip-tendency factors that are well-described by the Schmid's law and the Luster-Morris parameter [128].

4.4.3 The influence of grain orientations and local texture on fatigue short crack growth

The role of microstructural features is particularly significant during short crack growth. At this length scale, the crack growth behaviour is strongly crystallographic, following favourably oriented slip systems as it progresses. Such propagation often involves significant crack path deflections as the crack crosses grain boundaries with varying crystallographic orientations [42]. This behaviour is in sharp contrast with long crack growth, which tends to approximate a continuum response, with cracks propagating nominally perpendicular to the applied loading direction and less constrained by local crystallography or slip systems.

It is important to note that the fatigue crack growth measurements in this work were derived from compliance loss, obtained through the tracking of bending angles during cyclic loading. Although this is an indirect approach compared to conventional crack growth measurement techniques, such as potential drop or direct optical crack length monitoring, it remains effective in capturing key features governed by underlying microstructural mechanisms of short crack propagation. The sensitivity of this method to changes in compliance allows it to reflect transitions in crack growth behaviour that coincide with crystallographic or microstructural transitions.

A closer examination of individual samples illustrates these effects. In sample IFS10, the fatigue crack exhibited a distinct momentary deceleration followed by a rapid acceleration at approximately 70 microns from the initiation site. This transition coincided with a change in the active slip system from basal to prismatic, which occurred in grain number 8 in Figure 4.3. A similar transient reduction in the crack growth rate was observed for sample IFS19, coinciding with a pronounced crack-path deflection across grains 11, 12, and 13,

which also occurred at approximately 70 microns from the crack initiation site. Conversely, IFS21 displayed a fully near-basal oriented crack path, with the slip-trace analysis showing minimal deviation in crack paths. Apart from a brief reduction in growth rate during the crack initiation stage due to the low m', the crack in IFS21 maintained a relatively steady propagation rate, indicative of minimal resistance to slip transfer across neighbouring grains of similar orientation. In all samples, the trace analysis revealed that FCI has taken place in basal planes, which then propagated mainly in a trangranular manner through either basal or prismatic planes.

Research performed by Zhang et al. and Habib et al. demonstrated that fatigue cracks propagating within macrozones favourably oriented for basal slip tend to exhibit higher growth rates than those oriented for prismatic slip [129, 130]. This behaviour has been attributed to the reduced number of deflections and misalignment slip directions encountered at grain boundaries in basal-oriented regions compared to slip occuring in prismatic planes. Interestingly, this trend is not fully reflected in the present results when comparing across samples. Figure 4.39 displays the fatigue crack propagation of IFS-labeled samples as a function of the cyclic stress intensity factor range (ΔK). Sample IFS21, which showed a fully basal slip-trace pattern, exhibited a moderate propagation rate relative to the rest of the population. Two samples, IFS10 and IFS25, which exhibited clustering of the FCI and neighbouring grains within a textured region, showed the highest fatigue crack propagation rates (see Figure 4.38). In contrast, the remaining samples (IFS19, IFS21, and IFS24) which did not display a clear relationship between the orientations of the FCI and neighbouring grains and the texture of the corresponding 'hotspot' regions, exhibited lower propagation rates.

Overall, these observations underscore the highly microstructure-sensitive nature of short crack propagation in Ti-6Al-4V. The non-conventional crack growth measurement technique employed in this research still requires improving; however, it successfully displayed the

essential features that influence short crack growth rates and reaffirmed that the interplay between grain orientation, slip activity, and local texture connectivity plays a decisive role in governing short crack growth behaviour in Ti-6Al-4V.

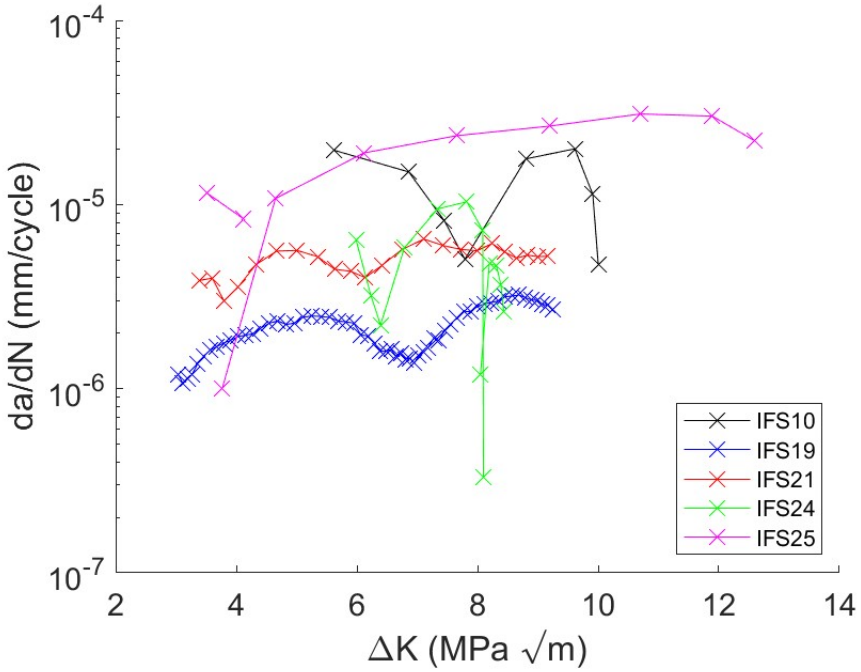


Fig. 4.39 Fatigue crack propagation rates of IFS-labeled samples as a function of the stress intensity factor

4.4.4 The grain size distribution of fatigue crack initiation features

Figure 4.40 presents the grain size distribution of the FCI grains in comparison with that of the 'hotspot' grains located near the edge of cantilever with high stress distribution and

Table 4.2 FCI grain sizes and the fatigue strength at 10^8 cycles for IFS-labeleds samples

Sample	Fatigue Stress (MPa)	FCI size (Microns)
IFS10	603	16.60
IFS19	616	8.73
IFS21	775	12.10
IFS24	650	14.09
IFS25	734	17.87

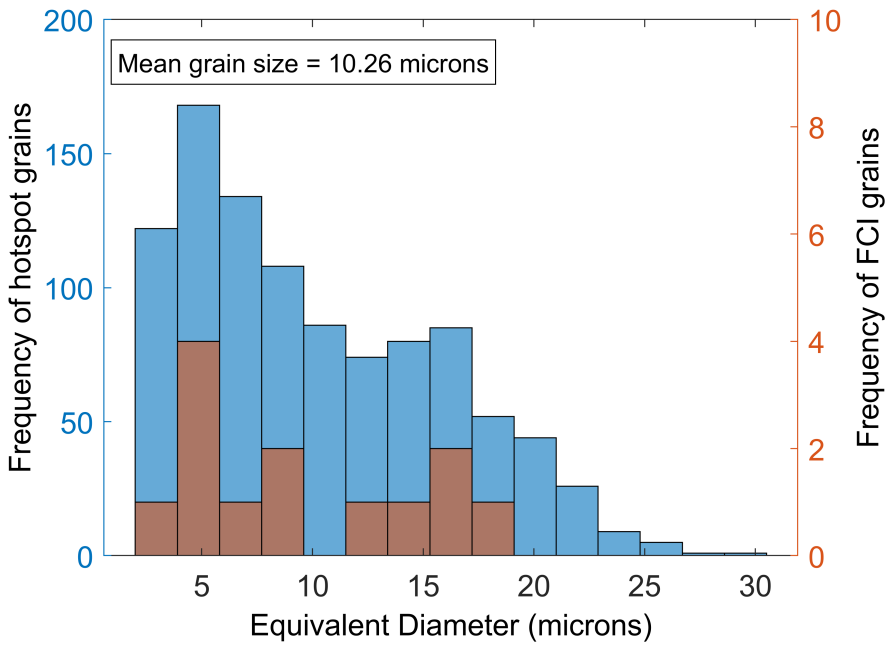


Fig. 4.40 The grain size distribution of 'hotspot' grains and FCI features

therefore serving as potential FCI sites. The results reveal two distinct distributions for the FCI grains, with mean equivalent diameters of 5.6 and 15.3 microns. The 'hotspot' grain distribution is presented in blue with an average diameter of 10.26 microns.

It is important to note that the smaller population of FCI grains within the average distribution of 5.6 microns in diameter are associated with grains situated at the outermost edge of the specimens, particularly in regions where the size was reduced by laser machining during specimen fabrication. Consequently, this finer-grained population is not a representative of the bulk microstructure. This distinction also clarifies why two or more grains have been categorised as FCI grains in this study. Although, in theory, cracks of bending fatigue should initiate at the free surface corner of the cantilever, the interrupted fatigue testing and subsequent characterisation techniques used in this study cannot definitively pinpoint whether initiation occurred at the absolute specimen edge or slightly within few grains inwards. Considering these factors, it is appropriate to treat the larger-sized distribution of grains (μ = 15.3 microns) as the true representative distribution of FCI grains that are responsible for

fatigue crack initiation under cyclic bending. Interestingly, this mean size is larger than the mean size of the 'hotspot' grain population (10.26 microns) in this study.

Table 4.2 summarises the fatigue stress and sizes of FCI grains for each IFS-labeled samples. The results do not show a clear trend between larger grain size and lower fatigue stress as might be predicted from the inverse square root relationship of the Hall-Petch effect. This does not conform with the common literature that have delved into the grain size effects on fatigue and yield properties [38, 119, 131–133]. The work from Sajadifar et al. similarly investigated how grain size affects the fatigue behaviour of titanium alloys and reported that ultra-fine-grained material exhibits superior fatigue performance in the HCF regime. Conversely, the fatigue strengths of coarse- and ultra-fine-grained alloys converged in VHCF. However, this convergence was attributed to the earlier onset of crack initiation in the ultra-fine-grained material, caused by local stress concentrations associated with microstructural inhomogeneities during fatigue loading. The absence of a distinct grain-size trend in our results suggests that the other factors that were previously discussed such as Schmid-factor and slip transfer readiness between grains, exert a larger influence in FCI behaviour.

4.5 Summary

Fatigue is a complex, hierarchical, and multiscale process governed by a range of microstructural attributes that collectively influence the initiation and subsequent propagation of fatigue cracks. At the length scale of crack initiation and short crack growth, the process is highly crystallographic. Therefore, it is important to evaluate the susceptible microstructural features during such process. The present study explored the influence of several microstructural features on fatigue behaviour, employing a suite of post-processing analyses based on the characterisation technique of EBSD.

The influence of texture, short-crack behaviour, and grain size on fatigue performance can be summarised as follows:

1. The analysis of grain orientation associated with FCI features revealed that all initiation events occurred on near-basal planes. When the results were evaluated using the normalised Schmid factor, the distribution of FCI features was shown to cover the full spectrum of basal-dominant orientations, ranging from approximately 15° to 65° relative to the loading direction.

2. No clear trend was identified when comparing overall specimen texture with fatigue strength. However, when focusing on the local texture of FCI and 'hotspot' grains, a distinct relationship emerged. Samples exhibiting clusters of FCI grains in regions of moderately high Schmid factor showed lower fatigue strength in the VHCF regime. Conversely, the specimen with the highest fatigue strength featured FCI grains initiating in regions characterised by a combination of low basal Schmid factor and a very low Luster-Morris parameter, suggesting that unfavourable slip conditions may delay the formation of crack nucleation.

3. The novel fatigue crack rate measurement technique developed in this work successfully captured key microstructural influences on local crack growth behaviour. These included a brief deceleration phase corresponding to a transition from basal to prismatic slip, as well as a pronounced angular crack-path deflection, both of which are characteristic of the microstructure-sensitive process of fatigue short crack growth. IFS10 and IFS25, which exhibited clustering of the FCI and neighbouring grains within a textured region, showed the highest fatigue crack propagation rates (see Figure 4.38). In contrast, the remaining samples (IFS19, IFS21, and IFS24) which did not display a clear relationship between the orientations of the FCI and neighbouring grains and the texture of the corresponding 'hotspot' regions, exhibited lower propagation rates.

4. The evaluation of grain size revealed no systematic correlation between grain size and fatigue strength across the population. This suggests that grain size alone is not the

dominant factor controlling fatigue performance under the present testing conditions. Instead, the collective influence of grain orientation, local texture clustering, and slip-transfer characteristics appears to exert a far greater effect on fatigue life and crack evolution.

Chapter 5

Crack tip strain evolution in fatigue short crack growth

5.1 Introduction

The integration of interrupted fatigue protocol within the ultrasonic setup enables the observation of short crack growth and lattice strain evolution at various crack lengths and bending angles. This approach represents a significant advancement over conventional short-crack fatigue studies, which are typically restricted to LCF regimes and high stress amplitudes, where substantial plastic deformation is introduced to generate pre-cracks and achieve measurable crack growth within practical timeframes using servo-hydraulic testing systems. In contrast, the present methodology allows the investigation of crack initiation and early propagation under conditions more representative of HCF and VHCF regimes. Furthermore, fatigue crack initiation and short crack growth are inherently highly localised phenomena, occurring at the micron scale. The meso cantilever specimen design, together with the complementary techniques employed in this work, addresses the classical "needle-in-a-haystack" challenge associated with identifying and analysing early fatigue damage in traditional bulk specimens. This combined approach therefore provides a powerful and targeted framework for

resolving microstructure-sensitive fatigue processes that are otherwise difficult to capture experimentally.

This chapter investigates the lattice strain and GND density evolution ahead of a fatigue short crack tip when the sample is bent through different angles. The characterisation will be performed using HR-EBSD. Due to the relative nature of HR-EBSD towards a reference pattern, it may be difficult to directly compare results across samples. As such, a new method is proposed and implemented to reduce the reference pattern bias and evaluates the results in comparison to the current standard method.

5.2 Experimental methods

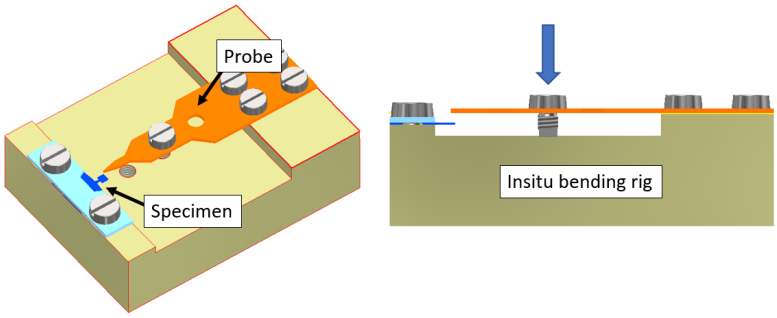
Ti-6Al-4V foils with an initial thickness of 250 microns were sectioned from a disc using EDM. The foils were then ground using SiC papers from 1200 to 4000 grit to remove EDM damage on the sample surface and to achieve a uniform final thickness of approximately 150 microns. Subsequent polishing was performed in a 5:1 mixture of colloidal silica and hydrogen peroxide for 1.5 hours to further remove the finest surface scratches. After polishing, the foils were laser-machined into meso cantilevers and then individually electropolished in a solution of 6% Perchloric acid, 35% Ethylene Glycol and 59% Methanol in volume at –50°C to achieve the necessary surface quality for high resolution EBSD characterisation.

The sample underwent fatigue testing at 10^8 cycles using the step-stress protocol which involves increasing the stress amplitude after each runout test. The interrupted fatigue protocol was setup to detect fatigue short crack growth and turn off the system before the sample fully fractures. This is done by detecting sudden growth in the laser reflection from the free-moving end of the meso cantilever, caused by the loss in compliance as crack initiation occurred.

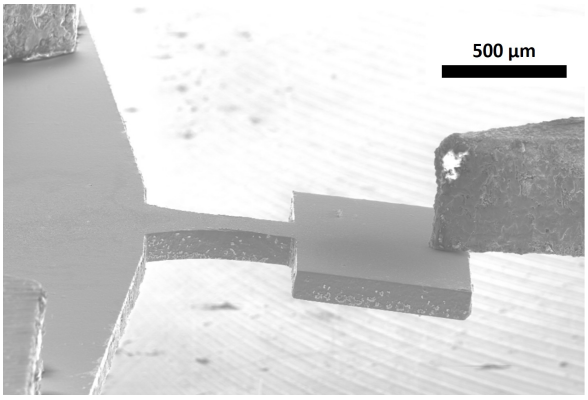
The interrupted fatigue specimen (IFS) was mounted on a bespoke in-situ EBSD bending rig, shown in Figure 5.1. The specimen was characterised using EBSD in three states: an unloaded configuration, an intermediate bending angle, and a maximum bending angle. This

procedure was designed to approximate the evolution of crack-tip strain over one quarter of a fatigue cycle. All EBSD measurements were conducted using a Zeiss Merlin FEG-SEM, operated at an accelerating voltage of 20 kV and a probe current of 10 nA. Electron backscatter patterns (EBSPs) were acquired with an Oxford Instruments Symmetry CMOS detector, using a 7 ms exposure time and a step size of 140 nm. Additional parameters included a working distance and camera distance of 18 mm.

Surface topography near the area of arrested crack tips was performed using atomic force microscopy (AFM) to complement the EBSD characterisation results. AFM was conducted using a VEECO Dimension 3100 AFM, operating in tapping mode at a scanning frequency of 0.5 Hz with a field of view of approximately 50 x 50 μm^2.



(a)



(b)

Fig. 5.1 Bespoke in-situ SEM bending setup used to probe meso cantilever specimens (a) Schematic of the setup (b) View of inside the SEM

5.3 High-angular Resolution EBSD

Cross-correlation based EBSD technique comprises of different processing techniques to traditional Hough transform-based EBSD [67, 134]. Since the core of the technique is based on image processing, high quality Kikuchi patterns with clear bands and zone axes are needed. As such, the collection of EBSPs were done at 1244 x 1024 resolution, no binning, 7 ms exposure time, and low gain. This leads for a compromise of the highest possible signal strength, contrast, signal to noise ratio, without over exposing and damaging the sample surface.

Another important parameter to be considered, particularly for the evaluation of GND densities, is the step size or spacing between scan points. GND evaluation based on Nye's technique will cancel two dislocations of the opposite sign within the same slip system; therefore, larger step sizes will less likely to detect dislocation densities of smaller scales. Conversely, smaller step sizes produces higher GND density noise floor. A more detailed review of the step size effects on GND density calculations from HR-EBSD has been discussed by Jiang et al [135]. A 140 nm step size was chosen throughout this study.

Processing of the EBSPs for HR-EBSD was done with xEBSD v3, a non-commercial version of Cross-Court developed within the Oxford Micromechanics Group. In a polycrystalline system, the cross-correlation technique is performed in each grain to a respective reference within the grain. The process first comprised of categorising each pixel of the EBSD to the respective grains using MTex, an open source Matlab toolbox for mainly analysing EBSD data. Normally, the reference pattern for each grain was then chosen with a combination of the pattern with the highest image quality (IQ), distance from grain boundaries, and the closest orientation to the mean orientation of the grain. High IQ has been correlated to low plastic strain which are preferred conditions for a cross-correlation technique as everything is measured relative to the reference pattern.

Preprocessing of the patterns took place once the coordinates for the reference patterns were chosen. This included the determination of numbers of ROIs around the EBSPs in which detailed evaluation of patterns shift occurs. Mathematically, a minimum of four ROIs are needed to obtain the components of the displacement gradient tensors. In this study, 40 ROIs of 256×256 pixels (an example is shown in Figure 5.2) were used to create an overdetermined system in a least-squares fitting, which reduces noise and improve the robustness of the calculation [66, 67]. Each ROI were then passed through an FFT filter which removes the high and low frequency components within the frequency domain to further remove background intensity (low frequency) and random detector noise (high frequency).

The cross-correlation technique starts after the preprocessing procedure. The algorithm determines the shift of each ROI relative to the reference pattern. The shift is used to calculate the displacement gradient tensor, which is then used to obtain the elastic strains and lattice rotations for each point of the EBSD map, relative to the lattice at the reference pattern position.

The relative calculations towards a reference pattern that is characteristic of HR-EBSD is an obstacle when trying to form a comparison across multiple strain states. The samples have undergone fatigue testing at 10^8 cycles, therefore the assumption of strain-free reference pattern is not probable in any sample probing setup throughout this EBSD characterisation. To overcome this issue, the HR-EBSD relative strain results have been combined with finite element analysis to achieve absolute strain values, which was similarly performed in the work by Karamched and Wilkinson [136].

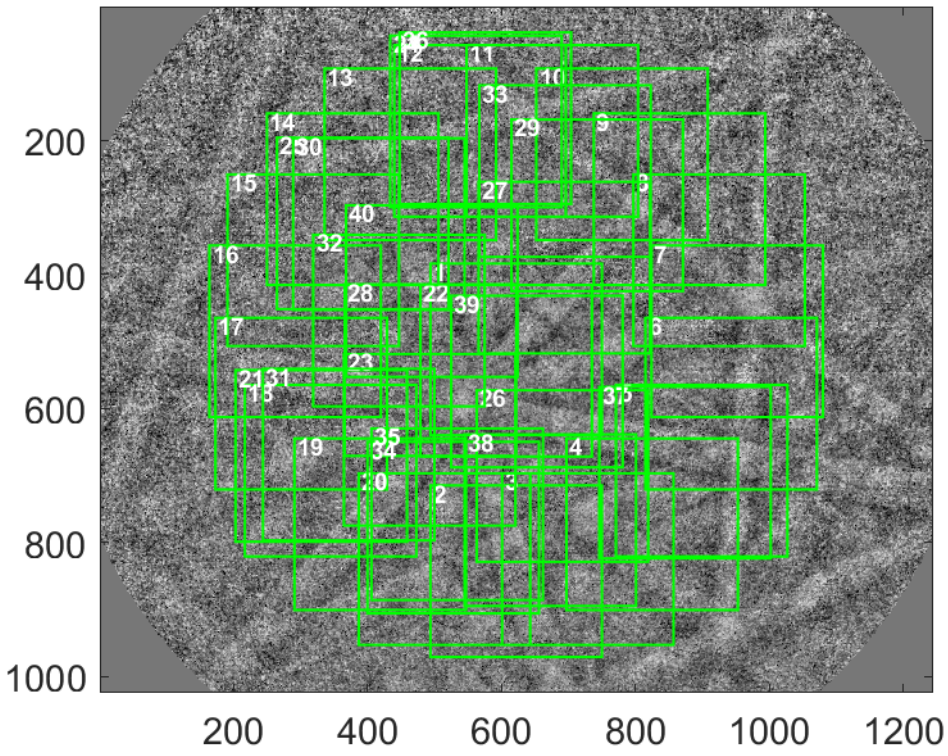


Fig. 5.2 An example of a reference EBSP with 40 ROIs (256×256 pixels) to be cross-correlated with test patterns

5.4 Results and discussions

5.4.1 The usage of multiple reference patterns

Measurements of elastic strain and lattice rotations in HR-EBSD introduce a bias that are relative to the reference pattern [136, 137]. Figure 5.4 presents the lattice rotation maps obtained using two different sets of reference patterns shown in Figure 5.3. The relative nature of the measurements is evident, as the overall rotation field appears shifted according to the location of the respective reference patterns. Figure 5.5 illustrates the difference between the two previous rotation datasets. Ideally, the offset between two relative measurements should remain constant across all grains, since only a uniform rotational reference shift is expected when different reference patterns are used. However, the results clearly demonstrate that the offset varies in the individual grains. This inconsistency originates from systematic errors introduced during the cross-correlation process, which propagate through the displacement gradient calculations.

More critically, the reference-dependent lattice rotation measurements lead to a loss of insensitivity to reference pattern selection in the lattice rotation gradients. In HR-EBSD, the rotation gradients form the basis for calculating the GND densities, under the assumption that such gradients are independent of reference choice [138, 139]. The present results, however, reveal that this assumption no longer holds when the reference bias is non-uniform. As shown in Figure 5.6, the computed GND density maps vary significantly depending on the reference pattern set employed. The GND density map reveals subcell regions which appear in the direct surrounding of the reference patterns. This variation highlights the sensitivity of GND density calculations to the rotation of reference patterns across the grain interior. Such findings underscore the importance of alternative reference pattern selection methods which reduce calculation bias. By distributing multiple reference patterns within each grain

and weighting their contribution according to image quality, the overall reference bias can be reduced, leading to more reliable and physically meaningful GND density evaluations.

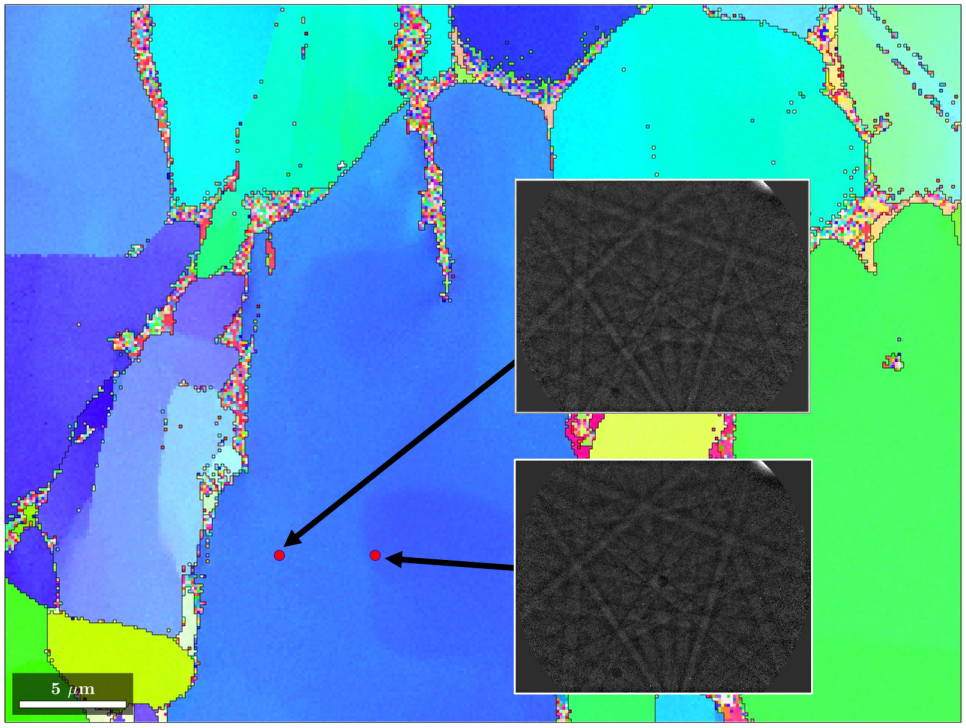


Fig. 5.3 Two EBSP located from different subcell regions within a grain, displayed by the slightly different shade of colour in the IPFX map

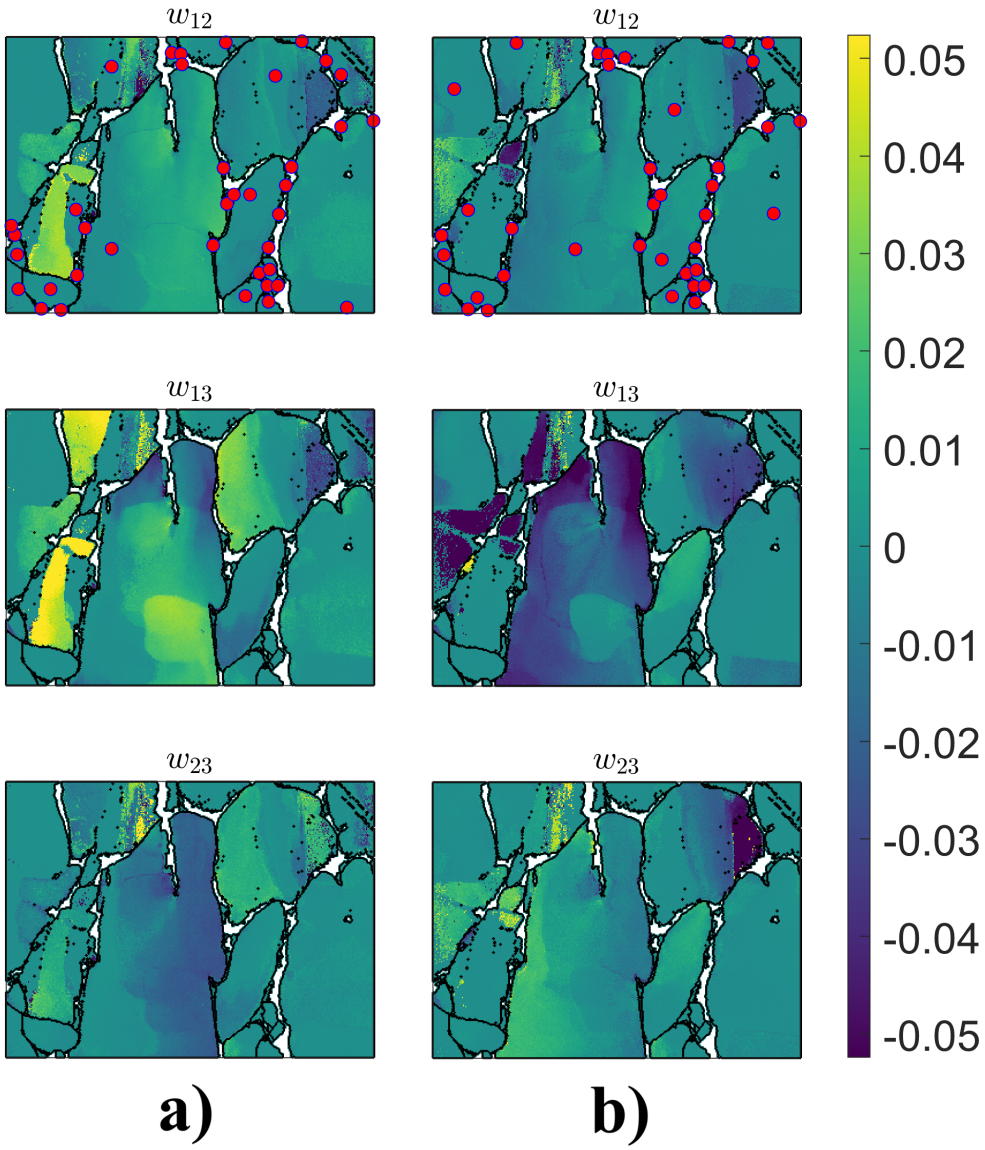


Fig. 5.4 Individual components of the lattice rotation using a different set of reference patterns. The locations of the reference patterns for (a) and (b) are displayed in the respective top subplots. Units are in radian

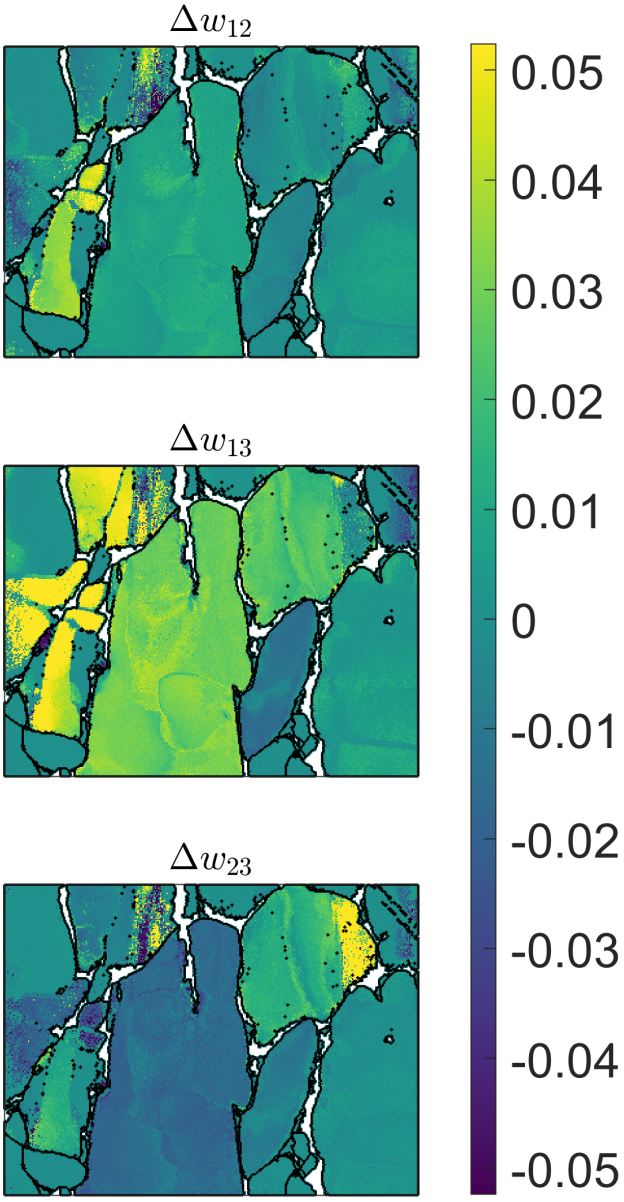


Fig. 5.5 Offset between Figures 5.4a and 5.4b. Units are in radian

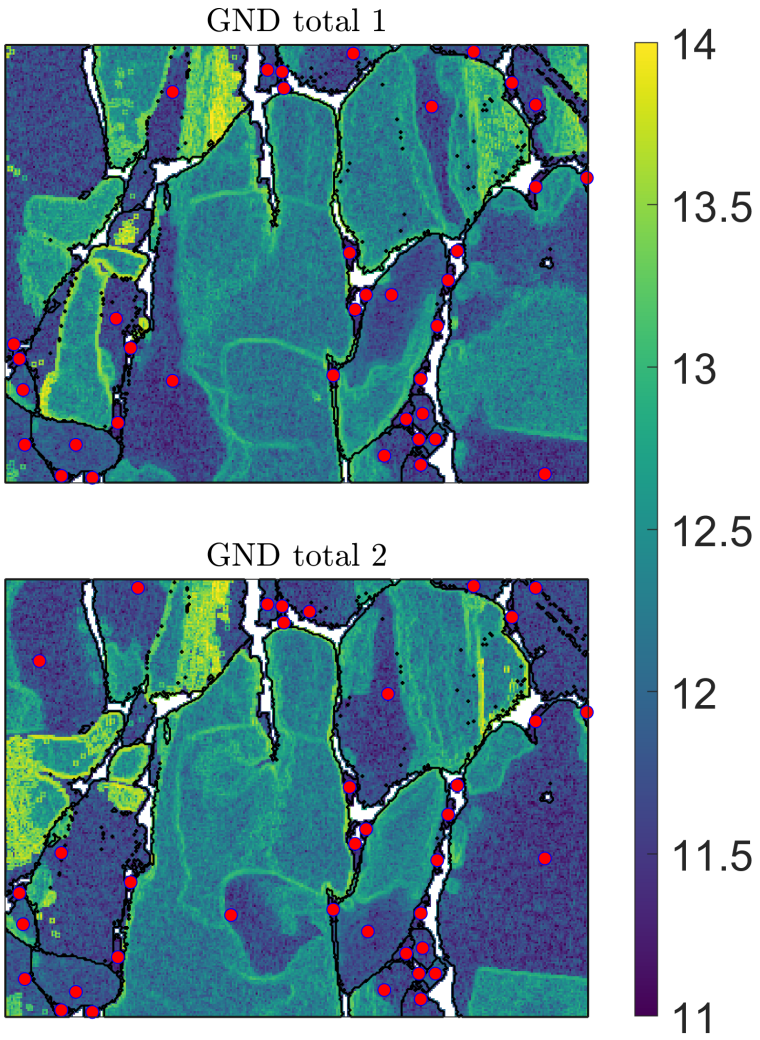


Fig. 5.6 GND comparison using two different sets of reference patterns. The scale is logged and the units are in m^{-2}

To visualise the post-processing of an ideal cross-correlation data, a synthetic/user constructed map was considered. It is displayed in Figure 5.7a. Figures 5.7b and 5.7c illustrate two relative maps, termed R1 and R2, that were processed using a different reference pattern that are indicated by black circles. In ideal conditions, the difference between R1 and R2 should remain constant across the entire dataset, as demonstrated in Figure 5.7d. Furthermore, when the spatial gradients of these relative maps are calculated (Figures 5.7e and 5.7f), the resulting distributions are identical, reconfirming the insensitivity of gradient maps to reference pattern selection in ideal settings.

To reduce the bias effect, a new post-processing approach is suggested in this study, employing multiple reference patterns per grain across the EBSD map. In this research, ten reference patterns were chosen for each grains with the following filtering procedure:

1. The effective grain area was reduced by offsetting the grain boundaries inward, thereby excluding potential reference locations near boundaries where pattern overlap or mixed-phase effects could occur.

2. Within the filtered region, ten equally spaced coordinates were assigned in large grains to ensure uniform spatial coverage. For smaller grains that are usually transformed β or secondary α phases, a single reference pattern was chosen using a combination criteria (i.e. high IQ, distance to grain boundaries and nearest orientation to the mean orientation of the grain) to minimise the computational processing time.

3. Each coordinate was instructed to identify the nearest EBSD pixel exhibiting high image quality (IQ). Only points within the top 10% of IQ values were eligible as reference patterns. Figure 5.8 presents an example of the resulting EBSD map with the overlaid reference pattern positions.

Each selected reference pattern was then cross-correlated to all corresponding test patterns within its respective grain. Remapping of the test patterns were performed to minimise strain

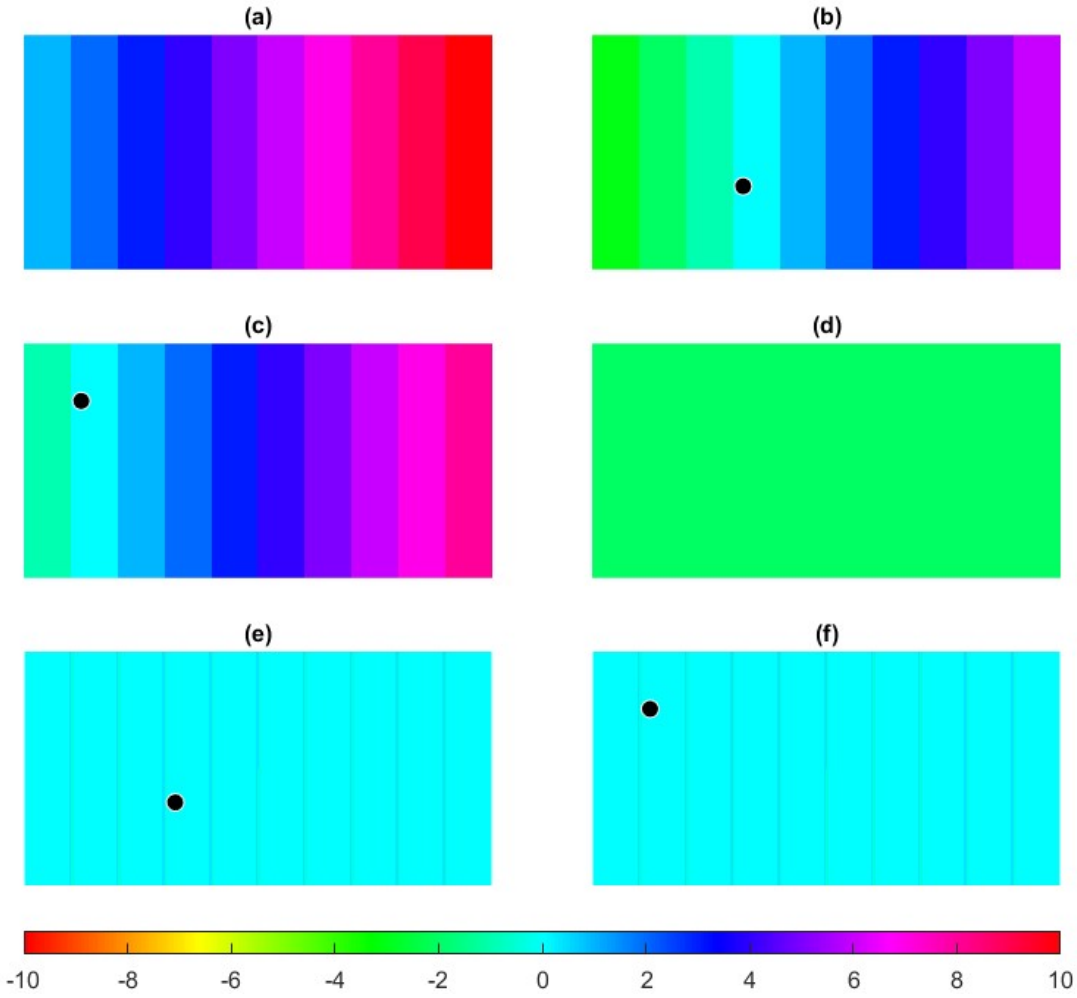


Fig. 5.7 An example of post-processing elastic strain and lattice rotation data simplified using an arbitrary data: (a) Synthetic map, (b-c) Relative maps, termed R1 and R2. The black circles are the respective reference points, (d) Constant offset at all coordinates between R1 and R2, (e-f) Gradient maps of R1 and R2, respectively

errors due to large rotations. The procedure involves calculating the local rotation matrix (first pass) to reorient the test patterns close to the orientation of the reference pattern for higher sensitivity of elastic strain measurements in the second pass [140]. The resulting elastic strain and lattice rotation tensors were computed for each reference pattern, and the individual tensor components were subsequently averaged in a weighted manner based on the image quality of each reference pattern. This weighting ensured that reference patterns with higher quality (expected lower strain) contributed proportionally more to the final averaged result.

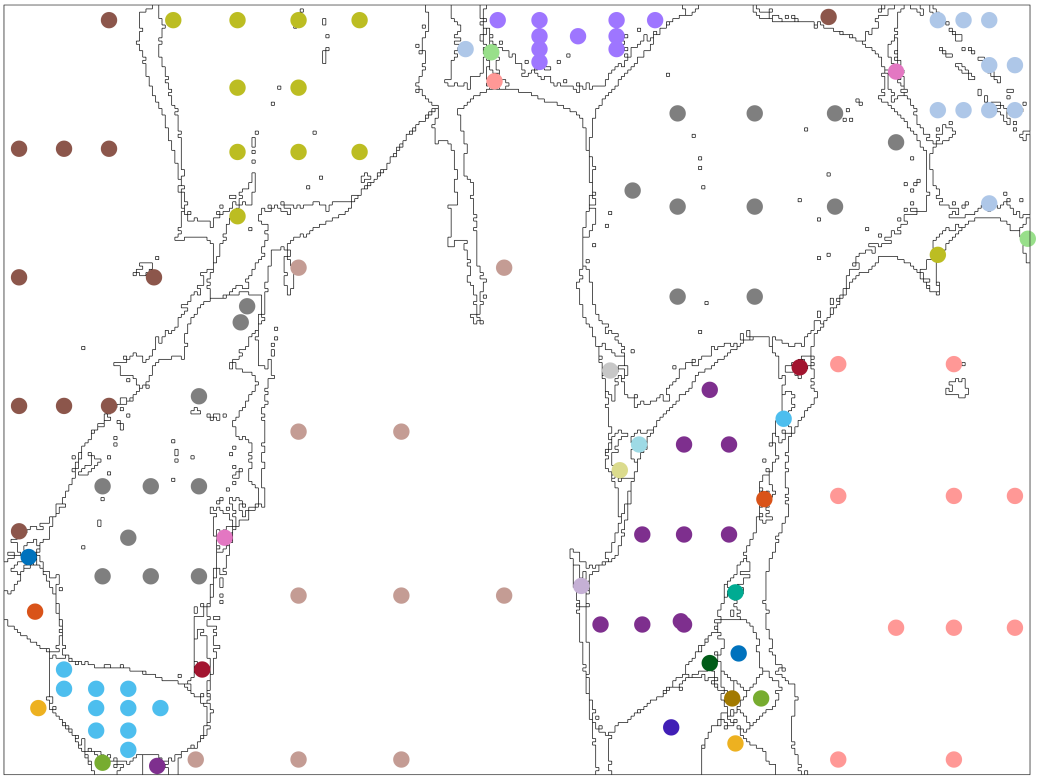


Fig. 5.8 The usage of multiple reference pattern overlaid on a grain boundary map

Figure 5.9, 5.10 and 5.11 display the weight-averaged elastic strains, lattice rotations and GND density maps obtained using the proposed multi-reference pattern approach. The GND density maps were calculated from the rotation gradients obtained from the weight-averaged lattice rotations and were numerically solved using the L^1 minimisation technique [69, 141].

The results demonstrate that the overall strain and rotation fields obtained using the proposed method successfully preserve key physical features, particularly around regions with high expected deformation such as around the crack-tip area. These high-strain zones are retained with improved continuity compared with maps derived from a single set of reference patterns (Figure 5.6). This finding suggests that the incorporation of multiple reference patterns effectively mitigates the spatial bias introduced by the cross-correlation process. The use of multiple reference patterns serves as a pragmatic solution to the discussed limitation of cross-correlating EBSD patterns.

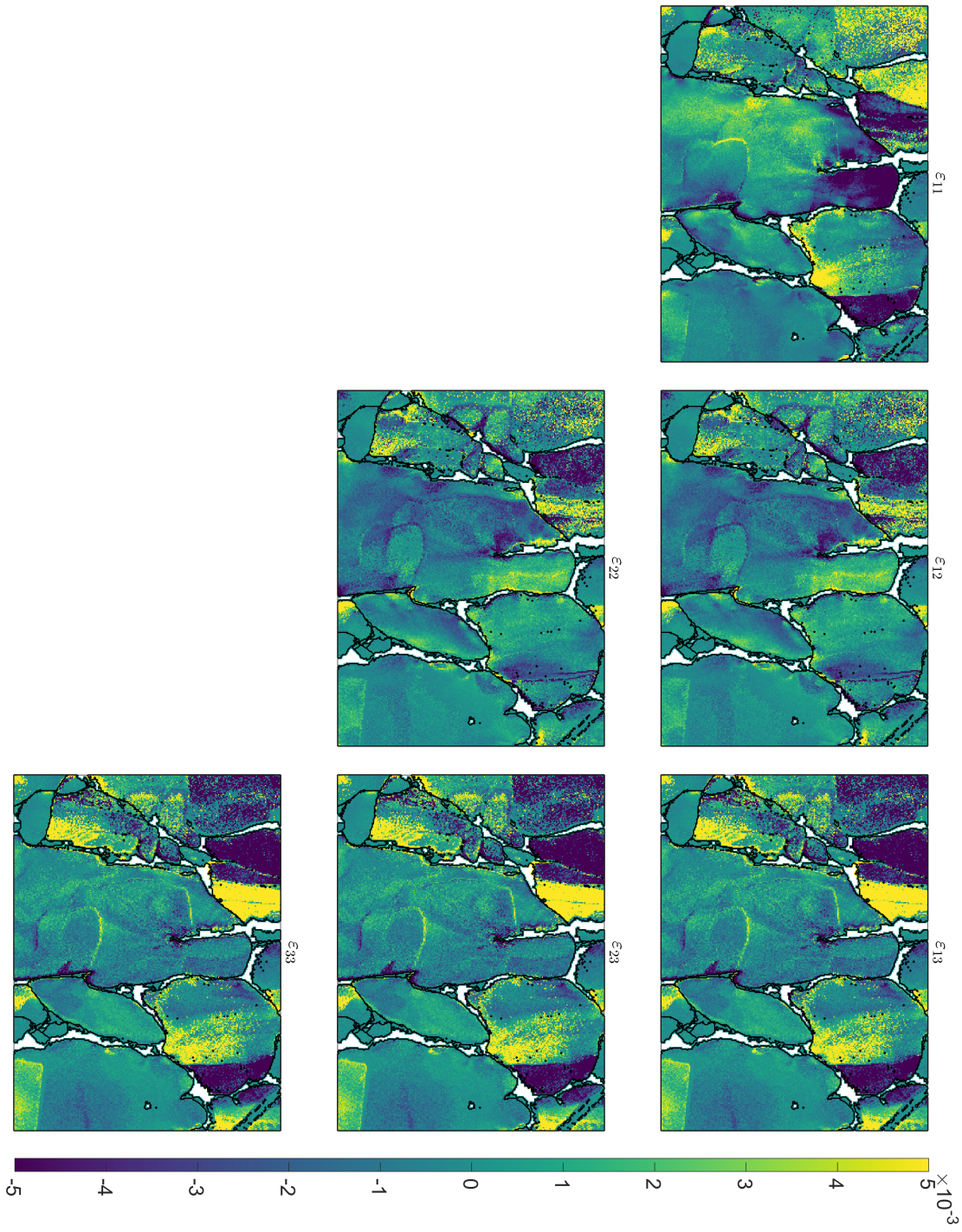


Fig. 5.9 Weight-averaged elastic strain map

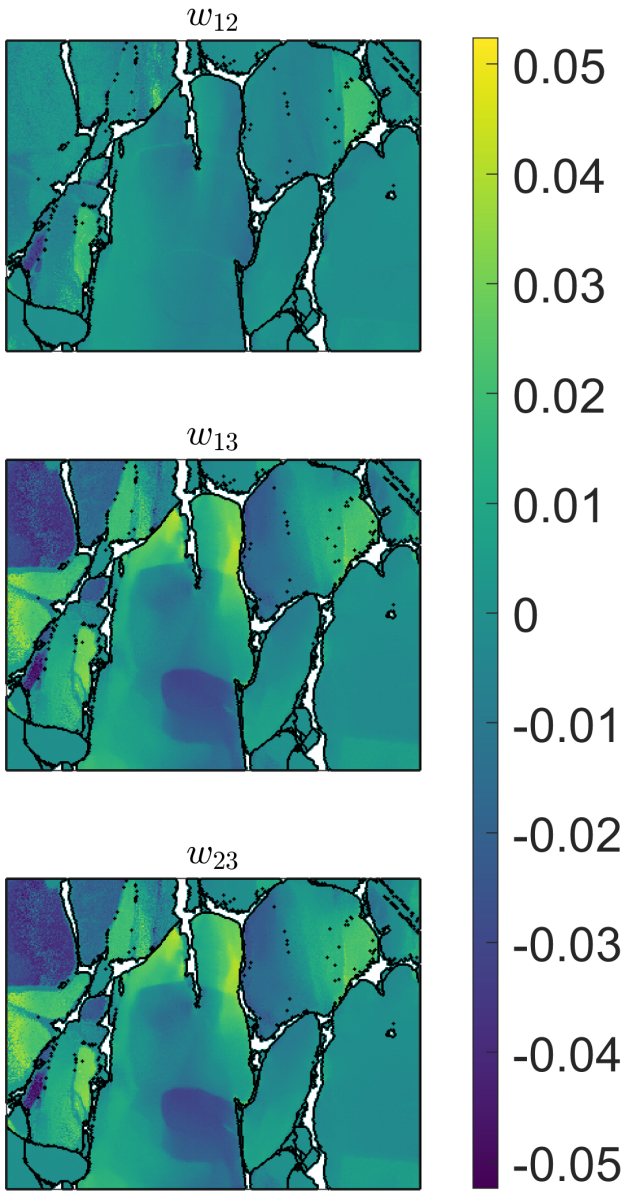


Fig. 5.10 Weight-averaged lattice rotation map. Units are in radian.

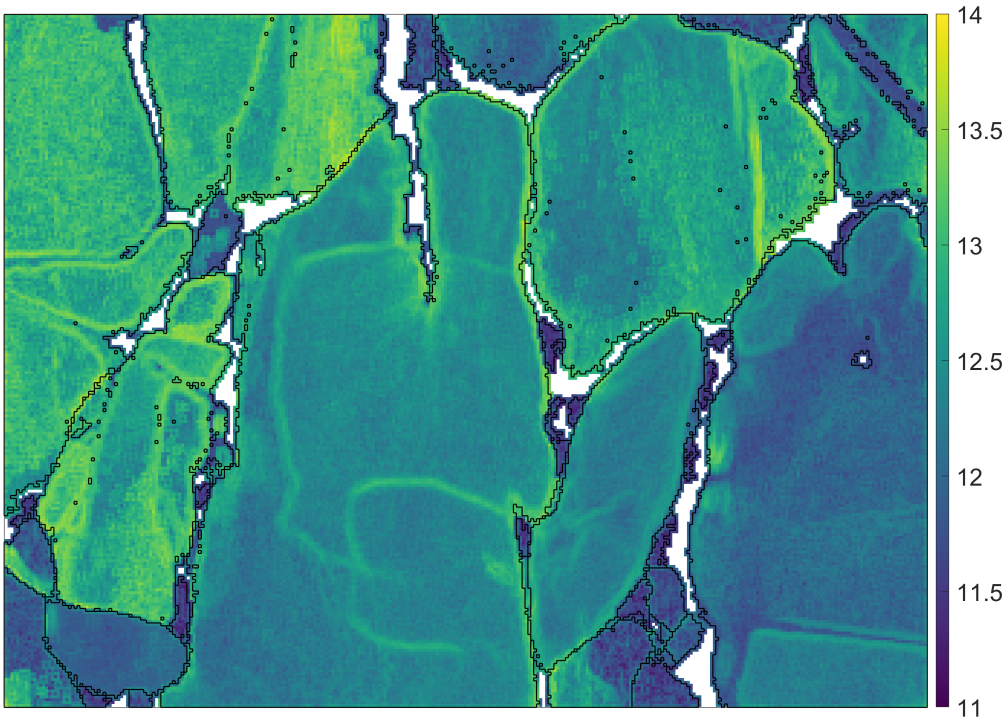


Fig. 5.11 Weight-averaged GND density map. Units are in m^{-2}.

5.4.2 Strain evolution and GND density analysis of a fatigue crack tip

The evolution of elastic strain and GND density ahead of a fatigue crack tip have been examined. The secondary electron image and mean crystal orientation map are shown in Figures 5.12 and 5.13. The interrupted-fatigue specimen was characterised at three bending angles (i.e. undeflected, 2.9°, and 5.1°) to simulate the strain evolution of a quarter fatigue cycle. The maximum angle corresponds to the bending angle at which the fatigue test was interrupted, as shown in Figure 5.14. This approach enables the observation of strain accumulation and dislocation density development as the crack tip experiences increasing deformation.

As discussed previously, the use of a strain-free reference pattern in HR-EBSD is problematic in a deformed sample. When a sample is deformed, the reference pattern itself is also strained, and therefore relative HR-EBSD results become difficult to interpret across loading steps or across different specimens. Several studies have attempted to convert relative HR-

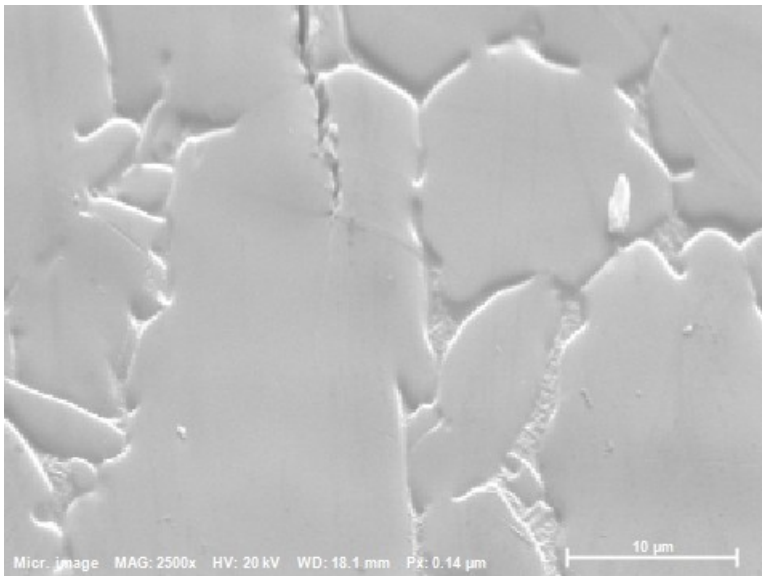


Fig. 5.12 SEM image of intragranular fatigue crack tip

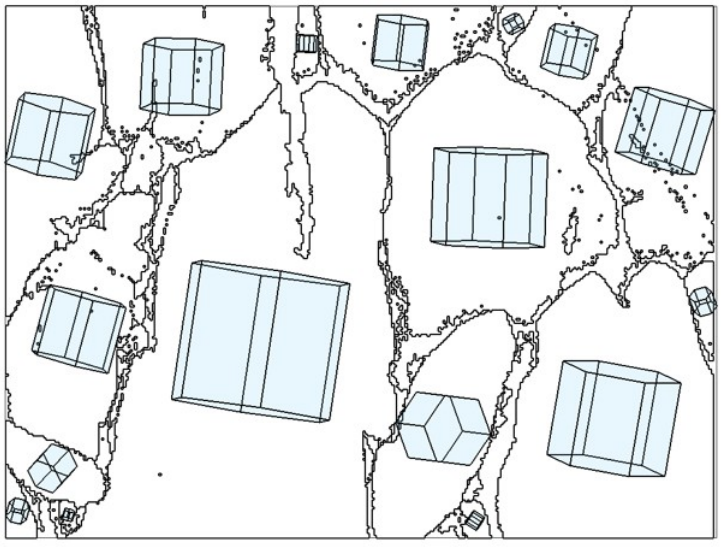


Fig. 5.13 Crystal orientation map

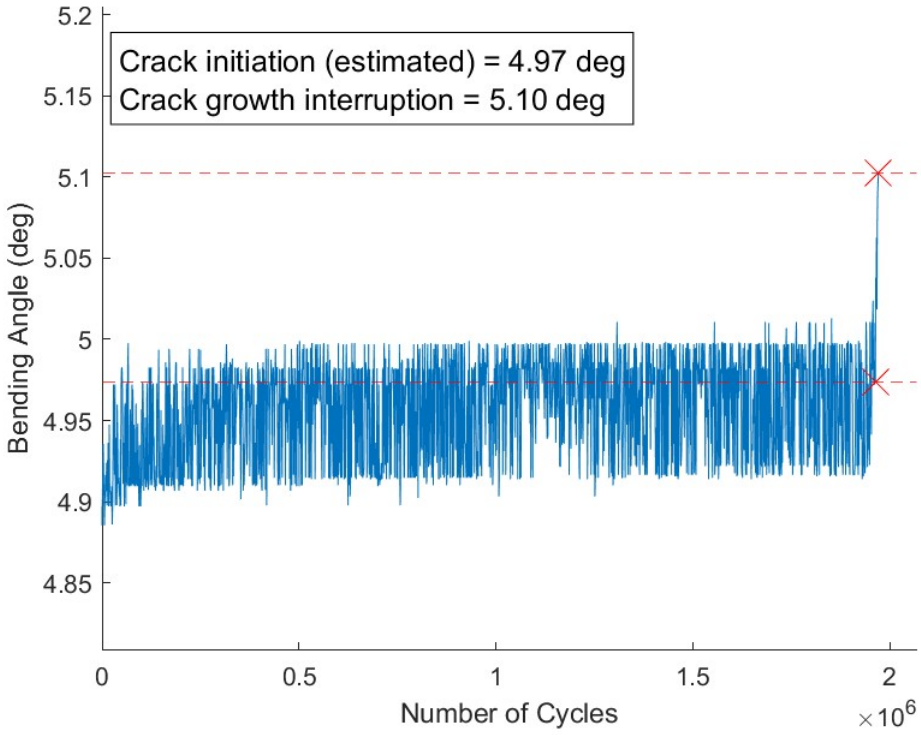


Fig. 5.14 Bending angle vs number of life cycles for IFS10

EBSD measurements into absolute strain fields, when strain-free references are unavailable. Attempts include the use of dynamically simulated EBSPs or reference patterns acquired in the undeformed state from another session [142–144]. HR-EBSD can measure sub-region (ROI) shifts with high precision, typically on the order of 0.1 pixels, which corresponds to elastic strains of approximately 10^{-3} [67]. Although simulated patterns offer a promising concept for measuring absolute strains, their current fidelity and level of detail are insufficient to match the accuracy achievable with experimentally collected EBSPs [143, 145–147]. Additional limitations which arise when using non-native reference patterns include uncertainties in the pattern centre, as well as geometric distortions and lens aberrations that vary with the microscope setup geometry. Such factors introduce systematic errors into the cross-correlation analysis, which translate to 'phantom' lattice distortions [148].

As such, the offsetting of relative elastic strains to absolute values in this study have been conducted by using OXFORD-UMAT, a crystal plasticity solver for Abaqus [149]. The experimentally acquired EBSD map was imported into Dream.3D to generate an equivalent polycrystalline representative volume element (RVE), as illustrated in Figure 5.15. The resulting three-dimensional microstructural model comprised $240 \times 319 \times 7$ elements, discretised using C3D8 eight-node linear brick elements. Plastic deformation within the CP-FE framework was governed by the elastic constants and critical resolved shear stresses (CRSS) of the constituent crystals. The material parameters employed in the simulations are summarised in Table 5.1.

Table 5.1 User Material values used for CP-FE

Elastic modulus (GPa)	114
Shear Modulus (GPa)	45
Poisson's ratio	0.33
Basal CRSS (MPa)	150
Prismatic CRSS (MPa)	100
Pyramidal CRSS (MPa)	350

A single line of elements were removed to create an equivalent fatigue crack matching the HR-EBSD map of interest. Boundary conditions were applied to the three normal surfaces which constrained movement in the surface normal direction and rotations to all inplane directions for every surface normal. As the predominant form of strain in the cyclic bending motion are parallel to the meso cantilever direction, a tension strain along the direction of the meso cantilever was applied to simplify the simulation. The strain applied in this crystal plasticity simulation is equivalent to the elastic strain at which interruption of the test occured. In this case, Figure 4.2 shows that it was interrupted at 619 MPa. Using the Hooke's Law, an elastic strain of 5.5×10^{-3} was obtained and applied to the crystal plasticity setup for the maximum strain. A strain of 3.1×10^{-3} was applied for the intermediate strain level. Using crystal plasticity allows for a more accurate strain distribution within the polycrystalline map compared to using a singular strain state. This is particularly important due to the presence of an intragranular crack which modifies the strain distribution, particularly for grains shielded behind the crack tip, as displayed in Figure 5.16. The average strain for the individual grains were then applied as a constant term across every pixel in each grain so that the individual components of elastic strain match the level found in the finite element simulation [136]. It is important to note that the strain history effects from the previous 10^8 cycles and crack propagation are neglected due to the difficulty in computationally doing such in crystal plasticity.

Figure 5.17 presents the individual components of the absolute elastic strain tensor measured at three levels of applied bending angles. A progressive increase in elastic strain is observed with increasing load, particularly in the direction perpendicular to the crack plane, consistent with deformation dominated by a near-basal orientation, as illustrated in Figure 5.13. The white box marked at the fatigue crack tip in these strain maps was sized according to the estimated plane-stress plastic zone radius, calculated using Irwin's expression:



Fig. 5.15 Crystal plasticity finite element (CP-FE) with symmetry boundary conditions (U1 = UR2 = UR3 = 0 for X plane normal, etc) and strain applied to the X direction There are $240 \times 319 \times 7$ elements used in this model

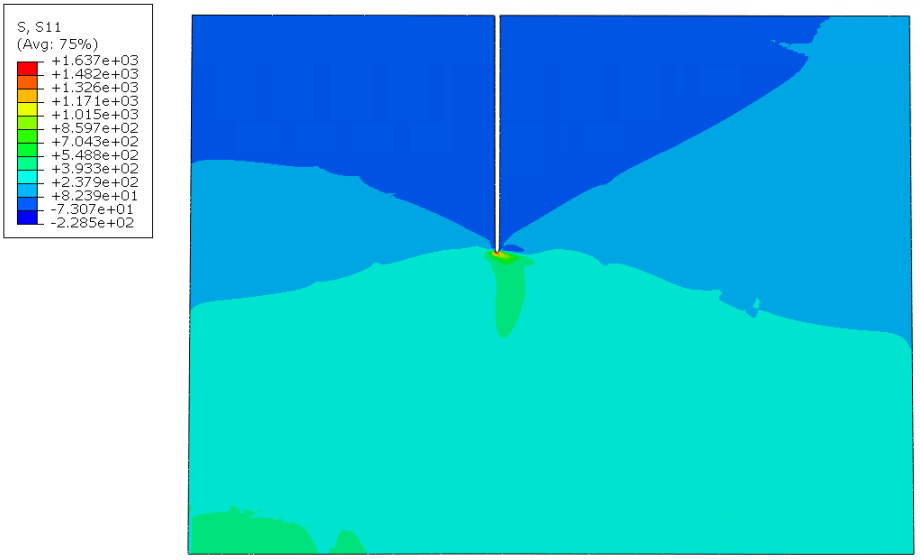


Fig. 5.16 An example of the obtained stress distribution for S11 (stress in the X direction). Units are in MPa

$$r_p = \frac{1}{2\pi}\left(\frac{K_{\mathrm{I}}}{\sigma_y}\right)^2 \tag{5.1}$$

where K_{I} is the mode I stress intensity factor and σ_y is the yield stress.

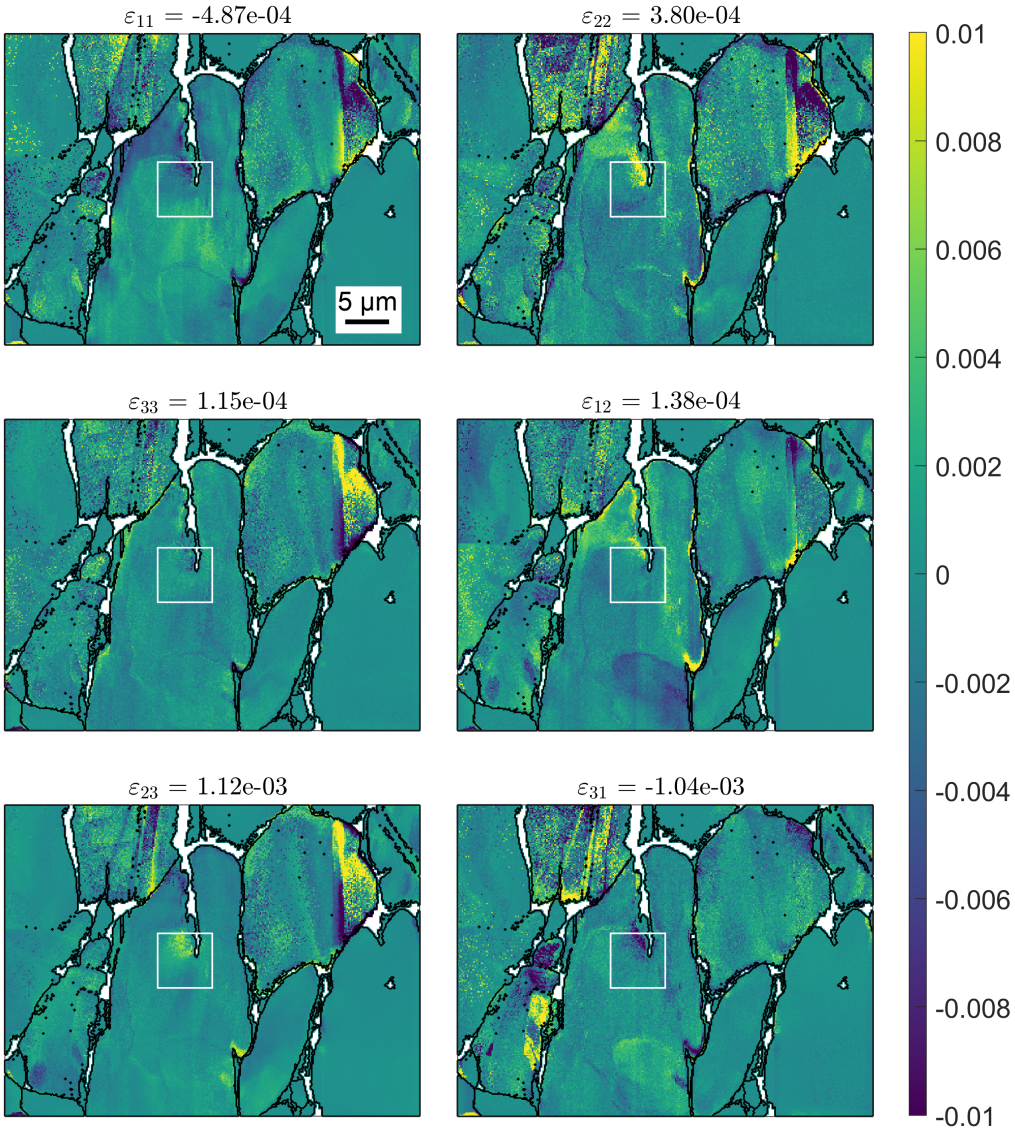
In the ε_{11} component, the crack-tip elastic strain increased across the three deformation states. At the unprobed position, the crack tip exhibits a compressive residual strain of -4.87×10^{-4}. Upon loading to 2.9°, the strain ahead of the crack tip transitions to a tensile strain of 3.22×10^{-3}, increasing further to 6.53×10^{-3} at the 5.1° bending condition. Additionally, it is particularly interesting that the growing elastic strain ahead of the crack tip aligned to the near-basal plane, despite it being roughly perpendicular to the crack growth direction.

The ε_{22} component exhibits a progressive increase in tensile elastic strain around the arrested fatigue crack tip, rising from 3.80×10^{-4} in the undeflected state to 1.10×10^{-3} at the maximum applied strain. At the maximum deflection angle (Figure 5.17c), the ε_{22} map further reveals the emergence of a pronounced compressive strain region forming ahead of the advancing tensile strain field. This behaviour suggests a complex redistribution of elastic strain in the crack-tip vicinity as loading increases.

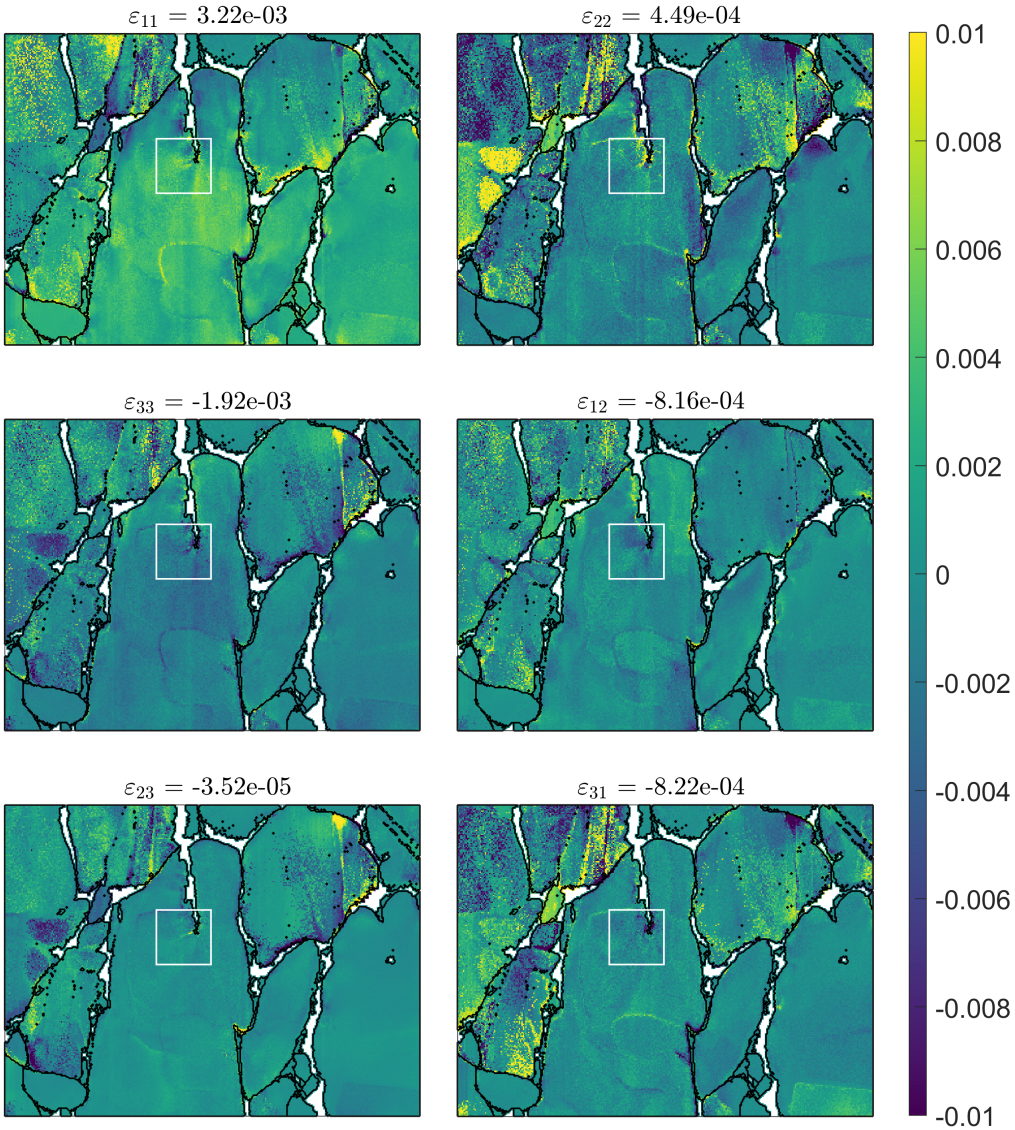
Finally, the ε_{33} component becomes increasingly negative, evolving from 1.15×10^{-4} to 5.31×10^{-3}, indicating enhanced out-of-plane contraction. This is a response for elastic compatibility requirements, whereby increasing in-plane tensile stresses in both the X and Y directions drive compressive strain in the out-of-plane direction.

The corresponding GND density maps at each bending angle are shown in Figure 5.18. Within the ROI, the GND density grew from 1.96×10^{12} to 4.19×10^{12} m with increasing bending angle, reflecting intensified lattice curvature associated with plasticity ahead of the crack tip. Distinct sub-cell features with elevated GND density emerge, particularly at the maximum bending angle. These features appear directly ahead of and parallel to the fatigue crack, suggesting features that may serve as precursors for subsequent crack advance by marking zones of concentrated slip or barrier breakdown. Figures 5.19 displays the GND

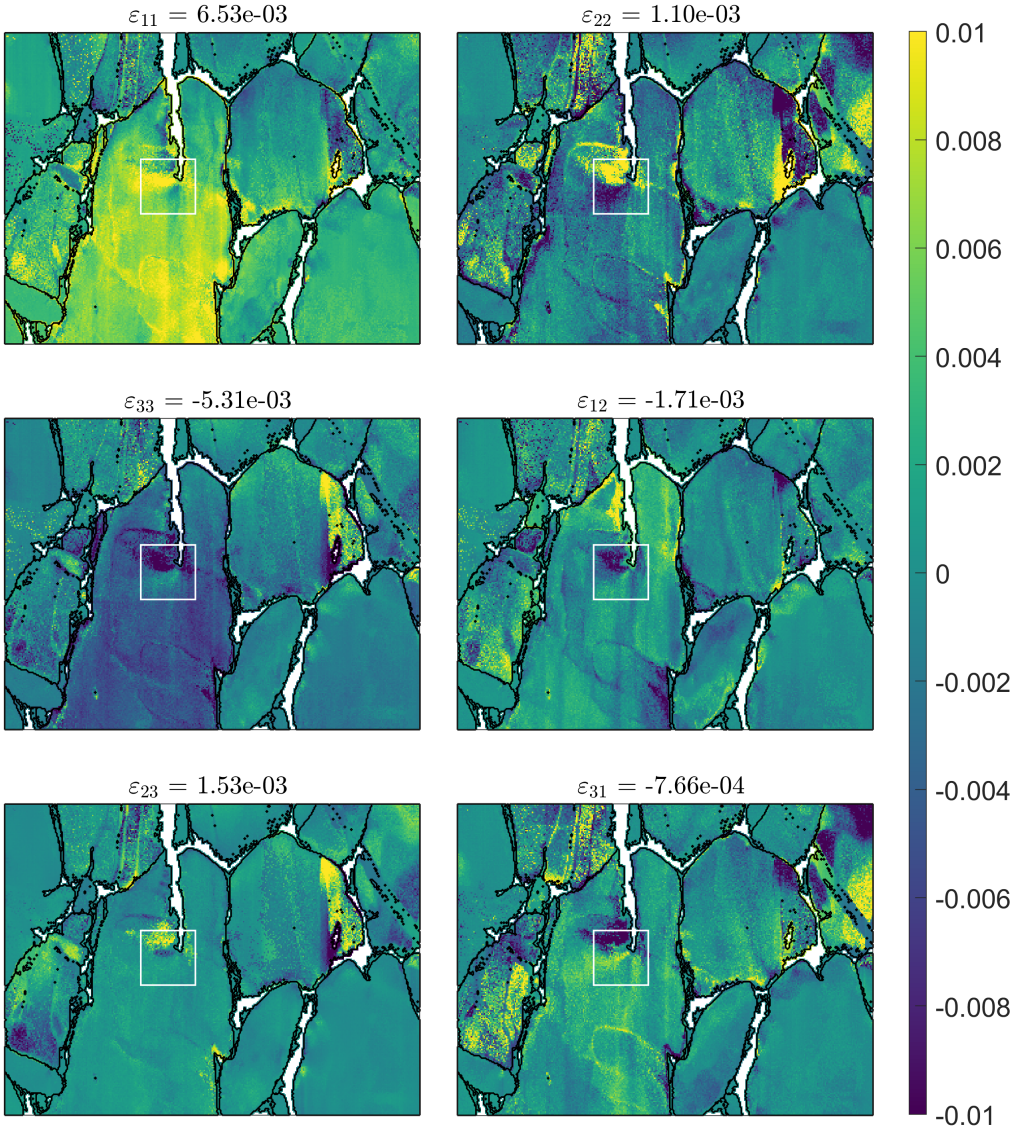
density maps that were calculated using the standard method using a single reference pattern for each grain. The reference patterns were chosen using a combination of high IQ, distance from grain boundaries and the nearest orientation to the mean orientation of the grain. The location of the reference points for each grains are shown in red circles. In these maps, it appears that the high GND densities are clustered in subcell regions away from the reference pattern locations. The distribution are more discontinued in comparison to the maps weight-averaged maps calculated using multiple reference patterns in Figure 5.18. Comparing 5.18c and 5.19c, we can see that the slip features ahead of the crack tip are not captured using a single reference pattern.


ε_{11} = -4.87e-04
ε_{22} = 3.80e-04
5 µm
ε_{33} = 1.15e-04
ε_{12} = 1.38e-04
ε_{23} = 1.12e-03
ε_{31} = -1.04e-03
0.01
0.008
0.006
0.004
0.002
0
-0.002
-0.004
-0.006
-0.008
-0.01

(a)

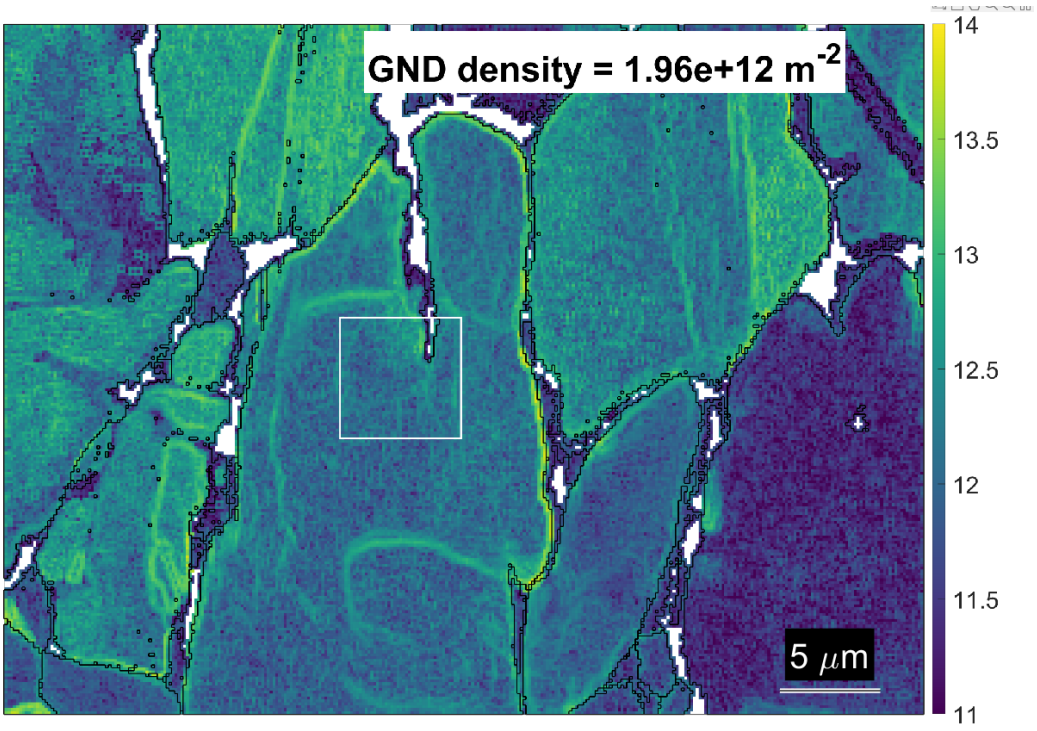

ε_{11} = 3.22e-03
ε_{22} = 4.49e-04
ε_{33} = -1.92e-03
ε_{12} = -8.16e-04
ε_{23} = -3.52e-05
ε_{31} = -8.22e-04
0.01
0.008
0.006
0.004
0.002
0
-0.002
-0.004
-0.006
-0.008
-0.01

(b)

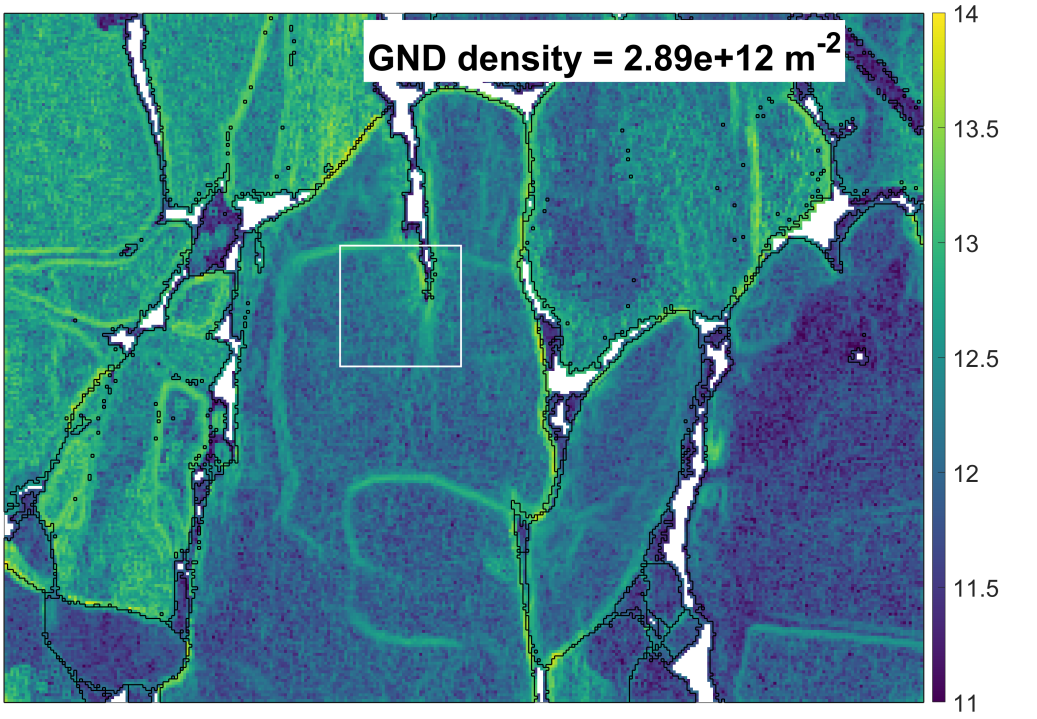


(c)

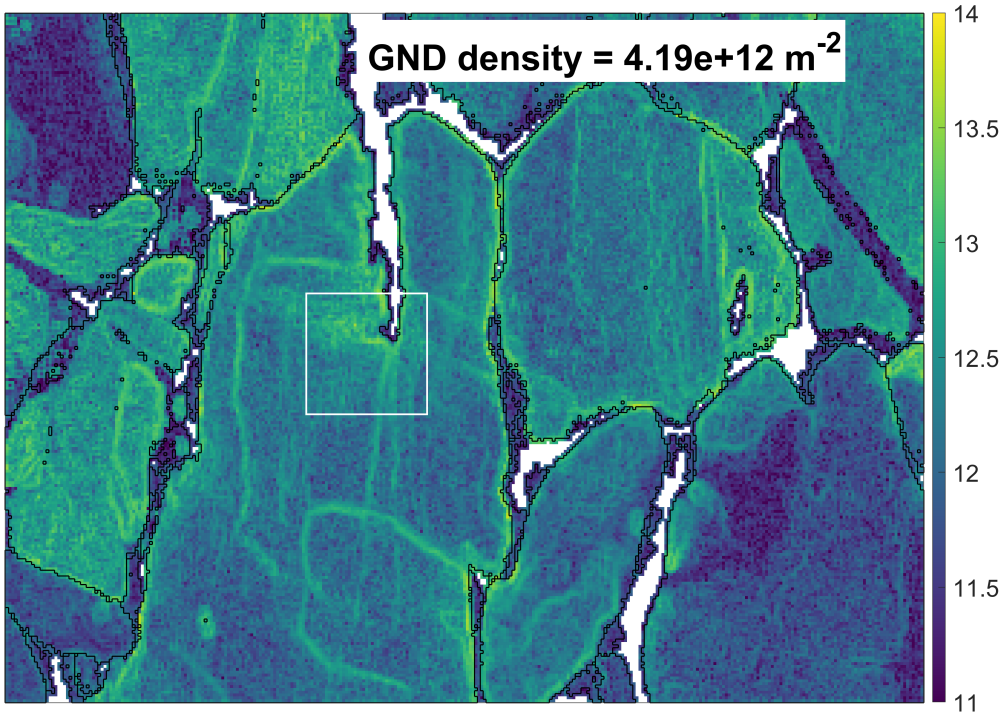
Fig. 5.17 The individual components of the elastic strain tensor at different bending angles (a) undeflected (b) 2.9 degrees (c) 5.1 degrees


GND density = 1.96e+12 m-2
5 μm
14
13.5
13
12.5
12
11.5
11

(a)

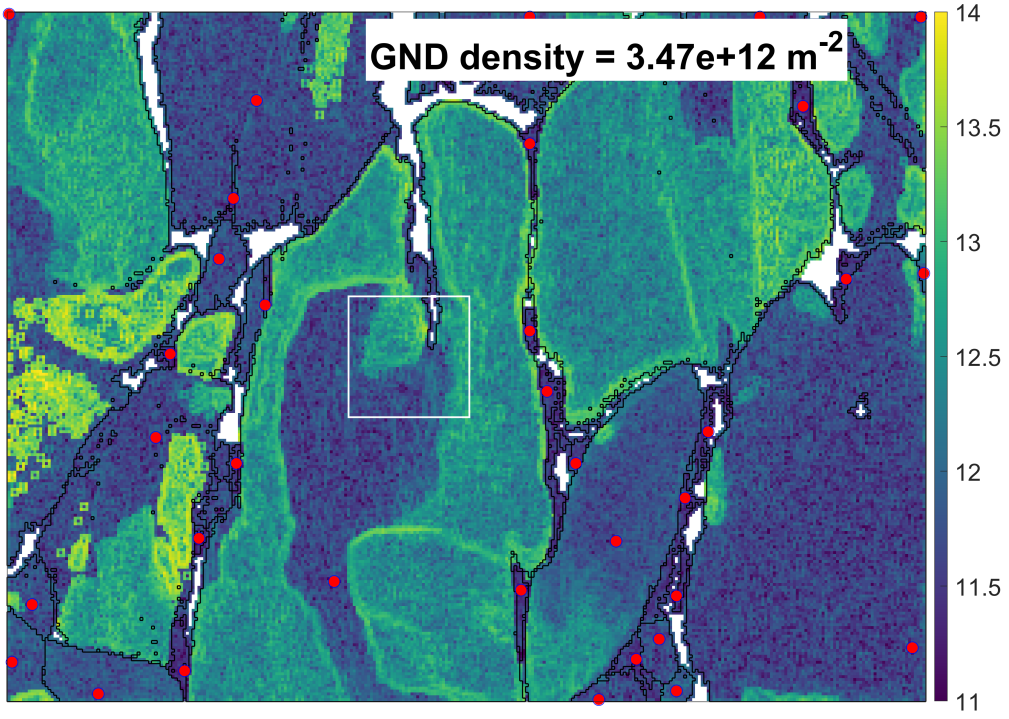

GND density = 2.89e+12 m-2
14
13.5
13
12.5
12
11.5
11

(b)

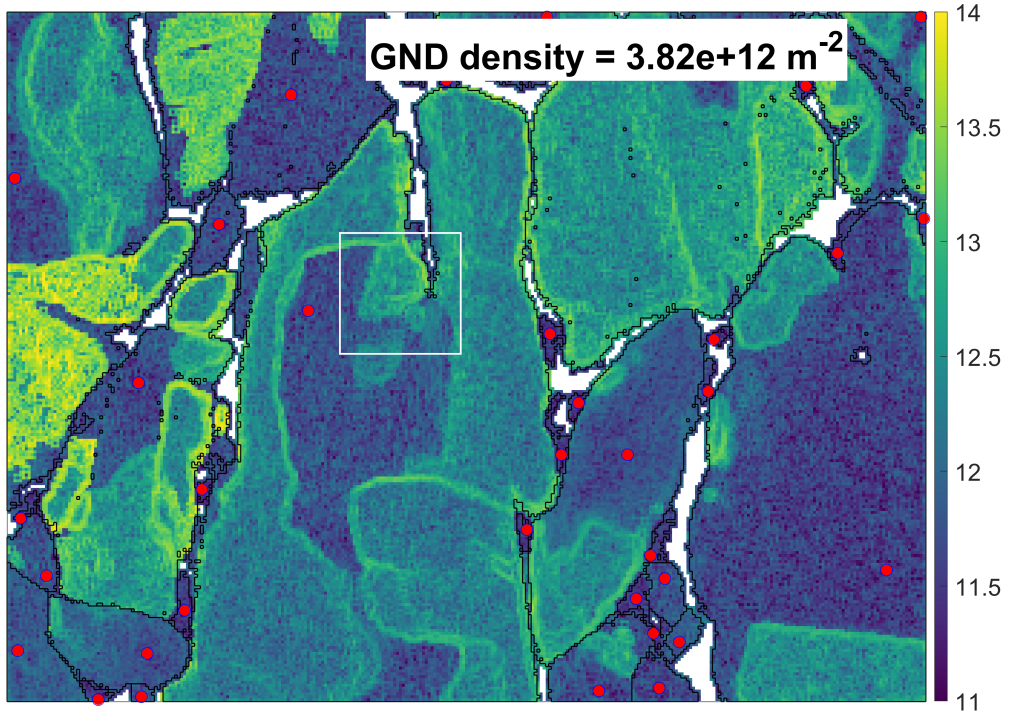


(c)

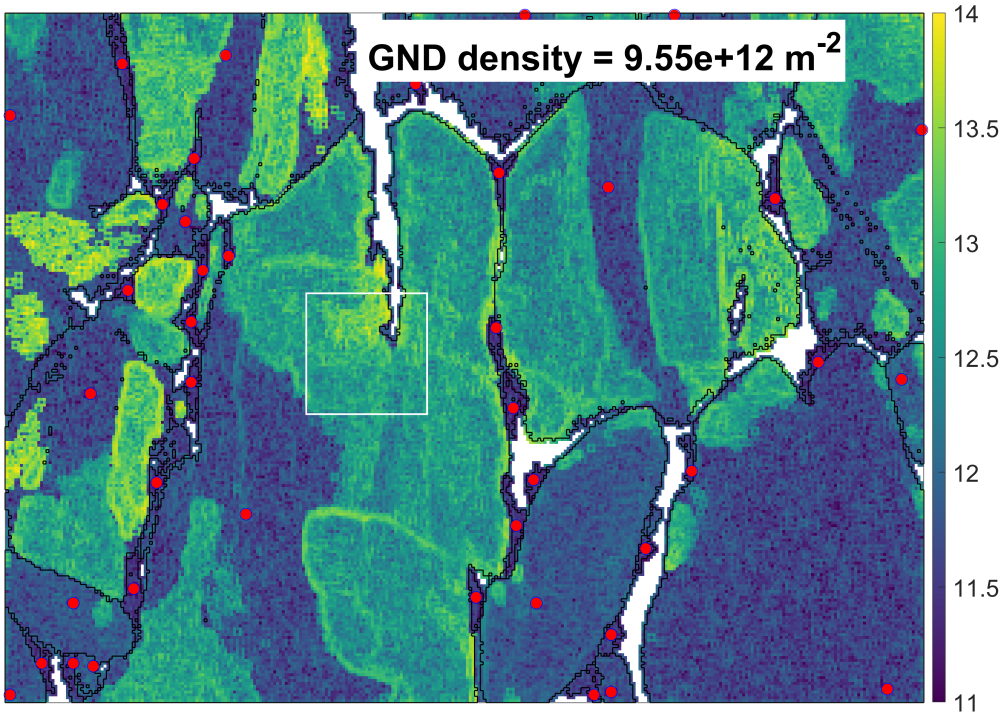
Fig. 5.18 The GND density maps subjected to different bending angles (a) undeflected (b) 2.9 degrees (c) 5.1 degrees


GND density = 3.47e+12 m-2
14
13.5
13
12.5
12
11.5
11

(a)


GND density = 3.82e+12 m-2
14
13.5
13
12.5
12
11.5
11

(b)



(c)

Fig. 5.19 The GND density maps calculated using a single reference pattern (chosen by a combination of high IQ, furthest distance to grain boundaries and nearest orientation to the mean orientation of the grain) and subjected to different bending angles (a) undeflected (b) 2.9 degrees (c) 5.1 degrees

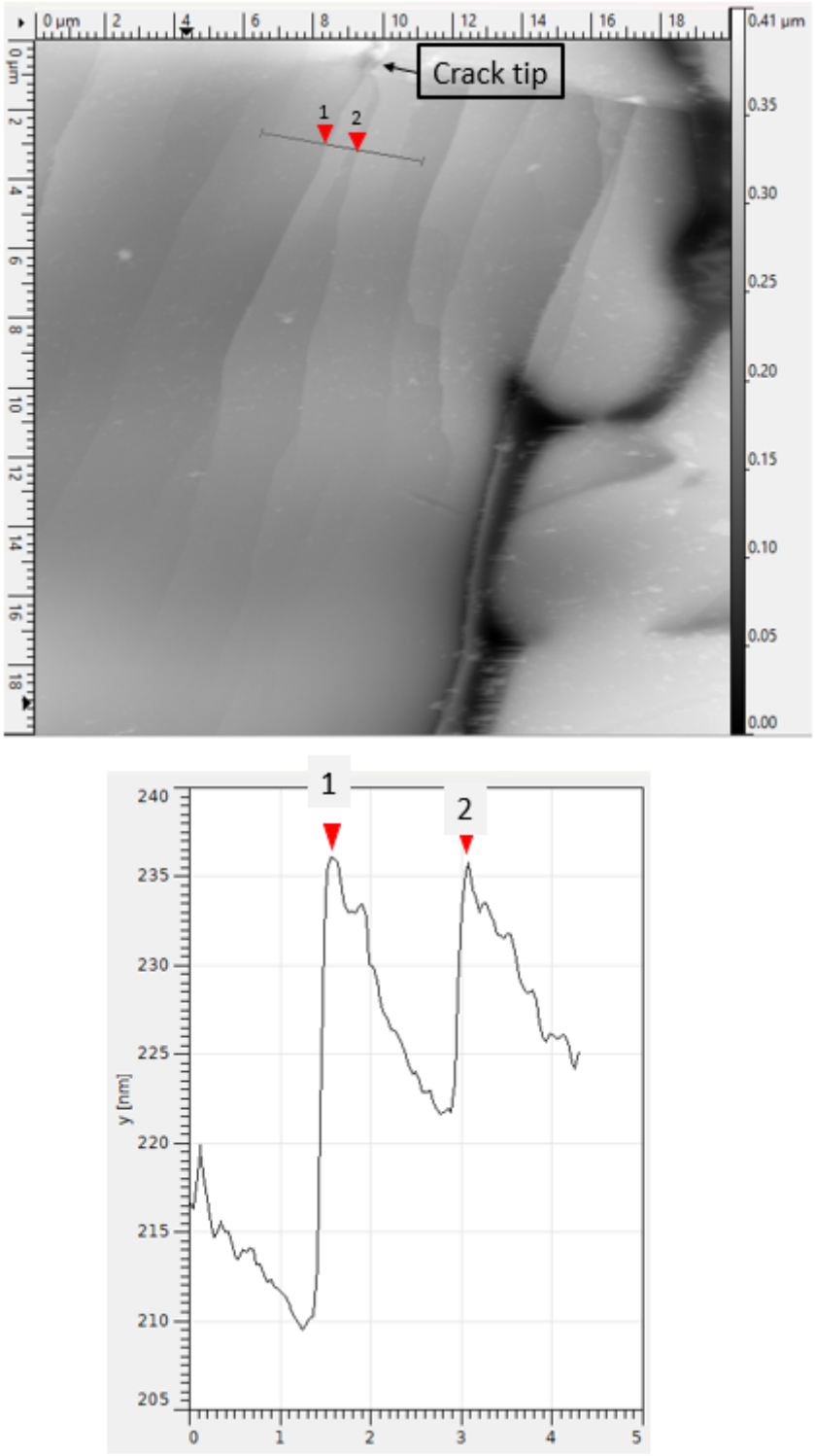


Fig. 5.20 AFM topography ahead of the fatigue crack tip

Additional characterisation using atomic force microscopy (AFM), shown in Figure 5.20, confirmed the presence of prominent slip features ahead of the fatigue crack tip that are also visible in Figure 5.18c. Two extrusions were measured in the line plot with a depth of 25 and 13 nm. With a magnitude of an $\langle a \rangle$ type Burgers vector of 0.295 nm, these depths are approximately 85 and 44 units of $\langle a \rangle$ Burgers vectors, respectively. If we only consider a five micron by five micron area, the estimated GND density from the slip height measured by AFM is to be 4.6×10^{12} m^{-2}, which are in the similar orders of magnitude with the measured ROIs in Figure 5.18. While the comparison is interesting, it is important to distinguish between the physical interpretations of GND density derived from HR-EBSD and dislocation measurements inferred from AFM. GND analysis based on HR-EBSD quantifies the density of dislocations within the near-surface volume that give rise to lattice curvature, and therefore reflects the subsurface dislocation content required to accommodate orientation gradients. In contrast, dislocation density estimated from AFM measurements is inferred from the surface relief or step height, representing the number of dislocations necessary to produce the observed surface displacement. As such, GND density estimates from AFM may include contributions from dislocations that have left the sample surface and are no longer present within the near-surface volume probed by HR-EBSD.

5.5 Summary

This chapter has demonstrated the pronounced and unexpected sensitivity of lattice rotation gradient calculations to the choice of reference pattern, as illustrated in Figure 5.6. Variations in reference selection were shown to introduce non-uniform offsets in the measured rotation fields, which affected the calculation of GND densities. To address this limitation, a multi-reference pattern approach was proposed, in which several reference patterns are selected within each grain of a polycrystalline EBSD map. By combining the resulting measurements through IQ-weighted averaging, the influence of any single reference pattern is reduced. The

resulting GND density maps exhibit improved spatial continuity relative to those obtained using the standard single-reference implementation in xEBSD, while still preserving and enhancing physically slip-related features that are otherwise obscured. The same features are visible in an AFM topographical map. These findings demonstrate that the use of multiple reference patterns provides a practical and pragmatic option in the HR-EBSD analysis.

Additionally, the specimen was characterised at three bending angles (0, 2.9, and 5.1 degrees) to examine the evolution of elastic strain and GND density ahead of a fatigue crack tip over approximately one quarter of a fatigue cycle. The challenge associated with reference pattern selection in HR-EBSD was addressed by combining the relative elastic strains with the absolute strain levels obtained from CP-FEA. This combined approach enables a more meaningful comparison across different loading conditions.

As expected, the largest elastic strain magnitudes were observed in the ε_{11} component. In the undeflected state, this component revealed a compressive strain field near the crack tip, oriented towards the basal plane. With increasing applied load, the strain state evolved to exhibit progressively larger tensile strains in the in-plane directions, accompanied by a corresponding compressive response in the out-of-plane direction.

The GND density maps across the loading sequence similarly indicate an increase in dislocation density ahead of the crack tip with increasing bending angle. The most pronounced change occurs at the maximum bending angle of 5.1 degrees, where new GND-rich features emerge ahead of the crack tip. These features roughly aligns with prismatic slip traces and extend over significant distances, penetrating through pre-existing sub-cell structures that were also seen in an undeflected state. Additional GND features are also observed at maximum load, broadly aligned with the basal plane and oriented perpendicular to the crack, highlighting the activation of multiple slip systems during crack-tip deformation.

Chapter 6

The conclusions of this work

This thesis has investigated the behaviour of microstructure-sensitive fatigue crack initiation and short crack growth in Ti-6Al-4V through the development and application of a novel ultrasonic fatigue testing method, combined with advanced EBSD characterisation techniques.

The first part of this work established the reliability and broader applicability of ultrasonic bending fatigue testing for Ti-6Al-4V, while also identifying factors that strongly influence fatigue performance. The effect of laser machining-induced redeposit layers was shown to be moderate, particularly in the HCF and VHCF regimes. Removal of these layers through electropolishing resulted in pronounced increases in fatigue strength from approximately 50 MPa at 10^7 cycles to 200 MPa at 10^9 cycles. This highlights the importance of surface condition in ultrasonic fatigue testing and providing practical guidance for specimen preparation.

A comparison between ultrasonic fatigue data and conventional low frequency fatigue data from the literature demonstrated a clear frequency dependence of fatigue strength. At 10^7 cycles, ultrasonic fatigue tests exhibited fatigue strengths approximately 200 MPa higher than tests conducted at 5 Hz, with the magnitude of this difference decreasing progressively as testing frequency increased. This trend indicates that the strain rate sensitivity of Ti-6Al-4V is most pronounced at lower frequencies and becomes less significant as the loading frequency increases.

Further comparison with previously published uniaxial ultrasonic fatigue data showed good agreement in the LCF and HCF regimes, while deviations in the VHCF regime were primarily attributed to the fundamental mechanistic differences between cyclic bending and cyclic uniaxial loading. These findings reinforce the necessity of considering loading mode when interpreting VHCF data and comparing datasets obtained using different test geometries.

Environmental effects were shown to play a significant role, as expected. Fatigue testing conducted in high vacuum (10^{-6} mbar) consistently produced higher fatigue strengths than tests performed in ambient air, with increases of approximately 150 MPa in LCF and 100 MPa in VHCF. Crack propagation rates were also markedly reduced in vacuum, with growth rates predominantly between 10^{-8} and 10^{-7}mm/cycle compared with 10^{-6} to 10^{-4} mm/cycle in air. Fractography and STEM-EDS characterisation provided compelling evidence that oxygen adsorption and environmental embrittlement significantly degrade fatigue performance in air. In contrast to the brittle, facet-dominated fracture surfaces observed in air, vacuum-tested specimens exhibited more ductile features, including dimples associated with microvoid coalescence, reflecting delayed onset of crack initiation and enhanced plasticity.

The second contribution of this thesis lies in elucidating the microstructural mechanisms governing fatigue crack initiation and short crack growth. At these small length scales, fatigue behaviour was shown to be highly crystallographic, necessitating detailed evaluation of grain orientation, local texture, and slip transfer behaviour.

All observed fatigue crack initiation events occurred on near-basal planes, with initiation orientations spanning a wide range of basal-dominant configurations (approximately 15° to 65° relative to the loading direction) when analysed using a normalised Schmid factor. While no direct correlation was found between bulk specimen texture and fatigue strength, a relationship emerged when attention was restricted to the local texture of FCI and ‘hotspot’ grains. Clustering of FCI grains within regions of moderately high Schmid factor was associated with reduced fatigue strength in the VHCF regime, whereas the highest fatigue

strength was observed in specimens where crack initiation occurred in regions characterised by both low basal Schmid factor and a very low Luster-Morris slip transfer parameter. These findings demonstrate that local microtexture plays a larger role than global texture in governing susceptibility to fatigue crack initiation.

The interrupted fatigue methodology developed in this work enabled characterisation of microstructure-sensitive crack propagation behaviour. Transient reductions in crack growth rate were linked to slip system transitions (e.g. basal to prismatic) and to pronounced crack-path deflections across grain boundaries. Samples exhibiting strong local texture clustering around the FCI site (IFS10 and IFS25) showed the highest fatigue crack propagation rates, while samples lacking such microtexture connectivity exhibited slower growth. In contrast, grain size alone showed no systematic correlation with fatigue stress, indicating that grain size is not the dominant controlling parameter under the present testing conditions. Instead, fatigue performance was governed by the combined effects of grain orientation, local texture clustering, and slip transfer compatibility.

The final part of this thesis addressed methodological challenges associated with HR-EBSD analysis, particularly the unexpected sensitivity of lattice rotation gradients and GND density calculations to the choice of reference pattern. This sensitivity was shown to introduce non-uniform offsets that directly affect GND estimates. To overcome this limitation, a multi-reference pattern approach was developed, in which several reference patterns were selected within each grain and combined using image-quality-weighted averaging. This approach produced GND density maps with improved spatial continuity while retaining physically meaningful slip-related features, many of which were corroborated by AFM topographical measurements. The method therefore represents a practical and robust improvement over conventional single-reference HR-EBSD analyses.

This proposed reference pattern selection method was then applied to investigate crack tip strains and GND density evolution during interrupted fatigue loading. By combining relative

HR-EBSD strain measurements with absolute strain levels obtained from crystal plasticity finite element analysis (CP-FEA), it was possible to examine strain and GND evolution across three bending angles (0°, 2.9°, and 5.1°), corresponding to approximately one quarter of a fatigue cycle. The largest elastic strains were observed in the ε_{11} component, evolving from a compressive residual field in the unprobed state to increasing tensile strain with applied load, accompanied by out-of-plane compression. GND density increased systematically with bending angle, with the most pronounced changes occurring at maximum load. Newly formed GND-rich features aligned with prismatic slip traces emerged ahead of the crack tip and penetrated existing sub-cell structures, while additional features aligned with the basal plane indicated activation of multiple slip systems during crack-tip deformation.

References

[1] James C. Williams and Rodney R. Boyer. Opportunities and issues in the application of titanium alloys for aerospace components, 2020.

[2] I. J. Polmear. *6 - Titanium alloys*, pages 299–365. Butterworth-Heinemann, Oxford, 2005.

[3] L. P. Jahnke. *TITANIUM IN JET ENGINES*, pages 1099–1115. Pergamon, 1970.

[4] Peter Merlin. *Design and Development of the Blackbird: Challenges and Lessons Learned*.

[5] Gerd Lütjering and J.C WIlliams. *Titanium*. Springer Berlin, Heidelberg, 2007.

[6] M. H. Yoo. Slip, twinning, and fracture in hexagonal close-packed metals. *Metallurgical Transactions A*, 12(3):409–418, 1981.

[7] J. C. Williams, R. G. Baggerly, and N. E. Paton. Deformation behavior of hcp ti-al alloy single crystals. *Metallurgical and Materials Transactions A*, 33(3):837–850, 2002.

[8] T. B. Britton, F. P. E. Dunne, and A. J. Wilkinson. On the mechanistic basis of deformation at the microscale in hexagonal close-packed metals. *Proceedings of the Royal Society A: Mathematical, Physical and Engineering Sciences*, 471(2178), 2015.

[9] R. Pederson. *Microstructure and phase transformation of Ti-6Al-4V*. Thesis, 2002.

[10] K. Maruyama, N. Yamada, and H. Sato. Effects of lamellar spacing on mechanical properties of fully lamellar ti–39.4mol*Materials Science and Engineering: A*, 319-321:360–363, 2001.

[11] Gerd Lütjering. Influence of processing on microstructure and mechanical properties of alpha + beta titanium alloys. *Materials Science and Engineering*, 1998.

[12] S. Suresh. *Fatigue of Materials*. Cambridge University Press, Cambridge, 2 edition, 1998.

[13] L. Tóth and S. Ya Yarema. Formation of the science of fatigue of metals. part 1. 1825–1870. *Materials Science*, 42(5):673–680, 2006.

[14] Yukitaka Murakami, Toshio Takagi, Kentaro Wada, and Hisao Matsunaga. Essential structure of s-n curve: Prediction of fatigue life and fatigue limit of defective materials and nature of scatter. *International Journal of Fatigue*, 146, 2021.

[15] Haël Mughrabi and Stephen D. Antolovich. A tribute to claude bathias – highlights of his pioneering work in gigacycle fatigue. *International Journal of Fatigue*, 93:217–223, 2016.

[16] Bathias. There is no infinite fatigue life in metallic materials. *Fatigue Fracture of Engineering Materials Structures*, 22(7):559–565, 1999.

[17] E. Bayraktar, I. Garcias, and C. Bathias. Failure mechanisms of automotive metallic alloys in very high cycle fatigue range. *International Journal of Fatigue*, 28(11):1590–1602, 2006.

[18] G. Chai and N. Zhou. Study of crack initiation or damage in very high cycle fatigue using ultrasonic fatigue test and microstructure analysis. *Ultrasonics*, 53(8):1406–11, 2013. Chai, Guocai Zhou, Nian eng Netherlands 2013/07/16 Ultrasonics. 2013 Dec;53(8):1406-11. doi: 10.1016/j.ultras.2013.05.008. Epub 2013 May 30.

[19] Q. Y. Wang, J. Y. Berard, S. Rathery, and C. Bathias. Technical note high-cycle fatigue crack initiation and propagation behaviour of high-strength sprin steel wires. *Fatigue Fracture of Engineering Materials Structures*, 22(8):673–677, 1999.

[20] A. Atrens, W. Hoffelner, T. W. Duerig, and J. E. Allison. Subsurface crack initiation in high cycle fatigue in ti6a14v and in a typical martensitic stainless steel. *Scripta Metallurgica*, 17(5):601–606, 1983.

[21] Mughrabi. On the life-controlling microstructural fatigue mechanisms in ductile metals and alloys in the gigacycle regime. *Fatigue Fracture of Engineering Materials Structures*, 22(7):633–641, 1999.

[22] Ashutosh Sharma, Min Chul Oh, and Byungmin Ahn. Recent advances in very high cycle fatigue behavior of metals and alloys—a review. *Metals*, 10(9):1200, 2020.

[23] Hael Mughrabi. Specific features and mechanisms of fatigue in the ultrahigh-cycle regime. *International Journal of Fatigue*, 28(11):1501–1508, 2006.

[24] C. Bathias. *Relation Between Endurance Limits and Thresholds in the Field of Gigacycle Fatigue*, pages 135–154. ASTM International, 100 Barr Harbor Drive, PO Box C700, West Conshohocken, PA 19428-2959, 2000. 1998-11-04 - 1998-11-05 Fatigue Crack Growth Thresholds, Endurance Limits, and Design Norfolk, Virginia.

[25] Nishijima and Kanazawa. Stepwise s-n curve and fish-eye failure in gigacycle fatigue. *Fatigue Fracture of Engineering Materials Structures*, 22(7):601–607, 1999.

[26] Daniel Spriestersbach, Patrick Grad, and Eberhard Kerscher. Crack initiation mechanisms and threshold values of very high cycle fatigue failure of high strength steels. *Procedia Engineering*, 74:84–91, 2014.

[27] V Kazymyrovych. Very high cycle fatigue of engineering materials. Report, Karlstads Universitet, 2009.

[28] Y. Murakami, T. Nomoto, T. Ueda, and Y. Murakami. On the mechanism of fatigue failure in the superlong life regime (n>107 cycles). part 1: influence of hydrogen trapped by inclusions. *Fatigue Fracture of Engineering Materials Structures*, 23(11):893–902, 2000.

[29] Claude Bathias and P. C. Paris. *Gigacycle fatigue in mechanical practice*. Marcel Dekker, New York, 2005. (Paul Croce).

[30] J. A. Hall. Fatigue crack initiation in alpha-beta titanium alloys. *International Journal of Fatigue*, 19(93):23–37, 1997.

[31] Harold Margolin. Fracture toughness: A rationalization of the role of microstructure in an - titanium alloy. *Metallurgical Transactions A*, 13(12):2191–2195, 1982.

[32] C. J. Szczepanski, S. K. Jha, J. M. Larsen, and J. W. Jones. Microstructural influences on very-high-cycle fatigue-crack initiation in ti-6246. *Metallurgical and Materials Transactions A*, 39(12):2841–2851, 2008.

[33] Xiaolong Liu, Chengqi Sun, and Youshi Hong. Effects of stress ratio on high-cycle and very-high-cycle fatigue behavior of a ti–6al–4v alloy. *Materials Science and Engineering: A*, 622:228–235, 2015.

[34] Zhi Yong Huang, Han Qing Liu, Hao Min Wang, Danièle Wagner, Muhammad Kashif Khan, and Qing Yuan Wang. Effect of stress ratio on vhcf behavior for a compressor blade titanium alloy. *International Journal of Fatigue*, 93:232–237, 2016.

[35] Xiaolong Liu, Erqing Chen, Fan Zeng, Tao Cong, and Joseph P. Domblesky. Mechanisms of interior crack initiation in very-high-cycle fatigue of high-strength alloys. *Engineering Fracture Mechanics*, 212:153–163, 2019.

[36] Stefan Heinz, Frank Balle, Guntram Wagner, and Dietmar Eifler. Analysis of fatigue properties and failure mechanisms of ti6al4v in the very high cycle fatigue regime using ultrasonic technology and 3d laser scanning vibrometry. *Ultrasonics*, 53(8):1433–1440, 2013.

[37] S. Heinz and D. Eifler. Crack initiation mechanisms of ti6al4v in the very high cycle fatigue regime. *International Journal of Fatigue*, 93:301–308, 2016.

[38] J Everaerts, B Verlinden, and M Wevers. The influence of the alpha grain size on the internal fatigue crack initiation in drawn ti-6al-4v wires. *21st European Conference on Fracture, ECF21*, 2016.

[39] Yoshiyuki Furuya and Etsuo Takeuchi. Gigacycle fatigue properties of ti–6al–4v alloy under tensile mean stress. *Materials Science and Engineering: A*, 598:135–140, 2014.

[40] Ioannis Bantounas, David Dye, and Trevor C. Lindley. The role of microtexture on the faceted fracture morphology in ti–6al–4v subjected to high-cycle fatigue. *Acta Materialia*, 58(11):3908–3918, 2010.

[41] R. O. Ritchie and J. Lankford. Small fatigue cracks: A statement of the problem and potential solutions. *Materials Science and Engineering*, 84:11–16, 1986.

[42] S. Suresh. Crack deflection: Implications for the growth of long and short fatigue cracks. *Metallurgical Transactions A*, 14(11):2375–2385, 1983.

[43] K. Tokaji, T. Ogawa, and K. Ohya. The effect of grain size on small fatigue crack growth in pure titanium. *International Journal of Fatigue*, 16(8):571–578, 1994.

[44] D. Davidson, K. Chan, R. McClung, and S. Hudak. *4.05 - Small Fatigue Cracks*, pages 129–164. Pergamon, Oxford, 2003.

[45] R. Pippan and A. Hohenwarter. Fatigue crack closure: a review of the physical phenomena. *Fatigue and Fracture of Engineering Materials and Structures*, 40(4):471–495, 2017. Export Date: 04 November 2025; Cited By: 321.

[46] V. Sinha, C. Mercer, and W. O. Soboyejo. An investigation of short and long fatigue crack growth behavior of ti–6al–4v. *Materials Science and Engineering: A*, 287(1):30–42, 2000.

[47] Stefanie Stanzl-Tschegg. Very high cycle fatigue measuring techniques. *International Journal of Fatigue*, 60:2–17, 2014.

[48] H. Mayer. Recent developments in ultrasonic fatigue. *Fatigue Fracture of Engineering Materials Structures*, 39(1):3–29, 2016.

[49] Choongdo Lee. Effect of strain rate on fatigue property of a356 aluminium casting alloys containing pre-existing micro-voids. *International Journal of Fatigue*, 131:105368, 2020.

[50] J. D. Campbell and W. G. Ferguson. The temperature and strain-rate dependence of the shear strength of mild steel. *The Philosophical Magazine: A Journal of Theoretical Experimental and Applied Physics*, 21(169):63–82, 1970. doi: 10.1080/14786437008238397.

[51] Ruslan Kuliiev, Stefan Riekehr, Volker Ventzke, Sören Keller, and Nikolai Kashaev. On the effect of testing frequency on high and very high cycle fatigue behavior of aa2024-t3, ti-6al-4v, and inconel 718. *Journal of Materials Engineering and Performance*, 32(23):10843–10856, 2023.

[52] R. J. Morrissey, D. L. McDowell, and T. Nicholas. Frequency and stress ratio effects in high cycle fatigue of ti-6al-4v. *International Journal of Fatigue*, 21(7):679–685, 1999.

[53] Dino A. Celli, Onome Scott-Emuakpor, Justin Warner, and Tommy George. Investigation of self-heating during ultrasonic fatigue testing and effect on very high cycle fatigue behavior of titanium 6al-4v. *Journal of Engineering for Gas Turbines and Power*, 145(3), 2022.

[54] Hamza Elhadri, Johann Petit, Naila Hfaiedh, Danièle Wagner, and Olivier Polit. Comparison of self-heating behavior between continuous and interrupted control modes. *Fatigue Fracture of Engineering Materials Structures*, 48(10):4517–4527, 2025.

[55] Claude Bathias. Piezoelectric fatigue testing machines and devices. *International Journal of Fatigue*, 28(11):1438–1445, 2006.

[56] HR Mayer, H Lipowsky, M Papkyriacou, R Rosch, A Stich, and S Stanzl-Tschegg. Application of ultrasound for fatigue testing of lightweight alloys. *Fatigue Fracture of Engineering Materials Structures*, 22, 1999.

[57] T. Straub, M. F. Berwind, T. Kennerknecht, Y. Lapusta, and C. Eberl. Small-scale multiaxial setup for damage detection into the very high cycle fatigue regime. *Experimental Mechanics*, 55(7):1285–1299, 2015.

[58] S. Nishikawa and S. Kikuchi. Diffraction of cathode rays by mica. *Nature*, 121(3061):1019–1020, 1928.

[59] O Engler and V Randle. *Introduction to Texture Analysis: Macrotexture, Microtexture, and Orientation Mapping, Second Edition*. 2009.

[60] A. J. Wilkinson and D. J. Dingley. Quantitative deformation studies using electron back scatter patterns. *Acta Metallurgica et Materialia*, 39(12):3047–3055, 1991.

[61] J. F. Nye. Some geometrical relations in dislocated crystals. *Acta Metallurgica*, 1(2):153–162, 1953.

[62] I. Brough, P. S. Bate, and F. J. Humphreys. Optimising the angular resolution of ebsd. *Materials Science and Technology*, 22(11):1279–1286, 2006.

[63] F. J. Humphreys and I. Brough. High resolution electron backscatter diffraction with a field emission gun scanning electron microscope. *J Microsc*, 195(Pt 1):6–9, 1999. Humphreys, F J Brough, I Journal Article Research Support, Non-U.S. Gov't England 1999/08/12 J Microsc. 1999 Jul;195(Pt 1):6-9.

[64] F. J. Humphreys. Characterisation of fine-scale microstructures by electron backscatter diffraction (ebsd). *Scripta Materialia*, 51(8):771–776, 2004.

[65] Angus J. Wilkinson. Measurement of elastic strains and small lattice rotations using electron back scatter diffraction. *Ultramicroscopy*, 62(4):237–247, 1996.

[66] Angus J. Wilkinson, David J. Dingley, and Graham Meaden. *Strain Mapping Using Electron Backscatter Diffraction*, pages 231–249. Springer US, Boston, MA, 2009.

[67] Angus J. Wilkinson, Graham Meaden, and David J. Dingley. High-resolution elastic strain measurement from electron backscatter diffraction patterns: New levels of sensitivity. *Ultramicroscopy*, 106(4):307–313, 2006.

[68] Tomohito Tanaka and Angus J. Wilkinson. Pattern matching analysis of electron backscatter diffraction patterns for pattern centre, crystal orientation and absolute elastic strain determination – accuracy and precision assessment. *Ultramicroscopy*, 202:87–99, 2019.

[69] Angus J. Wilkinson and David Randman. Determination of elastic strain fields and geometrically necessary dislocation distributions near nanoindents using electron back scatter diffraction. *Philosophical Magazine*, 90(9):1159–1177, 2010. doi: 10.1080/14786430903304145.

[70] T. B. Britton, H. Liang, F. P. E. Dunne, and A. J. Wilkinson. The effect of crystal orientation on the indentation response of commercially pure titanium: experiments and simulations. *Proceedings of the Royal Society A: Mathematical, Physical and Engineering Sciences*, 466(2115):695–719, 2010.

[71] T. Ben Britton, Soran Birosca, Michael Preuss, and Angus J. Wilkinson. Electron backscatter diffraction study of dislocation content of a macrozone in hot-rolled ti–6al–4v alloy. *Scripta Materialia*, 62(9):639–642, 2010.

[72] Angus J. Wilkinson, Graham Meaden, and David J. Dingley. Mapping strains at the nanoscale using electron back scatter diffraction. *Superlattices and Microstructures*, 45(4):285–294, 2009.

[73] A. Arsenlis and D. M. Parks. Crystallographic aspects of geometrically-necessary and statistically-stored dislocation density. *Acta Materialia*, 47(5):1597–1611, 1999.

[74] W. J. Dixon and A. M. Mood. A method for obtaining and analyzing sensitivity data. *Journal of the American Statistical Association*, 43(241):109–126, 1948. Export Date: 23 July 2025; Cited By: 1035.

[75] Sheng-Kuei Lin, Yung-Li Lee, and Ming-Wei Lu. Evaluation of the staircase and the accelerated test methods for fatigue limit distributions. *International Journal of Fatigue*, 23(1):75–83, 2001.

[76] Milton A. Miner. Cumulative damage in fatigue. *Journal of Applied Mechanics*, 12(3):A159–A164, 1945.

[77] Richard S. Bellows, Sandeep Muju, and Theodore Nicholas. Validation of the step test method for generating haigh diagrams for ti–6al–4v. *International Journal of Fatigue*, 21(7):687–697, 1999.

[78] Max Ahlqvist, Kenneth Weddfelt, Viktor Norman, and Daniel Leidermark. Probabilistic evaluation of the step-stress fatigue testing method considering cumulative damage. *Probabilistic Engineering Mechanics*, 74:103535, 2023.

[79] Muhammad Alsaadawy, Montasser Dewidar, Ahmed Said, Ibrahem Maher, and Taher A. Shehabeldeen. A comprehensive review of studying the influence of laser cutting parameters on surface and kerf quality of metals. *The International Journal of Advanced Manufacturing Technology*, 130(3):1039–1074, 2024.

[80] Laser cutting or metal stamping - which is right for you?

[81] Jonathan Pegues, Michael Roach, R. Scott Williamson, and Nima Shamsaei. Surface roughness effects on the fatigue strength of additively manufactured ti-6al-4v. *International Journal of Fatigue*, 116:543–552, 2018.

[82] S. Bagehorn, J. Wehr, and H. J. Maier. Application of mechanical surface finishing processes for roughness reduction and fatigue improvement of additively manufactured ti-6al-4v parts. *International Journal of Fatigue*, 102:135–142, 2017.

[83] Masanori Nakatani, Hiroshige Masuo, Yuzo Tanaka, and Yukitaka Murakami. Effect of surface roughness on fatigue strength of ti-6al-4v alloy manufactured by additive manufacturing. *Procedia Structural Integrity*, 19:294–301, 2019.

[84] L. M. Weldon, P. E. McHugh, W. Carroll, E. Costello, and C. O'Bradaigh. The influence of passivation and electropolishing on the performance of medical grade stainless steels in static and fatigue loading. *Journal of Materials Science: Materials in Medicine*, 16(2):107–117, 2005.

[85] K. Moussaoui, M. Mousseigne, J. Senatore, and R. Chieragatti. The effect of roughness and residual stresses on fatigue life time of an alloy of titanium. *The International Journal of Advanced Manufacturing Technology*, 78(1):557–563, 2015.

[86] Kamel Moussaoui, Michel Mousseigne, Johanna Senatore, Rémy Chieragatti, and Frédéric Monies. Influence of milling on surface integrity of ti6al4v—study of the metallurgical characteristics: microstructure and microhardness. *The International Journal of Advanced Manufacturing Technology*, 67(5):1477–1489, 2013.

[87] Niloofar Sanaei and Ali Fatemi. Analysis of the effect of surface roughness on fatigue performance of powder bed fusion additive manufactured metals. *Theoretical and Applied Fracture Mechanics*, 108:102638, 2020.

[88] André Reck, André Till Zeuner, and Martina Zimmermann. Fatigue behavior of non-optimized laser-cut medical grade ti-6al-4v-eli sheets and the effects of mechanical post-processing. *Metals*, 9(8):843, 2019.

[89] Yaou Zhang, Qian Zheng, Zeyu Wu, Hualin Liao, Yifan Lu, and Juncheng Lu. Recast layer-induced fatigue degradation in high-speed edm microholes: Experimental characterization. *Materials*, 18(9):1985, 2025.

[90] Todd M. Mower. Degradation of titanium 6al–4v fatigue strength due to electrical discharge machining. *International Journal of Fatigue*, 64:84–96, 2014.

[91] A. Pramanik and A. K. Basak. Effect of wire electric discharge machining (edm) parameters on fatigue life of ti-6al-4v alloy. *International Journal of Fatigue*, 128:105186, 2019.

[92] E. Takeuchi, Y. Furuya, N. Nagashima, and S. Matsuoka. The effect of frequency on the giga-cycle fatigue properties of a ti–6al–4v alloy. *Fatigue Fracture of Engineering Materials Structures*, 31(7):599–605, 2008.

[93] F. Berto, A. Campagnolo, and P. Lazzarin. Fatigue strength of severely notched specimens made of ti–6al–4v under multiaxial loading. *Fatigue Fracture of Engineering Materials Structures*, 38(5):503–517, 2015.

[94] H. Oguma and T. Nakamura. The effect of stress ratios on very high cycle fatigue properties of ti-6al-4v. *Key Engineering Materials*, 261-263:1227–1232, 2004.

[95] Igor Altenberger, Ravi K. Nalla, Yuji Sano, Lothar Wagner, and Robert O. Ritchie. On the effect of deep-rolling and laser-peening on the stress-controlled low- and high-cycle fatigue behavior of ti–6al–4v at elevated temperatures up to 550°c. *International Journal of Fatigue*, 44:292–302, 2012.

[96] Ryan J. Morrissey and Theodore Nicholas. Fatigue strength of ti–6al–4v at very long lives. *International Journal of Fatigue*, 27(10):1608–1612, 2005.

[97] Stan Lynch. Some fractographic contributions to understanding fatigue crack growth. *International Journal of Fatigue*, 104:12–26, 2017.

[98] Mingjie Zhao, Wenjia Gu, and Derek H. Warner. Atomic mechanism of near threshold fatigue crack growth in vacuum. *Nature Communications*, 13(1):812, 2022.

[99] Fumiyoshi Yoshinaka, Takashi Nakamura, and Kazuaki Takaku. Effects of vacuum environment on small fatigue crack propagation in ti–6al–4v. *International Journal of Fatigue*, 91:29–38, 2016.

[100] Louis Hebrard, Jean-Yves Buffiere, Thierry Palin-Luc, Nicolas Ranc, Marta Majkut, Andrew King, and Arnaud Weck. Environment effect on internal fatigue crack propagation studied with in-situ x-ray microtomography. *Materials Science and Engineering: A*, 882:145462, 2023.

[101] A. L. Pilchak, A. Bhattacharjee, A. H. Rosenberger, and J. C. Williams. Low k faceted crack growth in titanium alloys. *International Journal of Fatigue*, 31(5):989–994, 2009.

[102] Adam L. Pilchak. Fatigue crack growth rates in alpha titanium: Faceted vs. striation growth. *Scripta Materialia*, 68(5):277–280, 2013.

[103] M. R. Bache , W. J. Evans, and H. M. Davies. Electron back scattered diffraction (ebsd) analysis of quasi-cleavage and hydrogen induced fractures under cyclic and dwell loading in titanium alloys. *Journal of Materials Science*, 32:3435–3442, 1997.

[104] M. R. Bache. Processing titanium alloys for optimum fatigue performance. *International Journal of Fatigue*, 21:S105–S111, 1999.

[105] R. J. H. Wanhill, R. Galatolo, and C. E. W. Looije. Fractographic and microstructural analysis of fatigue crack growth in a ti-6al-4v fan disc forging. *International Journal of Fatigue*, 11(6):407–416, 1989.

[106] Anniina Kinnunen, Ivan V. Lomakin, Tero Mäkinen, Kim Widell, Juha Koivisto, and Mikko J. Alava. Striation lines in intermittent fatigue crack growth in an al alloy. *Physical Review Materials*, 7(5):053602, 2023. PRMATERIALS.

[107] A. Yuen, S. W. Hopkin, G. R. Leverant, and C. A. Rau. Correlations between fracture surface appearance and fracture mechanics parameters for stage ii fatigue crack propagation in tï-6ai-4v. *Metallurgical transactions*, 5(8):1833–1842, 1974.

[108] Z. N. Ismarrubie and M. Sugano. Environmental effects on fatigue failure micromechanisms in titanium. *Materials Science and Engineering: A*, 386(1):222–233, 2004.

[109] M. Sugano, S. Kanno, and T. Satake. Fatigue behavior of titanium in vacuum. *Acta Metallurgica*, 37(7):1811–1820, 1989.

[110] S. Adachi, L. Wagner, and G. Lütjering. *Influence of Mean Stress on Fatigue Strength of Ti-6A1-4V*, pages 2117–2122. Pergamon, 1986.

[111] M. J. Hordon. Fatigue behavior of aluminum in vacuum. *Acta Metallurgica*, 14(10):1173–1178, 1966.

[112] Takahiro Shiina, Takashi Nakamura, and Hiroyuki Oguma. Effects of high vacuum environment on high cycle fatigue properties of ti-6al-4v alloy. *Abstracts of ATEM : International Conference on Advanced Technology in Experimental Mechanics : Asian Conference on Experimental Mechanics*, 2003.2, 2003.

[113] T. P. Chapman, K. M. Kareh, M. Knop, T. Connolley, P. D. Lee, M. A. Azeem, D. Rugg, T. C. Lindley, and D. Dye. Characterisation of short fatigue cracks in titanium alloy imi 834 using x-ray microtomography. *Acta Materialia*, 99:49–62, 2015.

[114] Z. N. Ismarrubie, H. Yussof, and M. Sugano. Fatigue damage mechanism of titanium in vacuum and in air. *Procedia Engineering*, 41:1559–1565, 2012.

[115] Fumiyoshi Yoshinaka, Gaoge Xue, Nao Fujimura, and Takashi Nakamura. Effect of vacuum pressure on small crack propagation in ti-6al-4v. *International Journal of Fatigue*, 142:105961, 2021.

[116] G. Henaff, K. Marchal, and J. Petit. On fatigue crack propagation enhancement by a gaseous atmosphere: Experimental and theoretical aspects. *Acta Metallurgica et Materialia*, 43(8):2931–2942, 1995.

[117] M. R. Bache, W. J. Evans, and M. McElhone. The effects of environment and internal oxygen on fatigue crack propagation in ti-6al-4v. *Materials Science and Engineering: A*, 234-236:918–922, 1997.

[118] S W Smith and Piascik. The effect of o2, h2o, and n2 on the fatigue crack growth behavior of an alpha + beta titanium alloy at 24 c and 177 c, 2001.

[119] J Everaerts. *Fatigue crack initiation and facet formation in Ti-6Al-4V wires*. Thesis, 2017.

[120] J. Everaerts, B. Verlinden, and M. Wevers. Investigation of fatigue crack initiation facets in ti-6al-4v using focused ion beam milling and electron backscatter diffraction. *J Microsc*, 267(1):57–69, 2017. 1365-2818 Everaerts, J Verlinden, B Wevers, M Journal Article Research Support, Non-U.S. Gov't England 2017/03/16 J Microsc. 2017 Jul;267(1):57-69. doi: 10.1111/jmi.12547. Epub 2017 Mar 15.

[121] Wenyuan Zhang, Qiaonan Shu, Jiangkun Fan, Panpan Fan, Xiangyi Xue, Peng Jiang, Minjie Lai, Bing Tang, Zhiqian Liao, Hongchao Kou, and Jinshan Li. Crystallographic micro-mechanism of faceted crack initiation in near- titanium alloy ti6321 under room-temperature fatigue and dwell fatigue loadings. *Journal of Materials Science Technology*, 205:109–126, 2025.

[122] V. Sinha, M. J. Mills, and J. C. Williams. Crystallography of fracture facets in a near-alpha titanium alloy. *Metallurgical and Materials Transactions A*, 37(6):2015–2026, 2006.

[123] M. Peters, A. Gysler, and G. LÜtjering. Influence of texture on fatigue properties of ti-6al-4v. *Metallurgical Transactions A*, 15(8):1597–1605, 1984.

[124] Ioannis Bantounas, David Dye, and Trevor C. Lindley. The effect of grain orientation on fracture morphology during high-cycle fatigue of ti–6al–4v. *Acta Materialia*, 57(12):3584–3595, 2009.

[125] Shohtaroh Hashimoto, Hidenori Takebe, Kenichi Mori, and Mitsuo Miyahara. Effects of size of micro texture regions on the dwell fatigue properties of ti-6al-4v. *ISIJ International*, 63(10):1774–1785, 2023.

[126] F. Bridier, P. Villechaise, and J. Mendez. Slip and fatigue crack formation processes in an / titanium alloy in relation to crystallographic texture on different scales. *Acta Materialia*, 56(15):3951–3962, 2008.

[127] Conghui Liu, Rhys Thomas, Tianzhu Sun, Jack Donoghue, Xun Zhang, Tim L. Burnett, João Quinta da Fonseca, and Michael Preuss. Multi-dimensional study of the effect of early slip activity on fatigue crack initiation in a near- titanium alloy. *Acta Materialia*, 233:117967, 2022.

[128] K. Zhang, X. Wu, and C. H. J. Davies. Effect of microtexture on short crack propagation in two-phase titanium alloys. *International Journal of Fatigue*, 104:206–220, 2017.

[129] K. Zhang, K. V. Yang, S. Lim, X. Wu, and C. H. J. Davies. Effect of the presence of macrozones on short crack propagation in forged two-phase titanium alloys. *International Journal of Fatigue*, 104:1–11, 2017.

[130] Kishan Habib, Hideaki Nishikawa, Yoshiyuki Furuya, and Satoshi Emura. The role of crystallographic texture and basal plane slip on microstructurally short fatigue crack initiation and propagation in forged billet and rolled bar ti-6al-4v alloy. *Metallurgical and Materials Transactions A*, 52(9):3821–3838, 2021.

[131] J. H. Zuo, Z. G. Wang, and E. H. Han. Effect of microstructure on ultra-high cycle fatigue behavior of ti–6al–4v. *Materials Science and Engineering: A*, 473(1):147–152, 2008.

[132] Thiebaud Richeton, Francis Wagner, Cai Chen, and Laszlo S. Toth. Combined effects of texture and grain size distribution on the tensile behavior of -titanium, 2018.

[133] Yan Chong, Guanyu Deng, Si Gao, Jangho Yi, Akinobu Shibata, and Nobuhiro Tsuji. Yielding nature and hall-petch relationships in ti-6al-4v alloy with fully equiaxed and bimodal microstructures. *Scripta Materialia*, 172:77–82, 2019.

[134] N. C. Krieger Lassen, D. Juul Jensen, and K. Conradsen. Image processing procedures for analysis of electron back scattering patterns. *Scanning Microscopy*, 6, 1992.

[135] J. Jiang, T. B. Britton, and A. J. Wilkinson. Measurement of geometrically necessary dislocation density with high resolution electron backscatter diffraction: Effects of detector binning and step size. *Ultramicroscopy*, 125:1–9, 2013.

[136] Phani S. Karamched and Angus J. Wilkinson. High resolution electron back-scatter diffraction analysis of thermally and mechanically induced strains near carbide inclusions in a superalloy. *Acta Materialia*, 59(1):263–272, 2011.

[137] Abdalrhaman Koko, Thorsten H. Becker, Elsiddig Elmukashfi, Nicola M. Pugno, Angus J. Wilkinson, and T. James Marrow. Hr-ebsd analysis of in situ stable crack growth at the micron scale. *Journal of the Mechanics and Physics of Solids*, 172:105173, 2023.

[138] P. D. Littlewood, T. B. Britton, and A. J. Wilkinson. Geometrically necessary dislocation density distributions in ti–6al–4v deformed in tension. *Acta Materialia*, 59(16):6489–6500, 2011.

[139] P. D. Littlewood and A. J. Wilkinson. Geometrically necessary dislocation density distributions in cyclically deformed ti–6al–4v. *Acta Materialia*, 60(15):5516–5525, 2012.

[140] T. B. Britton and A. J. Wilkinson. High resolution electron backscatter diffraction measurements of elastic strain variations in the presence of larger lattice rotations. *Ultramicroscopy*, 114:82–95, 2012.

[141] W. Pantleon. Resolving the geometrically necessary dislocation content by conventional electron backscattering diffraction. *Scripta Materialia*, 58(11):994–997, 2008.

[142] Josh Kacher, Colin Landon, Brent L. Adams, and David Fullwood. Bragg's law diffraction simulations for electron backscatter diffraction analysis. *Ultramicroscopy*, 109(9):1148–1156, 2009.

[143] David Fullwood, Mark Vaudin, Craig Daniels, Timothy Ruggles, and Stuart I. Wright. Validation of kinematically simulated pattern hr-ebsd for measuring absolute strains and lattice tetragonality. *Materials Characterization*, 107:270–277, 2015.

[144] Abdalrhaman Koko, Elsiddig Elmukashfi, Kalin Dragnevski, Angus J. Wilkinson, and Thomas James Marrow. J-integral analysis of the elastic strain fields of ferrite deformation twins using electron backscatter diffraction. *Acta Materialia*, 218:117203, 2021.

[145] T. B. Britton, C. Maurice, R. Fortunier, J. H. Driver, A. P. Day, G. Meaden, D. J. Dingley, K. Mingard, and A. J. Wilkinson. Factors affecting the accuracy of high resolution electron backscatter diffraction when using simulated patterns. *Ultramicroscopy*, 110(12):1443–1453, 2010.

[146] Angus J. Wilkinson and T. Ben Britton. Strains, planes, and ebsd in materials science. *Materials Today*, 15(9):366–376, 2012.

[147] T. B. Britton and A. J. Wilkinson. Measurement of residual elastic strain and lattice rotations with high resolution electron backscatter diffraction. *Ultramicroscopy*, 111(8):1395–1404, 2011.

[148] Jon Alkorta. Limits of simulation based high resolution ebsd. *Ultramicroscopy*, 131:33–38, 2013.

[149] Eralp Demir, Alvaro Martinez-Pechero, Chris Hardie, and Edmund Tarleton. Oxford-umat: An efficient and versatile crystal plasticity framework. *International Journal of Solids and Structures*, 307:113110, 2025.

Appendix A

Appendix

A.1 MATLAB script for image processing of captured laser streaks

```
function maxdistance = IFS_Max_Distance_function(I, darkset,
   pxmin,laserspotdiameter)

if ndims(I) > 2
    darkened=I-darkset; %change accordingly
    gray = rgb2gray(darkened);
else
    gray = I-darkset;
end
bw = imbinarize(gray);
bw2 = bwareaopen(bw,pxmin);
bwimg = medfilt2(bw2);


```

```
try
    [y,x] = find(bwimg);
    points_coordinate = [x y];
    laserlength = pdist2(points_coordinate,points_coordinate,'
       euclidean','Largest',1);
    maxdistance = max(laserlength(:))-laserspotdiameter;
    if isempty(maxdistance) == true
        maxdistance = nan;
        fprintf('Max distance was empty\n')
    end
catch
    maxdistance = nan;
    fprintf('error\n');
end

end
```

A.2 MATLAB script for detecting fatigue crack initiation

```
function FailurePoint = IFS_Crack_L_Change(L, base_val,
   noise_val, relative_change)
%%
    if relative_change > 0
        Crit_Val = base_val+noise_val+relative_change;
        Fail_Criterion = L > Crit_Val;
    else
        Crit_Val = base_val-noise_val+relative_change;
```

```
8           Fail_Criterion = L < Crit_Val;
9       end
10
11      TF = Fail_Criterion==1;
12
13      Adiff = diff(TF);
14      ind_start = find(Adiff==1);
15      FailurePoint = [];
16      for i = 1:length(ind_start)
17          Values = TF(ind_start(i)+1:ind_start(i)+2);
18
19          disp(Values);
20          if Values == true(2,1)
21          fprintf('Failure␣found␣for␣index␣starting␣%d\n',
                ind_start(i)+1);
22              FailurePoint = ind_start(i)+1;
23          end
24      end
25
26  end
```